Universidade Estadual Paulista “Júlio de Mesquita Filho"

Doctoral Thesis

Dark Matter in the Milky Way: Uncertainties on its Distribution and Implications on its Particle Nature

---

Author:
María Benito

Supervisor:
Dr. Fabio Iocco

Instituto de Física Teórica

January 2019

IFT - UNESP
INSTITUTO DE FÍSICA TEÓRICA - UNESP

Benito, María
B467d Dark matter in the Milky Way: uncertainties on its distribution and implications on its particle nature/ María Benito. – São Paulo, 2019
139 f. : il.

Tese (doutorado) - Universidade Estadual Paulista (Unesp), Instituto de Física Teórica (IFT), São Paulo
Orientador: Fabio Iocco

1. Via láctea. 2. Matéria escura (Astronomia). 3. Galáxias. I. Título

Sistema de geração automática de fichas catalográficas da Unesp. Biblioteca do Instituto de Física Teórica (IFT), São Paulo. Dados fornecidos pelo autor(a).

Abstract

The detailed knowledge of the dark matter (DM) distribution in the Milky Way (MW) is important for understanding the interplay between baryons and DM in the processes involved in galaxy formation and evolution. It is further a key element for experiments that aim to directly or indirectly detect the DM particle due to theoretically predicted non-negligible, weak interactions between DM and Standard Model particles.

In this thesis, we aim to determine the distribution of DM in our Galaxy. First, we constrain the density profile of the DM halo by means of kinematical tracers of the total gravitational potential. We use objects in circular orbits around the Galactic centre (GC) as tracers of the total dynamical mass. By subtracting from the observed rotation velocities the velocities predicted for the visible component of the Galaxy (stars plus gas) -under the assumption of Newtonian gravity- we derive constraints on the DM distribution in the MW once a given parameterisation for the DM density profile is adopted. For the distribution of the visible, baryonic component of the Galaxy, we adopt a large array of observationally inferred, three-dimensional density profiles. In this way, we bracket current uncertainties on the shape and the normalisation of the Galactic visible component.

Our determination of the DM density profile in the MW proceeds from astrophysical observations. These observations have sizeable uncertainties that need to be properly taken into account. We further present a full data-driven analysis that quantifies astrophysical uncertainties that affect the determination of the DM distribution in the MW, and therefore, the interpretation of results from direct and indirect DM particle searches.

Furthermore, we study the DM distribution in the inner ~ 2 kpc of the Galaxy. The inner Galactic region is dynamically dominated by baryons, and it is at the centre of a long-standing debate on whether the DM profile in the inner regions of galaxies is core or cusp. In our analysis, we adopt an estimate of the total dynamical mass within the inner ~ 2 kpc of the MW. By simply subtracting from the total mass the stellar mass within the region under study, we infer the corresponding DM mass. We further study how this *allowed* DM mass translates into the parameter space of a particular parameterisation for the DM density profile.

Finally, we present a methodology based on kinematical tracers of the total gravitational potential of the Galaxy that can be used for testing modified gravity theories at the scale of spiral galaxies.

Acknowledgements

Son muchas las personas que han estado a mi lado durante el largo camino recorrido por este trabajo de investigación y sin cuyo apoyo, esta tesis no hubiera podido llegar a buen fin. A ellas debo agradecer su ayuda continua que les quiero expresar en mi lengua materna, el español. Más allá de las limitaciones lingüísticas, este agradecimiento trasciende mis palabras y queda también expresado en mis actos.

En primer lugar, quiero mostrar mi gratitud a Fabio Iocco, mi director de tesis doctoral, del que he aprendido mucho en estos años. De ti, Fabio, admiro la manera de ver la ciencia y de saber encontrar la luz en un mar de números, códigos y terminologías. Te agradezco tu esfuerzo, tiempo e infinita paciencia con ocasión de esta tesis doctoral, y antes, durante la investigación del máster.

Ekaterina Karukes me ha acompañado a lo largo de estos dos últimos años y sus discusiones han sido fundamentales en el transcurso del doctorado. Tengo que agradecer también a Alessandro Cuoco que ha actuado como un verdadero co-director de la tesis. Para mi formación han sido muy importantes las discusiones en el Journal Club de los lunes, quizás también porque nos recuerdan continuamente que discutir la ciencia puede ser algo divertido. Estoy agradecida a Manuela Vecchi, Nicolás Bernal, Susana Landau, Eduardo Pontón, Rodrigo Nemmen, Rogerio Rosenfeld y Raul Abramo, entre otros profesores, porque han sido, y siguen siendo, fuente de enseñanza y también de asistencia permanente. Quiero dejar también aquí señal de mi reconocimiento a los miembros del equipo de apoyo del GridUNESP por su disponibilidad constante y su amabilidad y eficacia a la hora de resolver problemas de programación.

A Carmen Lauret le agradezco por haberme hecho disfrutar de la física con sus clases en el ya lejano Bachillerato. Tengo que reconocer que esta investigación me ha hecho volver muchas veces a esas clases.

En el plano personal, me resulta muy grato agradecer a mucha gente que ha estado siempre ahí, especialmente en los momentos en que más lo necesitaba. A Lis, por recordarme que pasito a pasito se recorre el camino. A mis padres y hermana, a mi abuela y mis tíos, por su confianza en mi y su apoyo moral y material incondicional. Y a mis amigas y amigos, por quererme y respetar mis tiempos. No menciono a cada uno de ellos por su nombre, pero están siempre presentes en mi pensamiento.

Por último, aunque no menos importante, quiero agradecer a la agencia CAPES por la beca de estudios que me ha permitido *sustentarme* económicamente durante estos cuatro años.

Contents

List of Abbreviations

AGN	**A**ctive **G**alactic **N**uclei
BBN	**B**ig **B**ang **N**ucleosynthesis
BCG	**B**rightest **C**entral **G**alaxy
BF	**B**est **F**it
CBE	**C**ollisionless **B**oltzmann **E**quation
CL	**C**onfidence **L**evel
CMB	**C**osmic **M**icrowave **B**ackground
CMD	**C**olor **M**agnitude **D**iagram
CMZ	**C**entral **M**olecular **Z**one
CR	**C**redible **R**egion
DF	**D**istribution **F**unction
DIRBE	**D**iffuse **I**nfrared **B**ackground **E**xperiment
DM	**D**ark **M**atter
dSphs	**D**warf **Sph**eroidal**s**
EdS	**E**instein-**d**e **S**itter
ESA	**E**uropean **S**pace **A**gency
FSE	**F**ractional **S**tandard **E**rror
GC	**G**alactic **C**entre
GCE	**G**alactic **C**entre **E**xcess
gNFW	**g**eneralised **N**avarro-**F**renk-**W**hite
HKG	**H**alo **K** **G**iant stars
HPD	**H**ighest **P**osterior **D**istribution
HST	**H**ubble **S**pace **T**elescope
ICM	**I**ntra **C**luster **M**edium
IR	**I**nfra**R**ed
LG	**L**ocal **G**roup
l.o.s.	**l**ine **o**f **s**ight
LSR	**L**ocal **S**tandard of **R**est

MACHO	**MA**ssive **C**ompact **H**alo **O**bject
MAP	**MA**ximum of the **P**osterior
MCMC	**M**arkov **C**hain **M**onte **C**arlo
ML	**M**aximum **L**ikelihood
MW	**M**ilky **W**ay
M2M	**M**ade-to-**M**easure
NFW	**N**avarro-**F**renk-**W**hite
NIF	**N**ear **I**n**F**rared
OGLE	**O**ptical **G**ravitational **L**ensing **E**xperiment
PLI	**P**rofile **L**ikelihood **I**nterval
RAR	**R**adial **A**cceleration **R**elation
RCG	**R**ed **C**lump **G**iant
RC	**R**otation **C**urve
RCG	**R**ed **C**lump **G**iant
ROI	**R**egion **O**f **I**nterest
SIE	**S**ingular **I**sothermal **E**llipsoid
SN	**S**uper**N**ova
2MASS	Two **M**icron **A**ll **S**ky **S**urvey
SMBH	**S**uper **M**assive **B**lack **H**ole
WFIRST	**W**ide **F**ield **I**nfra**R**ed **S**urvey **T**elescope
WIMP	**W**eakly **I**nteracting **M**assive **P**article
WISE	**W**ide-**F**ield **I**nfrared **S**urvey **E**xplorer

Para vosotros, Papá y Mamá.
Que vuestra luz siempre ilumine
nuestras vidas.

Introduction

In the standard model of cosmology ΛCDM, 85% of the Universe matter content is in the form of a non-luminous, *dark* component of matter whose presence is inferred due to its gravitational effect. The nature of the dark matter (DM) particle is unknown. Nonetheless, from its gravitational effects we can infer some of its properties:

- DM is non-baryonic in nature. This is inferred from upper limits on the baryonic matter density derived from observations and predictions of Big Bang Nucleosynthesis (BBN) (e.g. Burles et al. 2001; Iocco et al. 2009) in combination with the dynamics of clusters of galaxies (Bergström 2000), Supernova (SN) data (e.g. Schmidt et al. 1998) and measurements of the cosmic microwave background (CMB) power spectrum (Planck Collaboration et al. 2016b, 2018a). Furthermore, the non-baryonic character of the DM is invoked to explain the growth and today existence of galaxies and clusters of galaxies (Reid et al. 2010; Dodelson 2011).
- At the epoch of structure formation, DM must be non-relativistic or cold, meaning that it has a negligible thermal energy, in order to have the same clustering properties as ordinary matter (e.g. Blumenthal et al. 1984).
- DM must be stable on cosmological time scales.
- DM particles must not experience electromagnetic or strong interactions, otherwise, the DM particle would have been detected yet.
- DM must be collisionless, i.e. there are no interactions within the dark sector, up to the constraints set by cluster mergers. From the offset (if any) between the total mass and galaxy peaks in merging clusters, upper limits on the self-interaction cross-section of DM per unit mass are inferred (e.g. Randall et al. 2008).

The basic processes underlying the formation of structures within the ΛCDM paradigm are well understood (e.g. Blumenthal et al. 1984).[1] Before recombination baryons and photons were coupled in the thermal bath of the young and hot Universe. DM perturbations were decoupled from this bath and grew, first mildly in the radiation dominated Universe, and as a power-law function of time after the matter-radiation equality. Firstly, overdensities grew with the expansion of the Universe until they *decoupled* from the Hubble flow due to their self-gravitational attraction and, thus, started to collapse. The end-product of the latter gravitational collapse is an equilibrium structure known as DM halo. After recombination, baryons decoupled from the photons and fell within the deep DM potential wells. Baryons cooled down through radiative losses, falling deeper into the centre of DM halos where they condensated forming the stars and galaxies we see today.

---

[1] We use the term *structure formation* when referring to the growth of collisionless DM overdensities, and the term *galaxy formation* in order to refer to the formation of the visible galaxy by dissipational collapse of gas in the DM potential well.

Galaxies are embedded in massive DM halos. For example, a typical star formation spiral galaxy like our own Galaxy, the Milky Way (MW), has a stellar disc that extends up to ≈ 15-20 kpc from the centre of the Galaxy, while the DM halo, in which the Galaxy is hosted extends up to ≈ 200 kpc. Furthermore, the mass of the halo of DM is an order of magnitude larger than the mass in stars and gas.

Structure and galaxy formation models are extensively studied through N-body simulations (e.g. Klypin et al. 2011; Schaye et al. 2015). Although the formation of structures is well understood, a complete, self-consistent theory of galaxy formation is still missing mainly due to its complexity. In the processes involved in galaxy formation and evolution, neither the interplay between DM and baryons nor how and by what extent baryonic processes modify the density profile of the DM component are fully understood. Parameterisations derived from simulations that describe the spatial distribution of DM halos are, thus, a jumping-off point for studies that aim to determine the distribution of DM in galaxies observationally.

In this regard, our Galaxy offers a unique opportunity since we have access to it in great detail. The goal of this thesis is to determine the distribution of DM in the MW by confronting DM density parameterisations obtained in N-body simulations with observations of our own Galaxy. In order to do so, we use tracers of the total gravitational potential, namely objects in circular orbits around the Galactic centre (GC). By subtracting from the total gravitational potential of the Galaxy the contribution expected from the pure effect of gravity of the baryonic matter (stars and gas), we infer constraints on the distribution of DM in our Galaxy once a given parameterisation for its density profile is adopted.

Confronting the *observed* DM distribution in our Galaxy with results from N-body simulations could help in a better understanding of the dynamical effects between baryons and DM, thus, constraining galaxy formation and evolution models. On the other hand, precise knowledge of the DM density profile in the MW is fundamental for DM particle searches whose aim is to unravel the very nature of the DM particle. In this thesis, we aim to further quantify astrophysical uncertainties that affect the determination of the DM distribution in the MW and, therefore, affect the interpretation of results from this kind of experiments.

The thesis is structured in three main sections:

- An introductory first section where:
    - We describe the basics of structure formation within a ΛCDM cosmology and present the benchmark DM density profiles obtained from analytical and numerical studies about structure and galaxy formation (chapter 1).
    - In chapter 2, we present a comprehensive, although incomplete review of methods to observationally determine the distribution of DM in astrophysical environments.
- A second part of the thesis is dedicated to the astrophysical setup and distribution of DM in the Galaxy.
    - We describe the three-dimensional distribution of the stellar and gas components of the MW, usually referred to as the baryonic component of the Galaxy in chapter 3.
    - We derive constraints on the distribution of DM in the MW by means of dynamical tracers of the total gravitational potential in chapter 4.

  - In chapter 5, we study the mass distribution in the Galactic bulge region, i.e. inner ≈ 3 kpc of the Galaxy.

- The last part of the thesis is related to the nature of the DM particle.
  - In chapter 6, we quantify astrophysical uncertainties that affect the determination of the DM distribution in the MW and its effects on interpreting results from DM particle searches.
  - In chapter 7, we describe alternative theories to the DM paradigm and present a methodology to test these theories at the scale of spiral galaxies using our own.

Chapter 1

Structure Formation in ΛCDM

Temperature anisotropies observed in the cosmic microwave background (CMB), which are shown in figure 1.1, are related to the field of initial matter density perturbations which are the seeds of the structures we see today. Dark matter (DM) halos are the end-product of the growth of initial perturbations with respect to the background density of the young Universe. Matter perturbations or overdensities are characterised by the density contrast,

$$\delta(t) = \frac{\rho(t) - \bar{\rho}(t)}{\bar{\rho}(t)}, \tag{1.1}$$

where $\bar{\rho}(t)$ is the background density and $\rho(t)$ is the average density of the perturbation both at time t. For perturbations of non-relativistic matter (e.g. cold DM and baryons after decoupling) and smaller than the Hubble radius (i.e. cH^{-1}), the evolution of the density contrast with time is well described by Newtonian gravity. The condition of perturbations being smaller than the Hubble radius can be rephrased in terms of mass: Newtonian gravity is a good description for perturbations (of non-relativistic matter) with an average mass smaller than the mass within the Hubble radius. At matter-radiation equality the mass within the Hubble radius is $\sim 10^{16}\,\mathrm{M}_{\odot}$[1], that is the growth of all relevant perturbations in the formation of galaxies and clusters of galaxies can be safely studied within Newtonian gravity.[2]

The growth of the relevant perturbations for the formation of galaxies and clusters of galaxies is driven by the continuity, Euler and Poisson equations given, respectively, by:

$$\begin{aligned} \frac{\partial \rho}{\partial t} + \boldsymbol{\nabla}(\rho \boldsymbol{u}) &= 0, \\ \frac{\partial \boldsymbol{u}}{\partial t} + (\boldsymbol{u}\boldsymbol{\nabla})\boldsymbol{u} &= -\frac{\boldsymbol{\nabla} P}{\rho} - \boldsymbol{\nabla}\Phi, \\ \nabla^2 \Phi &= 4\pi G \rho. \end{aligned} \tag{1.3}$$

---

[1] We have estimated the average mass within the Hubble radius at matter-radiation equality as

$$\mathrm{M}(< r_H) = \frac{4\pi}{3}\rho_{\mathrm{crit}}(z_{eq})\left[\frac{r_H(z_{eq})}{3}\right]^2, \tag{1.2}$$

where ρ_{crit} and r_H are the critical density and Hubble radius, respectively, at the time of matter-radiation equality z_{eq}. We have adopted the values of the cosmological parameters given in Planck Collaboration et al. 2016b. We have made use of Astropy, a community-developed core Python package for astronomy (Astropy Collaboration et al. 2013, 2018).

[2] The typical mass of a cluster of galaxies today is $\sim 10^{14} - 10^{15}\,\mathrm{M}_{\odot}$.

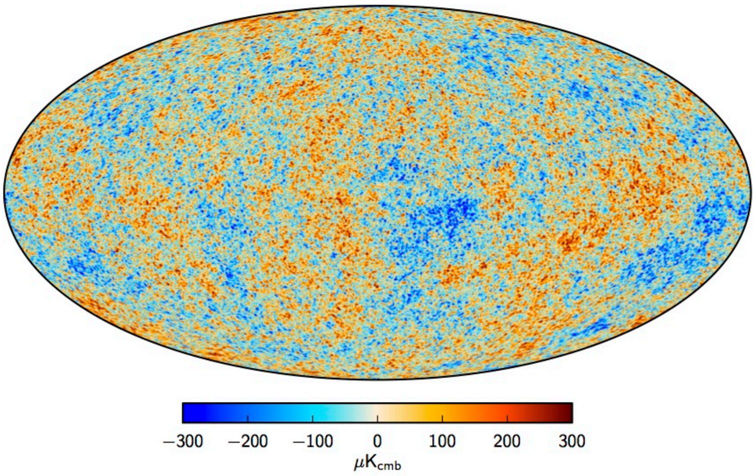

FIGURE 1.1: Temperature fluctuations observed in the CMB. Reddish regions are patches of the sky with higher temperature with respect to bluish regions. Figure taken from Planck Collaboration et al. 2016a.

We decompose the density, pressure, velocity and gravitational potential as a main component and a small perturbation:

$$\begin{aligned} \rho(\boldsymbol{x},t) &= \bar{\rho}(t) + \delta\rho(\boldsymbol{x},t) \\ P(\boldsymbol{x},t) &= \bar{P}(t) + \delta P(\boldsymbol{x},t) \\ \boldsymbol{u}(\boldsymbol{x},t) &= \boldsymbol{u}(t) + \delta u(\boldsymbol{x},t) \\ \Phi(\boldsymbol{x},t) &= \bar{\Phi} + \delta\Phi(\boldsymbol{x},t). \end{aligned} \tag{1.4}$$

At first order in perturbation theory, the combination of the equations of motion (1.3) gives the following expression for the evolution of the density contrast:

$$\frac{\mathrm{d}^2\delta}{\mathrm{d}t^2} + 2H\frac{\mathrm{d}\delta}{\mathrm{d}t} = 4\pi G\bar{\rho}\delta + \frac{c_s^2}{a^2}\nabla^2\delta. \tag{1.5}$$

where $c_s^2 = \delta P/\delta\rho$ is the adiabatic sound speed. The evolution of perturbations is driven by equation (1.5) while the perturbation is small, i.e. $\delta \ll 1$. At this regime called the linear regime, the cosmic density field is described by a linear superposition of sinusoidal perturbations, where each mode is independent of the others. It is clear from the right-hand side of equation (1.5) that the growth of perturbations depends on the balance between gravitational and pressure forces. This balance defines the Jeans scale,

$$\lambda_J = \frac{c_s}{a}\sqrt{\frac{\pi}{G\bar{\rho}}}. \tag{1.6}$$

Fluctuations can grow only when the gravitational force is bigger than the pressure gradient. This condition is satisfied when the size λ of the perturbation satisfies the inequality $\lambda > \lambda_J$.

On the other hand, there is another force affecting the linear growth of perturbations, that is the expansion of the Universe which drives the friction term in the left-hand side of equation (1.5). The rapid background expansion can prevent the growth if the timescale for expansion τ_{exp} is smaller than the time scale for gravitational collapse τ_{grav}. The time scale for gravitational collapse can be approximated by the free-fall timescale (i.e. the characteristic time on which an object would collapse under its own gravitational attraction if no other forces are present). The condition $\tau_{exp} < \tau_{grav}$ is satisfied before matter-radiation equality, therefore in the radiation epoch there is a mild growth of perturbations.

The cosmic density field (i.e. the density field of matter perturbations) is a superposition of modes with different wavelengths:

$$\delta(\boldsymbol{x}, t) = \int \frac{\mathrm{d}\boldsymbol{k}}{(2\pi)^3} \delta_{\boldsymbol{k}}(t) \exp\left(i\boldsymbol{k} \cdot \boldsymbol{x}\right). \tag{1.7}$$

The strength of a given perturbation is $|\delta(\boldsymbol{x}, t)|^2 \propto k^3 P(k)$, where the power spectrum $P(k) = \langle|\delta_{\boldsymbol{k}}|^2\rangle$ measures the power of perturbations on a given scale k. Using the mass scale ($k \sim M^{-1/3}$),

$$\delta \propto k^{3/2}|\delta_{\boldsymbol{k}}| \propto M^{-\frac{n+3}{6}}. \tag{1.8}$$

Therefore for $n > -3$, the spectrum of perturbations is a decreasing function of the mass, i.e. on average small scale fluctuations form earlier than larger fluctuations. This scenario of structure formation is known as hierarchical clustering. A scale-invariant initial power spectrum, i.e. $n \sim 1$, is compatible with CMB observations (Planck Collaboration et al. 2016b, 2018b).

After recombination and once $\delta \gtrsim 1$, the growth of perturbations enters the nonlinear regime: sinusoidal perturbations start interacting with each other, and the cosmic density field is not any more a linear superposition of modes. To properly track the evolution of overdensities in this regime, numerical simulations are needed in order to solve equations (1.3). Nonetheless, we can study the growth of nonlinear overdensities with analytical models. Even though these models are simplifications of the growth of structures, they provide useful insights into the underlying physics behind the formation of DM halos. A complete description of the formation of structures in the Universe in both linear (i.e. $\delta \ll 1$) and non-linear (i.e. $\delta \gtrsim 1$) regimes is presented in Padmanabhan 1993, which is used as a source in the development of this chapter.

In the first part of this chapter, we present analytical models for describing the non-linear gravitational collapse of initial overdensities and compare the results of these models with N-body simulations. In the second part, we describe different parameterisations for the DM density profile used in the literature.

1.1 Analytical Models for Gravitational Collapse

The structures we see today in the Universe were formed from the cosmic density field of initial perturbations by gravitational instability or gravitational collapse (e.g. Blumenthal et al. 1984). While perturbations are small, the growth of structure is described by linear perturbation theory. Once $\delta_i \gtrsim 1$, perturbation theory is not any more valid, and a full treatment of the evolution needs numerical simulations. Nevertheless, there are analytical models that describe the gravitational collapse of an over-density under certain assumptions, such as spherical symmetry. There is not an analytical model that fully describes the formation and growth of structures due to the nonlinear character of these processes. On the contrary, these models are simplifications that offer insight on the physics underlying the formation of structures through gravitational instability.

In this section, we repeat the calculation presented in Mo et al. 2010 in order to sketch two analytical models of gravitational collapse: the spherical collapse of a uniform, collisionless over-density (Gunn and Gott 1972; Gott 1975; Gunn 1977) and the self-similar collapse of collisionless matter (Fillmore and Goldreich 1984; Bertschinger 1985).

Since the formation of structures depends on the background cosmological model, in order to study the gravitational collapse of a given over-density we, firstly, need to choose a cosmology. For simplicity, let us adopt an Einstein-de Sitter (EdS) Universe, i.e. flat matter-only Universe ($\Omega_m = 1$). Table 1.1 summarises the evolution as a function of time of the density, scale factor and linear over-density in an EdS Universe.

$\rho(t) \propto t^2$	$a(t) \propto t^{2/3}$	$\delta_l(t) \propto t^{2/3}$

Table 1.1: Evolution of the density, scale factor and linear over-density in an EdS Universe as a function of time. We have not included the decay mode of the linear over-density $\delta(t) \propto t^{-1}$. The linear over-density can further be written in terms of the growth factor $g(a)$ as $\delta_l(a) \propto a \cdot g(a)$.

Let us assume a spherically symmetric region with an initial uniform density ρ_i slightly higher than the background (or "surrounding") density $\bar{\rho}_i$,

$$\rho_i = \bar{\rho}_i(1 + \delta_i). \tag{1.9}$$

A shell with radius r encompassing an initial mass M_i evolves according to Newton's equation,

$$\frac{\mathrm{d}^2 r}{\mathrm{d}t} = -\frac{GM_i}{r^2}. \tag{1.10}$$

Notice that the mass of the shell from the left-hand side and the right-hand side of the above equation cancel out. The shell has the following specific energy:

$$\varepsilon = \frac{1}{2}\left(\frac{\mathrm{d}r}{\mathrm{d}t}\right)^2 - \frac{GM_i}{r}. \tag{1.11}$$

For $\varepsilon \geq 0$ and assuming constant the mass M_i, the mass shell expands as $r \propto M_i^{1/3} t^{2/3}$ following the Hubble flow. If $\varepsilon < 0$, the mass shell is gravitationally bound: there is an initial period of expansion in which the mass shell is decelerated with respect to the general expansion of the Universe; at a certain time, the expansion is halted, the over-density decouples from the Hubble flow and it collapses under its own gravitational attraction. At the time of *decoupling* or turnaround, the radius of the mass shell, the so-called turnaround radius, is maximum. If there is no shell crossing (i.e. the mass M_i within the mass shell is conserved), the evolution of the mass shell can be written in the following parametric form:

$$r/r_{\mathrm{max}} = \frac{1}{2}(1 - \cos\theta) \qquad \text{and} \qquad t/t_{\mathrm{max}} = \frac{1}{\pi}(\theta - \sin\theta), \tag{1.12}$$

where r_{max} and t_{max} are, respectively, the turnaround radius and time. At $\theta = \pi$, the shell turns around and collapses to $r = 0$ at $\theta = 2\pi$ and time $t_{\mathrm{col}} = 2t_{\mathrm{max}}$. The turnaround radius and time are completely specified in terms of the initial conditions:

$$r_{\max} = \frac{r_i}{5\delta_i/3} \qquad \text{and} \qquad t_{\max} = \frac{3\pi}{4}\frac{t_i}{[5\delta_i/3]^{3/2}}. \tag{1.13}$$

It is convenient to use as variables the Lagrangian radius,

$$r_l(t) = [3M_i/4\pi\bar{\rho}(t)]^{1/3}\,, \tag{1.14}$$

which expands with the Hubble flow, and the initial over-density evolved to time t in linear perturbation theory, i.e. $\delta_l(t)$. With these new variables the evolution of the mass shell takes the following form:

$$\frac{r}{r_l(t)} = \frac{1}{2}\frac{(1-\cos\theta)}{[5/3\delta_l(t)/g_t]} \qquad \text{and} \qquad H_t t = \frac{1}{2}\frac{(\theta-\sin\theta)}{[5/3\delta_l(t)/g_t]^{3/2}}. \tag{1.15}$$

The mean over-density within the mass shell is given by

$$\rho(t) = \bar{\rho}(t)\left[\frac{r_l(t)}{r}\right]^3, \tag{1.16}$$

where $\bar{\rho}(t)$ is the background density at time t.[3] We obtain that the density of the perturbation at turnaround is 5.55 times larger than the background density, i.e.

$$\rho(t_{\max}) = 5.55\bar{\rho}(t_{\max}). \tag{1.17}$$

This corresponds to a linearly evolved perturbation of $\delta_l(t_{\max}) \approx 1.06$ at turnaround and an over-density at collapse:

$$\delta_l(t_{\rm col}) = 1.68. \tag{1.18}$$

This value is the threshold for the collapse of an object: whenever the linearly evolved over-density within a mass shell is ≈ 1.68, the object is said to have collapsed. From equation (1.15), we further obtain that the collapsed radius is $r = 0$ and, therefore, the density is infinite. This is an unphysical solution. Indeed the object collapses before reaching $r = 0$ when the virial theorem is satisfied,

$$E_{\rm kin} = |E_{\rm pot}|/2. \tag{1.19}$$

This implies that $r_{\rm vir} = r_{\max}/2$ at $t_{\rm vir} = t_{\rm col} = 2t_{\max}$. The final state of gravitational collapse is a system in equilibrium: a virialised halo whose structure is governed by collisionless dynamics. At virialisation, the over-density takes the value,

$$\Delta_{\rm vir} = 1 + \delta = \frac{\rho(t_{\max})(r_{\max}/r_{\rm vir})^3}{\bar{\rho}(t_{\rm vir})} = 18\pi^2 \approx 178. \tag{1.20}$$

Following Bryan and Norman 1998, this over-density has been largely used to characterise a DM halo. A DM halo is an object with mass

$$M_{\rm vir} = \frac{4}{3}\pi\, r_{\rm vir}^3\, \Delta\, \rho_m, \tag{1.21}$$

---

[3] Equation valid in the absence of shell crossing.

where $\Delta = 178$ and $\rho_m = \Omega_m \rho_{\rm crit}$ is the mean background density.[4] It is worth stressing here, that several definitions of Δ can be found in the literature. In this thesis, following Klypin et al. 2002; Kafle et al. 2014, we adopt the value $\Delta = 340$.

The above description, in which we have assumed that the mass within a shell is constant, is referred to in the literature as the spherical collapse model (Gunn and Gott 1972; Gott 1975; Gunn 1977). The assumption of no shell crossing is a good approximation during the first period of expansion up to $t_{\rm max}$. After the mass shell turned around for the first time, it starts oscillating about the centre of the perturbation due to its collisionless nature. The assumption of no shell crossing is not anymore valid and the evolution of the mass shell is described by Newton's equation (1.10) where we substitute M_i by

$$M(r) = 4\pi \int_0^r r'^2 \rho(r')\, \mathrm{d}r'. \tag{1.23}$$

In order to understand the oscillation of an individual shell, we must follow the evolution of all the mass shells that have already turned around. To simplify the problem, we can assume that the collapse proceeds in a self-similar way: the trajectory of any given mass shell is the same for all shells once it is rescaled with respect to characteristic length and time scales (Fillmore and Goldreich 1984; Bertschinger 1985). Before reaching turnaround, a mass shell does not cross the orbits of other shells, and, therefore, the evolution of the mass shell in this first period of expansion is given by the spherical collapse model. After the turnaround, we can follow the evolution of the mass shell using self-similarity solutions.

Self-similarity collapse implies that the trajectories of all shells are the same once rescaled with respect to a characteristic length and time. Particularly, the trajectories are the same in the plane ($\tau = t/t_{max}$, $\lambda_* = r/r_{max}$), where $t_{\rm max}$ is the time at the initial turnaround and $r_{\rm max}$ the initial turnaround radius of the shell. The characteristic scale for the mass is, however, the mass within the current turnaround radius $M_t = M(r_t, t)$. Notice that the variable $r_{\rm max}$ is the initial turnaround radius of a particular shell, and r_t is the radius of the shell that is turning around at time t. Equation (1.10) can be rewritten in terms of the new adimensional variables (τ, λ_*) and solved iteratively by numerical methods. For a proper derivation of the mentioned equation, see for example Mo et al. 2010.

We impose that the initial density perturbation is scale-free, i.e.

$$\delta_i = \frac{\Delta M_i}{M_i} \propto M_i^{-\epsilon}, \tag{1.24}$$

thus $r_{\rm max} \propto r_i/\delta_i \propto M_i^{(1/3+\epsilon)}$ and the density profile can be written as

$$\rho(r) \propto M_i/r^3 \propto r^{-\frac{9\epsilon}{(1+3\epsilon)}}. \tag{1.25}$$

For computing this expression, we have assumed that the apocenter of the radial orbit of a mass shell after first turn around is a fixed value of $r_{\rm max}$, that is the mass shell oscillates with a constant apocenter radius. The specific binding energy of a mass

---

[4] $\rho_{\rm crit}$ is the critical density given by

$$\rho_{\rm crit}(z) = \frac{3H^2(z)}{8\pi G}. \tag{1.22}$$

shell is then,

$$E \propto -\frac{M_i}{r_{\max}} \propto -\frac{M_i \delta_i}{r_i} \propto -\frac{M_i^{1-\epsilon}}{r_i} \propto -M_i^{(2/3-\epsilon)}. \tag{1.26}$$

For $\epsilon > \frac{2}{3}$, smaller masses have higher binding energy. Since smaller masses collapsed first, at $t \gg t_{\max}$, the first mass shells to collapse due to their high binding energy are deeply buried in the halo, their oscillation period is much smaller than the dynamical timescale, and the change of the gravitational potential during one oscillation is small. Thus, it can be considered that the apocenter radii of their orbits are constant and the final density profile is a function of the initial conditions. On the other hand, for $\epsilon \leq \frac{2}{3}$, smaller masses have lower binding energy, and the assumption $r_a \propto r_{\max}$ is not valid anymore. Physically, the radial orbits have apocenter radius that spread all over the halo. In this case, the density profile is independent of the initial conditions and has the form r^{-2}. See Mo et al. 2010 for a complete derivation of the density profile.

To sum up, starting with an initial perturbation $\delta_i(r) \propto M_i^{-\epsilon}$, the final density profile is given by

$$\rho(r) \propto \begin{cases} r^{-2}, & \text{if } \epsilon \leq \frac{2}{3}, \\ r^{-\frac{9\epsilon}{(1+3\epsilon)}}, & \text{if } \epsilon > \frac{2}{3}. \end{cases} \tag{1.27}$$

This means that self-similar collapsed models predict DM density profiles described by a single power law with a slope dependence on the initial conditions. Nevertheless, since the mass within the over-density region is not constant, the gravitational potential is, therefore, a function of time. A time-varying gravitational potential allows the change of the energy of individual particles within the mass shells through the process known as violent relaxation (Lynden-Bell 1967), a process that erased information on the initial conditions of the system.

1.2 Numerical Simulations

N-body simulations became a fundamental tool for studying the formation and evolution of structures in the Universe due to the non-linear character of the gravitational collapse process. Numerical simulations track the growth of over-densities from initial perturbations in the cosmic density background of the early Universe up to the structures we see today. Figure 1.2 shows an example of the time evolution of the DM density field tracked by the Millenium simulation (Springel et al. 2005).

The first simulations of a CDM Universe (e.g. Davis et al. 1985; White et al. 1987; Frenk et al. 1988; Dubinski and Carlberg 1991; Moore et al. 1993), which only included DM particles,[5] successfully reproduced the large-scale structure observed in surveys of galaxies. It was further realised that halos formed through collisionless hierarchical clustering have universal density profiles, independently of the mass of the halo and with no dependence on the initial conditions. On the other hand, from analytical models it is not fully understood the dependence on the initial conditions of the DM halo density profile, if any. In DM-only simulations, the spherically averaged density profile of halos from dwarf galaxies ($\sim 10^{11}\,\mathrm{M}_\odot$) to clusters of galaxies ($\sim 10^{15}\,\mathrm{M}_\odot$) is well described by the well-known Navarro, Frenk & White (NFW) profile (Navarro

---

[5] The first DM-only simulation included around $10^4 - 10^5$ DM particles. These particles, with masses $\sim 10^{13}\mathrm{M}_\odot$, are non-relativistic, dissipationless and collisionless.

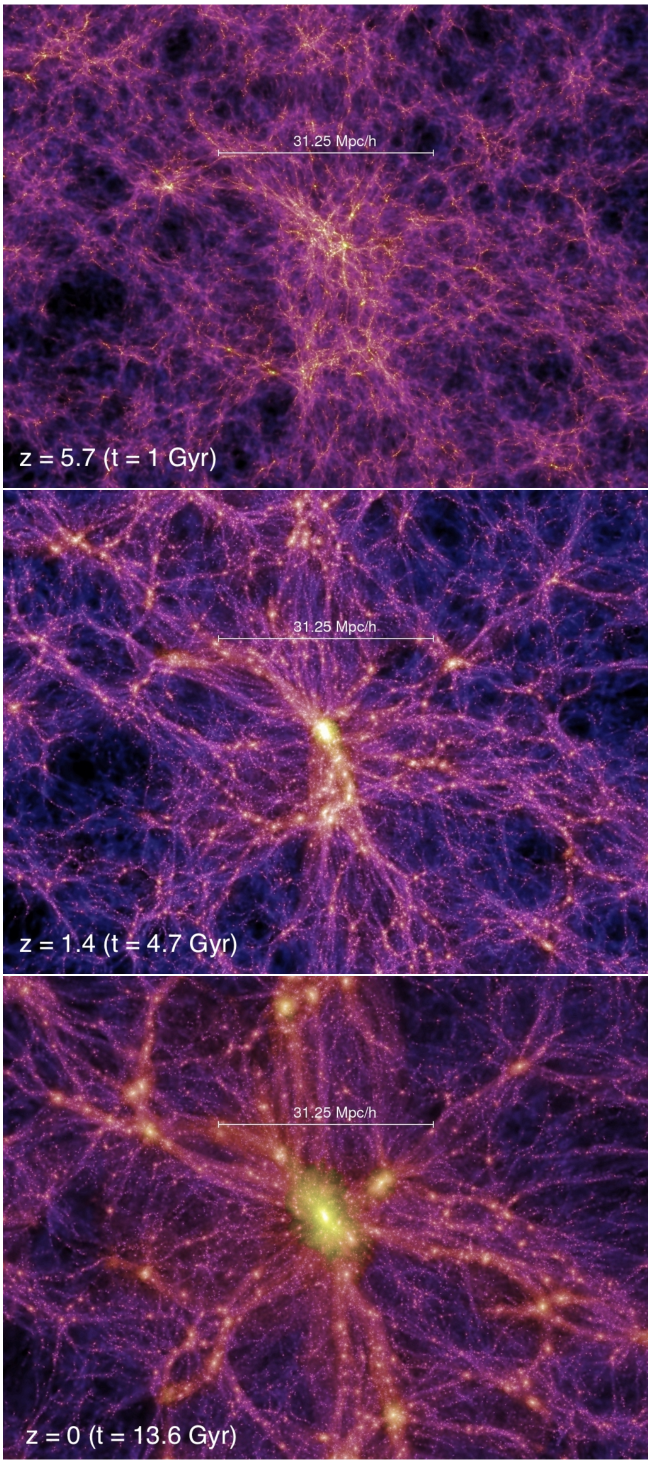

FIGURE 1.2: Slice of the DM density field at three different redshifts obtained in the Millennium simulation (Springel et al. 2005).

et al. 1995, 1996):

$$\rho_{\mathrm{DM}}(r) = \frac{\rho_s}{\left(\frac{r}{R_\mathrm{s}}\right)\left(1 + \frac{r}{R_\mathrm{s}}\right)^2}, \tag{1.28}$$

with R_s and ρ_s the scale radius and scale density, respectively. This density profile describes a broken power law. In the outer region of the halo, the density has a steeper slope than the self-similar analytical solution or isothermal profile, i.e. $\rho \propto r^{-2}$. Close to the scale radius, the profile is nearly isothermal, and the inner part of the DM halo has a shallower slope. The Einasto profile, given in equation (1.31), is another parameterisation found to also describe the spherically averaged density profile of halos from DM-only simulations (e.g. Merritt et al. 2006; Navarro et al. 2010; Gao et al. 2012).

While ΛCDM simulations where only DM is taken into account successfully describe the large-scale structure of the Universe, there are mismatches between DM-only simulations and observations at scales smaller than ~ 0.1 Mpc and masses smaller than $\sim 10^{11}\,\mathrm{M}_\odot$ (see Bullock and Boylan-Kolchin 2017 for a review). Since DM halos also contain baryons, it is actually unclear if the interplay between baryons and DM is able to alleviate these observed discrepancies. A complete, self-consistent theory of galaxy formation is lacking mainly due to its complexity. Galaxy formation poses a multi-scale problem. For example, a given galaxy

- with mass $\sim 10^{12}\,\mathrm{M}_\odot$ contains stars with masses $\sim 1\,\mathrm{M}_\odot$. This corresponds to a mass range of 12 orders of magnitude.
- Furthermore, a super massive black hole (SMBH) at the centre of the galaxy has a physical size $\sim 10^{-6}$ pc and a region of influence ~ 10 kpc, corresponding to a length scale range of $\mathcal{O} \sim 10^{10}$.

Simulations where baryons are also taken into account, the so-called hydrodynamical simulations, do not converge into a single picture of the interplay between baryons and DM. Nevertheless, they seem to agree on some common features (Silk et al. 2013) such as the effect of supernova (SN) driven flows in modelling low mass galaxies (e.g. Governato et al. 2010; Pontzen and Governato 2012) and the formation of stellar discs (Scannapieco et al. 2009; Brook et al. 2011) or Active Galactic Nuclei (AGN) feedback changing the fate of massive galaxies (e.g. Peirani et al. 2008; Martizzi et al. 2012; Choi et al. 2017).

Several processes where baryons are involved are known to affect the DM density profile of halos. For example, the cooling of baryons and their further condensation in the centre of the halo might steepen the inner slope of the DM density profile (Blumenthal et al. 1986). Or the above mentioned SN and AGN feedbacks might produce cores in dwarf and massive galaxies, respectively. Nevertheless, hydrodynamical simulations involve many physical scales, thus posing a complexity which prevents to realistically treat all the relevant physics involved.

1.3 Dark Matter Halo Density Profiles

In this section, we describe different parameterisations of the DM density profile as presented in the literature. We do not aim to give a complete list of profiles but to highlight the characteristics of the most relevant ones. Density profiles are written, firstly, in its *usual* formulation and, secondly, in terms of the Sun's galactocentric distance and the local DM density, i.e. R_0 and ρ_0, respectively. The reason for the latter formulation is twofold: first, to highlight the relevance of Galactic parameters in the determination of the DM distribution in our Galaxy and, second, due to the relevance of the DM density in the solar neighbourhood for searches of the DM particle.

All the parameterisations here described present spherical symmetry. This assumption might be a source of systematics in determinations of the shape of halos since DM-only simulations predict triaxial halos (e.g. Stadel et al. 2009; Muñoz-Cuartas et al. 2011; Vera-Ciro et al. 2011; Schneider et al. 2012; Vera-Ciro et al. 2014). However, the inclusion of baryons tends to rounder the distribution of DM (Kazantzidis et al. 2004; Bailin et al. 2005; Gustafsson et al. 2006; Kazantzidis et al. 2010; Bryan et al. 2013). The assumption of spherical symmetry might introduce systematic uncertainties as large as 35% in the determination of the DM distribution in the MW (Bernal et al. 2014) and $\sim 21\%$ in the estimation of the local DM density (Pato et al. 2010).

1.3.1 Isothermal

One of the first evidences of the existence of a missing component of non-luminous matter was the flat rotation curve (RC)[6] of spiral galaxies (e.g. Rubin et al. 1978, 1980). The flatness of the RC (i.e. $V_c(r) \sim$ constant) well beyond the end of the luminous matter could be explained by the existence of a missing mass with density profile $\rho \propto r^{-2}$. On top of that, dwarf galaxies seem to have a constant-density core up to the extent of the luminous component in order to explain the observed, approximate linear growth of rotation velocities with galactocentric distance (e.g. Carignan and Freeman 1988; Jobin and Carignan 1990; Moore 1994; de Blok et al. 2001; Oh et al. 2015). These observations, together with the observed flat RCs in spiral galaxies, favoured the isothermal density profile given by the following expression:

$$\rho_{\rm DM}(r) = \frac{\rho_c}{1+\left(\frac{r}{R_c}\right)^2} = \rho_0 \left(\frac{R_c+R_0}{R_c+r}\right)^2 . \qquad (1.29)$$

This profile is characterised by two parameters: the radius of the core R_c and the constant density within the core ρ_c. The r^{-2} density dependence of the isothermal profile is further obtained in analytical collapse models.

1.3.2 Generalized NFW

The density profile of DM halos has been extensively studied using numerical simulations (see Navarro et al. 1995, 1996; Fukushige and Makino 2001; Navarro et al. 2004 and references therein). Individual halos ranging from dwarf galaxies up to clusters of galaxies are selected from cosmological simulations,[7] and they are re-simulated with higher resolution. The density profiles are found to be independent of its mass (Dubinski and Carlberg 1991). Furthermore, the Navarro, Frenk & White profile in equation (1.28) is found to fit simulated density profiles averaged over spherical shells for a broad range of masses: from dwarf galaxies up to galaxy clusters (Navarro et al.

---

[6] The RC of disc galaxies, namely the rotation velocities as a function of the distance from the centre of the galaxy, is thought to trace the mass enclosed within the radius at which each velocity is measured (see chapter 2 for more details).

[7] Cosmological simulations describe the formation and evolution of structures at cosmic scales, that is at cosmologically representative volumes.

1996). At the inner part of the halo, the NFW profile has a shallower radial dependence r^{-1} with respect to the isothermal profile found in self-similar models for spherical collapse, i.e. $\rho \propto r^{-2}$. On the other hand, at the outer part of the halo, the slope is found to be steeper with radial dependence r^{-3}.

DM density profiles from dwarf galaxies inferred from HI rotation curves reveal the presence of an inner core of constant density (e.g. Carignan and Freeman 1988; Jobin and Carignan 1990; Moore 1994; de Blok et al. 2001; Oh et al. 2015).[8] On the other hand, the inner density profile of spiral galaxies, and in particular, the inner density profile of our own Galaxy, is at the centre of a long-standing debate on whether the profile has a core or a cusp. Furthermore, not all DM-only simulations found the same inner slope (Klypin et al. 2001). The generalised NFW (gNFW) profile is a generalisation of the NFW profile given in equation (1.28) which takes into account the unknown inner density profile of DM halos. It takes the following form,

$$\rho_{\rm DM}(r) = \frac{\rho_s}{\left(\frac{r}{R_s}\right)^{\gamma}\left(1+\frac{r}{R_s}\right)^{3-\gamma}} = \rho_0 \left(\frac{R_0}{r}\right)^{\gamma}\left(\frac{R_s+R_0}{R_s+r}\right)^{3-\gamma}, \tag{1.30}$$

allowing for a core, $\gamma = 0$ or a cusp $\gamma = 1$. The NFW profile is recovered with $\gamma = 1$. This profile is characterised by three free parameters: γ or the inner slope of the logarithmic density profile, the local DM density ρ_0 which is the DM density at the Sun's position and the scale radius $R_{\rm s}$ which is the radius at which the logarithmic density slope changes from γ to $3-\gamma$, i.e. the radius at which the profile changes its shape.

1.3.3 Einasto

With the improved resolution of dark matter-only N-body simulations, it was found that DM density profiles towards the centre of the halo become shallower more gradually than predicted by the NFW profile. This implies that the latter profile underestimates the density in the innermost regions of the halo (e.g. Merritt et al. 2006; Navarro et al. 2010; Gao et al. 2012). In order to account for this effect, an Einasto profile (Einasto 1965) was proposed to describe the spatial density profile of simulated halos (Navarro et al. 2004; Hayashi and White 2008). This profile takes the following form,

$$\rho_{\rm DM}(r) = \rho_s \exp\left\{-\frac{2}{\alpha}\left[\left(\frac{r}{R_s}\right)^{\alpha} - 1\right]\right\}. \tag{1.31}$$

Rewritten in terms of ρ_0,

$$\rho_{\rm DM}(r) = \rho_0 \exp\left\{-\frac{2}{\alpha}\left[\left(\frac{r}{R_s}\right)^{\alpha} - \left(\frac{R_0}{R_s}\right)^{\alpha}\right]\right\}. \tag{1.32}$$

The logarithmic slope is then a power law with a radial dependence,

$$\beta(r) \equiv -\frac{\mathrm{d}\ln\rho}{\mathrm{d}\ln r} = 2\left(\frac{r}{R_s}\right)^{\alpha}. \tag{1.33}$$

Thus, towards the centre of the halo, the density profile continues to become shallower, contrary to the r^{-1} cusp of the NFW profile.

---

[8] It is worth highlighting that these observations might be subject to systematic uncertainties (see, e.g. Genina et al. 2018 and references therein).

It is important to notice that not all DM-only simulations find the same slope of the density profile at $r \to 0$ (e.g. Fukushige and Makino 1997; Moore et al. 1999; Subramanian et al. 2000). This highlights the difficulty in simulating the innermost part of a halo. Simulated slopes should be taken with caution since they could be affected by systematics due to limited numerical resolution, thus highlighting the importance of testing the results of numerical simulations against observations.

1.3.4 DC14

Until now, we have referred to numerical simulations and analytical solutions that favour a single halo profile independently of the mass. This picture inferred from DM-only simulations is disfavoured by observations and hydrodynamical simulations (e.g. Di Cintio et al. 2014b; Di Cintio et al. 2014a; Schaye et al. 2015). Recent hydrodynamical simulations indicate a relation between the inner slope of the DM density profile and the star formation efficiency, i.e. the stellar-to-halo mass ratio M_*/M_{halo} (Di Cintio et al. 2014b; Di Cintio et al. 2014a; Tollet et al. 2016; Macciò et al. 2017). This dependency, which is shown in chapter 5, is taken into account in the DiCintio or DC14 profile which describes the distribution of halos in recent hydrodynamical simulations (Di Cintio et al. 2014b; Di Cintio et al. 2014a). It takes the following formula,

$$\rho_{\mathrm{DM}}(r) = \frac{\rho_s}{\left(\frac{r}{R_s}\right)^{\gamma}\left[1+\left(\frac{r}{R_s}\right)^{\alpha}\right]^{\frac{\beta-\gamma}{\alpha}}} = \rho_0\left(\frac{R_0}{r}\right)^{\gamma}\left[\frac{1+\left(\frac{R_0}{R_s}\right)^{\alpha}}{1+\left(\frac{r}{R_s}\right)^{\alpha}}\right]^{\frac{\beta-\gamma}{\alpha}} \tag{1.34}$$

with inner, intermediate and outer slopes given as a function of the stellar to halo mass ratio,

$$\begin{aligned}
\gamma &= 2.94 - \log_{10}\left[\left(10^{x+2.33}\right)^{-1.08} + \left(10^{x+2.33}\right)^{2.29}\right] \\
\alpha &= -0.06 + \log_{10}\left[\left(10^{x+2.56}\right)^{-0.68} + \left(10^{x+2.56}\right)\right] \\
\beta &= 4.23 + 1.34x + 0.26x^2,
\end{aligned} \tag{1.35}$$

where $x = \log_{10}(M_*/M_{\mathrm{halo}})$.

It is worth highlighting that not all hydrodynamical simulations have found a correlation between the shape of the DM density profile and the star formation efficiency (Vogelsberger et al. 2014; Schaye et al. 2015; Bose et al. 2018). This discrepancy between numerical simulations is due to different *subgrid* physics implementations. For example, the star formation threshold[9] adopted in the simulation plays a fundamental role in the formation of cores in simulated dwarf galaxies, as shown in Bose et al. 2018 and Benitez-Llambay et al. 2018. For this reason, although baryonic physics seems able to modify the shape of the DM density profile, the magnitude of this effect and its mass dependence remain unclear. Furthermore, the existence of a universal density profile that accounts for the effect of baryons in the DM halo is unknown.

---

[9] The star formation threshold is the value of the number density at which gas is turned into stars in a numerical simulation.

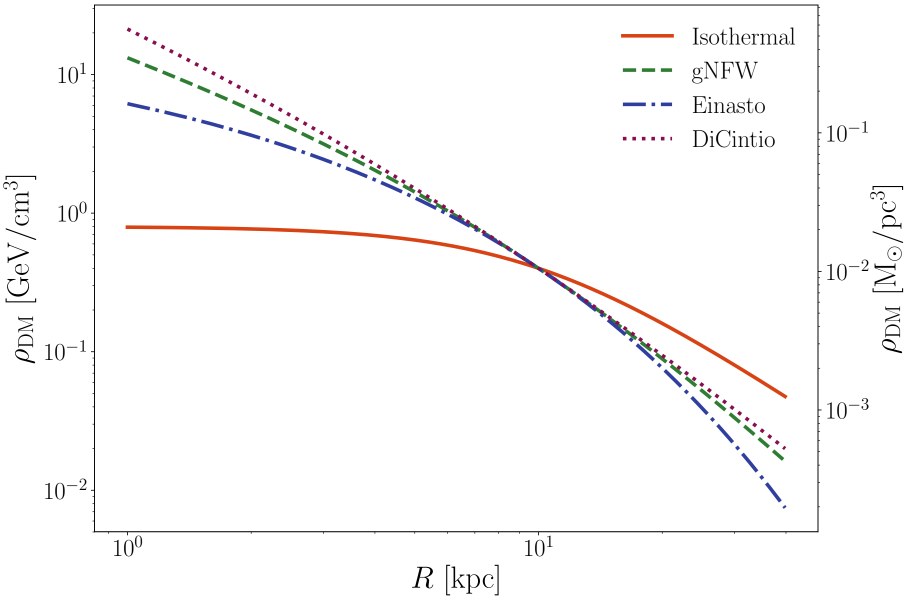

FIGURE 1.3: Isothermal (orange), gNFW (dashed green), Einasto (dash-dotted blue) and DiCintio (dotted purple) DM profiles. The core and scale radius are, respectively, $R_c = R_s = 10$ kpc, the scale density $\rho_s = 0.4\,\mathrm{GeV/cm^3}$. For the gNFW profile, $\gamma = 1$, for the Einasto profile $\alpha = 1$, for the DiCintio profile $\gamma = 1$, $\alpha = 0.5$ and $\beta = 3$. All the profiles are normalised to the same density at 10 kpc from the halo centre.

Chapter 2

Observational Methods to Determine the Distribution of Dark Matter in Astrophysical Objects

In this chapter we offer an overview of different existing methodologies which can be used to observationally infer the distribution of dark matter (DM) in halos. It is not intended to provide a complete list of methods, though to present a comprehensive review of the most-common methodologies found in the literature.

A precise knowledge of the distribution of DM in astrophysical objects of different scales, ranging from dwarf galaxies to clusters of galaxies, is important for constraining galaxy formation and evolution models. The Navarro-Frenk-White (NFW) or Einasto density profiles are good descriptions of the mass distribution of DM halos from DM-only simulations. These parameterisations are commonly adopted in studies that aim to observationally constrain the distribution of DM in astrophysical systems. The *goodness-of-fit* of these profiles to real objects can help understanding the interplay between baryonic processes and DM in the formation and evolution of galaxies. Whether DM-only simulations -within the ΛCDM paradigm- predict the same DM density profile independently of the mass of the halo, feedback processes from the modelling of baryons in hydrodynamical simulations affect the DM distribution in a way that is not fully understood but seems to correlate with the mass of the halo.

Different methodologies constrain the distribution of DM in different astrophysical environments. For instance, the rotation curve (RC) method applies to rotationally supported galaxies or the mass distribution in clusters of galaxies can be derived via gravitational lensing or/and X-ray measurements. The methods to constrain the distribution of DM which are described in this chapter are the following:

- Jeans analysis. For instance, this method is used for constraining the distribution of DM in the halo of the Milky Way (MW) or in dwarf galaxies. It is further used in studies of the gravitational vertical force in the solar neighbourhood.
- RCs trace the total dynamical mass in rotationally supported or disc galaxies.
- Gravitational lensing constrains the distribution of mass in clusters of galaxies or massive galaxies.
- X-ray measurements of hot gas applies to clusters of galaxies or elliptical galaxies.

In the following sections, we describe each of these methodologies.

2.1 Jeans Analysis

A stellar system can be described as a collection of particles in six-dimensional phase space, i.e. the system is instantaneously described by the distribution function (DF) $f(\boldsymbol{x}, \boldsymbol{v})$. The dynamics or time evolution of a self-gravitating stellar system, under the assumption that there is no interaction between individual stars, is driven by the collisionless Boltzmann equation (CBE),

$$\frac{\mathrm{d}f}{\mathrm{d}t} = \frac{\partial f}{\partial t} + \sum_i v_i \frac{\partial f}{\partial x_i} - \sum_i \frac{\partial \Phi}{\partial x_i} \frac{\partial f}{\partial v_i} = 0 \tag{2.1}$$

where the DF has a direct dependence on time t, $f(\boldsymbol{x}, \boldsymbol{v}, t)$, and Φ is the gravitational potential. The system is completely characterised by its six-dimensional DF, nonetheless, in practice it is extremely difficult to solve equation (2.1). For this reason, the CBE is integrated over velocity in order to obtain a set of functions of the three-dimensional position, the so-called Jeans equations (Mo et al. 2010; Binney and Tremaine 2011).

The Jeans equations describe the conservation of mass and momentum of a stellar system under the assumption of dynamic equilibrium, i.e. $\partial f / \partial t = 0$. In cartesian coordinates, Jeans equations take the following form:

$$\frac{\partial \langle v_j \rangle}{\partial t} + \sum_{i=1}^{3} \langle v_i \rangle \frac{\partial \langle v_j \rangle}{\partial x_i} = -\frac{1}{n} \sum_{i=1}^{3} \frac{\partial (n \sigma_{ij}^2)}{\partial x_i} - \frac{\partial \Phi}{\partial x_j} = 0, \tag{2.2}$$

where

$$\langle v_i^k \rangle(\boldsymbol{x}) \equiv \frac{1}{n} \int v_i^k f(\boldsymbol{x}, \boldsymbol{v}) \, \mathrm{d}^3\boldsymbol{v}, \tag{2.3}$$

is the k-th velocity moment of the DF, n is the number density (of the tracer population) or zeroth velocity moment,

$$n(\boldsymbol{x}) = \int f(\boldsymbol{x}, \boldsymbol{v}) \, \mathrm{d}^3\boldsymbol{v}, \tag{2.4}$$

and $\sigma_{ij} = \langle v_i v_j \rangle - \langle v_i \rangle \langle v_j \rangle$ is the velocity dispersion tensor, with

$$\langle v_i v_j \rangle(\boldsymbol{x}) \equiv \frac{1}{n} \int v_i v_j f(\boldsymbol{x}, \boldsymbol{v}) \, \mathrm{d}^3\boldsymbol{v}. \tag{2.5}$$

The Jeans equations do not form a closed set of equations. This is, there are three equations and nine unknowns (3 velocities plus 6 velocity dispersions). Therefore, we need to make further assumptions in order to solve the equations. This methodology is extensively used for studying the dynamics of diverse stellar systems. Among others, the equations constrain the mass distribution in the outskirts of the MW (i.e. region of the Galaxy with galactocentric distances larger than ≈ 20 kpc), the dynamics of dwarf galaxies or the gravitational vertical force in the solar neighbourhood. Depending on the stellar system we aim to study, the assumptions made for solving the set of equations vary accordingly.

2.1.1 Milky Way Stellar Halo

Jeans equations are used to study the dynamics of stars from the stellar halo of our Galaxy (e.g. Deason et al. 2013) or the dynamics of dwarf galaxies (e.g. Bonnivard et al. 2015b). For both cases, we assume spherical symmetry. Under this assumption, equations (2.2) reduce to

$$\frac{1}{\rho}\frac{\mathrm{d}\left(\rho\sigma_r^2\right)}{\mathrm{d}r} + 2\beta(r)\frac{\sigma_r^2}{r} = -\frac{GM_{\mathrm{tot}}(<r)}{r^2}, \tag{2.6}$$

where σ_r and ρ are the radial velocity dispersion and density profiles of the tracer population of stars, respectively, G is Newton's gravitational constant, $M_{\mathrm{tot}}(<r)$ is the total enclosed mass within radius r and $\beta(r)$ is the anisotropy parameter,

$$\beta(r) \equiv 1 - \frac{\sigma_\phi^2 + \sigma_\theta^2}{2\sigma_r^2}, \tag{2.7}$$

where σ_ϕ and σ_θ are the axial and azimuthal velocity dispersions, respectively. The anisotropy parameter can take values in the range $[-\infty, 1]$. If $\beta > 0$, radial motions dominate the dynamics of the stellar system. However, if $\beta = 0$, the system is isotropic and, if $\beta < 0$, tangential motions dominate the dynamics. If $\beta(r)$ is not known, this analysis suffers from the mass-anisotropy degeneracy, that is, the same radial velocity dispersion profile can be obtained by either increasing the mass of the system or by decreasing the anisotropy parameter.

Notice that for deriving equation (2.6), we have taken into account Poisson's equation,

$$\nabla^2\Phi_i(\mathbf{x}) = 4\pi G\rho_i(\mathbf{x}), \tag{2.8}$$

assuming that the total gravitational potential is spherically symmetric.

As an example, let us schematically study the dynamics of the outskirts of our Galaxy by means of stars from the stellar halo of the MW. Surveys, such as, the SDSS/SEGUE or LAMOST surveys measured line of sight (l.o.s.) velocities for large samples of different type of stars -belonging to the stellar halo- up to distances of approximately 160 kpc from the centre of the Galaxy (e.g. Kafle et al. 2014). These are heliocentric l.o.s. velocities that, first, need to be corrected for the solar motion relative to the Galactic centre (GC). In this way, l.o.s velocities in the local standard of rest (LSR)[1] are obtained.

There are three unknowns in left-hand side of equation (2.6): The stellar density profile ρ of the tracer population, the anisotropy parameter β and the radial velocity dispersion profile σ_r. For the former, a broken power-law distribution is commonly adopted. The slope of the density profile of the tracer stars, α, equals values in the range 2-3 up to ~ 20 kpc from the GC and beyond this radii, $\alpha \sim 3.8 - 5$ (e.g. Huang et al. 2016). The anisotropy parameter β can be obtained, for instance, from proper motions of halo stars (e.g. Deason et al. 2013) or by means of simulations (e.g. Xue et al. 2008). The radial velocity dispersion profile σ_r is related to the measured l.o.s. velocity dispersion profile by the following equation,

$$\sigma_r = \frac{\sigma_{l.o.s.}}{\sqrt{1 - \beta(r)A(r)}}, \tag{2.9}$$

---

[1] The LSR is a system co-moving along a circular orbit around the GC with a velocity equal to the local RC velocity Θ_0.

where $A(r)$ is a correction factor (Dehnen et al. 2006),

$$A(r) = \frac{r^2 + R_0^2}{4r^2} - \frac{(r^2 - R_0^2)^2}{8r^3 R_0} \ln \left| \frac{r + R_0}{r - R_0} \right| , \tag{2.10}$$

with R_0 the Sun's galactocentric distance. We can, thus, derive the mass distribution profile in the outer part of the Galaxy by solving equation (2.6). It is important to stress here that the procedure briefly described above it is not the unique way of solving equation (2.6), see, for instance, Kafle et al. 2012, 2014.

The Jeans equations under the assumption of spherical symmetry are also used to determine the mass distribution in the inner regions (up to $\approx 2\%$ of the virial radius[2]) of clusters of galaxies using individual galaxies as tracers of the total gravitational potential (Kelson et al. 2002; Newman et al. 2013b). Since for a given cluster only few individual galaxies are observed, a stacked analysis combining kinematics from several clusters is a common practise (see e.g. van der Marel et al. 2000; Newman et al. 2013b). This methodology has been further used to probe the DM density profile in the inner part of elliptical galaxies by means of stellar kinematics (e.g. Cappellari et al. 2006) and other tracers, such as globular clusters, for probing the outer density profile (e.g. Dekel et al. 2005).

2.1.2 Local DM density

Jeans equations can be used to constrain the gravitational vertical force in the vicinity of the Sun by means of stars with observed vertical number density and velocity dispersion profiles (Kuijken and Gilmore 1989). In this way, we can determine the DM density in the solar neighbourhood (e.g. Silverwood et al. 2016). For this specific application, we need to rewrite Jeans equations (2.2) in cylindrical coordinates. Under the assumption of axial symmetry (i.e. the coupling between axial and vertical motions and the tracer population density are independent of the axial angle ϕ), the Jeans equation in the z-direction takes the following form:

$$\frac{1}{Rn} \frac{\partial (R n \sigma_{Rz})}{\partial R} + \frac{1}{n} \frac{\partial}{\partial z} \left(n \sigma_z^2 \right) = -\frac{\mathrm{d}\Phi}{\mathrm{d}z}, \tag{2.11}$$

where the first term, the so-called tilt term, couples radial and vertical motions. With the further approximation that the tilt term is zero, equation (2.11) has the following analytical solution:

$$n = \frac{C}{\sigma_z^2} \exp \left(- \int_0^z \mathrm{d}z' \, \frac{1}{\sigma_z^2(z')} \frac{\partial \Phi(z')}{\partial z'} \right), \tag{2.12}$$

where $C = \sigma_z^2(0) n(0)$ is a normalisation factor that sets the number density at $z = 0$. It is important to highlight that using Jeans equations implies that tracer stars are in dynamical equilibrium. Furthermore, we are describing a simplified version of this

---

[2] The virial radius is the radius of the sphere which encloses an average DM density equal to ρ_{vir}. In this thesis, we use the following two definitions of ρ_{vir}:

$$\rho_{\mathrm{vir}} = 340 \times \Omega_m \rho_{\mathrm{crit}}$$

and

$$\rho_{\mathrm{vir}} = 200 \times \rho_{\mathrm{crit}}.$$

methodology. A more realistically analysis must include the tilt term since vertical and radial motions are not decoupled (Büdenbender et al. 2015).

As in the spherical case, we need to couple equation (2.12) with Poisson's equation. In cylindrical coordinates, assuming that the underlying gravitational potential has axial symmetry, i.e. $\partial\Phi/\partial\phi = 0$, Poisson's equation (2.8) takes the form:

$$\begin{aligned} 4\pi\rho(R,z) &= \frac{1}{R}\frac{\partial}{\partial R}\left(R\frac{\partial\Phi}{\partial R}\right) + \frac{\partial^2\Phi}{\partial z^2} \\ &= \frac{1}{R}\frac{\partial}{\partial R}\frac{\partial v^2(R)}{\partial R} + \frac{\partial^2\Phi}{\partial z^2} \\ &= \frac{\partial^2\Phi}{\partial z^2}. \end{aligned} \tag{2.13}$$

The flatness of the RC around the Sun's position allows the step from the second to the third line in the above equation. The final system of equations, that need to be solved, is composed of equations (2.12) and (2.13). It is important to highlight, that equation (2.13) depends on the total density and total gravitational potential, while n and σ_z in (2.12) refer to the number density and vertical velocity dispersion profiles of the stellar population used as tracers of the gravitational potential.

There are many approaches in order to solve the system of equations (2.12) and (2.13). The positions and vertical velocities for a sample of stars -of a given stellar population- are the observations, from which we can infer the number density and vertical velocity profiles by binning the data. By plugging these profiles of the tracer stellar population into equation (2.12), we can, thus, obtain the gravitational vertical force and, further, set constraints on the local DM density once a given model for the stellar and gas content in the solar neighbourhood is adopted.

This methodology schematically described above is referred to in the literature as a *local* method for determining the local DM density, ρ_0 (e.g. Read 2014). Contrary to *global* determinations of ρ_0 using the RC, *local* methods are model independent since no parametric DM density profile need to be adopted. *Local* estimations of ρ_0 result in an ample range of preferred ρ_0 values (see Buch et al. 2018; Sivertsson et al. 2018 and references therein). These estimations are affected by systematic uncertainties due to the type of stars used as tracers of the gravitational vertical force in the solar neighbourhood or/and the presence of disequilibria in the data (Banik et al. 2017).

2.2 Rotation Curves

The formation of stellar discs in galaxies has been largely studied using numerical simulations (e.g. Navarro and Benz 1991; Navarro and Steinmetz 2000; Scannapieco et al. 2009). From simulations we have learned that the timing of star formation and galactic winds play a fundamental role in forming discs (Scannapieco et al. 2009; Brook et al. 2011).

At early times, asymmetries in the field of initial perturbations produced tidal torques between surrounding over-densities that got, in this way, angular momentum (e.g. White 1984). Gas collapsed into DM halos and if angular momentum is conserved, it settled down into disc-like configurations where stars formed. Nonetheless, discs are unstable structures against rapid changes on the underlying gravitational potential. Loss of angular momentum occurred during mergers, interactions with other galaxies or gas accretion. For instance, if the angular momentum of the accreted gas and the stellar disc are misaligned, the stellar disc is destroyed (Scannapieco et al. 2009). Since the merger rate decreases with time in ΛCDM, stellar discs need to form late in order to survive until present. For this reason, there must be feedback processes, particularly supernova feedback for galaxies with masses similar to the MW and smaller, that delays the formation of stars to later times. Furthermore, supernova driven galactic winds remove low-angular momentum gas which is later re-accreted with higher angular momentum (Brook et al. 2011).

The stellar discs we observe today in the Universe are stable structures due to rotation around the centre of the galaxy with conservation of angular momentum. The stability of the disc is due to the balance between centrifugal and gravitational force,

$$v^2(r) = r\boldsymbol{F}(r), \tag{2.14}$$

where r is the distance to the centre of the galaxy, v is the circular velocity of an object around the centre of the galaxy and $\boldsymbol{F}$ is the gravitational force both at galactocentric distance r. Circular or rotation velocities in the disc trace, therefore, the underlying total gravitational potential.

Under the assumption of spherical symmetry the above equation takes the following form:

$$v^2(r) = r\frac{\mathrm{d}\Phi}{\mathrm{d}r} = \frac{GM_{\mathrm{tot}}(<r)}{r}. \tag{2.15}$$

Observed RCs of disc galaxies can be measured via the Doppler shift of the 21-cm emission line of neutral atomic hydrogen (e.g. de Blok et al. 2008). The observed velocities trace the total or dynamical mass distribution of the galaxy. By subtracting from the observed velocities, the velocities predicted by the pure effect of gravity of the visible matter, we can infer constraints on the distribution of DM once a given parameterisation for the DM halo is adopted.

Disc galaxies are morphologically decomposed into several components: Bulge, stellar disc, gas and DM halo. Predicted, total rotational velocities are the quadratic sum of the velocities of each of these components. This is,

$$v^2_{\mathrm{pred}}(r) = \sum_i r\frac{\mathrm{d}\Phi_i}{\mathrm{d}r} = \sum_i v_i^2(r) = v_{\mathrm{DM}}(r)^2 + v_{\mathrm{gas}}(r)^2 + \Upsilon v_{\mathrm{stars}}(r)^2, \tag{2.16}$$

where i runs for all the components of the galaxy and Υ is the mass-to-light ratio.[3] We have encoded the contribution of the bulge and stellar disc into a unique circular velocity profile for stars, $v_{\mathrm{stars}}(r)$. If the density profile ρ_i of each component is known, circular velocities are obtained by combining Poisson's equation (2.8) with equation (2.14), that is:

$$\rho_i(\mathbf{x}) \longrightarrow \Phi_i(\mathbf{x}) \longrightarrow v_i(R).$$

A parametric function for the three-dimensional density of stars can be constrained by means of the measured surface brightness profile. The same apply for the gas component whose surface profile can be inferred from the observed HI surface density. For the DM halo, a given parameterisation for its density profile needs to be further adopted.

---

[3] The mass-to-light ratio Υ is the ratio of the stellar mass within a given spatial volume over its luminosity, that is, it converts measured light distribution into mass distribution.

By comparing observed and predicted velocities, we can infer constraints on the parameters of the DM density profile. An important caveat of this methodology is the so-called disc-halo degeneracy due to the unknown mass-to-light ratio Υ. The latter ratio converts measured light distribution into mass distribution and it constitutes one of the main uncertainties of the RC technique (e.g. Lelli et al. 2017a). Its value varies with the measured luminosity waveband and it can be obtained from stellar population synthesis models (e.g. Bell and de Jong 2001).

The flatness of observed RCs from spiral galaxies constitute one of the first evidences for DM (see e.g.Bosma and van der Kruit 1979; van Albada et al. 1985; Sofue and Rubin 2001). The visible component of galaxies alone is unable to reproduce the observed rotation velocities. The mismatch between observed and predicted (only baryons) velocities is explained by means of a *dark* component of matter whose presence is inferred by its gravitational effect. RCs are the main technique to determine the mass distribution in disc galaxies and it is the methodology we are going to use to determine the distribution of DM in our own Galaxy (see chapters 4 and 6). This method can be further used to test modified gravity theories at the scale of spiral galaxies (see chapter 7).

2.3 Gravitational Lensing

Gravitational lensing describes the deflection -by an intervening object named the lens- of light, emitted by a source object, in its way to the observer. This phenomenon is a consequence of the fact that massive astrophysical systems change the geometry of space-time, curving the space-time itself as predicted by the theory of General Relativity. The deflection of light produces multiple images of the source and/or distortion of the source's image.

There are several applications of gravitational lensing such as, for example, measuring the projected two-dimensional mass distribution of the lens (e.g. Fort and Mellier 1994; Rusin and Ma 2001; Bolton et al. 2008a,b; Auger et al. 2010; Suyu et al. 2010) or constraining cosmological parameters (Refsdal 1964). Gravitational lensing further acts as a *cosmic telescope* magnifying faint and distant galaxies that would otherwise remain unobserved by current telescopes. *Micro* lensing of stars in the Galactic bulge by foreground galaxies (i.e. the amplification of the light curve of stars in the Galactic bulge) can be used to constrain the Galactic bulge mass (e.g. Iocco et al. 2011) - technique applied in the analyses of this thesis- or the structural properties of this inner component of the Galaxy (Stanek et al. 1997). Microlensing events had been further suggested as a tool for searches of DM in the form of massive compact halo objects (MACHOs) (Paczynski 1986).[4]

Under the thin lens approximation,[5] gravitational lensing is the transformation of the two-dimensional position, $\boldsymbol{\beta}$, of the source in the source plane into the two-dimensional position of the image, $\boldsymbol{\theta}$, in the image or deflector plane (see figure 2.1). This transformation is given by the following equation,

$$\boldsymbol{\beta} = \boldsymbol{\theta} - \boldsymbol{\alpha}, \tag{2.17}$$

---

[4] MACHOs are objects made of baryonic matter that do not emit radiation.

[5] In the thin lens approximation, the size of the deflector or lens is much smaller than the distances between the observer and the lens and between the lens and the source.

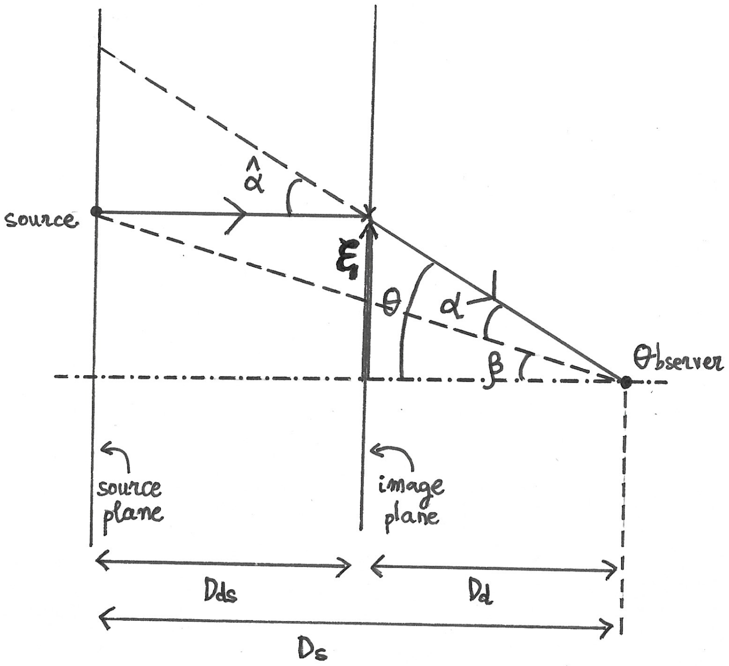

Figure 2.1: Schematic lensing geometry. $\mathrm{D_{ds}}$, $\mathrm{D_d}$ and $\mathrm{D_s}$ are the angular diameter distances between deflector and source, deflector and observer, and source and observer, respectively.

which depends on the total gravitational potential of the deflector, particularly on the projected mass distribution along the l.o.s, $\Sigma(\boldsymbol{\xi})$. For a circularly symmetric lens with constant surface density Σ, the deflection angle α is[6]

$$\alpha = \frac{4\pi G\Sigma}{c^2}\frac{\mathrm{D_d D_{ds}}}{\mathrm{D_s}}\theta. \tag{2.18}$$

It is useful to define the Einstein's radius which defines the radius of the image ring observed for a point source perfectly aligned with a circular surface density lens, i.e. $\beta = 0$. For this particular lens-source configuration, the Einstein radius takes the form,

$$\theta_E = \left[\frac{4G\,\mathrm{M}(<\theta_E)}{c^2}\frac{\mathrm{D_{ds}}}{\mathrm{D_d\,D_s}}\right]^{1/2}. \tag{2.19}$$

Although, this equation must be generalised for the case of non-circular deflectors, it highlights the dependence of the Einstein radius with the total enclosed mass $\mathrm{M}(<\theta_E)$ of the deflector and with the redshift of source and deflector.

There are two regimes of gravitational lensing: strong and weak lensing. Strong lensing occurs when equation (2.17) has multiple solutions, that is, we see multiple images of the same source. On the other hand, in the weak regime the shape of a background galaxy is distorted and there is only one image for each source.

---

[6] Notice that for this lens configuration, the dimensionality of the problem has been reduced to one-dimension.

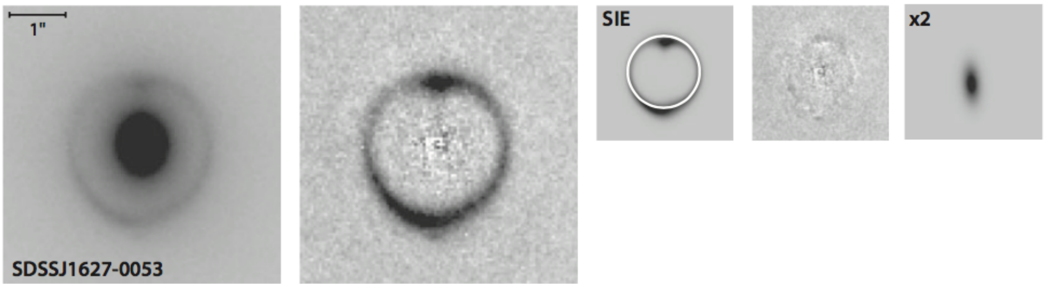

Figure 2.2: Foreground early-type galaxy lensing a background galaxy. From left to right: (1) Observed image, (2) image after subtracting the light from the foreground galaxy acting as deflector, (3) predicted image from the best fit lens model (superimposed in white the Einstein's circle), (4) residuals obtained by subtracting observed and predicted images, i.e. (2)-(3), (5) predicted image for the source in the best fit lens model. Figure taken from Treu 2010.

2.3.1 Strong regime

Strong lensing occurs when the lens equation (2.17) has multiple solutions. The typical distance between multiple images is given by the Einstein's radius which further defines the physical scale on which the surface mass distribution of the deflector can be determined by means of strong lensing.

In figure 2.2, we show an example of an early-type galaxy[7] acting as a deflector of a background galaxy. In order to study the lens system we need a model that simultaneously describes the distribution of light of the source and the mass distribution of the deflector. The background galaxy or source can be modelled by a Gaussian distribution, and for the deflector, a singular isothermal ellipsoid (SIE) is usually adopted. The surface mass density of a SIE model is given by,

$$\Sigma(\boldsymbol{\xi}) = \frac{\sigma_{\rm SIE}^2}{2G} \frac{1}{\sqrt{\xi_1^2 + f^2 \xi_2^2}}, \tag{2.20}$$

where f is the ratio between major and minor axis (Kormann et al. 1994), G is Newton's gravitational constant and $\boldsymbol{\xi} = (\xi_1, \xi_2)$ is a vector in the image plane (see figure 2.1). This model -that simultaneously described the distribution of source and deflector- constrains the total mass within the Einstein's radius θ_E. To further infer constraints on the mass distribution, photometric and spectroscopic measurements are needed. From the former, the stellar surface brightness profile of the deflector is obtained once a given parameterisation is adopted. The stellar surface brightness of the deflector is usually described by a de Vaucouleurs profile (de Vaucouleurs 1974), i.e. surface brightness $\propto R^{1/4}$. From spectroscopic surveys, we can infer the stellar velocity dispersion profile. We can, thus, combine these measurements in a spherical Jeans analysis in order to constrain the total mass distribution of the deflector within the Einstein's radius.

Strong lensing measurements have been used to probe the mass distribution of clusters of galaxies within radius between $\approx 10 - 100$ kpc (e.g. Fort and Mellier 1994). It was further used to probe the gravitational potential of early-type galaxies (e.g. Rusin and Ma 2001; Bolton et al. 2008a,b; Auger et al. 2010; Suyu et al. 2010) and to break

---

[7] We refer to elliptical and lenticular galaxies as early-type galaxies.

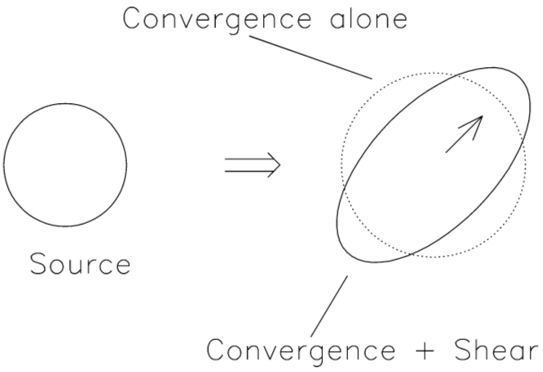

FIGURE 2.3: Effect of a background galaxy lensed by a foreground astrophysical system in the weak lensing regime. Figure taken from Narayan and Bartelmann 1996.

the mass-anisotropy degeneracy in combination with stellar kinematics in this type of galaxies (e.g. Barnabè et al. 2009).

2.3.2 Weak regime

In the weak regime, measurements of the coherent distortion of background sources trace the two-dimensional mass or surface density of the lens (Kaiser and Squires 1993). In this regime, the size of the sources are increased (due to convergence) and its shape is modified (due to shear) as seen in figure 2.3.

Weak gravitational lensing probes the distribution of mass in the outer parts of clusters of galaxies between approximately 100 kpc and a few Mpc. It is the only tool for measuring the distribution of mass up to the virial radius in clusters. Strong and weak lensing can be applied to study the distribution of mass at a certain range of distances from the centre of the cluster. In order to determine the DM density profile for the whole cluster, a combination of methods should be applied (see e.g. Newman et al. 2013a,b). Weak lensing has further been used to probe the mass distribution in the outer regions of elliptical galaxies (see Gavazzi et al. 2007 and references therein).

Using weak gravitational lensing for reconstructing the gravitational potential of the Bullet cluster[8], together with X-ray measurements of the hot gas, Clowe et al. 2006 found an offset between the peaks of the baryonic or hot gas[9] mass and that of the total mass. This offset is an evidence favouring the DM paradigm, while modified gravity theories have difficulties in explaining it.

2.4 X-ray Measurements

For gas in hydrostatic equilibrium, the gas pressure p_{gas} and the total gravitational force balance satisfying the following condition under the assumption of spherical

---

[8] The Bullet cluster is an astrophysical system that consists on two colliding clusters of galaxies.

[9] Hot gas is the main baryonic component of a cluster, corresponding to $\approx 85\%$ of the total baryonic mass budget of the cluster.

symmetry,

$$\frac{GM_{\rm tot}(<r)}{r^2} = -\frac{1}{\rho_{gas}}\frac{{\rm d}p_{gas}}{{\rm d}r}, \tag{2.21}$$

where $M_{\rm tot}(<r)$ is the total mass enclosed within a sphere of radius r and ρ_{gas} is the gas density. By differentiating both sides of the above equation with respect to r, we obtain the following expression that relates the distribution and temperature $T(r)$ of the gas with the total mass of the system:

$$M_{\rm tot}(<r) = -\frac{k_B T(r) r}{G\mu\, m_p}\left(\frac{{\rm d}\ln\rho_{gas}}{{\rm d}\ln r} + \frac{{\rm d}\ln T}{{\rm d}\ln r}\right) \tag{2.22}$$

where k_B is the Boltzmann constant, $\mu = \rho/(n m_p)$ is the mean molecular weight, m_p is the proton's mass and n is the number density of the gas. For deriving the last equation, we have used the ideal gas law,

$$p_{gas} = \frac{k_B T}{\mu\, m_p}\rho_{gas}. \tag{2.23}$$

Hot gas is the main baryonic component in clusters of galaxies. Its typical temperature is $10^7 - 10^8$ K, that is, it is highly ionised, and it radiates X-rays via thermal Bremsstrahlung (e.g. Buote and Lewis 2004). From the observed X-ray spectra and surface brightness, the gas density and temperature profiles of the cluster can be derived. Usually parametric functions are adopted for both gas density and temperature, which may introduce strong priors on the analysis (Newman et al. 2013a). By combining the gas density and the temperature in equation (2.22), we can infer the total mass of the cluster as a function of the radius (see Schmidt and Allen 2007 and references therein). A further source of systematic uncertainties within this method is the assumption of hydrostatic equilibrium and non-thermal contributions to the pressure. In order to avoid systematics of this kind, this method only applies for relaxed clusters, i.e. clusters with regular image morphologies.

X-ray measurements can be further used to probe the gravitational potential of bright elliptical galaxies surrounded by a hot gas coronae (e.g. Mushotzky et al. 1994).

Chapter 3

The Visible Component of the Milky Way

In this chapter we describe the three-dimensional distribution of baryons, i.e. stars and interstellar gas, in the Milky Way (MW). Likewise in external galaxies, the distribution of baryons can be described by a superposition of different morphologically identified components, such as the bulge, stellar disc and interstellar gas. Each of these components is an independent kinematic structure described by a parametrised density profile.

Modelling the large-scale distribution of the baryons in the MW has historically been a difficult undertaking, especially in the inner region of the Galaxy, mostly due to dust obscuration or extinction in the optical band. Despite of the many efforts, the actual mass distribution of baryons in the Galaxy is uncertain with different groups identifying different possible morphologies for each of the MW's baryonic components. For this reason, instead of picking one given parameterisation for the stellar distribution in the MW, we adopt a large array of observationally inferred density profiles to describe the three-dimensional morphology of baryons. The density profiles adopted in this thesis for each baryonic component (stellar bulge, disc and gas) are described in this chapter. By combining individually a selected choice of each component (and then varying one at the time) we obtain a large array of individual morphologies which bracket the systematic uncertainty on the distribution of the baryonic mass in our Galaxy.

From the three-dimensional density profile of each baryonic component, we can inferred -by solving Poisson's equation- the corresponding gravitational potential and, thus, the predicted rotation curve (RC). As we will show in chapter 4, by subtracting from the observed rotation velocities, the velocities predicted by the pure effect of gravity of the visible component of the MW, we can infer constraints on the distribution of DM in our Galaxy.

3.1 Stellar Bulge

The stellar bulge is a morphologically identified stellar component in the inner central region of the Galaxy. It extends up to 3-4 kpc from the GC and it contains approximately 15% of the luminous matter (Bland-Hawthorn and Gerhard 2016). Understanding the bulge's structure has been historically a difficult task, mostly due to dust extinction in the optical band. Due to our position within the Galaxy, we are able to resolve individual stars and star counts analyses help us unrevealing the three-dimensional structure of the Galactic bulge. The latter is important for galaxy formation models since the actual shape of the bulge correlates with its formation history: More spheroidal (classical) bulges are formed in the initial gravitational collapse of the Galaxy or by subsequent mergers. On the other hand, triaxial (pseudo-)bulges are formed through secular evolution processes and disc instabilities. Recent reviews on the Galactic bulge are Rich 2013; Gonzalez and Gadotti 2016; Shen and Li 2016

The galactic bulge is a triaxial bar with its semi-major axis rotated a given angle α from the Sun-GC line. The near end of the bar is in the first Galactic quadrant (positive Galactic longitudes). The bar-like structure was first suggested to explain non-circular gas kinematics (de Vaucouleurs 1974). It was confirmed by infrared observations (Blitz and Spergel 1991), and its presence was unambiguously established using near-infrared (NIR) photometry from the Diffuse Infrared Background Experiment (DIRBE) instrument on board the COBE satellite (Weiland et al. 1994). The bar has a boxy, peanut shape first revealed by the COBE data (Dwek et al. 1995). There is a debate on whether the bar has a further X-shape.

The observed bi-modality in the luminosity distribution of Red Clump Giants toward the GC (RCGs)[1] (McWilliam and Zoccali 2010; Nataf et al. 2010) has been interpreted as a bi-modality in distance, therefore representing the two edges of an X-shape. Furthermore, the bulge appears to have a faint X-shape structure in an image of the Wide-Field Infrared Survey Explorer (WISE) (Ness and Lang 2016). The robustness of this second evidence has been questioned since the X-shape appears after subtracting an ellipsoidal component from the main image and, as shown in Han and Lee 2018, this might be an artefact of the subtraction.

On the other hand, the bi-modality in the luminosity of RCGs has been explained by multiple stellar populations: the brightest luminosity peak is due to an helium-enhanced second-generation of stars and the faintest peak is explained by a normal first-generation of RCGs (Lee et al. 2015; Joo et al. 2017). On top of this, the X-shape has not been seen in RR Lyrae (Pietrukowicz et al. 2015), main sequence stars (López-Corredoira 2016) or Mira variables (López-Corredoira 2017). Not finding the X-shape in the old RR Lyrae or the young main sequence stars might not be a problem to the X-shape interpretation since it is widely accepted the view of a composite Galactic bulge. For example, it is well-established the coexistence within the bulge of a metal-rich stellar population traced by Red Clumps and a metal-poor population traced by RR Lyrae stars. The latter has been shown to be more spheroidally distributed (Dékány et al. 2013). Nonetheless, the Mira variables might pose a problem to the X-shape interpretation since both RCGs and Mira variables are though to have the same age, and therefore the same origin (López-Corredoira 2017). Nevertheless, a full analysis of the metallicity of the Mira variables is still missing. To sum up, the origin of the bi-modality in the Red Clump luminosity distribution will remain an open question after additional information on distances is available.

The discrepancies on the shape and orientation of the triaxial bar found in the literature might be originated by the presence of different stellar populations within the stellar bulge, the methodology adopted and/or the type and covered area of the measurements used in characterising the bulge structure. Within this work we adopt a ample array of observationally inferred density profiles in order to bracket systematic uncertainties on the spatial modelling of the bulge. The density profiles are separated

---

[1] RCGs are used as standard candles since their absolute magnitudes have mild dependence on age and metallicity.

into a spatial component normalised by a constant, further multiply by a cutting function:

$$\rho_b(x,y,z) = [\bar{\rho}_b \times f_b(x,y,z)] \times f_c(x,y), \tag{3.1}$$

where $\bar{\rho}_b$ is the normalised density, that is it describes the weight of the bulge with respect to the total mass budget, and $f_b(x,y,z)$ describes the spatial distribution. The bulge's density profile cannot extend beyond the corotation radius, beyond which there are no stable stellar orbits. This dynamical limitation is taken into account by multiplying the density profile by a cutoff function $f_c(x,y)$.

All coordinates are Galactic coordinates with the Sun at $(R_0, 0, 0)$,[2] the z-axis pointing to the North Galactic Pole (NGP), the x-axis pointing towards the Sun, and the y-axis in the direction of $\ell = -90^{\circ}$ (i.e. to the right, when seen from the NGP). All spatial distributions are given either in galactocentric cartesian coordinates (x,y,z), or in galactocentric cylindrical coordinates (r,ϕ,z), with ϕ increasing in the direction of Galactic rotation, i.e. clock-wise as seen from the NGP. The bulge morphologies adopted in this work are summarised in table 3.1 and, they are described in detail in the following sections. Bulge's density profiles are written as a function of the coordinates (x_p, y_p, z_p) which are the principal axes of the triaxial bar. This coordinate system is related to the galactocentric Cartesian coordinate system (x,y,z) by a clockwise rotation,

$$\begin{aligned} x_p &= x\cos\alpha - y\sin\alpha \\ y_p &= x\sin\alpha + y\cos\alpha \\ z_p &= z, \end{aligned} \tag{3.2}$$

where α is the angle between the principal axis of the triaxial bulge's density profile and the Sun-GC line.

Bulge 1

This density profile corresponds to the *gaussian-type function G2* given in Stanek et al. 1997. It describes a triaxial, boxy bar with the following spatial distribution:

$$f_b(x_p,y_p,z_p) = \exp\left(-r_s^2/2\right) \tag{3.3a}$$

$$r_s = \left\{\left[\left(\frac{x_p}{x_0}\right)^2 + \left(\frac{y_p}{y_0}\right)^2\right]^2 + \left(\frac{z_p}{z_0}\right)^4\right\}^{1/4}, \tag{3.3b}$$

where $x_0 = 1.239$ kpc, $y_0 = 0.609$ kpc and $z_0 = 0.438$ kpc.[3] The major axis x_0 is rotated an angle $\alpha = 24.9^{\circ}$ with respect to the line GC-Sun.

For *bulge 1* and *bulge 2*, the corotation radius is $R_c = 3.5\,\mathrm{kpc}$ (Bissantz and Gerhard 2002) and the cutting function takes the following form (Dwek et al. 1995),

$$f_c(x,y) = \begin{cases} 1.0 & \mathrm{for\ R_{xy} = \sqrt{x^2+y^2} \le R_c} \\ \exp\left(-R_{xy}^2/2r_0^2\right) & \mathrm{for\ R_{xy} > R_c} \end{cases} \tag{3.4}$$

---

[2] All parameters taken from observational studies can be rescaled to any other R_0 value: distances in the xy-plane scale as R_0, distances in the z-direction and surface densities as R_0^0, volume and number densities as R_0^{-1} and masses as R_0.

[3] We quote parameters' values as given in the original references, i.e. without rescale.

$f_b(x,y,z)$	Bar angle $[^o]$	$x_0 : y_0 : z_0$	Tracers	R_0 [kpc]	Reference
$e^{-r_s^2/2}$	24.9	3.6:1.5:1	RCGs counts	8	Bulge 1 Stanek et al. 1997
e^{-r}	23.8	2.8:1.4:1	RCGs counts	8	Bulge 2 Stanek et al. 1997
$e^{-r^2}/(1+r)^{1.8}$	15	3.2:2.2:1	bulge's stars counts	8.7	Bulge 3 Vanhollebeke et al. 2009
$e^{-r^2}/(1+r)^{1.8}$	20	2.6:0.8:1	COBE map, RCGs counts	8	Bulge 4 Bissantz and Gerhard 2002
$e^{-r_s^2/2}+r_a^{-1.85}e^{-r_a}$	20	3.7:1.5:1	COBE map, stellar kinematics	8	Bulge 5 Zhao 1996 Zhao 1996
$\text{sech}(-r_f)+e^{-r_f}$	12.9	3.7:1.3:1	bulge's star counts	8	Bulge 6 Robin et al. 2012

Table 3.1: Stellar bulge morphologies adopted in this work. The first column contains the bulge spatial distribution described by $f_b(x,y,z)$, see (3.1), the second column is the angle between the bar major axis and the GC-Sun line, with the major axis in the first Galactic quadrant. The third column is the axis ratio of the triaxial bar, the forth column is the type of measurements or tracers used to constraint the bulge's shape. The fifth column is the Sun's galactocentric distance adopted in the original reference given in the last column. The definitions of r_s, r and r_f are given, respectively, in (3.3b) (3.5b) and (3.9b).

With $r_0 = 0.5\,\text{kpc}$.

Stanek et al. 1997 used Red Clump Giants (RCGs) as tracers of the three-dimensional distribution of the Galactic bulge. RCGs were selected from the V, V-I color-magnitude diagrams (CMDs) across 12 fields within longitude $-6 < \ell < 9$ and latitude $-8 < b < 3$. The CMDs used in this analysis were obtained by the Optical Gravitational Lensing Experiment (OGLE).

Bulge 2

Bulge's profile also given in Stanek et al. 1997 where it is referred to as the *exponential-type E2*. It has the following shape,

$$f_b(x_p, y_p, z_p) = \exp\left(-r\right) \tag{3.5a}$$

$$r = \left[\left(\frac{x_p}{x_0}\right)^2 + \left(\frac{y_p}{y_0}\right)^2 + \left(\frac{z_p}{z_0}\right)^2\right]^{1/2}, \tag{3.5b}$$

where $x_0 = 0.899$ kpc, $y_0 = 0.386$ kpc, $z_0 = 0.250$ kpc. The angle between the major axis and the line GC-Sun is $\alpha = 23.8^o$.

As for *bulge 1*, the parameters of this density profile are obtained by fitting the histogram of RCGs in 12 CMDs across the bulge region (Stanek et al. 1997).

Bulge 3

Stellar bulge density profile describe by a truncated power-law (Vanhollebeke et al. 2009):

$$f_b(x_p, y_p, z_p) = \frac{\exp\left(-r^2/r_0^2\right)}{\left(1 + r/r_1\right)^{1.8}}, \tag{3.6}$$

where r is given in equation (3.5b), $x_0 = 1$ kpc, $y_0 = 0.68$ kpc, $z_0 = 0.31$ kpc, $r_0 = 2.5$ kpc and $r_1 = 0.095$ kpc. The bar is rotated an angle $\alpha = 15^{\text{o}}$ with respect to the Sun-GC line.

There is no cutting function for *bulge 3* and *bulge 4*. Both density profiles are truncated above r_0.

The parameters of this density profile are obtained in Vanhollebeke et al. 2009. The spatial distribution is traced by bulge's stars selected from $\mathrm{K_s}$, $\mathrm{J\text{-}K_s}$ CMDs from the Two Micron All Sky Survey (2MASS) and I, V-I CMDs from OGLE-II across 11 fields within $-12 < \ell < 11$ and $-6 < b < 3$.

Bulge 4

Same truncated power-law density profile as *bulge 3*. It differs from the latter by a multiplicative constant $1/(y_0 z_0 r_0^3)$ which can be understood as part of the normalisation,

$$f_b(x_p, y_p, z_p) = \frac{1}{y_0 z_0 r_0^3} \frac{\exp\left(-r^2/r_0^2\right)}{\left(1 + r/r_1\right)^{1.8}}, \tag{3.7}$$

where $x_0 = 1$ kpc, $y_0 = 0.31$ kpc, $z_0 = 0.38$ kpc, $r_0 = 2.8$ kpc, $r_1 = 0.1$ kpc and the angle between the bar major axis and Sun-centre line is $\alpha = 20^{\text{o}}$. Notice that this morphology describes a prolate bulge rather than oblate as the rest of bulge's morphologies.

The parameters of the density profile are obtained in Bissantz and Gerhard 2002 by fitting the infrared surface brightness map from COBE/DIRBE together with the luminosity function of RCGs across the 12 fields given in Stanek et al. 1997 (c.f *bulge 1* and *bulge 2*).

Bulge 5

This bulge's morphology describes a triaxial bar combined with an axisymmetric spheroidal bulge (Zhao 1996):

$$f_b(x_p, y_p, z_p) = \exp\left(-0.5 r_s^2\right) + r_a^{-1.85} \exp\left(-r_a\right) \tag{3.8a}$$

$$r_a = \frac{\left(x_p^2 + y_p^2\right)}{z_0^2/q_a^2} + \frac{z_p^2}{z_0^2} \tag{3.8b}$$

The parameter r_s is given in equation 3.3b, $x_0 = 1.49$ kpc, $y_0 = 0.58$ kpc, $z_0 = 0.4$ kpc, $q_a = 0.6$ and the angle between the major axis of the bar and the Sun-centre line is $\alpha = 20^{\text{o}}$. Notice that the spheroidal component and the triaxial bar are aligned, i.e. both major axis coincide.

The cutoff function is given by equation (3.4), where $R_c = 3.3\,\text{kpc}$ (Zhao 1996).

Zhao 1996 built a dynamical model of the Galactic bulge using the Schwarzschild orbit-superposition technique Schwarzschild 1979. This technique describes the collisionless system under study as a linear superposition of orbits in a common gravitational potential. The rationale of the Schwarzschild method is as follows. First, Poisson equation gives the gravitational potential once a density profile is adopted. Then, a large array of orbits are obtained by numerical integration of the equations of motion. Each orbit is characterised by a weight which are further determined by fitting observations. If there is no acceptable linear combination of weights that matches the set of observations, then the assumed density profile can be excluded.

The observational constraints used by Zhao 1996 in order to constraint his Galactic bulge's model are the NIR surface brightness map from COBE/DIRBE and stellar kinematic data. The stellar kinematic data comprises radial velocity and velocity density profiles across different fields toward the Galactic bulge region (see table 3 from Zhao 1996).

Bulge 6

Bulge's density profile that consists on two ellipsoidal components given by Robin et al. 2012,

$$f_b(x_p, y_p, z_p) = \mathrm{sech}^2(-r_f) + f_e \exp(-r_f) \tag{3.9a}$$

$$r_f = \left\{ \left[\left(\frac{x_p}{x_0} \right)^{c_\perp} + \left(\frac{y_p}{y_0} \right)^{c_\perp} \right]^{c_\parallel / c_\perp} + \left(\frac{z_p}{z_0} \right)^{c_\parallel} \right\}^{1/c_\parallel} \tag{3.9b}$$

The hyperbolic secant ellipsoid corresponds to the dominant component at latitudes below $\approx 5^{\mathrm{o}}$, while the exponential ellipsoid is seen mainly at high latitudes. The parameters for the hyperbolic secant are $x_0 = 1.46$ kpc, $y_0 = 0.49$ kpc, $z_0 = 0.39$ kpc, $c_\parallel = 3.007$ and $c_\perp = 3.329$. For the exponential part, $x_0 = 4.44$ kpc, $y_0 = 1.31$ kpc, $z_0 = 0.80$ kpc, $c_\parallel = 2.786$ and $c_\perp = 3.917$. The angle between the line of sight and the Galactic bar's major axis is $\alpha = 12.9^{\mathrm{o}}$.

There are two cutting functions. One that multiplies the hyperbolic secant ellipsoid, and another cuttoff function multiplying the exponential ellipsoid. Both cuttoff functions take the form of equation (3.4). For the hyperbolic secant and exponential ellipsoids, the corotation radius take the value $R_c = 3.43\,\mathrm{kpc}$ and $R_c = 6.83\,\mathrm{kpc}$, respectively (Robin et al. 2012).

The parameters of this density profile are constrained using bulge's stars from $\mathrm{K_s}$, J-$\mathrm{K_s}$ CMDs from the Two Micron All Sky Survey (2MASS) across 200 fields within $-20^{\mathrm{o}} < \ell < 20^{\mathrm{o}}$ and $-10^{\mathrm{o}} < b < 10^{\mathrm{o}}$.

3.2 Stellar Disc

The stellar disc extends up to ~ 20 kpc from the GC, presents axial symmetry and contains approximately $\sim 75\%$ of all Galactic stars (Bland-Hawthorn and Gerhard 2016). It is well described by a double exponential, with main uncertainties on the scale-radius and scale-height values. Discrepancies on the radial and vertical scale-lengths might be originated by the type of stars used as tracers of the three-dimensional distribution, the different patches of the sky observed and/or the technique adopted. The studies

$f_d(r,z)$		R_d [kpc]	z_h [kpc]	Tracers	R_0 [kpc]	Reference
$e^{-r}e^{-\|z\|}$	single	2.15	0.40	G-dwarfs	8	Disc 1
				kinematics		Bovy and Rix 2013
$e^{-r}\,\mathrm{sech}^2(z)$	thin	2.75	$0.27\ \eta(r)$	M-dwarfs	8	Disc 2
$e^{-r}e^{-\|z\|}$	thick	2.75	$0.44\ \eta(r)$	counts	8	Han and Gould 2003
$e^{-r}e^{-\|z\|}$	thin	2.75	0.25	-	8	Disc 3
$e^{-r}e^{-\|z\|}$	thick	4.10	0.75	-	7.6	Calchi Novati and Mancini 2011
$e^{-r}e^{-\|z\|}$	thin	2.75	0.25	thick & halo's	8	Disc 4
$e^{-r}e^{-\|z\|}$	thick	4.10	0.75	stars counts	7.6	de Jong et al. 2010
$(r^2+z^2)^{-2.75/2}$	halo	-	-		7.6	
$e^{-r}e^{-\|z\|}$	thin	2.60	0.30	disc's stars	8	Disc 4
$e^{-r}e^{-\|z\|}$	thick	3.60	0.90	counts	8	Jurić et al. 2008
$(r^2+z^2)^{-2.77/2}$	halo	-	-		8	

TABLE 3.2: Density profiles for the stellar disc. The spatial distribution for each of the components of the disc is given in the first column. Scale-radius and scale-height are given in the third and fourth column, respectively. The fifth column describes the tracers used for constraining the disc profile. The sixth column corresponds to the Sun's galactocentric distance and the references are given in the last column.

that aim to constraint the parameters of the stellar disc are based on limited regions of the sky and their results are extrapolated to the whole Galaxy.

Except for one, all the parameterisations we adopt in this work make a distinction between a thin and a thick stellar disc. Furthermore, two morphologies also include a stellar halo. Even though the stellar halo might be a distinct component, we include its density profile within the stellar disc morphology. The reason is that in the works considered here, the stellar halo is constrained together with the thin and thick discs (see Jurić et al. 2008; de Jong et al. 2010). Although the stellar halo is dynamically subdominant, it is a very important component for understanding the accreted events experienced by the MW.

As for the Galactic bulge, the disc profile can be decomposed into a normalisation constant and a spatial distribution function,

$$\rho_d(r,z) = \bar{\rho}_d \times f_d(r,z), \tag{3.10}$$

where we have adopted cylindrical coordinates. In table 3.2, we summarise the adopted spatial distribution functions.

Disc 1

Disc's morphology given in Bovy and Rix 2013. This disc does not make a distinction between a thin and a thick components of the stellar disc. Furthermore, it describes a single maximal disc, i.e. the disc is assumed to dominate the dynamics within the Solar circle where it contributes the maximum amount possible without exceeding the rotation curve anywhere. The density profile is given by a double exponential function,

$$f_d(r,z) = e^{-r/R_d} e^{-|z|/z_h}, \tag{3.11}$$

where the scale-radius is $R_d = 2.15$ kpc and $z_h = 0.40$ kpc is the scale-height.

The stellar disc is constrained by the vertical force at $|z| = 1.1\,\mathrm{kpc}$ as a function of galactocentric distance between $4-10$ kpc (Bovy and Rix 2013). The spatial distribution and the vertical kinematics of G-type dwarfs from the SDSS/SEGUE survey are used as tracers of the vertical force. The observed velocity distribution function in the z-direction and its corresponding velocity moments are reconstructed using the joint distribution function of different mono-abundance populations (MAPs), i.e. stars within a given region in the plane $[\alpha/\mathrm{Fe}]-[\mathrm{Fe/H}]$ that are independent tracers of the gravitational potential (see Ting et al. 2013 and references therein).

Disc 2

This morphology makes a distinction between thin and thick stellar discs. Its spatial density profile is given by the following expression (Han and Gould 2003),

$$f_d(r,z) = \frac{1}{\eta(r)} \exp\left(-\frac{r-R_0}{R_\mathrm{d}}\right)\left[(1-\beta)\,\mathrm{sech}^2\left(\frac{z}{\eta(r) z_{h,\mathrm{thin}}}\right) + \right. \tag{3.12}$$

$$\left. \beta \exp\left(-\frac{|z|}{\eta(r) z_{h,\mathrm{thick}}}\right)\right], \tag{3.13}$$

where

$$\eta(r) = \max\left\{\frac{r}{9.025\,\mathrm{kpc}} + 0.114,\, 0.670\right\}, \tag{3.14}$$

$\beta = 0.565$, $R_d = 2.75$ kpc, $z_{h,\mathrm{thin}} = 0.270$ kpc and $z_{h,\mathrm{thick}} = 0.440$ kpc. Notice that the thin component is described by an exponential only in the radial direction and that both thin and thick discs have the same scale-radius. The normalisation of the density has a radial dependence through the function $\eta(r)$ which further describes the gradual flaring of the disc.

Parameters are constrained by star counts of ≈ 1400 M-type dwarfs from the Hubble space telescope (HST) (Zheng et al. 2001).

Disc 3

Disc's density profile which includes a double exponential thin and thick components Calchi Novati and Mancini 2011,

$$f_d(r,z) = \exp\left(-\frac{r-R_0}{R_{d,\mathrm{thin}}} - \frac{|z|}{z_{h,\mathrm{thin}}}\right) + f_\mathrm{thick} \exp\left(-\frac{r-R_0}{R_{d,\mathrm{thick}}} - \frac{|z|}{z_{h,\mathrm{thick}}}\right). \tag{3.15}$$

For the radial and vertical scale lengths, we adopt the same values adopted in Calchi Novati and Mancini 2011 where the authors analysed microlensing measurements towards the Large Magellanic Cloud (LMC). The values adopted for the thin disc are $R_{d,\mathrm{thin}} = 2.75$ kpc and $z_{h,\mathrm{thin}} = 0.250$ kpc (taken from Han and Gould 2003), and for the thick component, $R_{d,\mathrm{thick}} = 4.1$ kpc, $z_{h,\mathrm{thick}} = 0.750$ kpc and $f_\mathrm{thick} = 0.11$ (taken from de Jong et al. 2010). The latter parameter gives the relative weight of the thick component with respect to the thin disc.

Disc 4

Disc's density profile that apart from the thin and thick discs, it includes an axisymmetric stellar halo (de Jong et al. 2010). The density profile takes the following form,

$$f_d(r,z) = \exp\left(-\frac{r-R_0}{R_{d,\mathrm{thin}}} - \frac{|z|}{z_{h,\mathrm{thin}}}\right) + f_{\mathrm{thick}} \exp\left(-\frac{r-R_0}{R_{d,\mathrm{thick}}} - \frac{|z|}{z_{h,\mathrm{thick}}}\right) \tag{3.16}$$

$$+ f_{\mathrm{halo}} \left(\frac{R_0}{\sqrt{r^2+(z/q_h)^2}}\right)^{n_h}, \tag{3.17}$$

where $R_{d,\mathrm{thin}} = 2.60$ kpc, $z_{h,\mathrm{thin}} = 0.250$ kpc, $R_{d,\mathrm{thick}} = 4.1$ kpc, $z_{h,\mathrm{thick}} = 0.750$ kpc. For the halo component, the flattening parameter is $q_h = 0.88$ and the power-law index is $n_h = 2.75$. f_{thick} and f_{thin} control the relative weight of the thick disc and stellar halo with respect to the dominant thin disc. We adopt the same normalisation for the thick disc and halo component as in de Jong et al. 2010, that is $f_{\mathrm{thick}} = (10^{-2.3}\ \mathrm{M_\odot pc^{-3}}/\bar{\rho}_d)$ and $f_{\mathrm{halo}} = (10^{-4.20}\ \mathrm{M_\odot pc^{-3}}/\bar{\rho}_d)$.

de Jong et al. 2010 used CMDs from the SDSS/SEGUE survey in order to constraint the parameters of the thick and halo components, while fixing thin parameter to the values given by Jurić et al. 2008. In order to avoid thin disc stars, the analysis was restricted to stars above 1 kpc from the Galactic plane.

Disc 5

As in *disc 4*, this morphology has thin and thick stellar discs and a stellar halo component. The density profile takes the following form (Jurić et al. 2008):

$$\begin{aligned} f_d(r,z) = {} & \exp\left(-\frac{r-R_0}{R_{d,\mathrm{thin}}} - \frac{|z+z_0|}{z_{h,\mathrm{thin}}}\right) + f_{\mathrm{thick}} \exp\left(-\frac{r-R_0}{R_{d,\mathrm{thick}}} - \frac{|z+z_0|}{z_{h,\mathrm{thick}}}\right) \\ & + f_{\mathrm{halo}} \left(\frac{R_0}{\sqrt{r^2+(z/q_h)^2}}\right)^{n_h}, \end{aligned} \tag{3.18}$$

where $R_{d,\mathrm{thin}} = 2.60$ kpc, $z_{h,\mathrm{thin}} = 0.250$ kpc, $R_{d,\mathrm{thick}} = 3.60$ kpc, $z_{h,\mathrm{thick}} = 0.900$ kpc, $n_h = 2.77$, $q_h = 0.64$ and z_0 is the distance of the Sun to the Galactic plane which is 0.025 kpc. We adopt the same relative weight of the thick and halo components with respect to the thin disc as in the original reference, that is $f_{\mathrm{thick}} = 0.12$ and $f_{\mathrm{halo}} = 0.0051$.

The parameters of this morphology are fitted to the number density profile reconstructed from measured photometric parallaxes for ~ 48 million stars using the SDSS survey (Jurić et al. 2008).

3.3 Gas

The interstellar gas is composed mainly by hydrogen (90.8% by number or 70.4% by mass), 9.1% by number (28.1% by mass) of helium and negligible amounts of heavier elements. It can be found in three different forms: molecular, atomic and ionised (Ferrière 2001). The description of the interstellar gas in the MW is decomposed in

Components	Form	Range	R_0 [kpc]	Reference
CMZ, disc	H_2	$r = 0.01 - 3$ kpc	8.5	Ferrière et al. 2007
CMZ, disc	HI		8.5	
warm, hot, very hot	HII		8.5	
molecular ring	H_2	$r > 3$ kpc	8.5	Ferrière 1998
cold, warm	HI		8.5	
warm, hot	HII		8.5	

Table 3.3: The interstellar gas distribution is decomposed into the inner 3 kpc and the region beyond 3 kpc. Each radial part is, furthermore, decomposed into different components: molecular hydrogen H_2, cold and warm atomic hydrogen (HI) and warm and hot ionized hydrogen (HII). CMZ stands for central molecular zone.

two parts: one that describes the interstellar gas within the inner 3 kpc of the Galaxy (Ferrière et al. 2007), and another for the distribution of gas beyond 3 kpc from the GC (Ferrière 1998). In table 3.3, we summarise the two morphologies adopted in this thesis.

Ferrière 1998 and Ferrière et al. 2007 describe the total distribution of hydrogen as the sum of the molecular, atomic and ionised contributions,

$$\rho_{\rm H} = m_p \times (2\, n_{\rm H_2} + n_{\rm HI} + n_{\rm HII})\,, \tag{3.19}$$

with m_p the proton's mass. In order to convert hydrogen into interstellar gas density, we need to know the abundance of elements in the interstellar medium. Following Ferrière et al. 2007, we assume that the interstellar gas has the solar helium fraction and twice the solar metallicity. Together with an helium-to-hydrogen mass fraction of 0.4 and a metal-to-hydrogen mass ratio of 2×0.0265, the conversion factor is 1.453, i.e. $\rho_{\rm gas} = 1.453 \times \rho_{\rm H}$.

Density profile between 0.01-3 kpc

Ferrière et al. 2007 describes the distribution of hydrogen within 3 kpc from the GC. The parameters of the distribution are constrained by combining theoretical studies of gas dynamics with a compilation of observations: studies of dust thermal emission, CO 2.6 mm and HI 21-cm emission lines and dispersion of radio signals from pulsars.

Each hydrogen form is further divided into different components. In the following, we describe the density profile for each of these components.

- *Molecular hydrogen:*

Molecular hydrogen cannot be traced directly since it has no permitted transitions in the radio waveband.The spatial distribution of molecular hydrogen is then traced by the 2.6 mm CO emission line which is not affected by dust obscuration. The CO-to-H_2 conversion factor, $X_{\rm CO}$, converts the observed integrated CO intensity into column density of molecular hydrogen. This conversion factor is highly uncertain and might vary with galactocentric distance (see for example Ackermann et al. 2012).

Molecular hydrogen in the inner 3 kpc of the Galaxy is described by a central ellipsoidal component, called the central molecular zone (CMZ), and a disc with an inner hole that encloses the CMZ. The CMZ corresponds to an ellipse centre at $(x_c, y_c, z_c) = (-50, -50, 0)\,\mathrm{pc}$.[4] Its major axis is in the first Galactic quadrant rotated an angle $\phi_c = 70^{\circ}$ with respect to the GC-Sun line. The density profile is defined in terms of the Cartesian coordinate system characterised by the principal axes of the ellipse (X, Y, Z) defined as:

$$\begin{aligned} X &= (x - x_c)\cos\phi_c - (y - y_c)\sin\phi_c \\ Y &= (x - x_c)\sin\phi_c + (y - y_c)\cos\phi_c \\ Z &= z. \end{aligned} \tag{3.20}$$

In this coordinate system, the number density profile takes the following form:

$$\begin{aligned} n(X, Y, Z) = \left(\frac{X_{\mathrm{CO}}}{5\times10^{19}\frac{\mathrm{s}}{\mathrm{cm^2\,K\,km}}}\right) n_0 \times \exp\left[-\left(\frac{\sqrt{X^2 + (2.5Y)^2} - X_c}{R_d}\right)^4\right] \\ \times \exp\left[-\left(\frac{Z}{z_h}\right)^2\right], \end{aligned} \tag{3.21}$$

with $n_0 = 150\,\mathrm{cm}^{-3}$, $X_c = 0.125\,\mathrm{kpc}$, $R_d = 0.137\,\mathrm{kpc}$ and $z_h = 0.018\,\mathrm{kpc}$. The conversion factor X_{CO} is taken as the normalisation of the gas.

Outside the CMZ, the molecular hydrogen is contained in an elliptical disc with an inner hole. The disc is tilted (rotated counterclockwise about the x-axis) an angle $\alpha = 13.5^{\circ}$ out of the Galactic plane and it is rotated counterclockwise an angle $\beta = 20^{\circ}$ about the new define y'-axis. The major axis is further clockwise rotated an angle $\phi_d = 48.5^{\circ}$ with respect to the x''-axis. The density profile is defined in the coordinate system $(\mathcal{X}, \mathcal{Y}, \mathcal{Z})$ of the major axis of the holed elliptical disc given by,

$$\begin{aligned} \mathcal{X} &= x\,\cos\beta\,\cos\phi_d \\ &\quad - y\,(\sin\alpha\,\sin\beta\,\cos\phi_d + \cos\alpha\,\sin\phi_d) \\ &\quad + z\,(\cos\alpha\,\sin\beta\,\cos\phi_d - \sin\alpha\,\sin\phi_d) \\ \mathcal{Y} &= x\,\cos\beta\,\sin\phi_d \\ &\quad - y\,(\sin\alpha\,\sin\beta\,\sin\phi_d + \cos\alpha\,\cos\phi_d) \\ &\quad + z\,(\cos\alpha\,\sin\beta\,\sin\phi_d + \sin\alpha\,\cos\phi_d) \\ \mathcal{Z} &= -x\,\sin\beta \\ &\quad - y\,\sin\alpha\,\cos\beta \\ &\quad + z\,\cos\alpha\,\cos\beta. \end{aligned} \tag{3.22}$$

In this new coordinate system, the density profile takes the following form,

$$\begin{aligned} n(\mathcal{X}, \mathcal{Y}, \mathcal{Z}) = \left(\frac{X_{\mathrm{CO}}}{5\times10^{19}\frac{\mathrm{s}}{\mathrm{cm^2\,K\,km}}}\right) n_0 \times \exp\left[-\left(\frac{\sqrt{\mathcal{X}^2 + (3.1\mathcal{Y})^2} - X_c}{R_d}\right)^4\right]^4 \\ \times \exp\left[-\left(\frac{\mathcal{Z}}{z_h}\right)^2\right], \end{aligned} \tag{3.23}$$

with $n_0 = 4.8\,\mathrm{cm}^{-3}$, $X_c = 1.2\,\mathrm{kpc}$, $R_d = 0.438\,\mathrm{kpc}$ and $z_h = 0.042\,\mathrm{kpc}$.

---

[4] Notice that we are using a right-handed, i.e. y-axis pointing towards $\ell = -90^{\circ}$, Cartesian grid centre at the GC, while Ferrière 1998; Ferrière et al. 2007 use a left-handed Cartesian grid.

- *Neutral atomic hydrogen:*

The distribution of atomic hydrogen is based on the premise that atomic and molecular gas have similar distributions (Liszt and Burton 1996). The HI component is, therefore, further divided into a CMZ and an ellipsoidal disc profile. The HI CMZ is defined in the same coordinate system (X, Y, Z) as the H_2 CMZ (see equation (3.20)) and given by equation (3.21) without the X_{CO} factor. The parameters are $n_0 = 8.8\,\mathrm{cm}^{-3}$, $R_d = 0.137\,\mathrm{kpc}$ and $z_h = 0.054\,\mathrm{kpc}$.

Likewise, a holed disc of atomic hydrogen is defined by equation (3.23) (again without the X_{CO} factor) in the coordinate system (3.22) with parameters $n_0 = 0.34\,\mathrm{cm}^{-3}$, $R_d = 0.438\,\mathrm{kpc}$, $X_c = 1.2\,\mathrm{kpc}$ and $z_h = 0.120\,\mathrm{kpc}$.

- *Ionised hydrogen:*

The ionised hydrogen can be further divided into a warm ($T \sim 10^4\,\mathrm{K}$), hot ($T \sim 10^6\,\mathrm{K}$) and very hot ($T \leq 10^8\,\mathrm{K}$) components.

The number density profile of the warm ionised hydrogen is composed of a GC component, an inner thin disc and an outer thick disc:

$$\begin{aligned} n(x,y,z) = n_0 \Bigg\{ & \exp\left[-\frac{x^2+(y-y_1)^2}{R_{d,1}^2}\right] \exp\left[-\frac{(z-z_1)^2}{z_{h,1}^2}\right] \\ & + 0.009 \exp\left[-\left(\frac{r-R_{d,2}}{R_{d,2}/2}\right)^2\right] \mathrm{sech}^2\left(\frac{z}{z_{h,2}}\right) \\ & + 0.005 \left[\cos\left(\pi \frac{r}{2R_{d,3}}\right) u(R_{d,3}-r)\right] \mathrm{sech}^2\left(\frac{z}{z_{h,3}}\right) \Bigg\}, \end{aligned} \tag{3.24}$$

where $n_0 = 8.0\,\mathrm{cm}^{-3}$. For the GC component, $y_1 = -10$ pc, $z_1 = -20$ pc, $R_{d,1} = 145$ pc and $z_{h,1} = 26$ pc. For the inner thin disc, $r = \sqrt{x^2+y^2}$, $R_{d,2} = 3.7$ kpc and $z_{h,2} = 0.140$ kpc. For the outer thick disc, $R_{d,3} = 17$ kpc, u is the unit step function and $z_{h,3} = 0.950$ kpc.

The spatial distribution of the hot ionised hydrogen takes the following form:

$$n(r,z) = \left\{(0.009\,\mathrm{cm}^{-3})^{2/3} - (1.54 \times 10^{-17}\,\mathrm{cm}^{-4}\,\mathrm{s}^2) \times [f(r,z) - f(0,0)]\right\}^{1.5}, \tag{3.25}$$

with

$$\begin{aligned} f(r,z) = & -(225\,\mathrm{km\,s}^{-1})^2 \\ & \times \left\{ \frac{C_1}{\sqrt{r^2 + \left(a_1 + \sqrt{z^2+b_1^2}\right)^2}} + \frac{C_2}{a_2 + \sqrt{r^2+z^2}} \right. \\ & \left. -C_3 \ln \frac{\sqrt{1 + \frac{a_3^2+r^2+z^2}{r_h^2}} - 1}{\sqrt{1 + \frac{a_3^2+r^2+z^2}{r_h^2}} + 1} \right\}. \end{aligned} \tag{3.26}$$

The parameters are $C_1 = 8.887$ kpc, $a_1 = 6.5$ kpc, $b_1 = 0.26$ kpc, $C_2 = 3.0$ kpc, $a_2 = 0.70$ kpc, $C_3 = 0.325$ kpc, $a_3 = 12$ kpc and $r_h = 210$ kpc.

Finally, the very hot ionised hydrogen is described by an ellipsoid tilted an angle $\alpha = 21^{\mathrm{o}}$ out of the Galactic plane. The Cartesian grid for the principal axes of the ellipsoid (x, η, ζ) given by,

$$\begin{aligned} \eta &= y\,\cos\alpha - z\,\sin\alpha \\ \zeta &= y\,\sin\alpha + z\,\cos\alpha. \end{aligned} \tag{3.27}$$

The density profile in this Cartesian grid takes the following form,

$$n(x,\eta,\zeta) = n_0 \exp\left[-\left(\frac{x^2+\eta^2}{R_d^2} + \frac{\zeta^2}{z_h^2}\right)\right], \tag{3.28}$$

with $n_0 = 0.29\,\mathrm{cm}^{-3}$, $R_d = 0.162$ kpc and $z_h = 0.090$ kpc.

Density profile above 3 kpc

For the interstellar gas distribution beyond 3 kpc we adopt the axisymmetric description given in Ferrière 1998. Different observations were used to constraint this gas distribution. Molecular hydrogen was traced by the 2.6 mm CO emission line, atomic hydrogen was probed with the 21-cm emission line, and the ionised hydrogen was constrained by a set of measurements such as the Hα recombination line, other emission lines and X-ray surface brightness from external galaxies.

- *Molecular hydrogen:*

The molecular hydrogen H_2 resides mainly in a ring between $\sim$ 3.5 and 6 kpc from the GC known as the Galactic disc molecular ring (Combes 1991). Its number density profile can be written in the following form,

$$\begin{aligned} n(r,z) = {}& \left(\frac{X_{\mathrm{CO}}}{3\times 10^{20}\,\frac{\mathrm{s}}{\mathrm{cm^2\,K\,km}}}\right) n_0 \exp\left[-\frac{(r-R_{\mathrm{ring}})^2-(R_0-R_{\mathrm{ring}})^2}{L_{\mathrm{ring}}^2}\right] \\ & \times \left(\frac{r}{R_0}\right)^{-0.58} \exp\left[-\left(\frac{z}{H_m(r)}\right)^2\right], \end{aligned} \tag{3.29}$$

with

$$H_m(r) = (0.081\,\mathrm{kpc})\left(\frac{r}{R_0}\right)^{0.58}. \tag{3.30}$$

The parameters are $n_0 = 0.58\,\mathrm{cm}^{-3}$, $R_{\mathrm{ring}} = 4.5$ kpc and $L_{\mathrm{ring}} = 2.9$ kpc. As for H_2 up 3 kpc, the conversion factor X_{CO} act as the normalisation of the gas component.

- *Neutral atomic hydrogen:*

We can distinguish between cold (T$\sim$ 80 K) and warm atomic hydrogen (T$\sim$ 8000 K). The number density of cold atomic hydrogen is given by,

$$\begin{aligned} n(r,z) = \frac{n_0}{\alpha(r)^2}\Bigg\{ & 0.859\exp\left[-\left(\frac{z}{H_1(r)}\right)^2\right] + 0.0047\exp\left[-\left(\frac{z}{H_2(r)}\right)^2\right] \\ & + 0.094\exp\left[-\frac{|z|}{H_3(r)}\right]\Bigg\}, \end{aligned} \tag{3.31}$$

with $n_0 = 0.340\,\mathrm{cm}^{-3}$. On the other hand, the warm atomic component takes the following form,

$$\begin{aligned} n(r,z) = \frac{n_0}{\alpha(r)}\Bigg\{ &\left[1.745 - \frac{1.289}{\alpha(r)}\right] \exp\left[-\left(\frac{z}{H_1(r)}\right)^2\right] \\ &+ \left[0.473 - \frac{0.070}{\alpha(r)}\right] \exp\left[-\left(\frac{z}{H_2(r)}\right)^2\right] \\ &+ \left[0.283 - \frac{0.142}{\alpha(r)}\right] \exp\left[-\frac{|z|}{H_3(r)}\right]\Bigg\}, \end{aligned} \tag{3.32}$$

with $n_0 = 0.226\,\mathrm{cm}^{-3}$. For both components,

$$\begin{aligned} H_1(r) &= (0.127\,\mathrm{kpc})\alpha(r), \\ H_2(r) &= (0.318\,\mathrm{kpc})\alpha(r), \\ H_3(r) &= (0.403\,\mathrm{kpc})\alpha(r) \end{aligned} \tag{3.33}$$

and

$$\alpha(r) = \max\left\{1, \frac{r}{R_0}\right\}. \tag{3.34}$$

- *Ionised hydrogen:*

The ionised hydrogen can be further divided into warm ($T \sim 8000\,\mathrm{K}$) and hot ionised hydrogen ($T \sim 10^6\,\mathrm{K}$).

The density profile of the warm ionised hydrogen is described by a thick disc and a thin ring centred at $\sim$ 4 kpc from the GC (Cordes et al. 1991). The ring might be related to the molecular H_2 ring defined above. The number density profile is given by,

$$\begin{aligned} n(r,z) = & n_{0,\mathrm{disc}} \times \exp\left(-\frac{r^2 - R_0^2}{R_d^2}\right) \exp\left(-\frac{|z|}{z_{h,\mathrm{disc}}}\right) + \\ & n_{0,\mathrm{ring}} \times \exp\left[-\frac{(r - R_{\mathrm{ring}})^2 - (R_0 - R_{\mathrm{ring}})^2}{L_{\mathrm{ring}}^2}\right] \exp\left(-\frac{|z|}{z_{h,\mathrm{ring}}}\right). \end{aligned} \tag{3.35}$$

where $n_{0,\mathrm{disc}} = 0.0237\,\mathrm{cm}^{-3}$, $R_d = 37\,\mathrm{kpc}$ and $z_{h,\mathrm{disc}} = 1\,\mathrm{kpc}$. For the ring component, $n_{0,\mathrm{ring}} = 0.0013\,\mathrm{cm}^{-3}$, $R_{\mathrm{ring}} = 4\,\mathrm{kpc}$, $L_{\mathrm{ring}} = 2\,\mathrm{kpc}$ and $z_{h,\mathrm{ring}} = 0.150\,\mathrm{kpc}$.

The number density profile for the hot ionised hydrogen takes the following form,

$$\begin{aligned} n_h(r,z) = n_0 &\left\{0.12 \exp\left(-\frac{R - R_0}{R_d}\right) + 0.88 \exp\left[-\frac{(r - R_{\mathrm{ring}})^2 - (R_0 - R_{\mathrm{ring}})^2}{L_{\mathrm{ring}}^2}\right]\right\} \\ &\times \left(\frac{r}{R_0}\right)^{-1.65} \exp\left[-\frac{|z|}{H(r)}\right], \end{aligned} \tag{3.36}$$

with $n_0 = 4.8 \times 10^{-4}\,\mathrm{cm}^{-3}$, $R_d = 4.9\,\mathrm{kpc}$, $R_{\mathrm{ring}} = 4.5\,\mathrm{kpc}$, $L_{\mathrm{ring}} = 2.9\,\mathrm{kpc}$ and

$$H(r) = (1.5\,\mathrm{kpc})\left(\frac{\max\{r, 1\}}{R_0}\right)^{1.65}. \tag{3.37}$$

3.4 Calibration of Baryonic Density Profiles

We have described the three-dimensional spatial distribution of baryons in the Galaxy as a decomposition in kinematical independent parts (bulge, bar, stellar disc and gas). To fully describe the distribution of baryons in the MW, we need to further calibrate the weight of each component with respect to the total mass budget of the Galaxy.

The stellar disc is normalised to the stellar surface density at the Sun's galactocentric distance (Bovy and Rix 2013),

$$\Sigma_*(R_0,\, z = 1.1\,\mathrm{kpc}) = (38 \pm 4)\,\mathrm{M}_\odot \mathrm{pc}^{-2}. \tag{3.38}$$

At the Sun's position, the bulge contribution to the total stellar density is negligable. Therefore, $\rho_* \approx \rho_d$ and the stellar surface density takes the form,

$$\Sigma_*(R_0,\, z = 1.1\,\mathrm{kpc}) = \int_{-1.1}^{+1.1} \mathrm{d}z\, \rho_d(R_0, z). \tag{3.39}$$

The bulge component is normalised to the microlensing optical depth towards the GC. We use the microlensing optical depth value presented in 2005 by the MACHO collaboration (Popowski et al. 2005),

$$\langle\tau\rangle = 2.17^{+0.47}_{-0.38} \times 10^{-6} \;\text{ for }\; (\ell = 1.50°, b = -2.68°). \tag{3.40}$$

This measurement equals the predicted mean optical depth which can be further decomposed into two contributions,

$$\langle\tau\rangle(\ell, b) = \langle\tau\rangle_{disc}(\ell, b) + \langle\tau\rangle_{bulge}(\ell, b, \bar{\rho}_b). \tag{3.41}$$

The first term on the right-hand side corresponds to microlensing events for which stars in the stellar disc act as lenses and bulge's stars act as sources. For the second term, bulge's stars act both as sources and lenses. The bulge's normalised density $\bar{\rho}_b$ is then obtained once a disc profile is adopted,

$$\bar{\rho}_b = \frac{\langle\tau\rangle(\ell, b) - \langle\tau\rangle_{disc}(\ell, b, \bar{\rho}_b = 1)}{\langle\tau\rangle_{bulge}(\ell, b, \bar{\rho}_b = 1)} \tag{3.42}$$

with

$$\langle\tau\rangle_i(\ell, b) = \frac{4\pi G}{c^2} \frac{\int_0^{r_\infty} \mathrm{d}D_s \left\{ \int_0^{D_s} \mathrm{d}D_l\, \rho_i(\ell, b) D_l \left(1 - \frac{D_l}{D_s}\right) \right\} \rho_{bulge}(\ell, b) D_s^2}{\int_0^{r_\infty} \mathrm{d}D_s\, \rho_{bulge}(\ell, b) D_s^2}, \tag{3.43}$$

where i runs for *disc* or *bulge*, D_s is the distance between observer and source, D_l is the distance from the observer to the lens and r_∞ is fixed to 20 kpc.

Normalisation of the stellar disc and bulge components of the Galaxy to the total stellar surface density and microlensing optical depth, respectively, is a well-established method for baryonic calibration. This technique was first presented in Iocco et al. 2011 and since then it was largely adopted in the literature (e.g. Bozorgnia et al. 2013; Benito et al. 2017).

On the other hand, for the interstellar gas –found in molecules, atomic form or ionised– we adopt the same normalisation factors, expect for the molecular gas, as in the papers from which the density profiles are taken from (Ferrière 1998; Ferrière et al. 2007).

The molecular gas, mainly H_2, is traced by the 2.6 mm CO emission line. For the CO-to-H_2 conversion factor, $X_{\rm CO}$, we adopt the following values:

- For the density profile up to 3 kpc from the GC, we adopt the value $X_{\rm CO} = (5.0 \pm 2.5) \times 10^{19}\,{\rm cm^{-2}\,s\,K^{-1}km^{-1}}$ (Ferrière et al. 2007).
- Beyond 3 kpc, we adopt $X_{\rm CO} = (1.9 \pm 1.4) \times 10^{20}\,{\rm cm^{-2}\,s\,K^{-1}km^{-1}}$ (Ackermann et al. 2012).

On figure 3.1, we show the density profiles for the individual stellar bulge, disc and gas morphologies adopted in this work. The profiles are normalised following the technique above depicted.

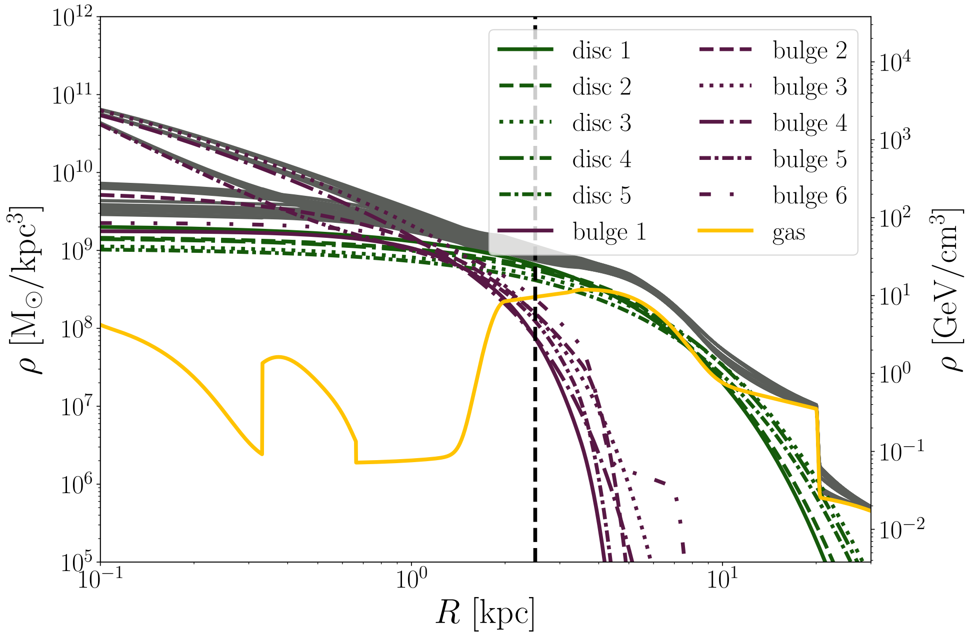

FIGURE 3.1: Bulge (purple), disc (green), gas (yellow) and total (grey) density profiles. Each bulge is normalised to the microlensing optical depth toward the GC (Popowski et al. 2005) once the *disc 3* is adopted. Stellar disc is normalised to the local stellar surface density (Bovy and Rix 2013). See text for details on the gas normalisation.

Chapter 4

Distribution of Dark Matter

Disc galaxies are rotation supported systems, that is they are stable structures due to the rotation of objects around the centre of the galaxy with conservation of angular momentum. Hence tangential velocities of the disc can be used to trace the enclosed amount of matter, which in turn dictates the gravitational pull that balances the circular motion. In ΛCDM, rotation velocities would trace (mostly) the dark matter (DM), which is expected to dominate the gravitational potential in the outskirts of galaxies.

In this chapter, we use the rotation curve (RC) of the Milky Way (MW) in order to study the overall distribution of DM. While observed rotation velocities probe the total gravitational potential of the Galaxy, and therefore, the total or dynamical mass, the baryonic RC is a proxy for the visible or baryonic mass. It is well known that the stellar content and interstellar gas of our Galaxy can not account for the total gravitational potential (see, e.g., Iocco et al. 2015a). This discrepancy between dynamical and baryonic masses is accounted for by a non visible, *dark* component of matter, whose density distribution can be obtained by fitting an appropriately parametrised function to the total RC.

The RC methodology, often referred to as a *global* method to determine the DM density in the solar neighbourhood, is a model dependent technique since a given parameterisation for the DM component must be adopted. This technique offers a series of advantages with respect to *local*, model independent methods, which determine the DM distribution in the Sun's neighbourhood by measuring the gravitational vertical force (e.g. Sivertsson et al. 2018). Even though the former, *global* methods are model dependent, the local DM density, ρ_0, is quite robust against different parameterisations. On the contrary, *local* ρ_0 determinations are sensitive to the type of stars used to probe the gravitational force (see, e.g., Buch et al. 2018).

4.1 Astrophysical Setup

Setting constraints on the overall distribution of DM by means of the RC relies on the following three inputs:

- Objects in circular orbits around the Galactic centre (GC) as tracers of the total gravitational potential of the Galaxy.
- Mass distribution for the baryonic component (stars and gas) of the Galaxy from which predicted rotation velocities are obtained.

Parameter	**Adopted value**
R_0 [kpc]	8.34
Θ_0 [km/s]	239.89
$(U_\odot, V_\odot, W_\odot)$ [km/s]	(7.01, 12.20, 4.95)

Table 4.1: Galactic parameters adopted in the *Huang et al* compilation (Huang et al. 2016). R_0 is the distance of the Sun from the GC, Θ_0 is the circular velocity at the Sun's position with respect to the GC and $(U_\odot, V_\odot, W_\odot)$ is the solar motion with respect to the local standard of rest (LSR). The LSR is the system co-moving along a circular orbit around the GC at R_0 with a velocity equal to the local RC velocity Θ_0.

- A given parameterisation for the DM density profile whose parameters are fit to the observed dynamical potential, after subtracting the component due to the pure effect of gravity of the visible matter.

In this first section, we present each of the elements adopted in our analysis in order to determine the DM distribution in the Galaxy.

It is important to highlight that the RC methodology relies on the following assumptions: The Galaxy is rotationally supported, objects move in circular orbits around the GC and the underlying gravitational potential is nearly axisymmetric.

4.1.1 Observed Rotation Curve

We adopt two compilations of kinematic tracers of the total gravitational potential of our Galaxy: `galkin` (Pato and Iocco 2017) and *Huang et al* (Huang et al. 2016). The `galkin` compilation (Pato and Iocco 2017) includes measurements of different kinematic tracers in the disc within the visible part of the Galaxy, i.e. galactocentric distances in the range $2.5 \lesssim R \lesssim 22$ kpc. It consists of 25 different data sets which are summarised in appendix A. On the other hand, the compilation presented in Huang et al. 2016, hereafter *Huang et al*, uses the following kinematic tracers of the gravitational potential:

- Between ≈ 8 and 15 kpc from the GC, *Huang et al* used $\sim 1.6 \times 10^4$ red clump giants (RCGs) from the stellar disc.
- From ≈ 15 up to 100 kpc, *Huang et al* used $\sim 5.7 \times 10^3$ halo K giant stars (HKGs).

The `galkin` and *Huang et al* compilations prove different acceleration regimes: the former has a denser number of tracers within the visible Galaxy while the latter compilation proves the outskirt of the Galaxy where the DM is expected to dominate the gravitational potential. The Galactic parameters adopted in *Huang et al* are summarised in table 4.1.[1]

In figure 4.1, we show the `galkin` and *Huang et al* compilations. It is inferred from this figure that the *Huang et al* compilation has two circular velocity dips between 10-20 kpc. The first dip is also noticeable in `galkin`. So far the origin of these dips are unclear. Huang et al. 2016 state that they can be either an artefact due to high

---

[1] We adopt the same notation as in table 1 from Bland-Hawthorn and Gerhard 2016.

measurement uncertainties or they might reflect some features of the used kinematic tracers. In order to check whether the dips in the data have any impact on the model fitting results, we perform a test where we exclude from our analysis the data between 10-20 kpc from the centre of the Galaxy (see 4.3 for the results).

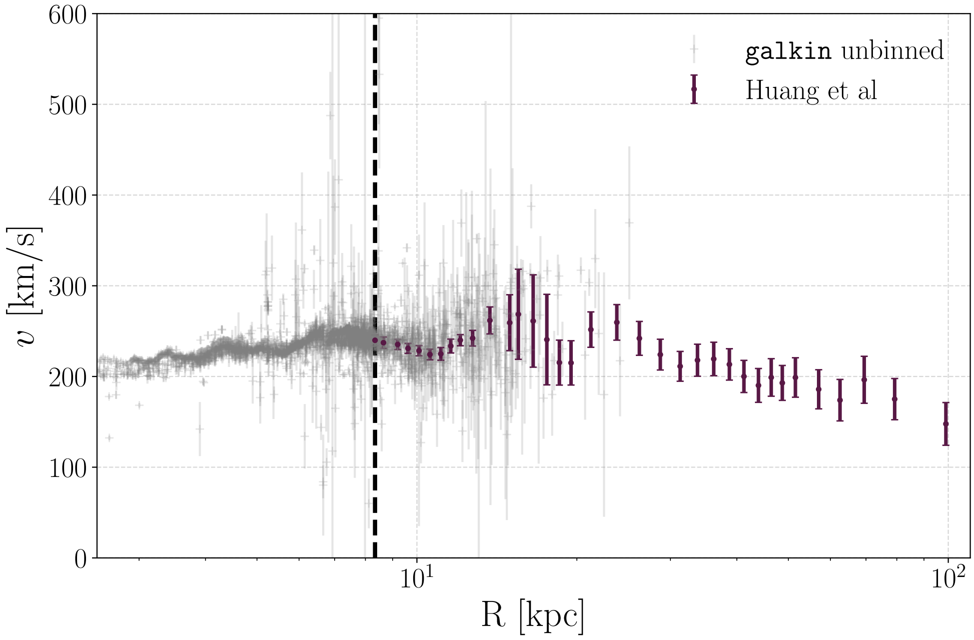

FIGURE 4.1: `galkin` (grey error bars) and *Huang et al* (purple error bars) observed RCs. The dashed black vertical line corresponds to the Sun's galactocentric distance R_0=8.34 kpc. We further assume the following Galactic parameters: $\Theta_0 = 239.89$ km/s and $(U_\odot, V_\odot, W_\odot) = (7.01, 12.20, 4.95)$ km/s.

Before binning the `galkin` compilation, and, thus, combine it with *Huang et al*, we have first studied the compatibility of the 25 data sets included in `galkin`. For doing so, we have followed a statistical procedure that allows to decide which subsample of the 25 data sets are a compatible compilation for the observed RC of the MW.

Compatibility of Data Sets via the Bayesian Evidence

Our method to select mutually compatible data sets uses a Bayesian model comparison framework (Feroz et al. 2008; Feroz et al. 2009; Trotta et al. 2011). In order to test the compatibility of data sets d_1 and d_2, we evaluate the Bayes factor, B, given by the following expression:

$$B = \frac{\mathrm{P}(d_1, d_2|H_0)}{\mathrm{P}(d_1|H_1)\mathrm{P}(d_2|H_1)}, \tag{4.1}$$

where $\mathrm{P}(d|H_i)$ is the Bayesian evidence for data d. H_0 is the hypothesis that our model jointly fits the two observables and H_1 is the hypothesis that the two observables preferred different regions in the parameter space. The Bayes factor B thus represents the ratio between the probability of both data sets being described by a single set of parameters over the probability of each of the data sets being described by its own set of parameters. If $B > 1$, the two data sets are deemed to be compatible (as their induced parameter space constraints overlap), and data set d_2 is added to the list of compatible data sets; otherwise, data set d_2 is deemed incompatible with the data sets previously accepted, and it is discarded. The details on the model we use and on the form of the likelihood are given in section 4.2.

Before applying the above procedure, we should first select one data set of the `galkin` compilation from which we are going to start. We have chosen Malhotra 1995 since by eye inspection it looks smooth with no outliers and it covers the inner ~ 8 kpc of the RC of the MW. Then, by every time adding a new data set and following equation (4.15), we end up with 12 compatible data sets. However, it is worth noticing that the order in which the data sets are tested is important. Indeed, if one starts from (or includes at the first steps) a data set that is incompatible with the rest (or with the most of it), then the final number of the compatible data sets is smaller than 12.[2] Furthermore, we have checked that among the 12 selected data sets the order of inclusion is not important, demonstrating the robustness of the procedure.

We have also performed a test of the above procedure adopting different –and extreme– baryonic morphologies: for the central, heaviest, and lightest discs (namely those that provide the central, highest, and lowest RCs) we have studied which subsample of data sets constitute a compatible compilation following the procedure above describe. The resulting compatible data sets are always the same 12, thus validating the procedure as insensitive to the actual baryonic morphology.

We then bin the subsample of 12 compatible data sets, hereafter $\texttt{galkin}_{12}$[3], following the binning scheme describe in the next part. We have further make sure that the derived RC is compatible with the *Huang et al* compilation. We have found that the outer data of *Huang et al* (data points between $\sim$ 15-100 kpc) is not compatible with $\texttt{galkin}_{12}$. In this regard, we will perform an errorbar rescaling analysis that should point to any systematic offsets (if any are present) between the data (see 4.2.2 for more details on this procedure).

We anticipate that, although the compatibility procedure discards a sizeable fraction of data from the `galkin` compilation, once the *Huang et al* compilation is added, the results or constraints on the DM parameters including `galkin` or $\texttt{galkin}_{12}$ compilations are indistinguishable.

Binning Scheme

In order to combine $\texttt{galkin}_{12}$ and *Huang et al* compilations, we first need to bin the former RC in order to use a binned likelihood approach across the entire range of radial distances. The binning procedure is as follows: We require an approximately equal number of data points per bin in order to obtain well-balanced bins. The total number of bins is 30 with ~ 25 data points within each bin. Although angular velocities are used for the fitting since they are uncorrelated with galactocentric distance R, we bin in circular velocities.[4] In this way, we avoid the steepness relation between angular velocities and galactocentric distances at small R. The mean circular velocity within

---

[2] Notice that we did not perform this test for all the possible combinations of the 25 data sets due to time limitations.

[3] In appendix A, we summarise the subsample of 12 data sets from `galkin` that constitute a compatible compilation of the RC.

[4] Notice that this is just a re-scaling of data points with $\sigma_{v_i} = \sigma_{\omega_i} \times R_i$. This is, uncertainties on R are not propagated into uncertainties on circular velocities.

each bin is given by the weighted mean and its corresponding standard deviation is the weighted standard deviation. This is,

$$\bar{v}_j = \frac{\sum_{i=1}^{N_{bin}} v_i/\sigma_{v_i}^2}{\sum_{i=1}^{N_{bin}} 1/\sigma_{v_i}^2}, \tag{4.2}$$

$$\sigma_{\bar{v}_j}^2 = \frac{\sum_{i=1}^{N_{bin}} (\bar{v}_j - v_i)^2/\sigma_{v_i}^2}{\sum_{i=1}^{N_{bin}} 1/\sigma_{v_i}^2}, \tag{4.3}$$

where σ_{v_i} is the measurement error on the circular velocity v_i and N_{bin} is the number of data points within the j-bin. We have verified that this procedure leads to residuals in each bin that follow closely a Gaussian distribution, which is a necessary condition for our likelihood function (defined in equation (4.13)) to be a good representation of the data in each bin.

Figure 4.2 shows `galkin`$_{12}$ binned and *Huang et al* observed RCs. From now on, in the radial region between 8-15 kpc where both compilations overlap, we only take into account those data points with smaller error bars.

4.1.2 Rotation Curve Expected from the Visible Component

Each of the baryonic components of the Galaxy (i.e. stellar bulge, stellar disc and gas) is described by an observationally inferred three-dimensional density parameterisation. We adopt a large array of bulge, and separately disc, density profiles described in chapter 3. By combining individually, one bulge, one disc, and the gas component (and then varying one at each time) we obtain an array of individual morphologies that bracket the systematic uncertainty on the mass distribution of the visible content in the Galaxy.

From the density profile, we can infer the corresponding gravitational potential, and therefore, circular velocities. Schematically, that is:

$$\rho_i(\mathbf{x}) \longrightarrow \Phi_i(\mathbf{x}) \longrightarrow v_i(R), \tag{4.4}$$

where i stands for the baryonic component (i.e. bulge, disc or gas), $\mathbf{x}$ is a three-dimensional vector in cartesian coordinates centre at the GC and R is the galactocentric distance. In the weak gravitational limit, the density profile $\rho_i(\mathbf{x})$ and its generated gravitational potential $\Phi_i(\mathbf{x})$ are related through Poisson's equation (Binney and Tremaine 2011),

$$\nabla^2\Phi_i(\mathbf{x}) = 4\pi G\rho_i(\mathbf{x}), \tag{4.5}$$

with the boundary condition $\Phi_i \to 0$ as $|\mathbf{x}| \to \infty$. A solution to this equation is Newton's gravitational field,

$$\Phi_i(\mathbf{x}) = -G\int \mathrm{d}\mathbf{x}' \frac{\rho_i(\mathbf{x}')}{|\mathbf{x}' - \mathbf{x}|}, \tag{4.6}$$

where G is Newton's gravitational constant. Circular velocities are then given by the radial gradient of the gravitational field. At the Galactic plane, circular velocities in spherical coordinates are given by the following expression[5]:

$$\begin{aligned} v_i^2(r,\,\phi) &= r\frac{\mathrm{d}\Phi_i}{\mathrm{d}r}(r,\,\phi,\,\theta=\frac{\pi}{2}) \\ &= rG\int_0^{\infty}\int_0^{2\pi}\int_0^{\pi}\mathrm{d}r'\mathrm{d}\phi'\mathrm{d}\theta'\,\frac{(r-r'\sin\theta'\cos(\phi'-\phi))r'\sin\theta'\rho_i(r',\phi',\theta')}{(r^2+r'^2-2rr'\sin\theta'\cos(\phi'-\phi))^{3/2}}; \end{aligned} \tag{4.7}$$

and in cylindrical coordinates[6]:

$$\begin{aligned} v_i^2(r) &= r\frac{\mathrm{d}\Phi_i}{\mathrm{d}r}(r,\,\phi=0,\,z=0) \\ &= rG\int_0^{\infty}\int_0^{2\pi}\int_{-\infty}^{+\infty}\mathrm{d}r'\mathrm{d}\phi'\mathrm{d}z'\,\frac{(r-r'\cos\phi')r'\rho_i(r',\phi',z')}{(r^2+r'^2-2rr'\cos\phi'+z'^2)^{3/2}}. \end{aligned} \tag{4.8}$$

Since axisymmetric density profiles are expressed in cylindrical coordinates, we have set $\phi = 0$ in this last equation. From the observationally inferred three-dimensional density profiles presented in chapter 3, we derive predicted rotation velocities for the visible component of the Galaxy by solving equations (4.7) and (4.8).

The RCs for the different parameterisations of stellar bulge, stellar disc and gas are shown in figure 4.2 together with the total baryonic curve for each possible combination of bulge, disc and gas. We have normalised each disc and bulge density profiles to the stellar surface density at the Sun's position (Bovy and Rix 2013) and the microlensing optical depth towards the GC (Popowski et al. 2005), respectively. It is worth stressing that the bulge's normalisation is indeed affected by the stellar disc adopted. Thus, for each bulge morphology, we plot its corresponding RC each time a disc density profile is adopted.

4.1.3 Study of Axial Symmetry

Equation (4.7) shows the dependence between circular velocity and axial angle ϕ. For the stellar disc, this dependence disappears due to the fact that the density profile is axisymmetric. Nonetheless, this is not the case for the stellar bulge or gas profiles, for which we need to average over ϕ. The RC methodology relies on the assumption that the underlying gravitational potential is nearly axisymmetric. Since this condition does not hold for the inner Galactic region due to the triaxial structure of the bulge component, the RC technique only applies for galactocentric distances larger than 2.5 kpc. Nonetheless, the bulge extends further than 2.5 kpc. For this reason, in the following, we study if $R_{\mathrm{cut}} = 2.5$ kpc is a valid assumption.

---

[5] We use galactocentric spherical coordinates (r, ϕ, θ) centre at the GC. ϕ increases in the direction of Galactic rotation, i.e. clock-wise as seen from the North Galactic Pole (NGP), and $\theta = \pi/2$ corresponds to the Galactic plane.

[6] We use galactocentric cylindrical coordinates (r, ϕ, z) centre at the GC. ϕ increases in the direction of Galactic rotation, i.e. clock-wise as seen from the NGP, and $z = 0$ corresponds to the Galactic plane.

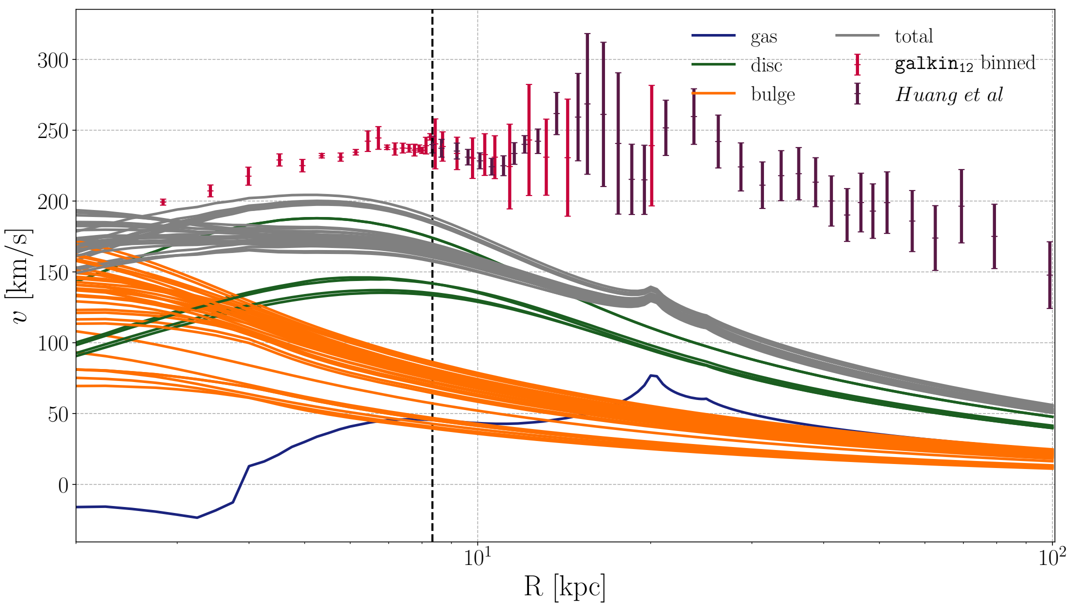

FIGURE 4.2: RCs for the different parameterisations of the bulge (orange), stellar disc (green) and gas (blue) morphologies adopted in our analysis (see chapter 3). The total baryonic curve for each possible combination of bulge, stellar disc and gas is shown in grey. `galkin`$_{12}$ binned and *Huang et al* observed RCs are also shown. The grey area corresponds to the inner Galactic region, i.e. $R < 2.5$ kpc. The dashed black line is the Sun's galactocentric distance $R_0 = 8.34$ kpc.

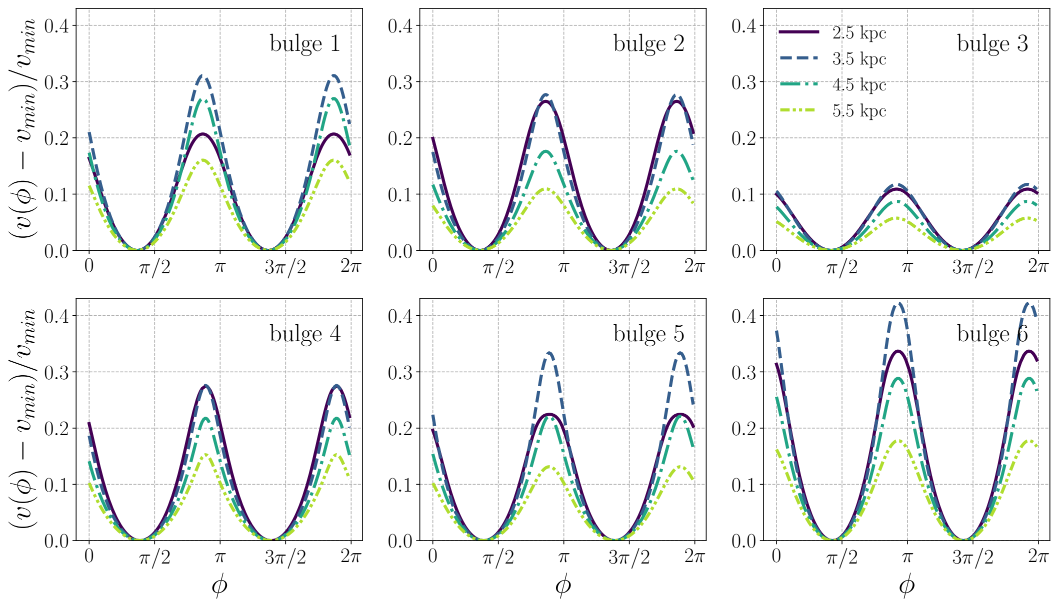

FIGURE 4.3: Relative variation of bulge's velocity with axial angle ϕ for different distances to the centre of the Galaxy. The asymmetry of the variation profile with respect to ϕ is due to the rotation of the semi-major axis of the bulge by an angle α with respect to the line of sight (i.e. $\phi = 0$). Notice that the semi-major axis of the bar is at negative Galactic longitudes. The nomenclature of the bulges is the same as in chapter 3 .

In figure 4.3 we show the relative change of bulge's velocity as a function of axial angle at different galactocentric distances (for each individual stellar bulge profile). Notice that this figure is independent of the adopted stellar disc. The relative change of circular velocities of the bulge is given by,

$$\frac{v(\phi) - v_{min}}{v_{min}}, \tag{4.9}$$

where v_{min} corresponds to the circular velocity at the axial angle ϕ_{min} that minimises the velocity profile as a function of axial angle ϕ at a given galactocentric distance R. Maximum departure from axial symmetry (at the level of $\sim 30\%$) peaks around 3.5 kpc. Nonetheless, for *bulge 3* (Vanhollebeke et al. 2009) the maximum level of departure from axial symmetry is $\sim 10\%$ and for *bulge 6* (Robin et al. 2012) it is of the order of $\sim 40\%$. The departure of the gas from axial symmetry is not important due to the negligible contribution of this component to the dynamics of the Galaxy.

In figure 4.4, we show the relative change of total velocity with respect to axial angle ϕ. We show the relative variation profiles for each stellar bulge morphology under the assumption of *disc 4*. Different from figure 4.3, this figure does indeed depend on the adopted disc morphology. We have chosen *disc4* since the baryonic morphologies with this particular stellar disc have the largest bulge-to-disc ratio, that is the departure of axial symmetry is the largest for this disc configuration with respect to the other discs. The maximum departure from axial symmetry reduces to $\sim 19\%$ and peaks at lower galactocentric distances with respect to the bulge's gravitational potential case (c.f. figure 4.3). This is because the relative weight of the bulge with respect to the total baryonic mass budget decreases with galactocentric distance. This level of departure of axial symmetry is of the same order of present relative uncertainties on the normalisation of the the baryonic component. For this reason, the assumption that for distances from the GC larger than 2.5 kpc the gravitational potential is nearly axisymmetric is a valid approximation.[7] Nonetheless, for increasing precision both in observed rotation velocities and in the normalisation of the baryonic component of the Galaxy, the cutting radius must increase too.

---

[7] If we increase the cutting radius from 2.5 to 4.5 kpc, our results do not change.

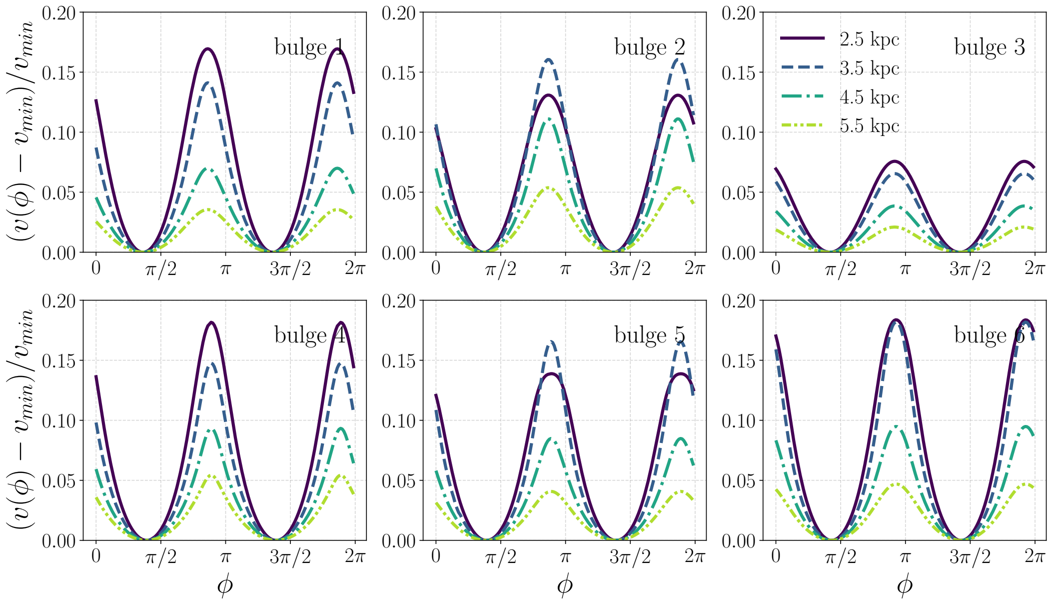

FIGURE 4.4: Relative variation of total velocity with axial angle ϕ for different distances to the centre of the Galaxy. The asymmetry of the variation profile with respect to ϕ is due to the rotation of the semi-major axis of the bar by an angle α with respect to the line of sight (i.e. $\phi = 0$). For this figure, we adopt *disc 4* (see text for details).

4.1.4 The Dark Matter Component

In order to set constraints on the distribution of DM by means of the RC of the Galaxy, we need to adopt a given parameterisation for the DM density profile. For this analysis, we adopt a generalised Navarro-Frenk-White density profile. This profile, which was already described in chapter 1, takes the following form,

$$\rho_{\mathrm{DM}}(r) = \frac{\rho_s}{\left(\frac{r}{R_s}\right)^{\gamma}\left(1+\frac{r}{R_s}\right)^{3-\gamma}} = \rho_0 \left(\frac{R_0}{r}\right)^{\gamma}\left(\frac{R_s+R_0}{R_s+r}\right)^{3-\gamma}. \tag{4.10}$$

It has three free parameters: The inner slope of the density profile or γ, the scale radius or R_s and the local DM density or ρ_0.

4.2 Setup and Methodology

For a given baryonic morphology (combination of stellar bulge, stellar disc and gas), our model has the following five free parameters:

- The three DM parameters: inner slope of the DM density profile, γ, the scale radius, R_s, and the local DM density, ρ_0.
- The two parameters related to the normalisation of the baryons: the stellar surface density at the Sun's position, Σ_*, and the microlensing optical depth towards the GC, $\langle\tau\rangle$. These are nuisance parameters.

Constraints on our model, and therefore on the distribution of DM, are inferred following frequentist and bayesian approaches.

4.2.1 Frequentist Approach

Observed and predicted (baryons plus DM) rotation velocities are compared by means of a χ^2 test statistics. We use angular velocities, $\omega(R) = v(R)/R$, instead of circular velocities since the former velocities are uncorrelated with galactocentric distance, i.e. angular velocities and radius are independent variables. When uncertainties both in angular velocities and galactocentric distances are taken into account, we use a two-dimensional χ^2 test statistic given by the following expression (Iocco et al. 2015a):

$$\chi^2_{\text{RC}} = \sum_{i=1}^{N} d_i^2 \equiv \sum_{i=1}^{N} \left[\frac{(R_i - R_{t,i})^2}{\sigma^2_{R_i}} + \frac{(\omega_i - \omega_{t,i})^2}{\sigma^2_{\omega_i}} \right]. \tag{4.11}$$

where $(R_i \pm \sigma_{R_i}, \omega_i \pm \sigma_{\omega_i})$ are the observations and $(R_{t,i}, \omega_{t,i})$ are the points that minimise d_i along the baryonic curve $\omega_b(R)$.[8] The sum runs over all the N objects in the observed compilation at $R \geq R_{\text{cut}} = 2.5$ kpc in order to exclude the innermost regions of the Galaxy where axial symmetry breaks down and some tracers may present non-circular orbits.

We use instead a one-dimensional χ^2 test statistic given by,

$$\chi^2_{\text{RC}} = \sum_{i=1}^{N} d_i^2 \equiv \sum_{i=1}^{N} \frac{(\omega_i - \omega_{t,i})^2}{\sigma^2_{\omega_i}}, \tag{4.12}$$

when only uncertainties on the angular velocities are taken into account.

4.2.2 Bayesian Approach

We explore the five-dimensional parameter space of the model using the uniform priors summarised in table 4.2. The two parameters Σ_* and $\langle\tau\rangle$, which regulate the normalisation of the baryonic component, are nuisance parameters.

$0 < R_s/[\text{kpc}] < 40$
$0 < \gamma < 3$
$0 < \rho_0/[\text{GeV cm}^{-3}] < 1$
$19 < \Sigma_*/[\text{M}_\odot\,\text{pc}^{-2}] < 57$
$0.1 \times 10^{-6} < \langle\tau\rangle < 4.5 \times 10^{-6}$

TABLE 4.2: Adopted ranges for the uniform priors of each free parameter of our analysis.

---

[8] By taking the points that minimise d_i along $\omega_b(R)$ instead of $\omega_t(R)$, we take the conservative approach of maximising the weight of baryons with respect to the total gravitational potential of the Galaxy.

The likelihood function of our analysis takes the form,

$$
\begin{aligned}
\mathrm{P}(d|\Theta, \Sigma_*, \langle\tau\rangle) = \prod_{j=1}^{M} & \left\{ \frac{1}{\sqrt{2\pi}\sigma_{\bar{\omega}_j}} \exp\left[-\frac{1}{2} \frac{(\omega(R_j, \Theta, \Sigma_*, \langle\tau\rangle) - \bar{\omega}_j)^2}{\sigma^2_{\bar{\omega}_j}} \right] \right\} \\
& \times \frac{1}{\sqrt{2\pi}\sigma_{\langle\tau\rangle}} \exp\left[-\frac{1}{2} \frac{\left(\langle\tau\rangle - \langle\tau\rangle^{obs}\right)}{\sigma^2_{\langle\tau\rangle}} \right] \\
& \times \frac{1}{\sqrt{2\pi}\sigma_{\Sigma_*}} \exp\left[-\frac{1}{2} \frac{\left(\Sigma_* - \Sigma_*^{obs}\right)}{\sigma^2_{\Sigma_*}} \right],
\end{aligned}
\tag{4.13}
$$

where $\Theta = \{\gamma, R_s, \rho_0\}$ are the DM parameters, j runs over the binned RC data and M is the total number of bins. Schematically, we can rewrite the likelihood as,

$$
\mathcal{L}(\Theta, \Sigma_*, \langle\tau\rangle) = \mathcal{L}(\Theta) \times \mathcal{L}(\Sigma_*) \times \mathcal{L}(\langle\tau\rangle). \tag{4.14}
$$

The first term of the likelihood function compares observed, $\bar{\omega}_j$, and predicted (baryons plus DM), $\omega(R_j, \Theta, \Sigma_*, \langle\tau\rangle)$, rotation velocities. The last two terms are related to the normalisation of the baryonic component with respect to the total gravitational potential of the Galaxy. For the observed values of the stellar surface density at the Sun's position, Σ_*^{obs}, and microlensing optical depth, $\langle\tau\rangle^{obs}$, we adopt the measurements provided in Bovy and Rix 2013 and Popowski et al. 2005, respectively.

The posterior from Bayes theorem is given by

$$
\mathrm{P}(\Theta, \Sigma_*, \langle\tau\rangle | d, \mathcal{M}) = \frac{\mathrm{P}(\Theta, \Sigma_*, \langle\tau\rangle | \mathcal{M}) \mathrm{P}(d|\Theta, \Sigma_*, \langle\tau\rangle, \mathcal{M})}{\mathrm{P}(d|\mathcal{M})} \tag{4.15}
$$

where $\mathcal{M}$ represents the adopted model and baryonic morphology, the likelihood $P(d|\Theta, \Sigma_*, \langle\tau\rangle, \mathcal{M})$ is given by equation (4.13), the prior $P(\Theta, \Sigma_*, \langle\tau\rangle|\mathcal{M})$ is uniform in the variables and ranges summarised in table 4.2, and the Bayesian evidence $P(d|\mathcal{M})$ is the normalisation constant, irrelevant for parameter inference.

The posterior distribution function is sampled by means of a Markov Chain Monte Carlo (MCMC) technique, particularly we use the open-source Affine Invariant MCMC Ensemble sampler `emcee` (Foreman-Mackey et al. 2013).

We further allow for the possible presence of residual undetected systematic offsets between the different data sets that we are using in the observed RC compilation (i.e. `galkin`$_{12}$, *Huang* RCGs and *Huang* HKGs) by using the procedure described in, e.g., Barnes et al. 2003; Trotta et al. 2011. For each data set k and bin j, we rescale the variances of the binned data by a factor $1/\epsilon_k$, and replace the variance in the likelihood by σ^2_{jk}/ϵ_k. The nuisance parameters ϵ_k describe possible error rescaling due to undetected systematics in each data set. If there are not residual systematics, the observed variance in the RC is fully explained by the statistical error in our binned data and the data sets are mutually compatible (as they should be, for in compiling them we used an appropriate compatibility test), then $\epsilon_k \approx 1$. Otherwise, we expect $\epsilon_k \ll 1$, which would inflate the binned data variance to account for sources of variance not captured by the statistical errors.

R_s [kpc]	5	8.5	12.5	16.5	20
γ	0.1	0.4	0.8	1.2	1.5
ρ_0 [GeV/cm^3]	0.4				
Σ_* [M$_\odot$/ pc^2]	38				
$\langle\tau\rangle$	2.17×10^{-6}				

Table 4.3: Fiducial parameter values used in the mock RC data generation. We use every possible combination of the parameters in the table, this corresponds to 25 fiducial points in our five-dimensional parameter space (see text for details).

The first term of the likelihood function in equation (4.13) needs to be modified to include the ϵ_k rescaling parameters and it takes the form

$$\mathrm{P}\left(\bar{\omega}_{jk}|\Theta,\Sigma_*,\langle\tau\rangle,\epsilon\right)=\frac{\sqrt{\epsilon_k}}{\sqrt{2\pi}\sigma_{\bar{\omega}_{jk}}}\exp\left[-\frac{1}{2}\frac{\left(\omega(R_j,\Theta,\Sigma_*,\langle\tau\rangle)-\bar{\omega}_{jk}\right)^2}{\sigma^2_{\bar{\omega}_{jk}}/\epsilon_k}\right], \tag{4.16}$$

where j runs for the number of bins in data set k.

For the rescaling parameter ϵ_k, following Trotta et al. 2011, we use Jeffreys' priors which are uniform in $\log\epsilon_k$ and take the following form,

$$\mathrm{P}(\log\epsilon_k)=\begin{cases}2/3 & \text{for} -3/2\le\log\epsilon_\mathrm{k}\le 0\\ 0 & \text{otherwise}\end{cases} \tag{4.17}$$

which correspond to a prior on ϵ_k of the form,

$$\mathrm{P}(\epsilon_k)\propto 1/\epsilon_k. \tag{4.18}$$

We further investigate whether our analysis is robust with respect to the $\sim$ 11 and 20 kpc dips – apparent in our data compilation but whose physical origin is unclear. In order to do so, we perform an alternative analysis excluding from the data sets the bins between 10 and 20 kpc.

4.2.3 Performance of Parameter Reconstruction

We wish to investigate the properties (over repeated data realisations) of our parameter reconstruction procedure in order to establish the accuracy and coverage properties of the Bayesian posterior distribution. As the posterior properties in general depend on the assumed true value for the model's parameters, we investigate 25 different choices for such fiducial parameter values summarised in table 4.3.

For each of the fiducial points in the five-dimensional parameter space of our model $\mathcal{M}$, we generate 100 mock data sets with the same statistical properties as the observed RC. Each mock RC is generated in the following way: First, we compute total angular velocities as the quadratic sum of the baryonic and gNFW angular velocities, with measurement error in each bin equal to the estimated standard deviation within that bin. Then, we add a Gaussian noise to this *perfect* RC, that is, we add to the total angular velocities a vector drawn from a Gaussian distribution centred at zero and with standard deviation equal to the measurement error.

For each of the 25 fiducial points, we estimate the accuracy of the reconstructed DM parameters by means of the fractional standard error (FSE). The FSE is defined as the square root of the mean squared error normalised by the true value:

$$\mathrm{FSE} = \frac{\sqrt{\frac{1}{n_i}\sum_{i=1}^{n_i}(\hat{\theta}_i - \theta_{true})^2}}{\theta_{true}}, \tag{4.19}$$

where $n_i = 100$ is the number of mock data realisations for each fiducial point (summarised in table 4.3), θ_{true} is the fiducial (true) value of a given parameter and $\hat{\theta}$ is the corresponding estimator of such parameter. We study the following four estimators: Mean, median, mode or maximum of the posterior estimator (MAP) and the maximum likelihood (ML) estimator. These estimators (except for the ML) are derived from the marginalised one-dimensional posterior distribution of the parameter in question.

We further study the coverage properties of the reconstructed intervals for each parameter. Coverage is the fraction of the time, over repeated data realisation, that the inferred interval contains the true value of the parameter. We consider three different definitions for our one-dimensional intervals:

- The shortest credible interval containing a given fraction of the total probability, the so-called Highest Posterior Density (HPD) interval.[9] We have assumed the shortest credible interval containing 68% of the total probability.
- The interval contained within the 16th and 84th percentile of the one-dimensional marginalised posterior distribution named the median credible region (CR) or equal-tailed interval.
- The profile likelihood interval (PLI) defined as the region satisfying the condition:

  $$2 \times [\log(\mathcal{L}_{max}) - \log(\mathcal{L})] \leq \chi^2_{1\sigma}(1) = 1, \tag{4.20}$$

  where $\mathcal{L}_{max}$ is the maximum likelihood.

4.3 Results

4.3.1 Degeneracy between γ and R_s

The inner slope γ and the scale radius R_s of a gNFW density profile are degenerate, i.e. the effect of increasing one of these parameters is mimic by decreasing the other. This correlation can be seen in figure 4.5 where we show best fit γ and ρ_0 values (top panels) for a two-parameter fitting while fixing R_s to different values between 5-30 kpc. For this exercise, we have fixed $\Sigma_* = 38\,\mathrm{M}_\odot/\mathrm{pc}^2$ (Bovy and Rix 2013) and $\langle\tau\rangle = 2.17\times10^{-6}$ (Popowski et al. 2005) and we have adopted the combine compilation `galkin`$_{12}$ plus *Huang et al* and a one dimensional χ^2 as our test statistics. The χ^2 for the best fit parameters, i.e. the (γ, ρ_0) points that minimise the χ^2, are shown in the bottom panel. Changing R_s by a factor 5, implies variations of $\rho_0 \sim 10\%$,

---

[9] Any value within the HPD interval has a higher probability than any other value outside of this interval.

while γ changes by a factor 7. This exercise points toward preferred smaller values for γ and R_s. Nonetheless, all fixed R_s values and corresponding best fit (γ, ρ_0) give a contribution of DM, which properly added to the baryonic part, can explain the observed RC at the 1σ level. This means that due to the actual precision in the measurements, we are unable to break the degeneracy between γ and R_s.

The strength of the coupling or correlation between γ and R_s depends on the values each of these parameters individually takes (c.f. figure 4.7). The strongest degeneracy occurs for smaller values of γ and R_s. Due to the correlation between γ and R_s and the present level of uncertainties in the observed rotation velocities, we are unable to determine (γ, R_s) simultaneously with a three-parameter χ^2 test statistics.

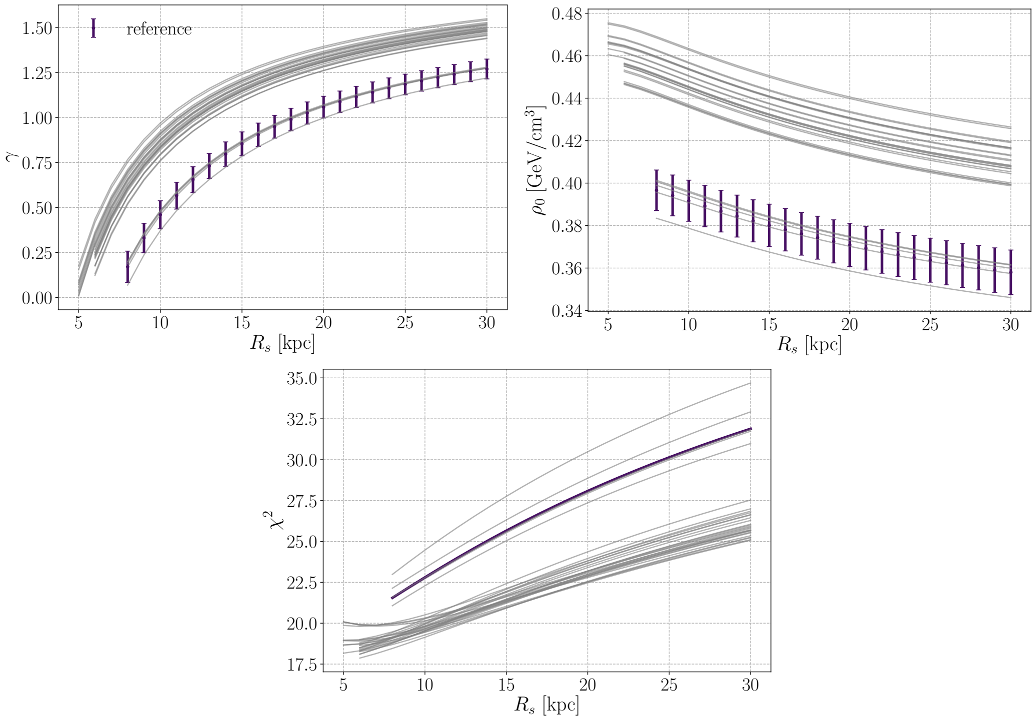

FIGURE 4.5: Best fit values of γ and ρ_0 (top panels) while fixing R_s to values between 5 and 30 kpc. The χ^2 values of the two-parameter fitting are shown in the bottom panel. The number of degrees of freedom is 52. Each error bar corresponds to the best fit values for γ and ρ_0 -at fixed R_s- with corresponding 1σ uncertainties for our reference morphology (*bulge 2* given in Stanek et al. 1997 plus *disc* 1 given in Bovy and Rix 2013). Results for the rest of the morphologies (central values) are shown by grey lines.

4.3.2 Mock Data Reconstruction

Using the Bayesian reconstruction formalism presented in 4.2.2, we have fit 100 mock RCs for each of the 25 fiducial points in the model parameter space summarised in table 4.3. In this way, we have studied the average properties of our reconstruction procedure over data realisations. Figure 4.6 shows the one and two-dimensional marginalised posterior distributions obtained for one data realisation at a given fiducial point. For this particular case, the local dark matter density, ρ_0, is well recovered while the inner slope of the DM density profile, γ, and the scale radius, R_s, are highly degenerate. These features are present in the posterior distribution functions for all 25 fiducial points.

We further estimate the accuracy of the reconstruction for the DM parameters by means of the FSE given by equation (4.19). We show the results of the FSE at different points in the DM parameter space and for different estimators (mean, median, MAP and ML) in figure 4.7. These results illustrate the following:

- The values for the FSE of ρ_0 vary between 0.03 and 0.06 (see figure 4.7) independently of the chosen point estimator. This indicates that the recovered value of the local DM density can be expected to have an accuracy better than 6% for any reasonable value of the DM halo parameter.
- The accuracy and precision on the local DM density, ρ_0, reconstruction gets slightly better for higher values of γ, except for the ML estimator.
- The inner DM density slope, γ, and the scale radius, R_s, are degenerate (see section 4.3.1), and though a combination of the two can be two-dimensionally well-constrained but not independently. Those parameters individually are reconstructed with a poor accuracy and precision.
- Nonetheless, the scale radius, R_s, is individually better reconstructed than γ. The MAP estimator of R_s has an accuracy better than 40% for any reasonable value of the DM halo parameter.
- The accuracy and precision for the inner DM density slope, γ, and that for the scale radius, R_s, (except MAP and ML estimators of R_s) gets better for higher values of γ and R_s.

We now turn our attention to the coverage properties of the reconstructed intervals for each parameter and the three different definitions of the one-dimensional intervals: 68% HPD, 68% CR and PLI. Coverage results from 100 mock data realisation as a function of the assumed fiducial parameter values are presented in figure 4.8, where the three rows correspond to the three DM parameters of interest, and columns correspond to the three interval definitions. In these plots, exact coverage would appear as a yellow square, with over-coverage shown in shades of green and under-coverage in orange/red. In the case of the local DM density, ρ_0, all intervals over-cover (i.e., they are conservative), with the most severe over-coverage occurring for the PLI (bottom right panel). The situation for the scale radius, R_s, is similar, but the CR interval suffer from under-coverage in some parts of the parameter space, notably for small values of γ. For γ we observe both over- and under-coverage both for HPD and CR intervals, while the PLI always over-cover.

The reasons for these behaviours can be traced back to the two-dimensional degeneracy between R_s and γ: once marginalised to one dimension the resulted intervals have poor coverage depending on where in the two-dimensional degenerate region the true value is located. The over-coverage observed for all the fiducial parameter values for the PLI is a consequence of the fact that this interval is typically larger than the credible intervals HPD and CR. The two nuisance parameters are always well recovered within the observed 1σ uncertainties, independently of where we are in the parameter space, as they are constrained by an independent piece of the likelihood.

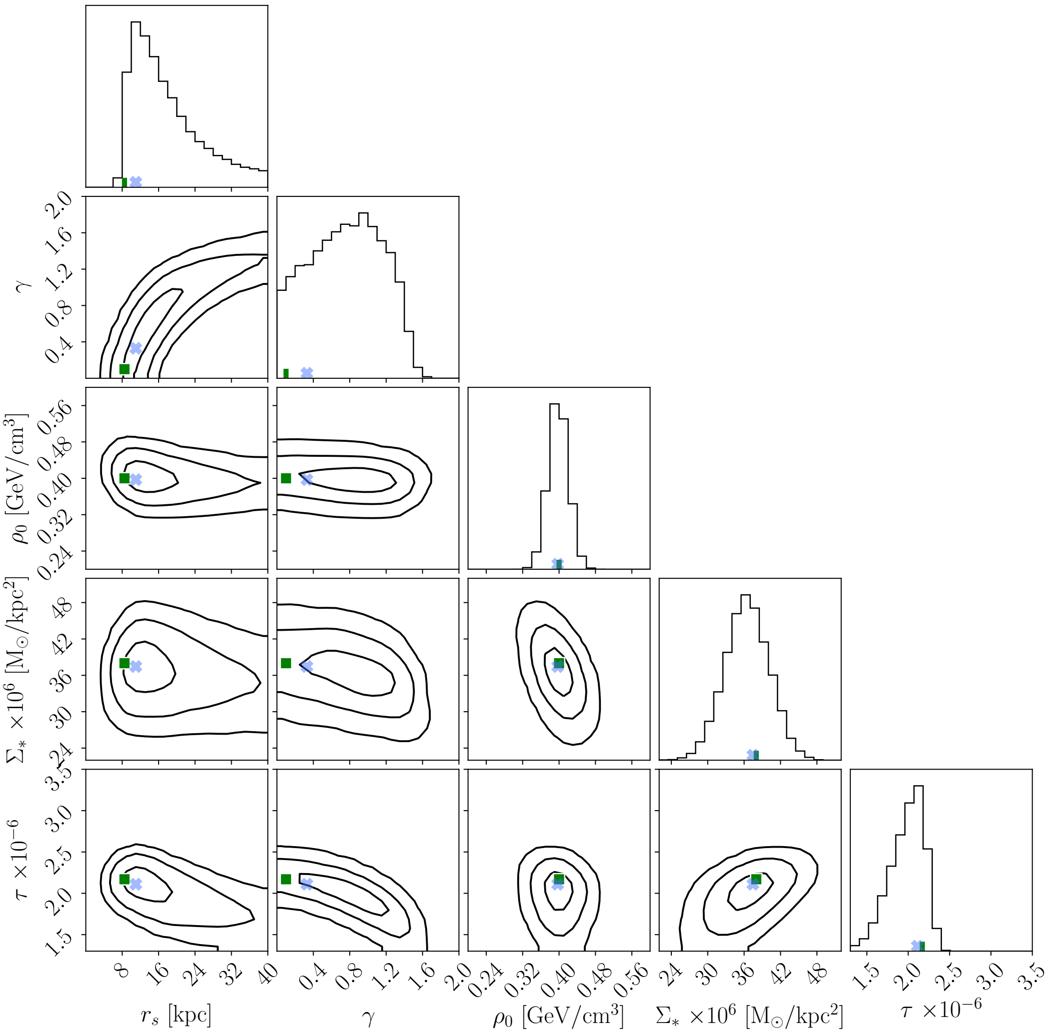

FIGURE 4.6: Example of the one and two-dimensional marginalised posterior distributions obtained by means of our five-parameter Bayesian reconstruction formalism applied to a given mock RC. Green squares indicate the true fiducial values used to generate the mock data, while blue crosses show the ML values. The contours delimit regions of 68%, 95% and 99% probability, while red shaded areas show the 68% HPD credible intervals.

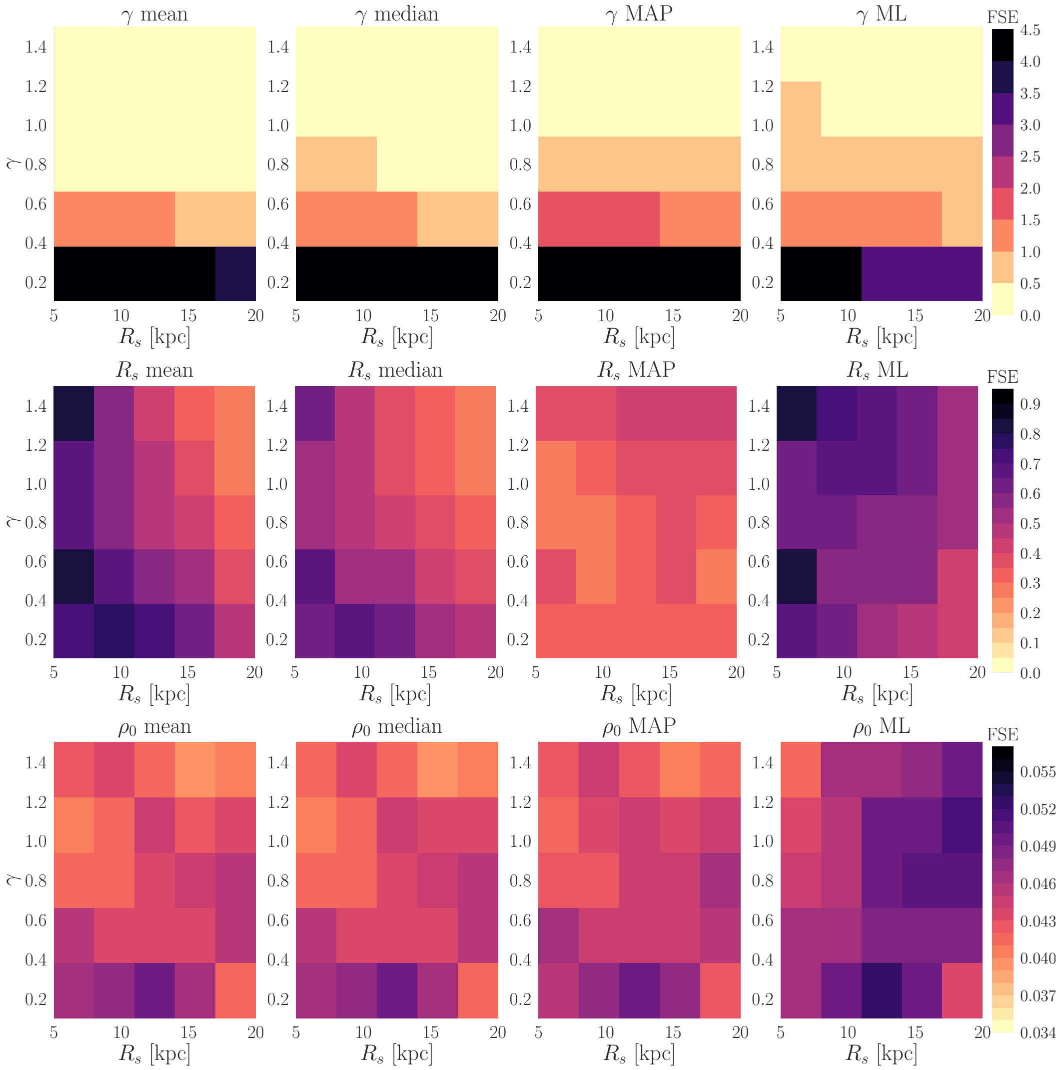

FIGURE 4.7: Values of the FSE for the inner slope, γ, scale radius, R_s, and local DM density ρ_0 (from top to bottom) and for different estimators (from left to right: mean, median, MAP and ML estimators). Notice the difference in the colour bar scale between the different parameters (i.e. different rows).

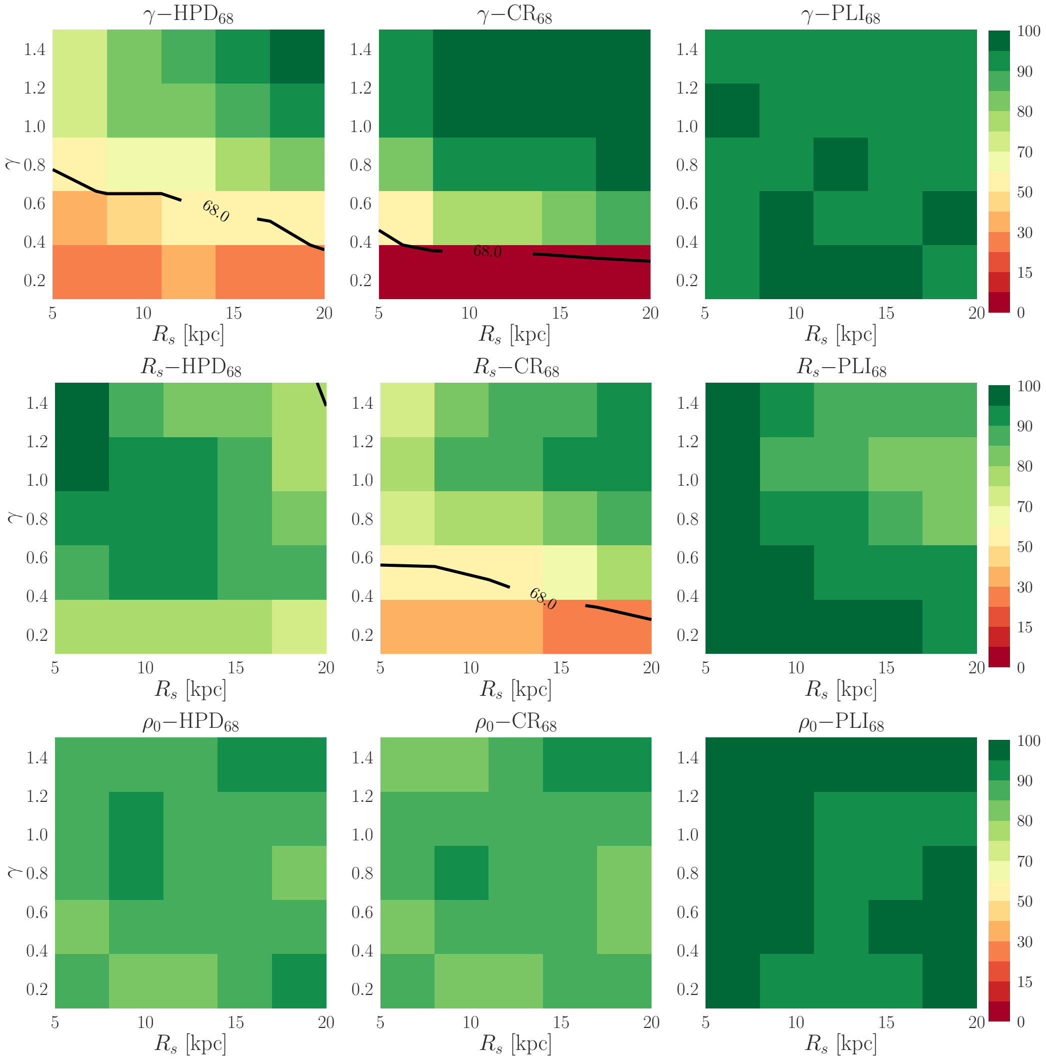

FIGURE 4.8: Credible intervals for the inner DM density slope, γ, the scale radius, R_s, and the local DM density ρ_0 (from top to bottom). From left to right, we show the 68% HPD, 68% CR and MPL intervals. The colour coding is as follows: For greenish regions the chosen credible interval contains the true value more frequently than orange, reddish regions.

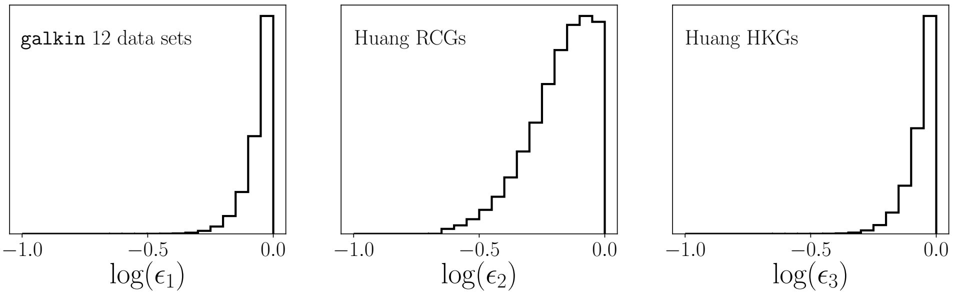

Figure 4.9: One-dimensional marginalised posterior probability distributions for the error bar rescaling parameters. Since the posteriors peak around $\log(\epsilon_j) = 0$, no systematic offsets are present among the data sets which are, therefore, mutually compatible.

4.3.3 Reconstruction of Parameters from Real Data

In this section, we present the results of our Bayesian inference procedure (see section 4.2.2) when applied to the actual RC of the MW. For the RC of our Galaxy, we adopt the `galkin`$_{12}$ plus *Huang et al* compilations. For clarity, we first present results for a reference morphology: *bulge 2* given in Stanek et al. 1997, *disc 1* given in Bovy and Rix 2013 and gas component from Ferrière 1998; Ferrière et al. 2007. We then present results for all baryonic morphologies.

Reference Baryonic Morphology

Our reference morphology (*bulge 2* plus *disc 1*) corresponds to the heaviest disc, i.e. this baryonic morphology provides the highest RC.

We have first checked for undetected systematic offsets between the different data sets of our RC's compilation: `galkin`$_{12}$, *Huang* RCGs and *Huang* HKGs. In order to do so we apply the Bayesian machinery explained in section 4.2.2. This is, we introduce a variance scaling parameter ϵ_k (see equation (4.16)) for each of the three data sets above mentioned. Figure 4.9 shows the one-dimensional marginalised posterior distributions for each rescaling parameter. Since $\epsilon_k \approx 1$ for all cases, there is no significant shift between the data sets. The observed variance in the RC is fully explained by the statistical error in our binned data and, therefore, there is no need for increasing uncertainties. Furthermore, as seen in figure 4.10, results of this analysis are compatible at the 1σ-level with the results of the standard analysis (i.e. likelihood function given by equation (4.13)). This is, our inference procedure is robust with respect to undetected systematic offsets. For this reason, from now on, we do not consider the rescaling parameter analysis.

Secondly, we have checked whether the two dips in the RC at galactocentric distances $\sim$ 11 and 20 kpc (see figure 4.1) affect the reconstructed constraints in the DM parameter space. In order to do so we run the standard MCMC analysis for the following two cases: First, the whole combined RC and, second, omitting the bins between 10 and 20 kpc. The results of these two runs are shown on figure (4.11), where no changes are seen in the resulting posterior distribution functions. This is, the presence of the dips around 11 and 20 kpc in the observed RC -whose nature is unknown- do not affect the reconstruction properties of our Bayesian inference technique.

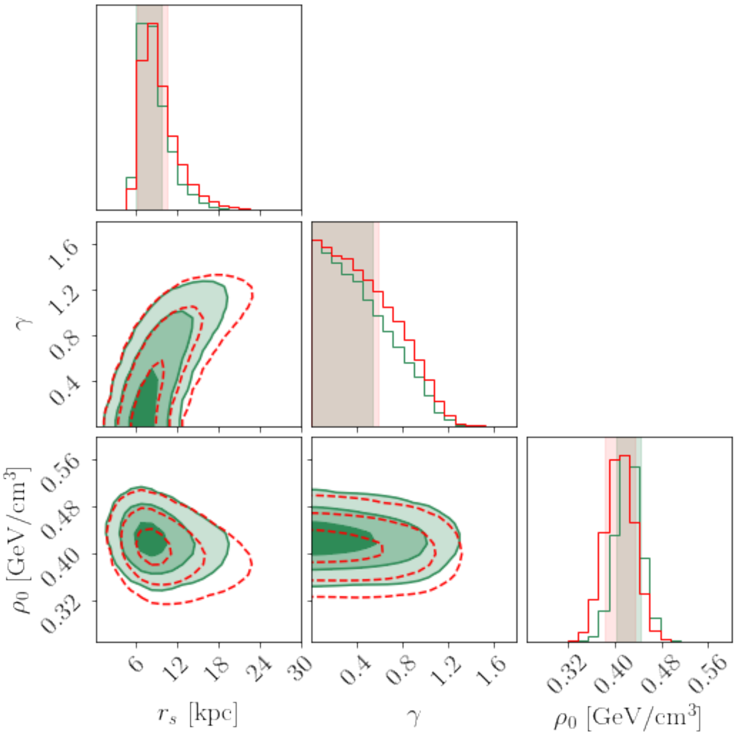

FIGURE 4.10: One and two-dimensional marginalised posterior probability distributions for each of the DM parameters of a gNFW profile. The results of the standard analysis (likelihood given by equation (4.13)) are shown in green. The results of the errorbar rescaling analysis (likelihood given by equation (4.16)) are shown in red. Light green and light red bands indicate 68% HPD region for the standard analysis and the errorbar rescaling analysis, respectively. Two-dimensional contours delimit 1, 2 and 3σ credible regions.

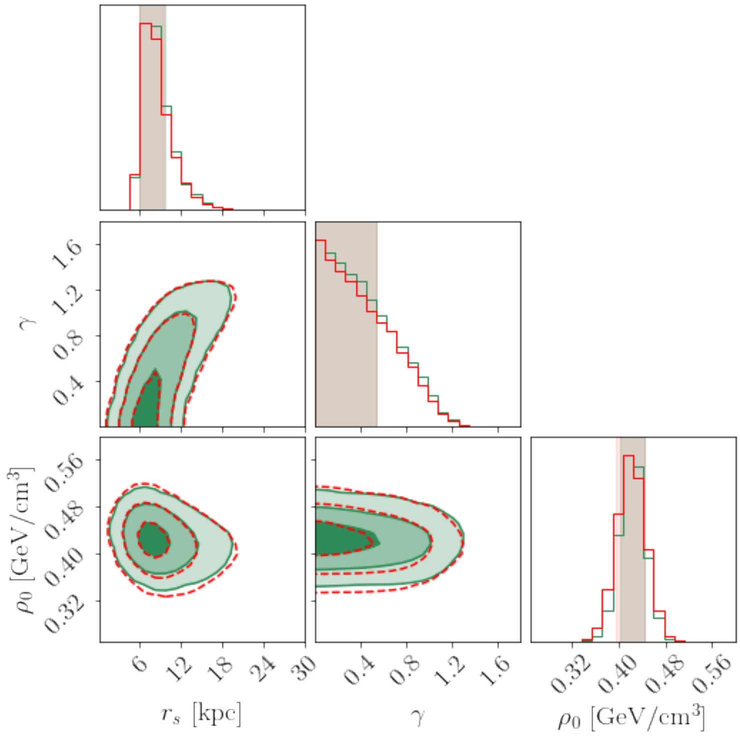

FIGURE 4.11: One and two-dimensional marginalised posterior probability distributions for DM parameters. The results of the standard analysis taking into account the whole RC compilation are shown in green. The results when bins in the region from 10 to 20 kpc are dropped from the likelihood are shown in red. Light green and light red bands indicate 68% HPD region for the whole RC compilation analysis and the dropped bins analysis, respectively.

Parameter	ML	MAP ± HPD_{68}	mean	median ± CR_{68}
γ	0.03	$<0.56_{\mathrm{HPD}_{68}}$	0.40	$0.36^{+0.38}_{-0.26}$
R_s	6.6	$7.1^{+2.5}_{-1.1}$	8.6	$8.1^{+2.6}_{-1.5}$
ρ_0	0.43	$0.43^{+0.02}_{-0.02}$	0.42	$0.42^{+0.02}_{-0.02}$

TABLE 4.4: Values for ML, MAP (with uncertainties estimated from the 68% HPD region), mean and median (with uncertainties estimated from the 68% CR) estimators obtained with the standard analysis applied to the actual RC of the MW (`galkin`$_{12}$ plus *Huang et al*) for our reference morphology (Stanek et al. 1997; Ferrière 1998; Ferrière et al. 2007; Bovy and Rix 2013). Notice that for γ we indicate only the upper limit of the HPD 68% (instead of MAP ± HPD_{68}). This is because the one-dimensional marginalised posterior distribution is compatible with zero.

In table 4.4, we summarise ML, MAP, mean and median estimators obtained for our reference morphology for each of the DM parameters of a gNFW density profile.

All Baryonic Morphologies

In section 4.1.1, we studied which subsample of the `galkin` data sets constitute a compatible compilation of the observed RC of the MW. We did this study for the extreme morphologies, that is, for those morphologies containing the heaviest (*disc 1*), central (*disc 2*) and lightest (*disc 3*) discs. Since the resulting compatible data sets are the same 12 for the three configurations, we concluded that the compatibility procedure is insensitive to the adopted baryonic morphology. Furthermore, the constraints infer on the DM parameters are independent whether the `galkin` or `galkin`$_{12}$ compilation is adopted as tracer of the total gravitational potential within the visible region of the Galaxy. For these reasons, we can safely apply our reconstruction procedure for each possible combination of stellar disc and stellar bulge while adopting `galkin`$_{12}$ plus *Huang et al* compilations for the observed RC of the MW.

In this section, we present the results of the MCMC analysis for the rest of baryonic morphologies. The results of the standard analysis (likelihood profile given in equation (4.13)) are summarised in table 4.5. Figure 4.12 shows the one and two-dimensional marginalised posterior distributions for three disc configurations: lightest (*disc 3*), central (*disc 2*) and heaviest (*disc 1*). For the three cases, we adopted *bulge 2*.

4.4 Conclusions

In this analysis, we have developed a novel Bayesian methodology to reliably and precisely infer the distribution of DM within the MW using the RC technique. We first selected a subset of tracers that are mutually compatible with each other, thus excluding the ones that might be suffering from systematic bias. We then demonstrated the statistical performance of our reconstruction procedure (over many data realisations) by applying it to simulated data, which we generated in order to mimic the statistical properties of the observed RC. We generalised our procedure against (systematic) uncertainties on the visible component of the MW, by applying it to an array of possible baryonic morphologies that bracket the current uncertainties on the

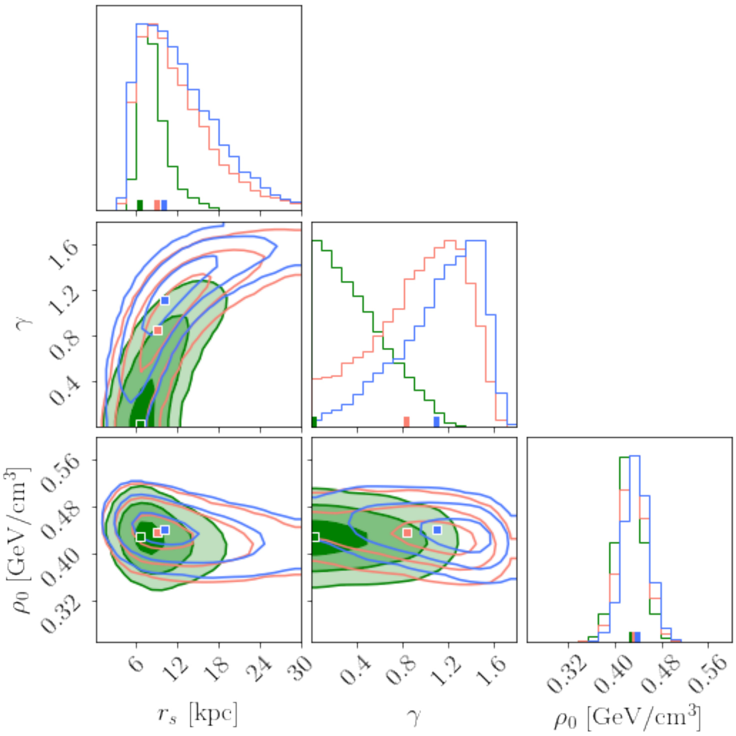

FIGURE 4.12: Green - the heaviest *disc 1* (our reference disc given in Bovy and Rix 2013), pink - the central *disc 2* given in Han and Gould 2003, blue - the lightest *disc 3* given in Calchi Novati and Mancini 2011. The marks in the one and two-dimensional marginalised posterior distribution plots indicate the ML values.

Baryonic	$\boldsymbol{\gamma}$		$\boldsymbol{R_s}$		$\boldsymbol{\rho_0}$		χ^2/dof
Morph.	ML	MAP $\pm$ HPD$_{68}$	ML	MAP $\pm$ HPD$_{68}$	ML	MAP $\pm$ HPD$_{68}$	
11	0.01	< 0.48	6.5	$7.4^{+1.9}_{-1.4}$	0.43	$0.43^{+0.02}_{-0.02}$	0.94
21	0.03	< 0.54	6.6	$7.1^{+2.5}_{-1.1}$	0.43	$0.43^{+0.02}_{-0.02}$	0.95
31	0.00	< 0.42	6.4	$7.3^{+2.2}_{-1.3}$	0.43	$0.43^{+0.02}_{-0.02}$	0.94
41	0.00	< 0.47	6.5	$7.1^{+2.0}_{-1.0}$	0.43	$0.42^{+0.02}_{-0.02}$	0.94
51	0.01	< 0.52	6.4	$7.4^{+1.9}_{-1.5}$	0.43	$0.43^{+0.02}_{-0.02}$	0.94
61	0.01	< 0.50	6.3	$7.1^{+2.2}_{-1.0}$	0.43	$0.43^{+0.02}_{-0.02}$	0.94
12	1.00	$1.44^{+0.11}_{-0.54}$	10.4	$9.3^{+6.8}_{-4.0}$	0.44	$0.43^{+0.02}_{-0.02}$	0.96
22	0.77	$1.26^{+0.25}_{-0.53}$	8.5	$8.1^{+6.4}_{-3.2}$	0.44	$0.43^{+0.02}_{-0.02}$	0.94
32	1.05	$1.39^{+0.17}_{-0.46}$	10.6	$9.6^{+6.8}_{-3.8}$	0.43	$0.43^{+0.02}_{-0.02}$	0.95
42	0.96	$1.28^{+0.23}_{-0.47}$	10.0	$9.2^{+6.1}_{-4.3}$	0.43	$0.42^{+0.03}_{-0.02}$	0.95
52	1.03	$1.25^{+0.28}_{-0.42}$	10.5	$9.6^{+5.8}_{-4.6}$	0.44	$0.43^{+0.02}_{-0.02}$	0.94
62	0.96	$1.25^{+0.23}_{-0.51}$	9.9	$8.7^{+5.6}_{-3.7}$	0.44	$0.44^{+0.02}_{-0.03}$	0.94
13	1.39	$1.46^{+0.16}_{-0.33}$	14.3	$8.2^{+8.9}_{-2.1}$	0.43	$0.43^{+0.02}_{-0.02}$	1.00
23	1.09	$1.29^{+0.31}_{-0.32}$	9.8	$10.5^{+5.0}_{-5.4}$	0.44	$0.43^{+0.02}_{-0.02}$	1.00
33	1.38	$1.50^{+0.16}_{-0.25}$	14.2	$11.5^{+8.7}_{-4.2}$	0.43	$0.43^{+0.02}_{-0.02}$	1.00
43	1.19	$1.29^{+0.30}_{-0.28}$	11.0	$9.3^{+6.0}_{-4.5}$	0.44	$0.44^{+0.02}_{-0.02}$	1.01
53	1.25	$1.51^{+0.12}_{-0.41}$	11.6	$10.7^{+6.7}_{-5.6}$	0.44	$0.44^{+0.01}_{-0.03}$	1.00
63	1.20	$1.35^{+0.24}_{-0.35}$	11.3	$10.7^{+4.6}_{-5.7}$	0.44	$0.43^{+0.02}_{-0.02}$	1.00
14	1.29	$1.47^{+0.19}_{-0.32}$	13.1	$10.2^{+9.6}_{3.8}$	0.43	$0.43^{+0.03}_{-0.02}$	0.99
24	1.07	$1.32^{+0.23}_{-0.41}$	9.9	$7.8^{+7.3}_{-2.5}$	0.44	$0.43^{+0.02}_{-0.02}$	0.98
34	1.38	$1.45^{+0.17}_{-0.33}$	14.7	$11.8^{6.6}_{-5.3}$	0.43	$0.43^{+0.02}_{-0.03}$	0.99
44	1.20	$1.41^{+0.21}_{0.36}$	11.5	$10.3^{+6.4}_{-5.0}$	0.43	$0.43^{+0.02}_{-0.02}$	0.99
54	1.24	$1.48^{+0.13}_{-0.38}$	12.3	$11.1^{+6.9}_{-4.8}$	0.43	$0.43^{+0.02}_{-0.02}$	0.99
64	1.17	$1.31^{+0.29}_{-0.33}$	11.4	$8.6^{+7.2}_{-3.8}$	0.44	$0.44^{+0.02}_{-0.02}$	0.99
15	1.31	$1.41^{+0.18}_{-0.33}$	15.2	$11.1^{+8.0}_{-4.7}$	0.42	$0.42^{+0.02}_{-0.02}$	0.96
25	1.05	$1.36^{+0.20}_{-0.53}$	11.0	$7.8^{+8.0}_{-2.6}$	0.43	$0.43^{+0.02}_{-0.03}$	0.95
35	1.31	$1.39^{+0.20}_{-0.32}$	14.8	$12.5^{+6.9}_{-6.1}$	0.42	$0.42^{+0.02}_{-0.02}$	0.96
45	1.14	$1.39^{+0.18}_{-0.42}$	12.3	$10.2^{+6.7}_{-4.8}$	0.42	$0.42^{+0.02}_{-0.02}$	0.96
55	1.23	$1.48^{+0.11}_{-0.51}$	13.3	$9.4^{+7.2}_{-3.7}$	0.42	$0.42^{+0.03}_{-0.02}$	0.96
65	1.14	$1.32^{+0.21}_{-0.43}$	11.9	$8.1^{+8.9}_{-1.8}$	0.43	$0.43^{+0.02}_{-0.02}$	0.96

Table 4.5: Values for ML and MAP (with uncertainties estimated from the 68% HPD region) for the DM parameters for all baryonic morphologies obtained with the standard analysis applied to the actual RC of the MW (`galkin`$_{12}$ plus *Huang et al*). For the values of γ corresponding to *disc 1* we indicate only the upper limit of the HPD 68% (instead of MAP$\pm$HPD$_{68}$) since the one-dimensional marginalised posterior distribution is compatible with zero. The coding for the baryonic morphology is as follows: The first and second numbers correspond to the bulge and disc morphologies, respectively, following the nomenclature in chapter 3. We report the reduced χ^2 for the ML estimator, the number of degrees of freedom is 49.

shape and normalisation of the Galactic stellar disc(s) and bulge, as well as of the (subdominant) interstellar gas component.

We conclude that the local DM density is reconstructed with very high precision (with 1σ relative uncertainties in the range 5-7%) and high accuracy (the estimated value never falls farther than $\sim 6\%$ from the true value in simulated data). The inferred values and error bars on this parameter are stable with respect to variations in the baryonic morphology (with a $\sim 5\%$ shift due to the adoption of different baryonic morphologies). Our results are also stable with respect to various tests for the presence of systematic errors in the RC data used. We report a value for ρ_0 of

$$\rho_0 = 0.43 \pm 0.03,$$

where the central value is the most-likely value from the MAP estimators of all baryonic morphologies. The uncertainty corresponds to a relative uncertainty of 7% which is the largest statistical uncertainty of our analysis. Notice that systematic uncertainties are $\lesssim 6\%$. It is important to highlight, nonetheless, that our reconstruction of the DM density profile in the MW relies on the assumption that the DM halo is spherically symmetric, wether this is a good approximation of reality remains an open question.

With the current uncertainties in the observed RC of the MW, we are unable to break the degeneracy between γ and R_s. Nonetheless, the combination of the two is relatively well constrained in a two-dimensional parameter space, whether the individual, one-dimensional marginalised posteriors of these two parameters are not very informative.

Chapter 5

Dark Matter Distribution in the Inner Galactic Region

In this chapter we study the distribution of dark matter (DM) in the inner region of our Galaxy, i.e. inner ≈ 2.5 kpc of the Milky Way (MW). The Rotation Curve (RC) methodology, described and applied in previous chapter 4, does not apply in the innermost region of the Galaxy. Due to the triaxial morphology of the Galactic bulge, axisymmetry breaks down and some tracers may present non-circular orbits. For this reason, the RC analysis applies only for galactocentric distances larger than 2.5 kpc, and the distribution of DM derived for the inner 2.5 kpc is just an extrapolation.

Characterising the distribution of DM in the inner region of the Galaxy is a difficult task. Baryons dominate the gravitational potential and the DM is a subdominant component. Furthermore, the Galactic bulge region can not be studied in the optical waveband due to dust extinction and obscuration, and it has been mainly studied in the infrared band. As we will see in this chapter, the actual amount and distribution of DM in the innermost regions of the Galaxy is highly uncertain. In order to study the DM content in the Galactic bulge region, we adopt a simple methodology, following the one presented in Hooper 2017. This methodology is described in section 5.2. We present the results of our analysis in 5.3 and our conclusions in 5.4. A large fraction of the material of this chapter was already presented in Iocco and Benito 2017.

5.1 Introduction

The DM density profile in the inner region of the MW is at the centre of a long-standing debate on whether the profile is cusped ($\gamma \sim 1$[1]) or cored ($\gamma \sim 0$) (see e.g. de Blok 2010). On the one hand, observations of dwarf galaxies seem to indicate a core profile at the centre of these galaxies (e.g. Oh et al. 2015). Nonetheless, the presence of a core is still debated (e.g. Genina et al. 2018). On the other hand, cusp profiles are preferred in DM-only N-body simulations independently of the size of the halo (Navarro et al. 1996). Some recent hydrodynamical simulations found a correlation between the slope of the innermost DM density profile and the stellar-to-halo mass ratio (Di Cintio et al. 2014b; Di Cintio et al. 2014a; Tollet et al. 2016;

---

[1] γ is the logarithmic slope of the DM density profile in the inner part of the Galaxy, i.e. $\gamma = -\mathrm{d}\ln(\rho_{\mathrm{DM}})/\mathrm{d}\ln(R)$.

Macciò et al. 2017) as seen in figure 5.1.[2] This relation implies that the DM profile in the MW is cusp, even cuspier than $\gamma \sim 1$ which is the typical value preferred by DM-only simulations. It is important to highlight that this correlation is not found in all hydrodynamical simulations (e.g. Vogelsberger et al. 2014; Schaye et al. 2015) and it might be a consequence of the subgrid physics model[3] describing star formation. Particularly, it might be due to the value adopted for the density threshold at which gas is turned into stars as shown in Benitez-Llambay et al. 2018.

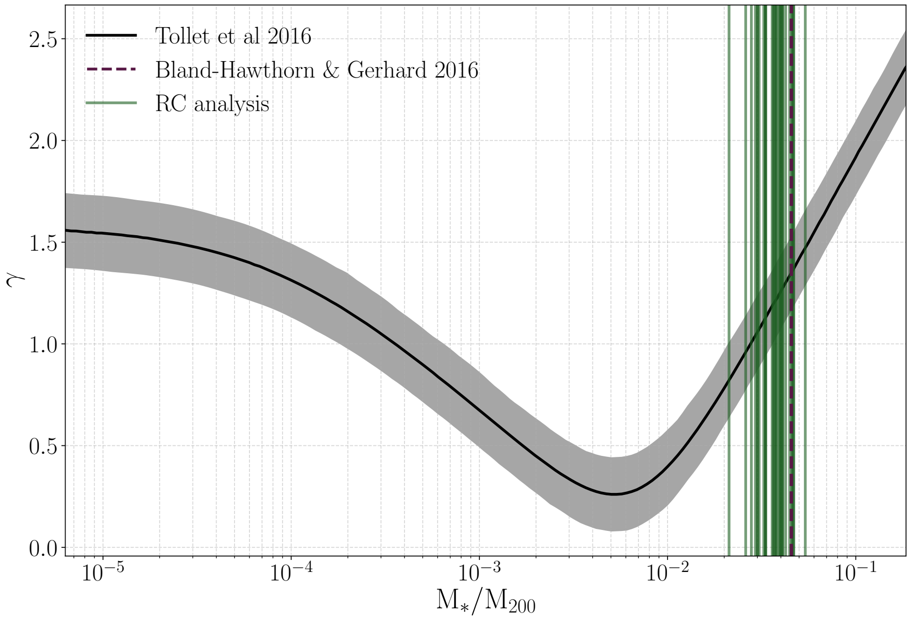

FIGURE 5.1: Relation between the inner slope of the DM density profile and the star formation efficiency of a galaxy, measured by means of the stellar-to-halo mass ratio, as found in Tollet et al. 2016. The vertical lines corresponds to the values of the stellar-to-halo mass ratio obtained for the MW in the review by Bland-Hawthorn and Gerhard 2016 (dashed purple line) and by means of the RC analysis from Benito et al. 2017 (solid green lines).

A precise estimation of the distribution of DM in the innermost region of the MW might, therefore, help us in understanding the interplay between baryons and DM in the processes of galaxy formation and evolution. Many mechanisms that can destroy a cusp profile have been proposed in the literature, such as, for example, a bursty and extended in time star formation activity (e.g. Benitez-Llambay et al. 2018). However, a cusp can be restored due to the response of the DM density profile to the cooling and condensation of baryons at the centre of the Galaxy (Blumenthal et al. 1986), or the accretion of smaller DM halos (Syer and White 1996).

---

[2] M_{200} is another widely used estimator of the mass of a DM halo. It is given by the following expression:

$$M_{200} = \frac{4}{3}\pi\, R_{200}^3\, 200\rho_{\rm crit}, \tag{5.1}$$

where R_{200} is the radius of the sphere with average density 200 times the critical density of the universe, $\rho_{\rm crit}$.

[3] Subgrid models are numerical recipes for implementing physical phenomena that occur at scales smaller than the resolution scale of the hydrodynamical simulation.

Indirect searches of the DM particle at the Galactic centre (GC) rely on the geometrical distribution of DM within this inner region. For this reason, a precise characterisation of the DM density profile in the innermost region of our Galaxy is fundamental for the interpretation of results from these experiments.

5.2 Methodology and setup

The distribution of DM in the inner ≈ 2.5 kpc of our Galaxy is determined following the methodology originally presented in Hooper 2017 and further used in Iocco and Benito 2017. A sketch of this method is as follows:

- First, we adopt an estimate of the total mass within a specific, central region of our Galaxy.
- Second, we compute the stellar mass (within the very same region) by integrating the stellar three-dimensional density profile.
- We then obtain the allowed DM mass simply as total minus stellar mass.
- Finally, we study the constraints that the allowed DM mass imposes on the parameter space of a generalised Navarro-Frenk-White (gNFW) density profile.

In the following, we describe in more detail each element of the adopted methodology. The first element of our analysis is the total, dynamical mass within a squared box, centred at the Galactic centre, with coordinates,

$$[x,\, y,\, z] = [\pm 2.2,\, \pm 1.4,\, \pm 1.2]\,\mathrm{kpc}; \tag{5.2}$$

which reads,

$$M_{\mathrm{total}} = (1.85 \pm 0.05) \times 10^{10}\,\mathrm{M}_{\odot}. \tag{5.3}$$

This value is estimated in Portail et al. 2017 by means of a Made-to-Measure (M2M) technique (Syer and Tremaine 1996; de Lorenzi et al. 2007). This technique relies on a N-body simulation of the Galaxy from which the phase-space distribution function is constructed by sampling a large number of particles. A weight is assigned to each of these particles. These weights are iteratively updated until the distribution function satisfies certain observational constraints on the stellar kinematics and stellar density profile in the region of interest (ROI). Portail et al. 2017 used the following set of observational constraints:

- radial velocity and velocity dispersion profiles from the BRAVA (Rich et al. 2007; Howard et al. 2008; Kunder et al. 2012) and ARGOS (Ness et al. 2013) surveys;
- proper motions from the OGLE-II survey (Rattenbury et al. 2007);
- star counts of Red Clump Giants (RCGs) from VVV, UKIDS and 2MASS surveys (Wegg et al. 2015) and
- a three-dimensional density map of RCGs from Wegg and Gerhard 2013.

The stellar kinematic constraints prove the total gravitational potential and, therefore, the total dynamical mass. Portail et al. 2017 used RCGs as tracers of the stellar mass. RCGs have been proved to be a good tracer of the stellar mass -the number of RCGs per unit stellar mass is constant- for a stellar population of 10 Gyr old with metallicities in the range $-1.5 \leq [\mathrm{Fe/H}] \leq 0.2$ (Salaris and Girardi 2002). The stellar Galactic bulge is known to have several stellar populations with debatable ages (see e.g. Calamida et al. 2015; Bensby et al. 2017). For this reason, we only rely on the total dynamical mass estimation of Portail et al. 2017.

In the estimation of the stellar (baryonic) mass is where our analysis most diverges from that in Hooper 2017. Rather than relying on the results of Portail et al. 2015, based on N-body simulations implementing a peanut-shaped bulge and different disc-to-halo ratios -resulting in five morphologies characterised by the degree of maximality of the disc-, we adopt a wider array of stellar morphologies modelled and normalised after observational data.

The stellar mass within the ROI is obtained by integrating each possible combination of stellar bulge and stellar disc three-dimensional density profiles, $\rho_*^i(R,\, \theta,\, \phi)$, described in chapter 3. We neglect the diffuse, interstellar gas since its contribution to the stellar mass is smaller than quoted uncertainties. The stellar bulge and disc are normalised to the microlensing optical depth toward the Galactic centre (Popowski et al. 2005) and the stellar surface density at the solar neighbourhood (Bovy and Rix 2013), respectively. Both measurements carry a statistical uncertainty that is propagated into the stellar mass, therefore obtaining an uncertainty on the stellar mass which is statistically comparable to that of the total mass. It is worth stressing that the bulge normalisation through microlensing optical depth is indeed affected by the stellar disc adopted, and we, therefore, present self-consistent results for all bulges and disc morphologies in our sample.

The DM mass allowed in the ROI, and its uncertainty, is the difference between the observational derivation of the total mass M_{tot}, and the inference of the stellar mass from observationally inferred density profiles M_*^i, where the index i runs over all the possible combinations of bulge and disc. Note that the allowed DM mass will be a function of the adopted morphology. Therefore, for each stellar morphology, we study how its corresponding allowed DM mass constrains the parameter space of a gNFW density profile. In order to do so, we scan the parameter space (γ, ρ_0, R_s) and find those points that give a mass of DM compatible at the 1 and 2σ levels with the value obtained simply as the difference between M_{tot} and M_*^i.

5.3 Results

5.3.1 Stellar and Dark Matter Masses

Our estimations of the stellar and DM masses in our ROI as a function of stellar (bulge plus disc) morphology are shown in figure 5.2. For the stellar mass, we obtain central values in the range $(1.2-1.7)\times10^{10}\,\mathrm{M}_\odot$, corresponding to 63-93% of the mass budget within the inner ≈ 2.5 kpc of the Galaxy. This is, the baryons dominate the gravitational potential and dynamics of the Galactic bulge region. Half of the stellar morphologies give a value of the DM mass compatible with zero at the 1σ level. This is not surprising due to the fact that DM is a sub-leading component in the inner region of the Galaxy and the uncertainties on the actual amount of DM in this region are large. Relative uncertainties on the allowed DM mass range from 30% up to 400%. Obtained DM masses are in the range $(0.1-0.7)\times10^{10}\,\mathrm{M}_\odot$, corresponding to 7-37% of the total mass budget of the Galactic bulge region, depending on the adopted stellar morphology.

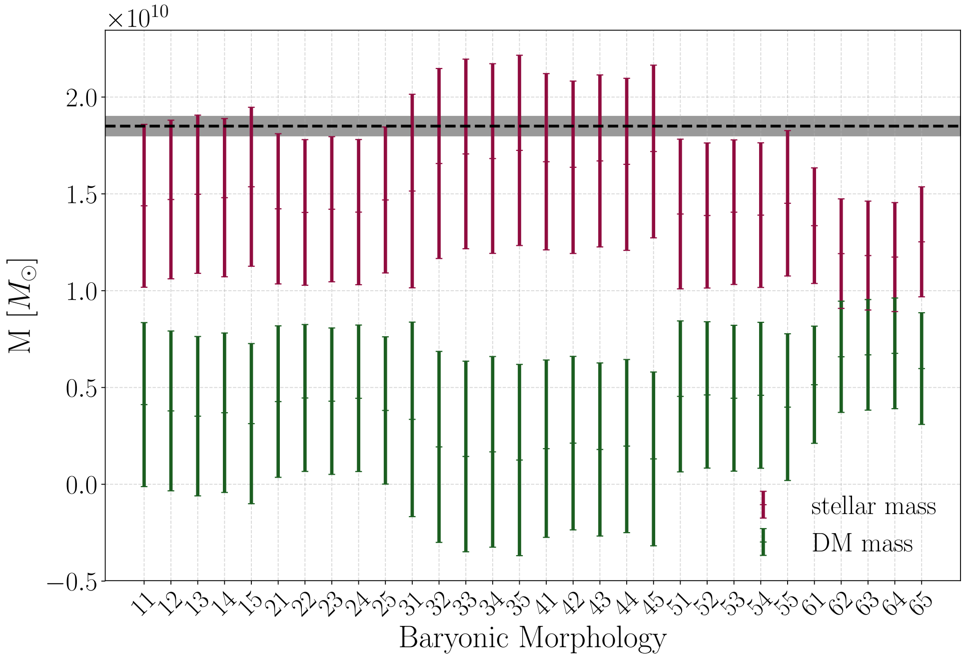

FIGURE 5.2: Stellar and DM masses, with corresponding 1σ uncertainties, as a function of baryonic (bulge plus disc) morphology. The dashed, horizontal, black line corresponds to the total dynamical mass and 1σ uncertainty (grey band) from Portail et al. 2017. X-tick labels stand for the bulge and disc numbers as in chapter 3. For instance, *11* stands for *bulge 1* (Stanek et al. 1997) and *disc 1* (Bovy and Rix 2013).

There are two sources of uncertainties that affect our estimation of the stellar mass: Uncertainties on the bulge's mass due to the microlensing optical depth and uncertainties on the disc's mass arising from the stellar surface density at the Sun's position. In figure 5.3, we breakdown each relative contribution to the overall uncertainty on the stellar mass as a function of baryonic morphology. It is clear from the figure that the principal source of uncertainties on the stellar mass comes from the bulge's normalisation.

In an attempt to reduce uncertainties on the stellar mass, we perform the following *stacked* analysis: Instead of normalising each bulge density profile to one measurement of the microlensing optical depth toward the GC as in Iocco and Benito 2017, we adopt, following Iocco et al. 2011, a set of microlensing optical depth measurements for different directions toward the GC:

- MACHO (Popowski et al. 2005): $\langle\tau\rangle = 2.17^{+0.47}_{-0.38} \times 10^{-6}$ for $(\ell, b) = (1.50^{\rm o}, -2.68^{\rm o})$.
- OGLE-II (Sumi et al. 2006): $\langle\tau\rangle = 2.55^{+0.57}_{-0.46} \times 10^{-6}$ for $(\ell, b) = (1.16^{\rm o}, -2.75^{\rm o})$.
- EROS 1-4 (Hamadache et al. 2006): $\langle\tau\rangle = (2.90 \pm 1.30) \times 10^{-6}$ for $(\ell, b) = (-4.5^{\rm o}, 2.40^{\rm o})$; $\langle\tau\rangle = (2.32 \pm 1.73) \times 10^{-6}$ for $(\ell, b) = (-1.5^{\rm o}, 2.42^{\rm o})$; $\langle\tau\rangle = (2.20 \pm 1.56) \times 10^{-6}$ for $(\ell, b) = (1.5^{\rm o}, 2.22^{\rm o})$; $\langle\tau\rangle = (1.65 \pm 0.83) \times 10^{-6}$ for $(\ell, b) = (4.5^{\rm o}, 2.53^{\rm o})$.

For each bulge density profile, we compute the normalised density and its corresponding uncertainty for each of the six microlensing optical depth measurements. The final normalised density of the bulge is given by the weighted average. Its uncertainty is the quadratic sum of the weighted standard deviation and the propagation of weighted uncertainties.

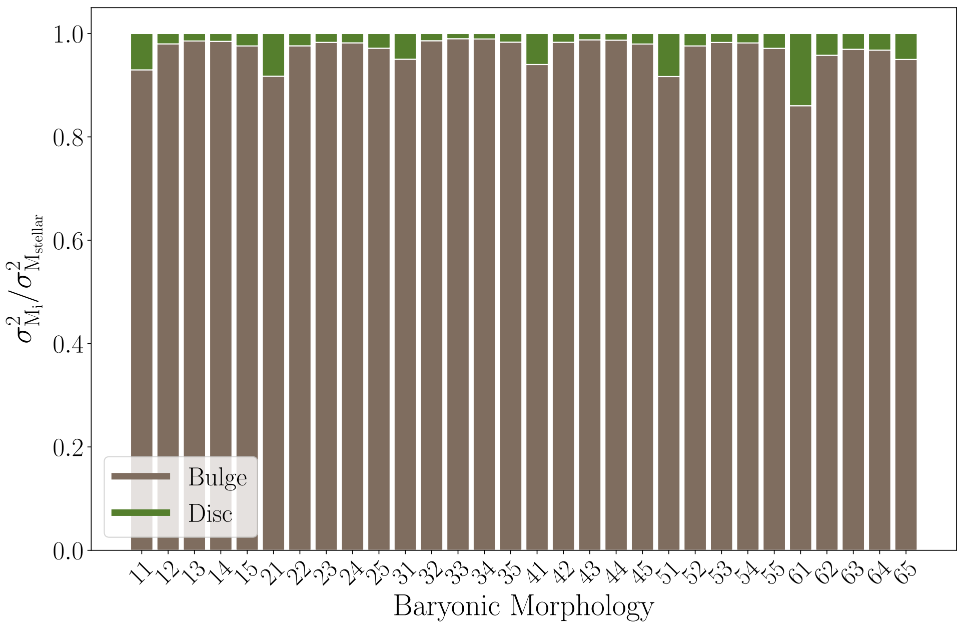

FIGURE 5.3: Breakdown of the relative contribution to the overall uncertainty on the stellar mass as a function of baryonic (bulge plus disc) morphology. From top to bottom, the bars show the mean contribution due to the stellar disc's normalisation (green) and the normalisation of the bulge (brown). X-tick labels stand for the bulge and disc numbers as in chapter 3 (see figure 5.2 for more details).

In figure 5.4, we compare relative uncertainties on the stellar mass between the analysis in Iocco and Benito 2017 and the new stacked analysis presented here. In the latter, uncertainties on the stellar mass are reduced by a factor $\sim 10\%$, with respect to the former analysis, for all stellar morphologies except for those morphologies carrying *bulge 3* (Vanhollebeke et al. 2009). This is due to the fact that *bulge 3* can not simultaneously describe the set of microlensing measurements toward different GC directions, therefore, the dispersion between the estimated normalised densities computed from each of the optical depth measurements is large.

In the stacked analysis, relative uncertainties in stellar and DM masses are decreased by a factor $\sim 10\%$ with respect to the analysis presented in Iocco and Benito 2017. Nonetheless, the relative uncertainty on the DM mass ranges from 30 to 400%. Therefore, a reduce of 10% is not significant. Furthermore, it is important to highlight that there might be systematic offsets between the different estimations of the microlensing optical depth. We are unable to perform a proper study of systematics with only six measurements. This methodology can, nevertheless, be used in the future with more microlensing measurements. For these reasons, from now on, we show the results obtained in Iocco and Benito 2017, i.e. the bulge density profile is calibrated to only one microlensing optical depth measurement.

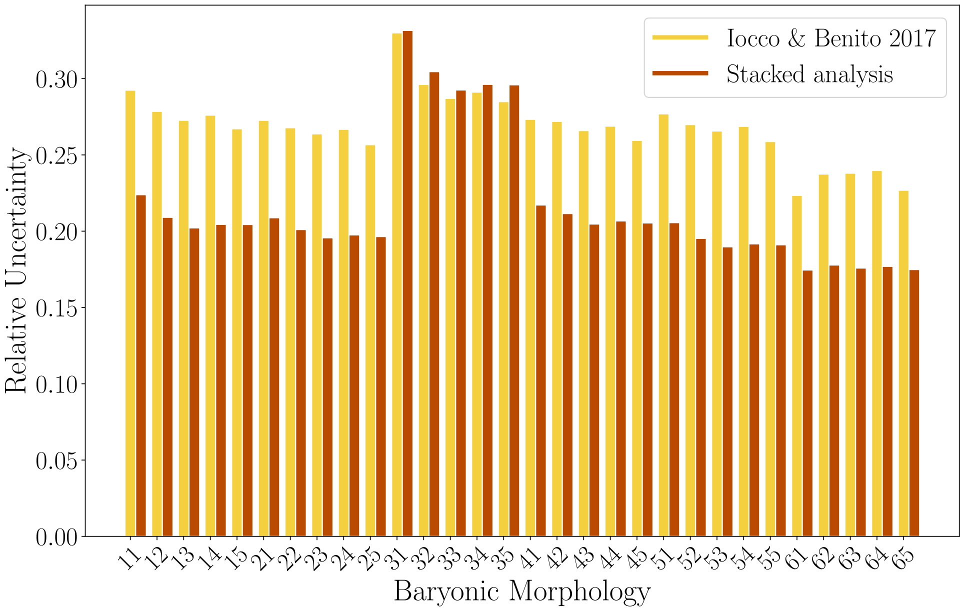

FIGURE 5.4: Relative uncertainty on the stellar mass as a function of baryonic (bulge plus disc) morphology. Yellow bars correspond to the analysis presented in Iocco and Benito 2017 (i.e. bulge density profile normalised to one microlensing optical depth toward the GC). Orange bars correspond to the stacked analysis (i.e. bulge density profile normalised to six microlensing optical depth toward different GC directions).

5.3.2 Constraints on a gNFW Profile

For each stellar morphology, the allowed DM mass is simply the difference M_{tot} and M_*^i, where the index i runs for all morphologies. At this point, we adopt a gNFW profile and study the constraints in the parameter space $(\gamma,\, \rho_0)$ imposed by this allowed DM mass.

We first study the effect of the Galactic parameters $(R_0\,, \Theta_0)$. Neither of the elements of the analysis depend on the Sun's velocity Θ_0, therefore our technique is insensitive to the local circular velocity. On the other hand, the bulge and disc density profiles have a dependence on the Sun's position. Furthermore, the normalisation of the stellar and DM components depends also on the distance between the Sun and the GC R_0. The dependence of the constraints in the parameter space $(\gamma,\, \rho_0)$ with the Sun's position are shown in figure 5.5. While setting constant the morphology of the bulge and disc and set the scale radius to $R_{\text{s}} = 20$ kpc, three different values of R_0 are adopted in each of the plots of the figure. We let the Sun's distance to the GC to vary in the range $7.5 - 8.5$ kpc. The region of the parameter space that gives a mass compatible at 1σ with the allowed DM mass is shown in white; in light purple, the area compatible at the 2σ level; and, in dark purple, the area excluded at more than 2σ. From the same figure, we deduce that the constraints mildly depend on the distance from the Sun to the GC. For this reason, we adopt the value $R_0 = 8$ kpc for the rest of the analysis.

Second, we study the effect of varying the sale radius R_s. We adopt a stellar morphology and assume three different values of the scale radius. The results are shown in figure 5.6 and motivate us to fixe the scale radius to $R_s = 20$ kpc since again there is a mild dependence of the constraints on this DM parameter.

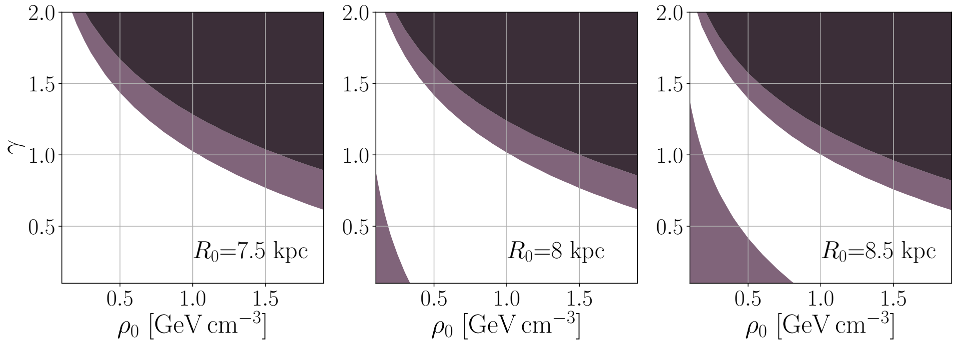

FIGURE 5.5: Constraints on the parameter space (γ, ρ_0) of a gNFW profile as a function of the Sun's galactocentric distance R_0 for *bulge 2* (*E2* bulge from Stanek et al. 1997) and *disc 2* (Han and Gould 2003). The points within the white region give a DM mass compatible at 1σ with the allowed DM mass obtained as the difference between M_{tot} and M_*^i. In light purple, the region compatible at 2σ and dark purple the region excluded at mored than 2σ.

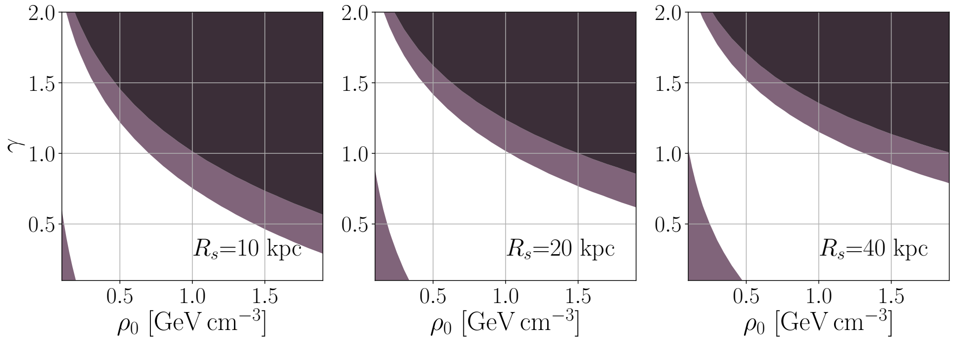

FIGURE 5.6: Constraints on the parameter space (γ, ρ_0) as a function of the scale radius R_s for *bulge 2* (*E2* bulge from Stanek et al. 1997) and *disc 2* (Han and Gould 2003). The colour coding is the same as in figure 5.5.

In figure 5.7, we show the results varying the bulge morphology (which sets most of the stellar mass in the region of interest), and by keeping $R_0 = 8$ kpc, disc component and scale radius $R_s = 20$ kpc.

Figure 5.8 shows the constraints for each possible combination of bulge and disc morphology. The red contours correspond to the 3σ confidence intervals from the RC analysis from Benito et al. 2017. We highlight in yellow the preferred ρ_0 region of this analysis, that can act as a prior in the estimation of a preferred region of γ. As it can be easily noticed, due to the uncertainties on the stellar mass the allowed region in the parameter space is quite sizeable. Most of the morphologies show no real preference for a cusp DM distribution ($\gamma \sim 1$) in the ROI, the lowest values of γ being disfavoured for few configurations only. For those configurations with *bulge 6* (Robin et al. 2012), core profiles for typical values $\rho_0 = 0.4$ GeV cm^{-3} are disfavoured at more than 2 σ. It is interesting to notice that the extremes of the region in exam are complementary to the validity limit of analysis based on dynamical tracers, which as discussed are typically restricted to galactocentric radii $R \geq 2.5$ kpc. The results

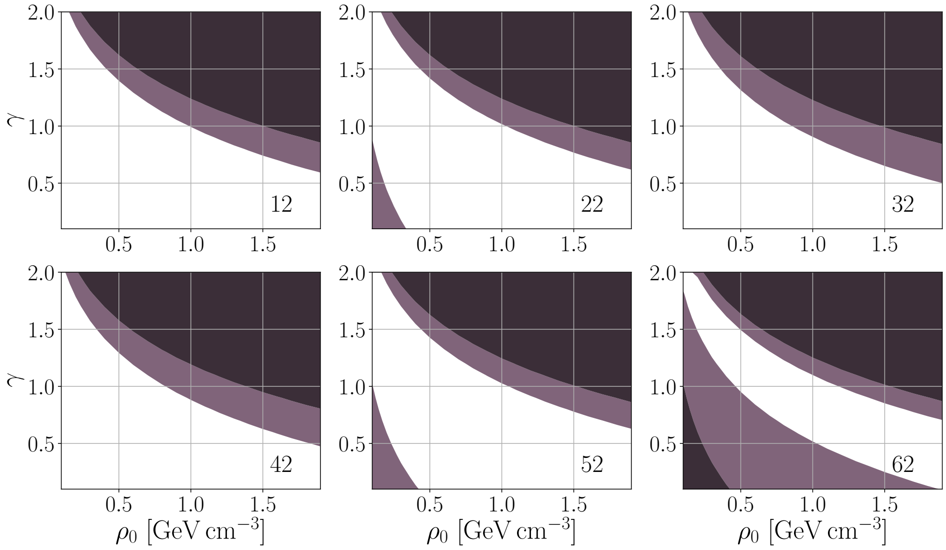

FIGURE 5.7: Constraints in the gNFW parameter space, for assigned values $R_s = 20$ kpc, $R_0 = 8.0$ kpc. Different panels show the result of changing the bulge morphology. The disc component is fixed to the morphology given in Han and Gould 2003. The numbers within each plot correspond to the number of bulge (first number) and the number of disc (second number), following the nomenclature presented in chapter 3.

from this and the RC analyses are compatible, except for the *61* configuration (bulge given in Robin et al. 2012 and disc from Bovy and Rix 2013). For this particular configuration, the tension might be caused due to several reasons: This particular combination of bulge and disc density profiles does not resemble the actual spatial distribution of baryons in the Galaxy; the gNFW parameterisation is not a good description of the DM distribution; or/and we can not describe the DM distribution everywhere in the Galaxy with the same global function.

We summarise the content of figure 5.8 in the tables of Appendix B, where we list the stellar mass content (and its uncertainty) and the estimated DM mass for all of our bulge and disc morphologies. We also report the range of γ allowed, if one imposes a prior on the local DM density, as discussed above.

5.4 Conclusions

We have presented an analysis of the DM density profile in the Galactic bulge region, following and complementing upon the recent analysis in Hooper 2017. By adopting an observational estimate of the total dynamical mass, and a large array of observationally-derived morphologies for the stellar components (bulge and disc), we are able to estimate the current statistical uncertainties on the allowed DM mass. We find that the DM mass vary between 7% and 37% of the total dynamical mass of the Galactic bulge region. These figures are compatible with those of the analysis in Hooper 2017, yet they define a bigger range (compatible with zero at one sigma) as a consequence of our ignorance on the actual distribution of stars in the region of the bulge and on the actual normalisation of the visible component. Both type of uncertainties are sizeable and prevent general conclusions on the preferred region of

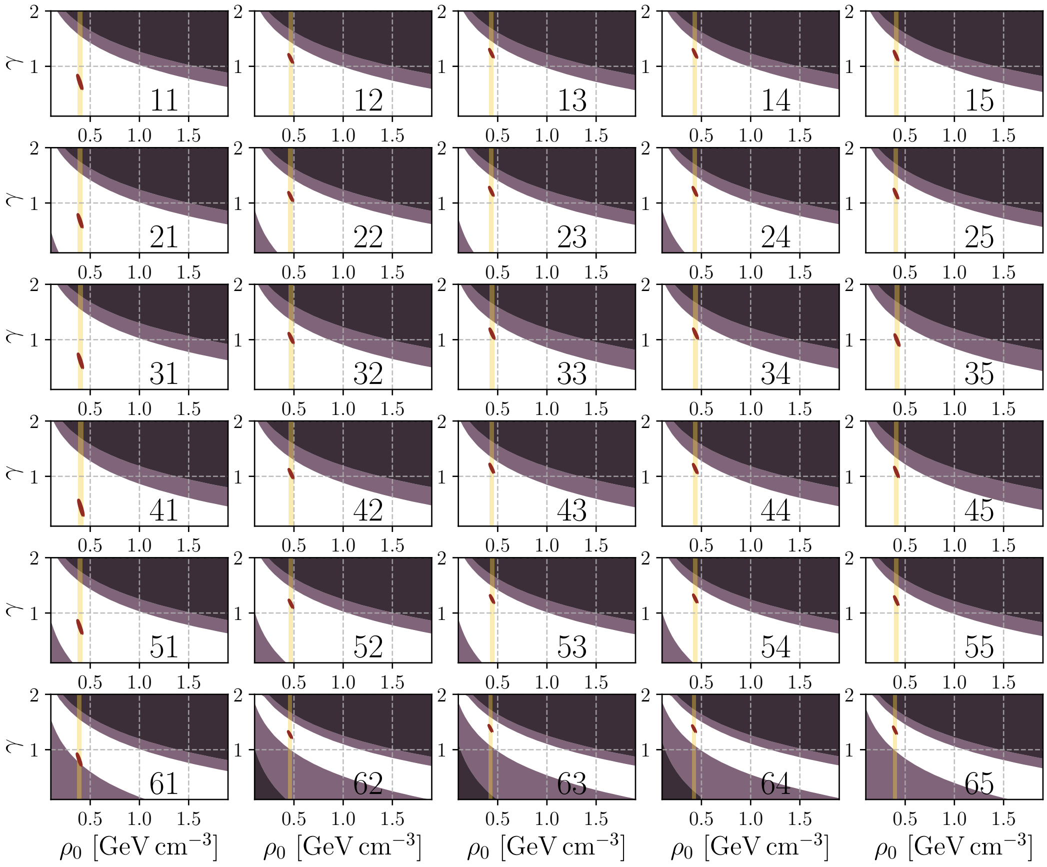

FIGURE 5.8: Constraints in the parameter space (γ, ρ_0) for all bulge (vertical axes) and disc (horizontal axis) morphologies presented in chapter 3. The small red regions are the 3σ region as from the RC analysis in Benito et al. 2017. The yellow bands highlight the extremes of the latter for the local DM density ρ_0. $R_s = 20$ kpc, $R_0 = 8.0$ kpc. The numbers within each plot correspond to the number of bulge (first number) and the number of disc (second number), following the nomenclature presented in chapter 3.

the parameter space (if the DM mass is fit to a gNFW profile): whereas cusp profiles are not strictly prohibited (although indexes $\gamma \sim 1.5$ are generally disfavoured at 1σ at least, depending on the bulge/disc configuration), neither are flat profiles, an index $\gamma = 0$ allowed for many of the morphologies at study. These results are compatible with analysis of outer regions, at galactocentric radii $R \geq 2.5$ kpc, performed with global techniques based on a fitting of the RC, but this is hardly indicative, nor surprising, given the very large degree of uncertainty described above.

We argue that it is still early for a conclusive answer about the distribution of DM in the GC due to sizeable uncertainties on the actual distribution of the visible component and its normalisation, rather than that on the total dynamical mass. Future surveys dedicated to the stellar census and dynamics in that region, like the forthcoming Wide Field InfraRed Survey Telescope (WFIRST) will help in the endeavour of reducing uncertainties.

A future prospect for reducing uncertainties on the normalisation of the bulge, and therefore on the stellar mass, is by means of a map of microlensing optical depth measurements as shown above. Gravitational microlensing can be further used as a tool for studying the structural properties of the Galactic bulge (e.g. Stanek et al. 1997). In this way, microlensing measurements can help us in discarding actual proposed parameterisations for this component of the Galaxy.

Chapter 6

Particle Dark Matter Searches

Although dark matter (DM) is approximately 85% of the matter content of the Universe, the nature of the DM remains unknown. Unraveling the nature of the DM particle has become one of the main problems in physics. For this purpose, different search strategies has been followed (e.g. Aprile et al. 2017; Akerib et al. 2018; Du et al. 2018).

From the various candidates proposed as the DM particle, Weakly Interacting Massive Particles (WIMPs) are among the most studied class of candidates over the last decades.[1] These particles with masses ($\sim$ 100 GeV) and coupling strengths ($\langle \sigma v \rangle \sim 3 \times 10^{-26}$ cm^3/s) at the electroweak scale can provide the relic abundance of DM observed today, if they were thermally produced in the early Universe. This has motivated direct and indirect WIMP searches, as well as searches from collider experiments. We schematically describe direct and indirect searches, and their dependence on astrophysical quantities in the first part of this chapter.

As seen in chapter 4, the determination of the DM distribution in the Milky Way (MW) proceeds from astrophysical observations. These observations have sizeable uncertainties that need to be properly quantified and accounted for while interpreting results from direct and indirect DM searches. In this way, astrophysical uncertainties can be further propagated into the parameter space of the DM particle candidate (e.g. Benito et al. 2017). Motivated by this, we quantify uncertainties on the determination of the DM distribution in the MW by means of the Rotation Curve (RC) method. In 6.2, we qualitatively study the different sources of uncertainties that affect the determination of the DM distribution in the MW. While in 6.3, we present a full-data driven analysis that quantifies those astrophysical uncertainties. The likelihood profile of this latter analysis is publicly available and can be used for properly accounted for astrophysical uncertainties while interpreting the results of direct and indirect searches, as we will show in an example in the last part of the chapter.

Some material of this chapter has been already published in Benito et al. 2017 and most of the content will be publish in a forthcoming paper (Benito et al. in preparation).

6.1 Direct and Indirect WIMP Searches

Under the assumption that the DM particle is a WIMP, direct and indirect searches aim to constrain the parameter space of a given WIMP candidate. Both experiments

---

[1] Along this chapter, if not specified otherwise, the words DM and WIMP are interchangeable.

have as input astrophysical quantities, such as the spatial distribution of DM in the target for indirect searches, and its phase space distribution in the solar neighbourhood or the local DM density for direct ones. These quantities of astrophysical nature, on which the interpretation of these kind of experiments rely on, have sizeable uncertainties that should be correctly accounted for and propagated in the determination of new physics.

In this section, we sketch the underlying physics behind direct and indirect DM experiments. Although there are collider experiments that also aim at detecting WIMPs, we do not touch on these searches since they do not have a dependence on astrophysical quantities.

6.1.1 Direct Detection

Direct detection experiments aim at measuring, in underground detectors, the small recoil energy of a nucleus after the collision with a WIMP arriving from the DM halo of the MW. For the case of spin-independent scattering, the differential recoil spectrum[2] for a DM particle scattering elastically off a nucleus with atomic mass number A can be written as,

$$\frac{dR}{dE_R} = \frac{\rho_0 \, A^2 \, \sigma_{\rm SI}}{2 \, m_{\rm DM} \, \mu_p^2} \, F^2(E_R) \, \eta(v_{\rm min}, t), \tag{6.1}$$

where E_R is the nuclear recoil energy, ρ_0 is the local DM density, $m_{\rm DM}$ is the DM mass, μ_p is the reduced mass of the DM-nucleon system, $\sigma_{\rm SI}$ is the spin-independent DM-nucleon scattering cross-section, and $F(E_R)$ is a form factor. The minimum speed needed for the DM particle to deposit a recoil energy E_R in the detector is

$$v_{\rm min} = \sqrt{m_A E_R / (2\mu_A^2)}. \tag{6.2}$$

Here m_A is the mass of the nucleus, and μ_A is the DM-nucleus reduced mass. The halo integral, $\eta(v_{\rm min}, t)$, which together with the local DM density encompasses the astrophysics dependence of the recoil rate, is defined as,

$$\eta(v_{\rm min}, t) \equiv \int_{v > v_{\rm mim}} d^3v \, \frac{f_{\rm det}(\mathbf{v}, t)}{v} \,, \tag{6.3}$$

where $f_{\rm det}(\mathbf{v}, t)$ is the local DM velocity distribution in the detector rest frame. The differential recoil spectrum from equation (6.1) can be schematically rewritten as,

$$\frac{dR}{dE_R} = C_{\rm PP} \, F^2(E_R) \, \rho_0 \, \eta(v_{\rm min}, t), \tag{6.4}$$

where the coefficient $C_{\rm PP} = A^2 \, \sigma_{\rm SI} / (2 \, m_{\rm DM} \, \mu_p^2)$ contains the particle physics dependence of the event rate, while $\rho_0 \, \eta(v_{\rm min}, t)$ contains the astrophysics dependence.

6.1.2 Indirect Detection

Indirect detection aims at detecting the flux of final stable particles produced by DM annihilation or decay in astrophysical environments. The differential flux of final

---

[2] The differential recoil spectrum is the event rate per unit energy, per unit detector mass and per unit time.

stable particles[3] from self-annihilation of DM particles of mass $m_{\rm DM}$ in a solid angle $\Delta\Omega$ is given by

$$\frac{{\rm d}\Phi}{{\rm d}E} = \frac{\langle \sigma v \rangle}{8\pi\, m_{\rm DM}^2} \frac{{\rm d}N}{{\rm d}E} \times \mathcal{J}. \tag{6.5}$$

The first term on the right-hand side encodes the particle physics information: $\langle \sigma v \rangle$ is the thermally-averaged velocity-weighted self-annihilation cross-section and ${\rm d}N/{\rm d}E$ is the number of particles produced per annihilation. The function $\mathcal{J}$, the so-called $\mathcal{J}$-factor, is defined as the integral along the line of sight (l.o.s.) of the DM density, $\rho_{\rm DM}$, in case of DM decay, or of the DM density squared, $\rho_{\rm DM}^2$, in case of DM annihilation. It encodes the geometrical distribution of DM within the target and it takes the following form for the case of DM self-annihilation,

$$\mathcal{J}_{\rm annih} = \int_{\Delta\Omega} {\rm d}\Omega \int_{\rm l.o.s} {\rm d}s\, \rho_{\rm DM}^2(R(s,\psi)), \tag{6.6}$$

where ψ is the opening angle between the l.o.s. s and the direction towards the target and $\Delta\Omega$ is the region of interest over which the angular integration is performed.

We can rewrite the flux of final stable particles schematically as a function of a particle physics term Φ_{PP} which encodes all the information of the underlying DM particle physics model, and an astrophysical term $\mathcal{J}$. This is,

$$\Phi_{\rm DM}(E) = \Phi_{\rm PP}(E)\, \mathcal{J}. \tag{6.7}$$

In this analysis, we remain agnostic about the particular form of the particle physics term $\Phi_{\rm PP}$, for the case of indirect searches, and $C_{\rm PP}$, in direct experiments.

There are several astrophysical environments where we can look for a DM annihilation or decay signal, such as dwarf galaxies and clusters of galaxies. Nonetheless, it is worth stressing here that the material presented in this chapter is only relevant for those searches within our Galaxy.

6.2 Uncertainties on the Dark Matter Distribution: Qualitative Analysis

In this analysis, we account for the following sources of astrophysical uncertainties affecting the determination of the DM distribution in the MW:

- Uncertainties on the morphology of the visible, i.e. baryonic, component of the Galaxy;
- Uncertainties on the normalisation of the baryonic component;
- Uncertainties on Galactic parameters: Sun's galactocentric disctance, R_0, and local circular velocity, Θ_0.[4]

Uncertainties on the baryonic morphology arise due to our ignorance on the actual mass distribution of stars and gas in the Galaxy. We account for this source of uncertainty by adopting a large array of observationally inferred density profiles for

---

[3] Differential flux is the number of particles produced per unit time, unit area and unit energy.

[4] Uncertainties on the Local Standard of Rest (LSR) are indirectly taken into account within the uncertainties in R_0 and Θ_0.

the stellar bulge and stellar disc components. The array of baryonic morphologies, obtained by individually combining each alternative description of bulge and disc, represents a nearly complete set of all possible morphologies still consider viable to date. Their spread can be considered a satisfactory indicator of the systematics present for the mass modelling of the MW, with the conclusion that the actual physical reality must reasonably lie within them.

Uncertainties on the normalisation of the baryonic component reflect our ignorance on the actual weight of baryons with respect to the total Galactic mass budget. The bulge component is normalised through microlensing optical depth toward the Galactic centre (GC). On the other hand, the stellar disc is normalised to the stellar surface density at the Sun's galactocentric distance. Both observational quantities have associated statistical uncertainties that propagate into the determination of the DM distribution in our Galaxy (see chapter 3 for more details).

Finally, the distribution of DM is sensitive to quoted uncertainties on the Galactic parameters (R_0, Θ_0). On the one hand, the observed RC depends on (R_0, Θ_0) since l.o.s. velocities are measured with respect to the Sun. These velocities are translated into rotation velocities with respect to the GC by convolution with the distance from the Sun to the GC, R_0, and the circular velocity at the Sun's position, Θ_0. On the other hand, each baryonic density profile depends on R_0. The stellar bulge, stellar disc and gas mass distributions are obtained by optical and infrared (IR) observables and depend on the value for R_0 adopted in the original publication (c.f. chapter 3).

We, firstly, test the effect of each of the mentioned uncertainties one at a time, and in section 6.3, we present a full data-driven analysis that quantifies these astrophysical uncertainties. For this section, we adopt a generalised Navarro-Frenk-White (gNFW) density profile and a two-parameter fitting while fixing $R_s = 20$ kpc. For the observed RC, we adopt the `galkin` unbinned compilation. In this chapter, we restrict ourselves to the `galkin` compilation, although this implies a limitation to the innermost region of the Galaxy. L.o.s. velocity dispersion profiles of stellar halo stars are used to trace the RC in the range $\sim 20 - 100$ kpc from the GC. These stellar tracers do not follow circular orbits around the centre of the Galaxy. Therefore, the use of this data requires further assumptions such as, for example, about the virialisation of the system and the anisotropy parameter $\beta(r)$. Observed and predicted (baryons plus DM) rotation velocities are compare by means of a two-dimensional χ^2 statistics (see chapter 4).

Figure 6.1 shows the effect of each source of uncertainties on the determination of the DM distribution in the MW. Top panels show DM density profiles as a function of the distance to the GC, and bottom panels show the relative difference of the profiles with respect to a reference morphology. The reference morphology corresponds to:

- *Bulge 2* given in Stanek et al. 1997, *disc 2* taken from Han and Gould 2003 and gas (Ferrière 1998; Ferrière et al. 2007).
- Central values of Σ_* (Bovy and Rix 2013) and $\langle\tau\rangle$ (Popowski et al. 2005), and
- Galactic parameters $R_0 = 8$ kpc and $\Theta_0 = 230$ km/s.

Left panels show variations on the DM distribution induced by uncertainties on the actual mass distribution of baryons. For these panels, we fix baryonic normalisation and Galactic parameters and vary baryonic morphology. Middle panels show variations on the distribution of DM due to uncertainties on the actual weight of baryons with respect to the total mass budget for fixing baryonic morphology and Galactic parameters. The different lines of these middle panels correspond to constraints on the DM distribution while varying the central baryonic rotation curve within 1σ uncertainties on Σ_* (Bovy and Rix 2013) and $\langle\tau\rangle$ (Popowski et al. 2005). Finally, right panels show variations on the DM distribution constraints for three combinations of (R_0, Θ_0): (8 kpc, 230 km/s) - reference, (7.5 kpc, 312 km/s), (8.5 kpc, 180 km/s); for fixing morphology and baryonic normalisation. From this figure we can infer:

- Systematic uncertainties on the baryonic morphology (left panels of figure 6.1) affect the DM distribution specially in the inner 2.5 kpc by at most 2 orders of magnitude. It is worth stressing that any inference of the DM density profile below 2.5 kpc is an extrapolation since the RC analysis only applies for galactocentric distances $\geq$ 2.5 kpc due to the triaxial morphology of the Galactic bulge.
- Statistical uncertainties due to the normalisation of baryons (middle panels of figure 6.1) are $\lesssim 20\%$ and, therefore, negligible with respect to the other two sources of uncertainties.
- The extreme values for the Galactic parameters are chosen to vary between $R_0 = [7.5 - 8.5]$ kpc and $\Theta_0 = [180 - 312]$ km/s, for the representative morphology. The local circular speed can range from (200 ± 20) km/s to (279 ± 33) km/s (McMillan and Binney 2010). Hence, we take $\Theta_0 = 180$ km/s and 312 km/s as lower and higher estimates, respectively. Uncertainties on Galactic parameters (right panels of figure 6.1) affect both the inner and outer part of the Galaxy, the change in the DM density profile with respect to our standard set of Galactic parameters, i.e. $R_0 =$8 kpc and $\Theta_0 =$230 km/s, is four orders of magnitude.

From these we can conclude that indirect searches of DM in the GC will be affected mainly by uncertainties on the actual distribution of baryons in the Galaxy and the choice of Galactic parameters. On the other hand, direct searches are primary affected by the choice of Galactic parameters (R_0, Θ_0). Uncertainties on the baryonic normalisation are swamped by the other two uncertainties and are irrelevant at this stage (Benito et al. 2017).

6.3 Uncertainties on the Dark Matter Distribution: Quantitative Analysis

In the last section, we have qualitative studied the effect of astrophysical uncertainties on the determination of the DM distribution in the MW and their effect on WIMP searches within our Galaxy. We have studied the effect of each astrophysical source of uncertainty individually. In this section, we present a full data-driven analysis whose output is a practical tool that encodes all the above astrophysical uncertainties that affect the reconstruction of the DM density profile in our Galaxy. The main goal of this analysis is to provide results in a general form such that they can be used by the community in order to properly accounted for astrophysical uncertainties while interpreting the results from direct and indirect DM searches. The likelihood profile of this analysis is available at https://github.com/mariabenitocst/UncertaintiesDMinTheMW.

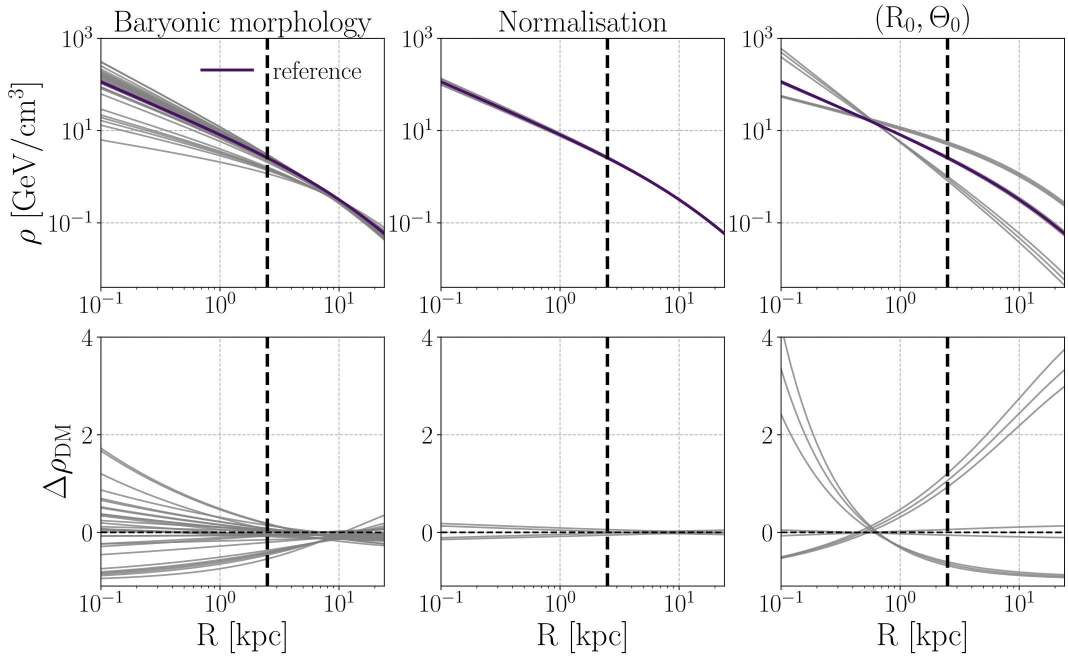

FIGURE 6.1: Top panels: The DM density, ρ_{DM}, as a function of radial distance from the GC, R. Reference morphology (*bulge 2* plus *disc 2*) is shown by the purple line, rest baryonic morphologies are shown in grey. Bottom panels: relative error of ρ_{DM} with respect to the reference morphology. The dashed black line in the bottom panel corresponds to a perfect match between the morphology considered and the reference morphology. Left panels correspond to changes on the DM distribution due to baryonic morphology. Middle panels show the variation of the DM density profile due to changes on the baryonic normalisation. Right panels show changes due to variations in the Galactic parameters (R_0, Θ_0) (see text for more details). The vertical dashed line corresponds to $R = 2.5$ kpc.

6.3.1 Setup

The distribution of DM in our Galaxy is determined by means of the RC. As already pointed out, tangential velocities of the disc trace the enclosed amount of matter, which in turn prove the total gravitational potential that balances the circular motion around the GC. By subtracting from the observed rotation velocities, the velocities predicted by the pure effect of gravity of the visible component, we can infer constraints on the DM distribution for a given parameterisation of the DM density profile.

For the observed RC, we use the `galkin` compilation (Pato and Iocco 2017). This compilation includes a large number of different kinematical tracers within the visible Galaxy, i.e. up to galactocentric distance ~ 22 kpc. The `galkin` RC consists of 25 different data sets (c.f. appendix A). Due to systematic effects, or other data-collection artefacts, there are points within the compilation that are incompatible at more than 5σ. In order to avoid possible bias when binning the data, we proceed as follows: For those velocity data points above 9 kpc with relative uncertainty lower than 1%, we artificially increase the uncertainty to 10%.

In this analysis, we adopt the following binning scheme: We bin the data in the non-dimensional variable $x = R/R_0$, rather than in galactocentric distance R, due to the fact that when varying R_0 the data *move* along the R-axis. Binning in x mitigates this effect, so that, for different values of R_0, a given x-bin contains roughly the same unbinned data points. We use angular velocities $\omega(x)$ rather than circular velocities both for binning and fitting. This is because the former velocities are uncorrelated with the x-variable (see e.g. Iocco et al. 2015a). Our analysis is restricted to $x \geq 2.5/8$ in order to avoid the inner region of the Galaxy where the underlying gravitational potential significantly departures from axial symmetry and objects might follow non-circular orbits due to the triaxial morphology of the Galactic bulge. More in detail, we apply the following binning scheme:

- 15 bins from $x = 2.5/8$ to $x = 10/8$ with a step of $\Delta x = 0.5/8$;
- 7 bins from $x = 10/8$ to $x = 18/8$ with a step of $\Delta x = 1/8$;
- 2 bins from $x = 18/8$ to $x = 22/8$ with a step of $\Delta x = 2/8$.

Which make a total of 25 x-bins. A bin of $\Delta x = 0.5/8$ or smaller for $x < 10/8$ is necessary to properly account for the steepness relation between angular velocities and galactocentric distances. If the size of the bin is increased, the uncertainty on the binned velocity reflects not only the dispersion of the observed data points, but also the slope on the $w-x$ relation. At large x the binning is larger also due to the scarcity of data. In order to assign a given data point to a bin we consider only the central value x_i and neglect the error δx_i. Within each bin, the average angular velocity, $\bar{\omega}_j$, and its corresponding uncertainty $\sigma_{\bar{\omega}_j}$ are given by

$$\bar{\omega}_j = \frac{\sum_{i=1}^{N_{bin}} \omega_i/\sigma^2_{\omega_i}}{\sum_{i=1}^{N_{bin}} 1/\sigma^2_{\omega_i}}, \tag{6.8}$$

$$\sigma^2_{\bar{\omega}_j} = \frac{\sum_{i=1}^{N_{bin}} (\bar{\omega} - \omega_i)^2/\sigma^2_{\omega_i}}{\sum_{i=1}^{N_{bin}} 1/\sigma^2_{\omega_i}} + \frac{N_{bin}}{\sum_{i=1}^{N_{bin}} 1/\sigma^2_{\omega_i}}, \tag{6.9}$$

i.e., $\bar{\omega}_j$ is just the weighted mean of the data in the bin and N_{bin} is the number of data points in the bin. The uncertainty $\sigma_{\bar{\omega}_j}$ is composed of two terms: The first is the

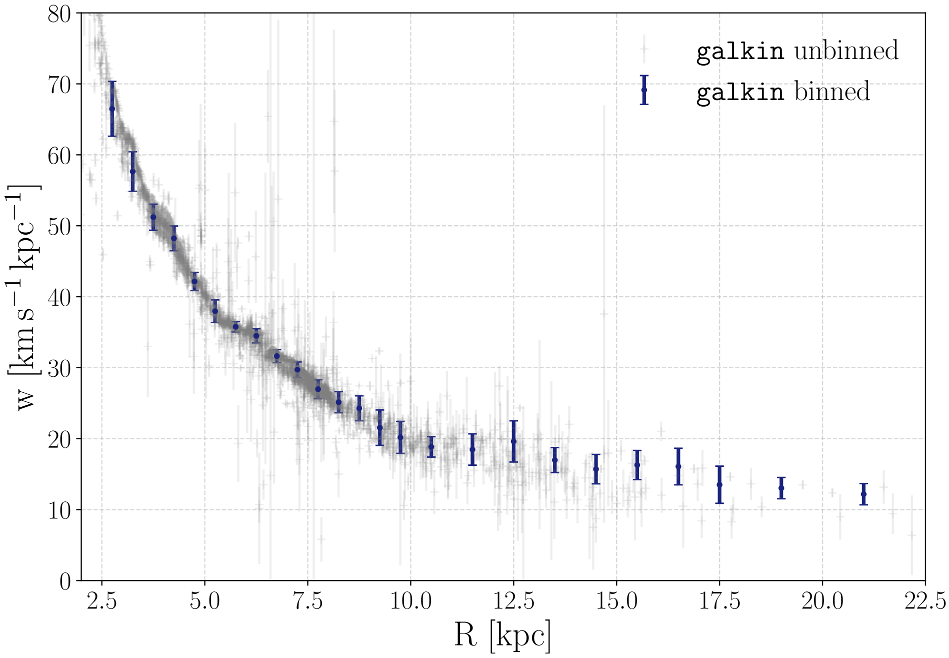

FIGURE 6.2: Rotation curve of the Milky Way. `galkin` compilation and binned data for $R_0 = 8$ kpc, $\Theta_0 = 230$ km/s, and $(U_\odot, V_\odot, W_\odot) = (11.1, 12.24, 7.25)$ km/s (Schönrich et al. 2010).

weighted dispersion of the data and the second term gives the mean weighted error of the data. An example of the binned and unbinned RCs for $R_0 = 8$ kpc, $\Theta_0 = 230$ km/s, and $(U_\odot, V_\odot, W_\odot) = (11.1, 12.24, 7.25)$ km/s (Schönrich et al. 2010) is given in figure 6.2.

For each baryonic component of the Galaxy (i.e. stellar bulge, stellar disc and gas), we adopt the array of observationally-inferred three dimensional density profiles presented in chapter 3. In this way, we bracket systematic uncertainties due to our ignorance on the actual shape of baryons in the Galaxy. The discrete variable $\mathcal{M}_i$ accounts for the different baryonic morphologies adopted in our analysis.

For the DM component, we adopt a gNFW density profile. This profile has three free parameters: the inner slope, γ; the scale radius, R_s; and the local DM density, ρ_0. It is important to notice that observed, baryonic and DM velocities depend on the adopted value for the Sun's galactocentric distance.

A further source of uncertainty is the actual peculiar motion of the Solar system, $(U_\odot, V_\odot, W_\odot)$, with respect to the local standard of rest (LSR).[5] $(U_\odot, V_\odot, W_\odot)$ are, respectively, the velocity orthogonal to the circle of the orbit and pointing outward the GC, the velocity tangential to the circle, and the velocity orthogonal to the circle pointing in the z-direction. In this analysis, we adopt the values $(U_\odot, V_\odot, W_\odot) = (11.10, 12.24, 7.25)$ km/s from Schönrich et al. 2010. The most relevant quantity for the RC analysis is $V_\odot$ which is found to have a large scatter in the range $5 - 24$ km/s from different analyses in the literature (e.g. Schönrich et al. 2010; Bovy et al. 2012; Reid et al. 2014). Combining $V_\odot$ together with the total Solar system angular velocity

---

[5] The LSR is the system comoving along a circular orbit around the GC with a velocity equal to the RC velocity at the Sun's position, Θ_0.

$\Omega_{g,\odot} = 30.24 \pm 0.12$ km s^{-1}kpc^{-1} (Bland-Hawthorn and Gerhard 2016),[6] we can infer the local circular velocity Θ_0, once R_0 is specified, through the equation,

$$\Omega_{g,\odot} = \frac{V_{g,\odot}}{R_0} = \frac{\Theta_0 + V_{\rm LSR} + V_\odot}{R_0}, \tag{6.10}$$

where $V_{g,\odot}$ is the Sun's total tangential velocity relative to Sgr A*, $V_{\rm LSR}$ is the tangential velocity of the LSR relative to the rotational standard of rest, 0 ± 15 km s^{-1} (Bland-Hawthorn and Gerhard 2016); and $V_\odot$ is the tangential solar motion relative to the LSR. For $R_0 = 8.0$ kpc, equation (6.10) gives $\Theta_0 = 230$ km/s, which are commonly adopted values.

6.3.2 Methodology

Our analysis has 7 free parameters:

- The discrete variable $\mathcal{M}_i$ running over the 30 different baryonic morphologies;
- the 3 DM parameters $\Theta_{\rm DM}$, i.e. γ, R_s, ρ_0;
- the galactocentric distance R_0; and
- the two parameters that normalise the baryonic component: $\langle\tau\rangle$ and Σ_*.

We use R_0 as free parameter and fix $V_\odot = 12.24$ km/s and $V_{\rm LSR} = 0$ km/s since the uncertainties in $V_\odot$ and $V_{\rm LSR}$ introduce a variation in Θ_0 similar or smaller than the one caused by R_0.

For each point in the seven-dimensional parameter space, we compute the corresponding $\chi^2_{\rm RC}$ given by the following expression:

$$\chi^2_{\rm RC}(\Theta_{\rm DM}, R_0, \mathcal{M}_i, \langle\tau\rangle, \Sigma_*) = \sum_j \left[\frac{(\omega(x_j, \Theta_{\rm DM}, R_0, \mathcal{M}_i, \langle\tau\rangle, \Sigma_*) - \bar{\omega}_j)^2}{\sigma^2_{\bar{\omega}_j}}\right] + \chi^2_{\langle\tau\rangle}(\langle\tau\rangle) + \chi^2_{\Sigma_*}(\Sigma_*), \tag{6.11}$$

where $\omega(x_j, \Theta_{\rm DM}, R_0, \mathcal{M}_i, \langle\tau\rangle, \Sigma_*)$ is the model prediction which takes the following form:

$$\omega(x_j, \Theta_{\rm DM}, R_0, \mathcal{M}_i, \langle\tau\rangle, \Sigma_*) = \sqrt{[\omega_b(x_j, R_0, \mathcal{M}_i, \langle\tau\rangle, \Sigma_*)]^2 + [\omega_{\rm DM}(x_j, \Theta_{\rm DM}, R_0)]^2}, \tag{6.12}$$

i.e., it is given by the sum of the DM and baryonic contribution. For $\chi^2_{\Sigma_*}$ and $\chi^2_{\langle\tau\rangle}$ we use the expressions:

$$\chi^2_{\Sigma_*} = \frac{(\Sigma_* - 38)^2}{4^2} \tag{6.13}$$

and

$$\chi^2_{\langle\tau\rangle} = \frac{(\langle\tau\rangle - 2.17)^2}{0.42^2}, \tag{6.14}$$

where we have adopted the measurement of the stellar surface density at the Sun's position from Bovy and Rix 2013 and the microlensing optical depth given in Popowski et al. 2005. Notice that the error on $\langle\tau\rangle$ has been symmetrised for simplicity.

---

[6] The angular velocity of the Solar system, $\Omega_{g,\odot}$, is inferred from the proper motion of the source Sagittarius A* in the Galactic plane under the assumption that this source is at rest at the GC.

The number of parameters in our analysis is sufficiently small to use a grid scan rather than a Monte Carlo approach. We thus scan the following discrete grid:

- 50 values for ρ_0 linearly spaced in the range $[0.0, 1.0]$ GeV/cm^3;
- 50 values for R_s logarithmically spaced in the range $[5.0, 100.0]$ kpc;
- 15 values of γ linearly spaced in the range $[0.0, 1.5]$;
- 11 values of R_0 linearly spaced in the range $[7.5, 8.5]$;
- 30 morphologies $\mathcal{M}_i$;
- For $\langle\tau\rangle$ and Σ_* we use 10 values each, linearly spaced in the range $[-2\sigma, +2\sigma]$.

We verified that including $\langle\tau\rangle$ and Σ_* in the $\chi^2_{\rm RC}$ does not crucially affect the analysis. Keeping $\langle\tau\rangle$ and Σ_* fixed to their central values only reduces slightly the error in the determination of the other parameters of the analysis. This is likely due to the fact that the bulk of the uncertainty from the baryonic morphology is already taken into account considering the 30 different morphologies $\mathcal{M}_i$, as already shown in the qualitative analysis presented in 6.2. Nonetheless, for consistency of the analysis and for a more robust error determination, we include $\langle\tau\rangle$ and Σ_* in the overall $\chi^2_{\rm RC}$. Furthermore, for the above same reason, just 10 grid values of $\langle\tau\rangle$ and Σ_* are already enough to properly include the effect of their uncertainty on the analysis.

In order to derive constraints in sub-spaces of the seven-dimensional parameter space we use the frequentist method of profiling (e.g. Rolke et al. 2005). For instance, in order to build the two-dimensional χ^2 in two given parameters, we take the minimum χ^2 over the remaining 5 parameters for each two-dimensional grid point.

6.3.3 Results

We show in the following the constraints on the DM parameters from the above χ^2 analysis. First, we present results while fixing $\gamma = 1$. In this way, we are able to study how varying R_0 affects the constraints on the DM parameter space. Second, we present the constraints profiled over R_0 in order to generalise our results as a function of γ.

NFW $\gamma = 1$ case

Figure 6.3 shows the results of the fit for $\gamma = 1$ and different values of R_0. The left panel shows 2σ contours in the $R_s - \rho_0$ plane for fixed values of R_0 and profiled over $\mathcal{M}_i$, $\langle\tau\rangle$ and Σ_*. The 2σ contour corresponds to the region in the plane (R_s, ρ_0) that satisfies the condition $\chi^2 \leq \chi^2_{BF} + \Delta\chi^2$, where χ^2_{BF} is the minimum χ^2 and $\Delta\chi^2 = 6.18$ for two degrees of freedom. This figure shows that the constraints on ρ_0 strongly depend on R_0. This is best seen in the right panel where 1σ ($\Delta\chi^2 = 2.30$ from the minimum) and 2σ contours in the $R_0 - \rho_0$ plane, profiled over the remaining parameters, are shown. The plot shows that the analysis is sensitive to R_0, although not strongly. R_0 is better constrained by different types of analysis than the RC ones (see Malkin 2013 for a list of works on the determination of R_0).

In the absence of strong priors on R_0 and ρ_0 values between 0.3 and 0.8 GeV/cm^3 at 2σ are allowed, which is in agreement with the conservative estimate provided in Salucci et al. 2010. Interestingly, the combination $\rho_0 = 0.4$GeV/cm^3, $R_0 = 8$ kpc, often used in the literature, is in tension at 2σ level with our result. The previous *standard* used value until recently, that is $\rho_0 = 0.3$ GeV/cm^3 for $R_0 = 8.5$ kpc has a χ^2 of 53.6 (in the profiled R_0-ρ_0 plane), therefore being excluded at more than 4σ.

The use of a flat prior on R_0 in the range $[7.5, 8.5]$ kpc is perhaps too conservative and, instead, more stringent priors could be used, as for example the Gaussian prior $R_0 = 8.2 \pm 0.1$ kpc given in Bland-Hawthorn and Gerhard 2016. Similar considerations apply to γ or to the other parameters. For this reason, our constraints are not necessarily the optimal ones. Nonetheless, extra information or priors on the parameters can be easily included starting from the tables we provide. The main goal of this analysis is to provide results in a general form such that they can be used by the community together with complementary information, with the aim to simplify the use of a thorough data-driven approach on astrophysical uncertainties to analysis including direct and indirect DM searches.

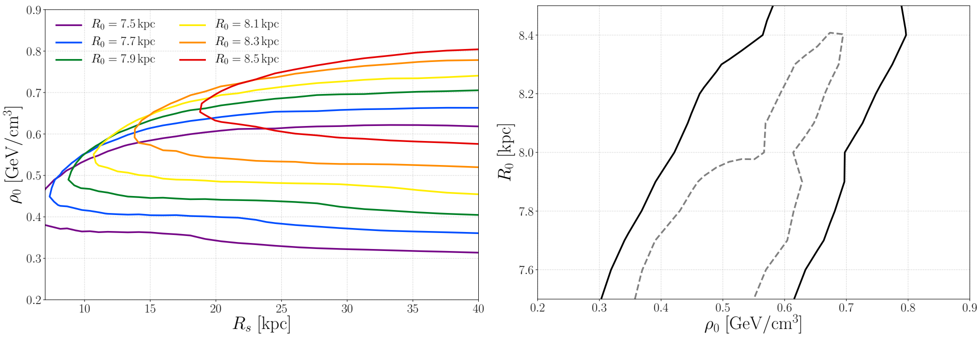

FIGURE 6.3: Left panel: 2σ contours in the (R_s, ρ_0) plane for fixed $\gamma = 1$ and for various values of R_0. The contours are profiled over $\mathcal{M}_i$, $\langle\tau\rangle$ and Σ_*. Right panel: 1-2σ contours in the (ρ_0, R_0) plane for fixed $\gamma = 1$. The contours are profiled over R_s, $\mathcal{M}_i$, $\langle\tau\rangle$ and Σ_*.

Results as function of γ

In figure 6.4 we show the analogous of figure 6.3 for the case in which γ is varied. It can be seen that the results are similar, except for the fact that when large values of γ are used ($\gamma > 1$), the largest values of ρ_0 (in the range $0.6 - 0.8$ GeV/cm^3) are disfavoured. Including the uncertainty on γ, the couple $\rho_0 = 0.3$ GeV/cm^3 and $R_0 = 8.5$ kpc has now a χ^2 of 42.3 (versus 53.6 when γ is fixed to 1) which is still excluded at more than 4σ.

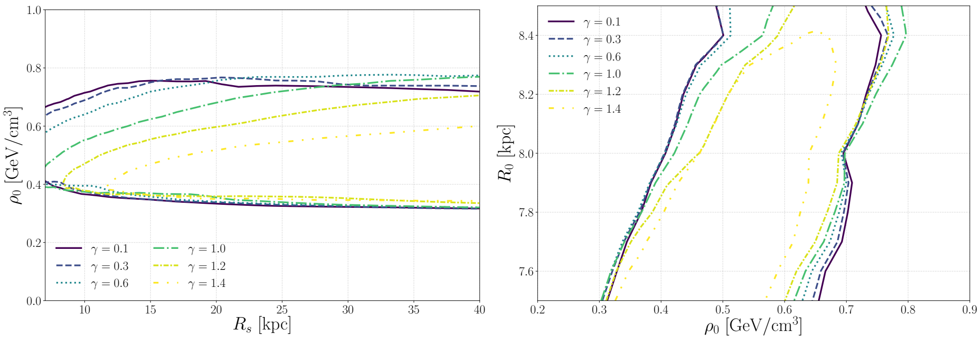

FIGURE 6.4: Left panel: 2σ contours in the (R_s, ρ_0) plane for various fixed values of γ profiled over $\mathcal{M}_i$, $\langle\tau\rangle$, Σ_* and R_0. Right: 2σ contours of the profile χ^2 in the (ρ_0, R_0) plane for different fixed values of γ.

Comparison with Other Results

A general result of our quantitative analysis of astrophysical uncertainties, that affect the determination of the DM density profile in the MW, is that the single DM parameters are only weakly constrained by the fit (even for the case of fixed NFW profile, i.e., without varying γ). For instance, at 2σ confidence level (CL), ρ_0 lies in the range 0.3-0.8 GeV/cm^3, thus with an error of ~ 0.25 GeV/cm^3, while R_0 is simply unconstrained by the analysis with respect to the prior range 7.5-8.5 kpc. Instead, the degeneracy and correlation among the parameters, like, noticeably, the one between R_0 and ρ_0 is robustly constrained by the fit. This is somewhat at odd with similar analyses performed in the past, which, typically, tend to find very small errors and strong constraints on the parameters. We attribute this difference to three main effects. First, the adopted accurate statistical treatment, which explores and maps in detail the degeneracies among the parameters. This is important, since if strong degeneracies are present, as in this case, and they are not well characterised, the error on the single parameters will be underestimated. Second, we do not use stellar tracers up to ~100 kpc, as sometimes adopted in other analysis. The DM potential is the dominant component in the range 20-100 kpc, so this data could actually provide an important contribution in reducing the uncertainties on the DM parameters, although this comes at the cost of adding further assumptions. Third, we use binned data, with an uncertainty estimated from the spread of the data points in the bin. The last effect was already found to be an important point in Pato et al. 2015 which shares the same data set and similar methods as the present analysis. More precisely, when using the unbinned analysis, in Pato et al. 2015 the authors report $\rho_0 = 0.420^{+0.021}_{-0.018}(2\sigma) \pm 0.025$ GeV/cm^3 where the first error is statistical and the second comes from the uncertainty on the baryonic morphology. On the other hand, a test with binned data gives errors a factor of ~ 5 larger, thus more compatible with the analysis performed here.

Other analyses that give small errors, like in Catena and Ullio 2010 which reports $\rho_0 = 0.389 \pm 0.025$ GeV/cm^3, also use unbinned data. A noticeable exception is the work in Nesti and Salucci 2013, where a binned analysis is performed, with bin errors estimated in a similar way as in this work. We thus expect an uncertainty similar to the one of our analysis. The authors indeed find $\rho_0 = 0.471^{+0.048}_{-0.061}$ GeV/cm^3, which has an uncertainty larger than Catena and Ullio 2010; Pato et al. 2015, but still smaller than our analysis. This might be related to the larger data set used in Nesti and Salucci 2013 which includes also stellar velocity dispersion measurements at $R > 20$ kpc, or to the simplified procedure used to estimate the errors, as explained in the mentioned paper.

Finally, in chapter 4, we perform a binned analysis using, for the inner Galaxy, the *galkin* data set also employed here, in combination, for the outer Galaxy, with *Huang et al* (Huang et al. 2016) which has stellar tracers up to 100 kpc. The final uncertainties derived there are thus smaller. A further difference is that in chapter 4 a fixed value of $R_0 = 8.34$ kpc is used, whereas one of the goals of this present analysis is indeed to estimate the very impact of the uncertainties on R_0 –which we therefore vary as discussed in the previous sections– on the determination of the DM distribution.

In the literature several other works are present, for example Xue et al. 2008; Weber and de Boer 2010; McMillan 2011; Huang et al. 2016; McMillan 2017 which we do not discuss in detail given the wide range of methodologies, data sets and assumptions employed, which makes difficult a proper comparison.

6.4 Implications for Direct and Indirect WIMP Searches

In this section, we provide an example of how to use the χ^2 or likelihood profile of the full data-driven analysis derived above. This likelihood profile is publicly available at https://github.com/mariabenitocst/UncertaintiesDMinTheMW. In particular, we consider the GC excess observed in γ-rays and assume it is due to DM self-annihilation.

Accounting for astrophysical uncertainties on the predicted flux of final stable particles due to DM annihilation or decay is crucial when comparing results from different targets. On the one hand, a positive signal interpreted in terms of DM annihilation implies a preferred region in the particle physics parameter space, typically the average velocity self-annihilation cross-section $\langle \sigma v \rangle$ versus DM mass $\mathrm{m_{DM}}$. On the other hand, null results from other targets impose upper limits on the ($\langle \sigma v \rangle$, $\mathrm{m_{DM}}$) parameter space. It might occur that the latter constraints are in tension with the signal. However, such a tension relies on the assumed $\mathcal{J}$-factor and, thus, the uncertainty on the $\mathcal{J}$-factor must be properly accounted for before claiming a strong tension.

6.4.1 Dark Matter Interpretation of the Galactic Centre Excess

An excess in the γ-ray emission from the centre of our Galaxy was confirmed by the Large Area Telescope on-board of the Fermi satellite (Ajello et al. 2016). The excess emission covers the inner $\sim 10^o$, peaks at ~ 2 GeV and has the spectral and morphological shape expected from DM self-annihilation. The origin of this signal is still debatable. Although several groups have interpreted this excess in terms of DM annihilation (Goodenough and Hooper 2009; Hooper and Goodenough 2011; Calore et al. 2015; Cuoco et al. 2016; Daylan et al. 2016), there are potential astrophysical explanations such as, for example, the presence of an unresolved population of millisecond pulsars (Petrović et al. 2014, 2015). Furthermore, it was recently claim that the interpretation of the Galactic centre excess (GCE) in terms of DM annihilation is in conflict with current upper limits from dwarf spheroidal galaxies (dSphs) (Abazajian and Keeley 2016; Chan and Leung 2017).

We use the results of the GCE analysis presented in Calore et al. 2015. Calore et al. 2015 performed a detailed spectral and morphological analysis of the GCE. The inferred energy spectrum and error covariance matrix of this analysis have been made publicly available. Calore et al. 2015 considered a square of 40°×40° around the GC, with a stripe of ±2° along the Galactic plane excluded, for a total area of 0.43 sr.

Figure 6.5 shows the χ^2 profile of the GCE $\mathcal{J}$-factor from our analysis for different cases described in the caption. When a derived parameter as $\mathcal{J}$ is involved, our frequentist profiling methodology is slightly more involved. First, we derive the corresponding $\mathcal{J}$ value for each point in our seven-dimensional grid. Then, to build, for example, the one-dimensional χ^2 profile for $\mathcal{J}$, we bin all the derived $\mathcal{J}$ values in a new $\mathcal{J}$ grid. For each $\mathcal{J}$-bin we then take the minimum χ^2 among the χ^2 corresponding to the $\mathcal{J}$ values falling in that bin.

In order to include astrophysical uncertainties that affect the determination of the DM distribution in the MW, that is the uncertainties on the $\mathcal{J}$-factor, we define the following χ^2,

$$\chi^2_{\mathrm{total}} = \chi^2_{\mathrm{GCE}}(\langle \sigma v \rangle, m_{\mathrm{DM}}, J) + \chi^2_{\mathrm{RC}}(\mathcal{J}, \gamma) + \chi^2_{\gamma}. \tag{6.15}$$

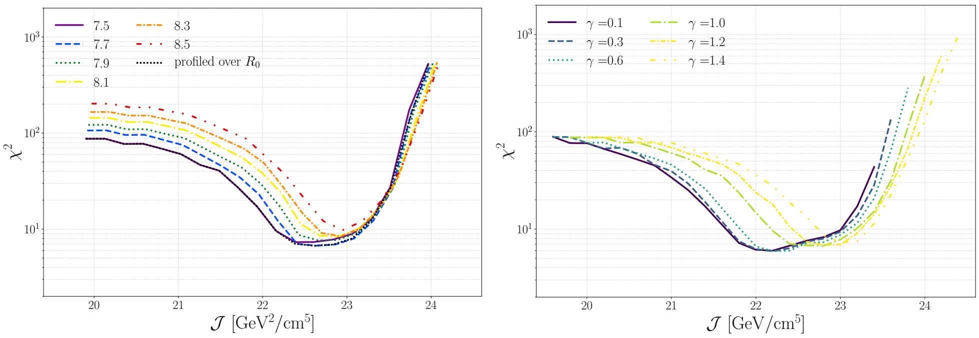

FIGURE 6.5: Left panel: χ^2 profile for the GCE $\mathcal{J}$-factor for fixed $\gamma = 1$. The colour lines correspond to profiles over $\mathcal{M}_i$, $\langle\tau\rangle$, Σ_*, R_s and ρ_s for different R_0. The black-dashed line is the χ^2 profiled furthermore over R_0. Right panel: Colour lines correspond to the profiles over $\mathcal{M}_i$, $\langle\tau\rangle$, Σ_*, R_s, ρ_s and R_0 for different γ.

The first term of the above equation corresponds to the GCE analysis and is given by

$$\chi^2_{\rm GCE} = \sum_{i,j}(d_i - t_i)\left(\Sigma_{ij} + \delta_{ij}(\sigma_{\rm rel}\, t_i)^2\right)^{-1}(d_j - t_j), \tag{6.16}$$

where d_i are the GCE fluxes in the 24 energy bins given in Calore et al. 2015, t_i is the model prediction from equation (6.5). Fluxes in Calore et al. 2015 are normalised to the area of the region analysed, so equation (6.5) needs to be further divided by 0.43 sr. Finally, Σ_{ij} is the covariance matrix among the energy bins, again given in Calore et al. 2015. Following Cuoco et al. 2016, we further add to the covariance matrix a diagonal error equal to $\sigma_{\rm rel}$ per cent of the model prediction t_i to account for the model uncertainty in the annihilation spectrum dN/dE. In particular, as explained in Cuoco et al. 2016, a choice of $\sigma_{\rm rel} = 10\%$ is appropriate.

The second term in equation (6.15), $\chi^2_{\rm RC}(\mathcal{J}, \gamma)$, is build from equation (6.11) profiling over R_0, R_s, ρ_s, $\langle\tau\rangle$, Σ_* and $\mathcal{M}_i$ (but not γ). Finally, $\chi^2_\gamma = (\gamma - 1.2)^2/0.08^2$ is a Gaussian prior on γ, with mean 1.2 and $\sigma = 0.08$ again coming from the analysis of the morphology of the GCE in Calore et al. 2015.

Constraints in the plane $(m_{\rm DM}, \langle\sigma v\rangle)$ derived from the $\chi^2_{\rm total}$ in equation (6.15) and further profiled over γ and $\mathcal{J}$, are shown in figure 6.6 and compared with the results of Calore et al. 2015. As a test of consistence we have checked that fixing the $\mathcal{J}$-factor to the value adopted in Calore et al. 2015 we obtain their same $(m_{\rm DM}, \langle\sigma v\rangle)$ contours, which, for comparison are also shown in the same plot. It can be seen that including the uncertainties on the distribution of DM significantly enlarges the contours, both at large and small $\langle\sigma v\rangle$. In particular, while the preferred region of Calore et al. 2015 is in (mild) tension with the null observations of a γ-ray signal from local dwarf galaxies (Ackermann et al. 2015; Albert et al. 2017), this tension disappears when considering the $\mathcal{J}$-factor uncertainties. It should be mentioned, nonetheless, that the tension with dwarfs constraints can also be further relieved if more conservative estimates of the DM content of the dwarfs is adopted (Bonnivard et al. 2015a), or, similarly, if a more conservative analysis of the γ-ray background at the dwarfs positions is performed (see Mazziotta et al. 2012; Calore et al. 2018).

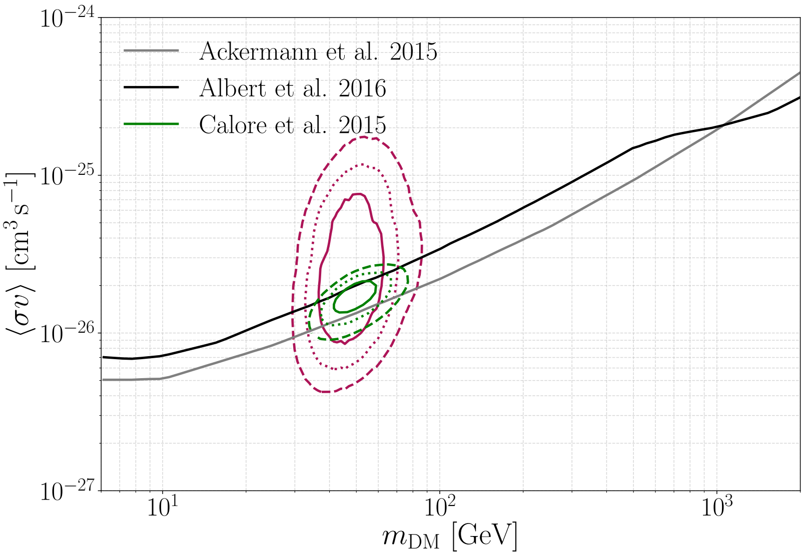

FIGURE 6.6: 1, 2 and 3 σ contours in the DM particle parameter space $(m_{\mathrm{DM}}, \langle \sigma v \rangle)$ for the $b\bar{b}$ DM annihilation channel from our analysis, and from the Calore et al. 2015 work. Also included are the upper limits from the analysis of MW dwarf galaxies from Ackermann et al. 2015; Albert et al. 2017.

6.5 Conclusions

We have used the observed RC of the MW up to ≈ 25 kpc in Galactocentric radius to study and quantify astrophysical uncertainties that affect the constrains on the parameters of a gNFW DM density profile.

The main source of uncertainty on the determination of the DM density profile in the MW by means of the RC is the uncertainty on the actual shape or spatial distribution of baryons in the Galaxy. Notice that in 6.2, we have shown that the change in the DM density profile due to variations in the Galactic parameters (R_0, Θ_0) is larger than that of the baryonic morphology. Nonetheless, we have adopted a too conservative prior on R_0 in the range $[7.5, 8.5]$ kpc. When using a more realistic prior, such as, for example, the Gaussian prior $R_0 = 8.2 \pm 0.1$ kpc given in Bland-Hawthorn and Gerhard 2016, the effect of Galactic parameters on the DM determination decreases to a level lower than that of the baryonic morphology. On the other hand, uncertainties on the normalisation of the baryons, that is uncertainties on the measured Σ_* and $\langle \tau \rangle$, play a negligible role with respect to the other sources of uncertainty.

Our quantitative analyses in section 6.3 improves with respect to other works in several ways. First, we have adopted a systematic statistical approach, scanning the relevant parameter space and accurately exploring the various degeneracies present. This last point is particularly important since several degeneracies exist, and precisely mapping them is a necessary condition to have reliable final error estimates. Second, we use an accurate treatment of the systematic uncertainties arising from the modelling of the visible components of the MW. We adopt a large array of bulge, and separately disc, density profiles. By combining individually, one bulge, one disc and the gas component (and then varying one at the time each individual component) we obtain an array of baryonic morphologies that bracket the systematic uncertainty on the actual distribution of baryons within our Galaxy. We further allow mass variations for each morphology due to uncertainties given by microlensing and stellar surface density measurements. These baryonic uncertainties are fully marginalised (profiled) away within our statistical framework.

We find that the local DM density ρ_0 is constrained to the range $0.3 - 0.8$ GeV/cm^3 at the 2σ level, showing a strong positive correlation with the Sun's Galactocentric distance R_0. The inner slope of the DM profile, γ, is very weakly constrained and both core ($\gamma \sim 0$) and cusp ($\gamma \sim 1$) DM density profiles are allowed. Some combinations of parameters can be, however, strongly constrained. For example, the often used standard $\rho_0 = 0.3$ GeV/cm^3, $R_0 = 8.5$ kpc is disfavoured at more than 4σ.

We release the likelihood of our analysis, namely a four-dimensional table listing χ^2 values over a grid in γ, R_0, R_s, ρ_s, the latter two parameters being the scale radius and density scale of the gNFW profile.[7] In the above likelihood, the dependence on baryonic parameters (morphology and normalisation) and related uncertainties have been already profiled away. We have provided some example for the use of the likelihood, in particular we have employed it in the analysis of the GC γ-ray excess. We have found that the uncertainties in the DM profile significantly enlarge the allowed cross-section range, by a factor 3 to 4. Other contexts in which our tabulated likelihood can be employed involve GC or Galactic halo DM searches in γ-rays at GeV energies or TeV with Cherenkov telescopes, DM neutrinos searches, direct DM searches, local DM searches with antimatter, and combined local and GC searches.

---

[7] The likelihood is available at https://github.com/mariabenitocst/UncertaintiesDMinTheMW.

cross-section

Chapter 7

Alternative Theories to the Dark Matter Paradigm

The dark matter (DM) is invoked to explain the mismatch between the observed dynamical mass and that inferred by observations of the visible component. This discrepancy is observed for a vast range of masses and scales: From dwarf (e.g. Oh et al. 2015) and spiral galaxies (e.g. Sofue and Rubin 2001) to clusters of galaxies (e.g. Schmidt and Allen 2007). The DM paradigm further provides a consistent explanation of the Cosmic Microwave Background (CMB) power spectrum (Planck Collaboration et al. 2018a) and the structure formation in the Universe (Blumenthal et al. 1984).

An alternative proposal to the DM paradigm relies on a modification of general relativity. There are numerous proposals for modify gravity in the literature, such as MOND (Milgrom 1983), T*e*V*e*S (Bekenstein 2004), MOG (Moffat 2006) or $f(R)$ theories (Sotiriou and Faraoni 2010) amongst others.

Our Galaxy can be used for testing modifications of gravity, at the galactic scale, by comparing observed rotation velocities with the velocities predicted for the visible component by the effect of the underlying gravity theory. Tracers of the total gravitational potential of the Milky Way (MW) have already been used for testing MOND phenomenology (Famaey and Binney 2005; McGaugh 2008; Iocco et al. 2015b), MOG theory (Moffat and Toth 2015; Negrelli et al. 2018) and other modifications of gravity (Finch and Said 2018).

In the first part of this chapter, we briefly review some modify gravity theories. In the second part, we test MOG gravity theory (Moffat 2006) on the galactic scale using our own Galaxy. Part of the material of this chapter has been taken from Negrelli et al. 2018.

7.1 Modifications of gravity

From the different proposals of modifications of gravity, we briefly review MOND (Milgrom 1983) and MOG theories. The former is chosen since it is a phenomenological theory built for reproducing observations at the galactic scale, and this is the precise scale we are interested in probing by means of kinematical tracers of the total gravitational potential of our Galaxy. On the other hand, we briefly describe the main aspects of the MOG theory since it is further tested in the second part of this chapter. It is worth highlighting that the methodology presented for testing MOG theory can be easily tuned for testing the validity of other modified gravity theories at the galactic scale by using our own Galaxy.

MOND

MOND is a non-relativistic, phenomenological theory of gravity proposed by Milgrom 1983 in order to explain flat rotation curves (RCs) in spiral galaxies. It is characterised by a fundamental acceleration scale, below which Newtonian gravity breaks down.

This theory correctly predicts the baryonic Tully-Fisher relation[1] (e.g. McGaugh et al. 2000), and its modern counterpart: The radial acceleration relation (RAR) (McGaugh et al. 2016; Li et al. 2018). The latter is a tight correlation between observed and baryonic accelerations along galactocentric distance for galaxies with stellar masses in the range $10^3 - 10^{12}\,\mathrm{M}_\odot$. The small intrinsic scatter of the observed RAR implies a tight correlation between the baryonic mass and the observed dynamics. This relation has been used to prove the existence of a fundamental acceleration scale $a_0 \sim 10^{10}\,\mathrm{m\,s}^{-2}$ (Lelli et al. 2017b). This would favour MOND dynamics as the correct explanation for the mismatch between observed and baryonic masses at the galactic scale. Nonetheless, the existence of a fundamental acceleration scale a_0 is still debated. Rodrigues et al. 2018 have recently showed that a_0 -obtained in Lelli et al. 2017b- is indeed a statistical artefact, rather than a fundamental scale, due to the process of stacking galaxies in the analysis. Furthermore, the tight relation between observed and baryonic accelerations and the emergence of an acceleration scale a_0 have been successfully explained within ΛCDM (Ludlow et al. 2017).

While satisfactory reproducing rotation curves (RCs) of galaxies (e.g. Sanders and Noordermeer 2007), MOND theories failed to explain the observed offset between dynamical and hot gas masses[2] in mergers of clusters, such as e.g. the Bullet cluster (Clowe et al. 2006).

Several relativistic expansions of MOND dynamics have been proposed such as e.g. T*e*V*e*S (Bekenstein 2004). This theory was recently ruled out by the time delay between the gravitational wave event GW170817 and its electromagnetic counter part (Boran et al. 2018).[3] Other examples of relativistic *MONDian* theories that have not been ruled out by this measured time delay are nonlocal MOND (Deffayet et al. 2011) and BIMOND (Milgrom 2014).

MOG

MOG is a relativistic modified gravity theory proposed by Moffat 2006. This theory has been able to explain measurements coming from numerous and diverse sources such as the motion of globular and galaxy clusters (Moffat and Toth 2008; Moffat and Rahvar 2014; Moffat and Zhoolideh Haghighi 2017), and RCs of spiral and dwarf galaxies (Moffat and Rahvar 2013; Zhoolideh Haghighi and Rahvar 2017). As well as MOND, it has difficulties in explaining the Bullet cluster (Clowe et al. 2006), while Brownstein and Moffat 2007 and Israel and Moffat 2016 claim that MOG can fit both the Bullet and the Train Wreck merging clusters, respectively. Other authors also

---

[1] The Tully-Fisher relation correlates the blue luminosity with the maximum rotation velocity of a disc galaxy, i.e. $L_H \propto v^4$ (Tully and Fisher 1977). This relation can also be written as a scaling relation between the baryonic mass of a disc galaxy and its maximum rotation velocity, i.e. $M_{\mathrm{bar}} \propto v^4$ (McGaugh et al. 2000).

[2] Hot gas represents the bulk of the baryonic mass in clusters of galaxies.

[3] T*e*V*e*S predicts that gravitational waves (GWs) and photons couple to non-conformal metrics, i.e. GWs and photons propagate on different null geodesics. Therefore the expected time delay between the time it takes for a GW and for a photon to reach the Earth differs significantly from general relativity.

claim that MOG is unable to reconcile gas profile and strong-lensing measurements in well known cluster systems (Nieuwenhuizen et al. 2018). The main problem with MOG and other modified gravity theories is the fact that they are unable to explain the observed matter power spectrum and, therefore, the growth and formation of the structures we see today from the small density perturbations seen at the CMB (Dodelson 2011). Since some of the above controversies are yet to be resolved, it is currently unclear if MOG phenomenology can offer a solution at all scales. In this analysis we remain agnostic, and we test the validity of MOG theory at the galactic scale using our own Galaxy.

MOG theory includes a massive vector field ϕ^{μ} and two scalar fields: G which represents the gravitational coupling strength and μ which corresponds to the mass of the vector field. The gravitational action can be expressed as:

$$S_G = -\frac{1}{16\pi}\int \frac{1}{G}\left(R+2\Lambda\right)\sqrt{-g}\; d^4x, \tag{7.1}$$

Besides, the massive vector field ϕ_{μ} action is:

$$S_{\phi} = -\frac{1}{4\pi}\int \omega\left[\frac{1}{4}B^{\mu\nu}B_{\mu\nu} - \frac{1}{2}\mu^2\phi_{\mu}\phi^{\mu} + V_{\phi}(\phi_{\mu}\phi^{\mu})\right]\sqrt{-g}\; d^4x, \tag{7.2}$$

where $B_{\mu\nu}$ is the Faraday tensor of the vector field defined as follows: $B_{\mu\nu} = \partial_{\mu}\phi_{\nu} - \partial_{\nu}\phi_{\mu}$, and ω is a dimensionless coupling constant commonly taken as 1. The action for the scalar fields can be written as:

$$S_S = -\int \frac{1}{G}\left[\frac{1}{2}g^{\alpha\beta}\left(\frac{\nabla_{\alpha}G\nabla_{\beta}G}{G^2} + \frac{\nabla_{\alpha}\mu\nabla_{\beta}\mu}{\mu^2}\right) + \frac{V_G(G)}{G^2} + \frac{V_{\mu}(\mu)}{\mu^2}\right]\sqrt{-g}\; d^4x. \tag{7.3}$$

Here, ∇_{ν} is the covariant derivative with respect to the metric $g_{\mu\nu}$ and $V_{\phi}(\phi_{\mu}\phi^{\mu})$, $V_G(G)$ and $V_{\mu}(\mu)$ are the self-interaction potentials associated with the vector field and the scalar fields, respectively.

In order to study the behaviour of MOG on astrophysical scales, we can use the weak field approximation obtained by perturbing the fields around Minkowski metric for an arbitrary distribution of non-relativistic matter. Following Moffat and Rahvar 2013, the dynamics of a test particle is driven by an effective potential Φ_{eff}. Therefore, the MOG acceleration of a test particle can be obtained from the gradient of the potential, $\vec{a} = -\vec{\nabla}\Phi_{\text{eff}}$, yielding the result:

$$\vec{a}(\vec{x}) = -G_N\int \frac{\rho(\vec{x}')(\vec{x}-\vec{x}')}{|\vec{x}-\vec{x}'|^3} \times \left[1+\alpha-\alpha e^{-\mu|\vec{x}-\vec{x}'|}(1+\mu|\vec{x}-\vec{x}'|)\right] d^3\vec{x}', \tag{7.4}$$

where G_N is Newton's gravitational constant. The resulting force is composed by two components: a Newtonian attractive force and a repulsive, Yukawa style force. For length scales shorter than μ^{-1}, the repulsive force cancels the strong attractive force recovering Newtonian gravity. On the other hand, at larger length scales the repulsive force becomes weaker and we obtain a Newtonian potential with a larger Newtonian constant.

Moffat and Toth 2013 yield an estimation of the values of α and μ as functions of the source mass M:

$$\alpha = \frac{M}{(\sqrt{M}+E)^2}\left(\frac{G_\infty}{G_N}-1\right), \tag{7.5}$$

and

$$\mu = \frac{D}{\sqrt{M}}, \tag{7.6}$$

where μ is in units of kpc^{-1}, G_∞ represents the effective gravitational constant at infinity and its value ($\simeq 20G_N$) is established so that at the horizon distance, the effective strentgh of gravity is about six times G_N (for details see Moffat and Toth 2013).

In the most general case, α and μ are scalar fields. Here, as in other similar analyses (Brownstein and Moffat 2006; Moffat and Toth 2015), both fields are treated as constants, with a value set to that determined by the whole baryonic mass of the Galaxy. We have however checked that the values adopted by the fields at different positions in the Galaxy -as an effect of the change of the enclosed mass- falls within the range of values adopted to test our analysis, thus leaving our conclusions unchanged.

7.2 An Example: Testing MOG Theory in the Milky Way

As seen in the above chapter, it is currently unclear if MOG phenomenology can offer a solution at all scales. Nevertheless, we adopt an agnostic approach, and only focus on the prediction of MOG theory on the scale of spiral galaxies. We test the most common MOG scenarios with data of the RC of our Galaxy.

7.2.1 Methodology and Setup

We use a compilation of kinematic tracers of the MW and a state-of-the-art modelling of the baryons, both presented in Iocco et al. 2015a. With respect to previous studies of MW data (Moffat and Toth 2015), we improve the analysis on two separate fronts:

- First, as tracers of the RC, we adopt two separate compilations of data that have a high density of data in the galactocentric distances $2.5 < R < 100$ kpc, whereas the above mentioned analysis adopts a data set more focused toward external regions $20 < R < 200$ kpc.
- Second, for what concerns the RC expected by the baryonic component, we implement a full set of three-dimensional, observationally-inferred baryonic morphologies including the stellar bulge, disc and gas components of the Galaxy. We solve the integral in equation (7.4) numerically - using the CUBA library (Hahn 2006)-, whereas the previous analysis (Moffat and Toth 2015) employs an analytical formulation to express the contribution of the bulge and disc to the circular velocity.

As tracers of the actual, observed gravitational potential, we adopt the compilation of halo stars data from Huang et al. 2016 (hereafter *Huang et al.*), which extends up to 100 kpc. We also test our final results against the compilation of tracers `galkin` (Pato and Iocco 2017), that offers -with respect to Huang et al. 2016- an enhanced number of diverse types of objects in the inner region of the MW (thus offering a test in slightly different acceleration regimes); we anticipate that our conclusions are qualitatively unchanged when using the two compilations.

In order to model the density field of the baryonic content (stars and gas), we adopt the set of observationally inferred morphologies presented in chapter 3, separating the stellar component in bulge and disc, and also accounting for the interstellar gas. We adopt a large array of bulge, and separately disc, density profiles. By combining individually, one bulge, one disc and the gas component, we obtain an array of baryonic morphologies that bracket the systematic uncertainty on the actual distribution of baryons within our Galaxy.

The (three-dimensional) bulge density profiles are individually normalised to the MACHO microlensing optical depth observation in the GC region (Popowski et al. 2005), an observation carrying a statistical uncertainty that propagates to the normalisation of the bulge. The disc profiles are normalised to the surface stellar density at the Sun's position (Bovy and Rix 2013), a measurement that also carries a statistical uncertainty. Together with the gas component (also carrying a statistical uncertainty), we can thus associate a well-posed statistical uncertainty to the total baryonic density of the Galaxy each time a single morphology (combination of the gas, bulge, and disc component) is selected. This in turn propagates to the rotational velocity computed through the gravitational potential adopted (Newton, MOND, or MOG), thus allowing a statistically meaningful test of the RC obtained for each single morphology against observations.

Once the full three-dimensional density functions of bulge, disc and gas are normalised as summarised above, we integrate them through equation (7.4) -using the cuba library (Hahn 2006)- in order to obtain the MOG acceleration at each galactocentric distance, and its corresponding circular velocity at the Galactic plane, i.e. z=0.

The RC for the baryonic component under the MOG potential is then compared to the observed RC by means of a χ^2 statistics. We compare angular velocities, $w(R) = v(R)/R$, instead of circular velocities, $v(R)$, since the uncertainties on R and w are uncorrelated. We adopt the uncertainties on the observed RC, and that for baryons as described above. For both compilations, the data is taken individually, without binning. Only when the `galkin` compilation is adopted, we use a two-dimensional χ^2 test statistics, which allows to account for uncertainties both in angular velocities and galactocentric distances.

The analysis is run only for data points with galactocentric distances larger than $R_{\rm cut}$=2.5 kpc (whereas the potential generated from the mass enclosed in this region is obviously taken into account), in order to avoid spurious results due to the departure from axisymmetry of the potential, or the failure of the target gas to follow circular orbits due to the triaxial morphology of the Galactic bulge.

The galactic parameters chosen for our analysis are,

$$(R_0, \Theta_0) = (8.34\ kpc, 239.89\ \text{km/s}) \tag{7.7}$$

and the peculiar solar motion is

$$(U_\odot, V_\odot, W_\odot) = (7.01, 12.20, 4.95)\ \text{km/s}. \tag{7.8}$$

Varying these parameters within the currently accepted range of systematic uncertainties does not qualitatively modify our conclusions.

$(\alpha, \mu\ [\mathrm{kpc}^{-1}])$	*Huang et al* (Huang et al. 2016)	`galkin` (Pato and Iocco 2017)
$(15.01, 3.13 \cdot 10^{-2})^{\mathrm{MW}}$	5.02	4.90
$(8.89, 4.2 \cdot 10^{-2})^{\mathrm{SG}}$	5.20	4.90
$(15.80, 2.41 \cdot 10^{-2})^{\mathrm{C}}$	9.14	6.65
Newton	32.65	11.72
5 σ equivalent $\tilde{\chi}^2_{5\sigma}$	2.41	1.14

TABLE 7.1: Reduced χ^2-values for our representative morphology: *bulge 2* (Stanek et al. 1997), *disc 3* Calchi Novati and Mancini 2011 and gas given in Ferrière 1998; Ferrière et al. 2007. The MW baryonic mass in this case is $\mathrm{M}_{\mathrm{C}}^{\mathrm{MW}}$=$(6.7^{+0.7}_{-0.6}) \times 10^{10}\,\mathrm{M}_\odot$.

7.2.2 Results

We use the setup built above in order to test the MOG theory for each single morphology in our catalogue. For the sake of clarity, we first describe the results for a single morphology, which we denote as *representative*. This morphology is composed of *disc 3* presented in Calchi Novati and Mancini 2011, *bulge 2* taken from Stanek et al. 1997, and the gas given in Ferrière 1998; Ferrière et al. 2007. We generalise our results to all other morphologies at the end of this section.

For our representative morphology, we first test the MOG theory in its *standard* formulation adopting the couple of parameters (α, μ) indicated by Moffat and collaborators as the best possible values to fit the spiral galaxies (Moffat and Rahvar 2013) and the MW (Moffat and Toth 2015), which we respectively denote $(\alpha, \mu)^{\mathrm{SG}}$ and $(\alpha, \mu)^{\mathrm{MW}}$. The latter values, are however obtained as a function of the MW baryonic mass on the basis of equation (7.5) and (7.6). The MW baryonic mass adopted by Moffat to derive $(\alpha, \mu)^{\mathrm{MW}}$ is $\mathrm{M}_{\mathrm{Mof}}^{\mathrm{MW}}$=$4 \times 10^{10}\,\mathrm{M}_\odot$, different from the value $\mathrm{M}_{\mathrm{C}}^{\mathrm{MW}}$=$(6.7^{+0.7}_{-0.6}) \times 10^{10}\,\mathrm{M}_\odot$ that we self-consistently obtain from our morphological model; we therefore use equations (7.5) and (7.6) to obtain the set of parameters $(\alpha, \mu)^{\mathrm{C}}$, based on the self-consistent value $\mathrm{M}_{\mathrm{C}}^{\mathrm{MW}}$.

In Table 7.1 we show the values of the reduced χ^2 for each of these three set of parameters, which as it can be seen falls far away from the customary 5σ equivalent $\tilde{\chi}^2_{5\sigma}$, thus indicating that for this morphology, MOG theory with these parameters is ruled out with a large degree of confidence (way beyond the 5σ level, which carries a statistical significance here given the purely statistical nature of the uncertainties involved). We also perform a safety check by using the recent-most data compilation `galkin`, which has an extended data set in the galactocentric radii 3-15 kpc, and we find no qualitative change, leaving thus intact the above conclusion[4].

It is however to be noticed that existing work assigns an uncertainty to the value of (α, μ) defining an interval based on equations (7.5) and (7.6) and to current uncertainties on the leading constants which are settled by fits to the galaxy RCs (Brownstein

---

[4] It is to be noticed that the difference in the χ^2 between the `galkin` and *Huang et al* case are due to the enhanced amount of data of the `galkin` compilation in the range of galactocentric radii 3-5 kpc. *Huang et al* compilation is insensitive to this region due to the lack of data, so the difference in χ^2 reflects the behaviour of a morphology in this region. The results of the two compilations are perfectly compatible at a qualitative level, and their quantitative discrepancies are perfectly explainable.

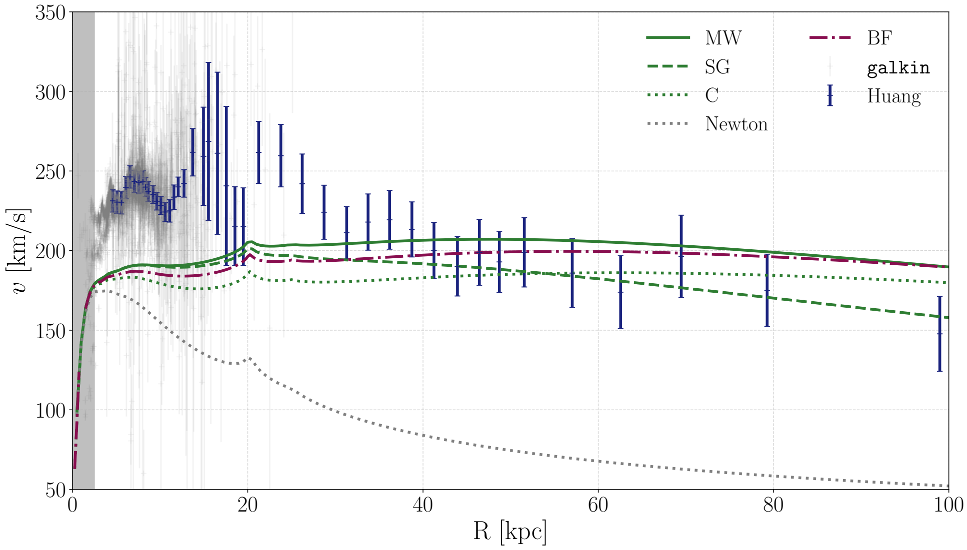

FIGURE 7.1: Rotation curves for the MOG four relevant cases (MW, SG, C, BF) and Newton for our representative morphology. Uncertainties are shown only for the observational data, while the central value only is shown for the RCs expected from different *flavours* of MOG, in order to ease visualisation. The grey band corresponds to the inner 2.5 kpc.

2009):

$$D = (6.44 \pm 0.20)\, \mathrm{M}_\odot^{1/2} \mathrm{pc}^{-1}, \tag{7.9}$$

$$E = (28.4 \pm 7.9)\, \mathrm{M}_\odot^{1/2}, \tag{7.10}$$

In such way by applying equations (7.5) and (7.6) to the actual value of the baryonic mass of the Galaxy (which we derive self-consistently from the assigned, representative morphology) with its uncertainties, we obtain the parameter interval $\alpha = 15.4 \pm 1.0$ and $\mu = (2.5 \pm 0.2) \times 10^{-2}$. We scan this interval, and find that for each point in this two-dimensional space, the reduced χ^2 is beyond 5σ (we use the *Huang et al* compilation's $\tilde{\chi}^2$ as reference in the scan), with the lowest one being $\tilde{\chi}^2_{BF} = 8.60$, for the parameter point $(\alpha, \mu)_{\mathrm{BF}} = (16.4, 2.7 \times 10^{-2})$. This bears the conclusion that MOG theory fails to explain the observed RC of the MW, for the morphology at study. We show the RCs for the 4 relevant cases (MW, SG, C, BF) in figure 7.1. As it may be appreciated from both figure and table, MOG admittedly performs better than Newtonian gravity, but both fails to describe the shape of the RC, and its normalisation in the inner regions (R $\lesssim$ 10kpc).

Results for all morphologies

We now extend our methodology to the entire set of morphologies. It is worth to recall here that each one of these possible morphologies, arises from an alternative description of disc(s) and bulge, obtained from the study of corresponding regions of the Galaxy in the infrared or optical wavebands. Each possible morphology is alternative to another one and they represent a nearly complete set of all possible morphologies still consider viable to date, and their spread can be considered a satisfactory indicator of the systematics present for the MW, with the conclusion that the actual physical reality must reasonably lie within them.

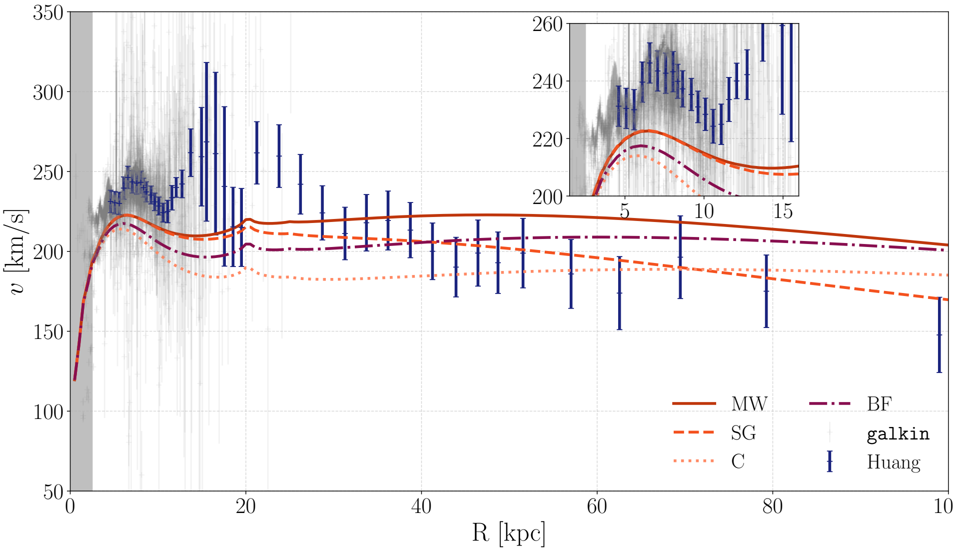

FIGURE 7.2: Rotation curves for the MOG four relevant cases (MW, SG, C, BF), for the *best-fitting* morphology (morphology *41*), see text for details. Uncertainties are shown only for the observational data, while the central value only is shown for the rotation curves expected from different *flavours* of MOG, in order to ease visualisation. See table 7.3 for details on the values of reduced $\tilde{\chi}^2$.

Separately and for each of the morphologies, we self-consistently compute the baryonic mass, and identify the corresponding *corrected* point in the (α, μ) plane by applying equations (7.5) and (7.6), as already described in the previous section. We then produce the RC and its uncertainties, and compute the reduced χ^2 by using the *Huang et al* data compilation.

The reduced χ^2 values for all morphologies are shown in table 7.2, for parameters $(\alpha, \mu)^{\mathrm{MW}}$, $(\alpha, \mu)^{\mathrm{SG}}$ and $(\alpha, \mu)^{\mathrm{C}}$, respectively. As it can be seen, the reduced χ^2 is very high for all considered morphology -with the exception of one set of morphologies, which we discuss in the following section- showing the disagreement between the MOG RC and the observed one at more than 5σ. A visual inspection of the actual RCs against the data bears results as disappointing as in the above section, and we remit the reader to figure 7.2 as to that for the representative case. It is to be noticed that our results differ from those obtained in Moffat and Toth 2015. The latter adopts only an approximation for the calculation of equation (7.4), and a different data set for the RC (Bhattacharjee et al. 2014) whose reduced number of points in the innermost regions of the Galaxy with respect to the *Huang et al* and `galkin` compilations is the main source for the discrepancy between our analysis.

The *best-fitting* morphology

As it can be appreciated from table 7.2, one set of morphologies, namely the ones carrying disc 1 (Bovy and Rix 2013), bears χ^2 visibly better than other ones (although still excluded at more than 5σ when tested against the `galkin` compilaton, see table 7.2). The explanation of this lies in the fact that this disc morphology is the heaviest

Baryonic Morph.	Newton $\tilde{\chi}^2$ Huang – `galkin`	MW $\tilde{\chi}^2$ Huang – `galkin`	SG $\tilde{\chi}^2$ Huang – `galkin`	C $\tilde{\chi}^2$ Huang – `galkin`	$(\alpha, \mu \times 10^{-2})^{\mathrm{C}}$	$\mathrm{M}_{\mathrm{C}}^{\mathrm{MW}}$ $[10^{10}\ \mathrm{M}_{\odot}]$
11	24.48 – 4.87	1.94 – 1.50	1.79 – 1.51	4.50 – 2.07	(15.94, 2.30)	$7.4^{+0.7}_{-0.6}$
21	24.02 – 4.64	1.84 – 1.42	1.68 – 1.43	4.30 – 1.97	(15.94, 2.29)	$7.4^{+0.8}_{-0.7}$
31	23.23 – 4.15	1.70 – 1.29	1.53 – 1.29	3.97 – 1.72	(15.95, 2.29)	$7.5^{+0.8}_{-0.7}$
41	22.9 – 4.47	1.58 – 1.26	1.32 – 1.27	3.82 – 1.84	(15.98, 2.26)	$7.7^{+0.8}_{-0.7}$
51	24.93 – 3.89	2.03 – 1.58	1.90 – 1.59	4.76 – 2.20	(15.93, 2.30)	7.4 ± 0.7
61	25.78 – 5.88	2.20 – 1.81	2.08 – 1.81	5.40 – 2.62	(15.92, 2.31)	$7.3^{+0.7}_{-0.6}$
12	31.83 – 10.69	4.50 – 4.25	4.68 – 4.25	8.59 – 5.96	(15.79, 2.43)	$6.6^{+0.6}_{-0.4}$
22	30.80 – 9.89	4.11 – 3.83	4.25 – 3.83	8.00 – 5.39	(15.80, 2.41)	$6.7^{+0.7}_{-0.6}$
32	32.90 – 8.51	3.36 – 3.10	3.43 – 3.10	6.85 – 4.37	(15.83, 2.39)	$6.8^{+0.7}_{-0.6}$
42	29.85 – 9.45	3.71 – 3.51	3.79 – 3.51	7.47 – 5.03	(15.83, 2.39)	$6.8^{+0.7}_{-0.6}$
52	35.73 – 11.40	4.93 – 4.66	5.16 – 4.66	9.21 – 6.51	(15.77, 2.44)	6.6 ± 0.6
62	28.67 – 13.65	6.17 – 6.00	6.48 – 6.00	13.00 – 8.43	(15.74, 2.47)	$6.4^{+0.6}_{-0.5}$
13	33.84 – 12.69	5.51 – 5.45	5.74 – 5.44	9.86 – 7.37	(15.79, 2.42)	$6.6^{+0.6}_{-0.4}$
23	32.65 – 11.72	5.02 – 4.90	5.20 – 4.90	9.14 – 6.65	(15.80, 2.41)	$6.7^{+0.7}_{-0.6}$
33	30.19 – 10.04	4.06 – 3.93	4.17 – 3.93	7.72 – 5.23	(15.84, 2.38)	$6.9^{+0.7}_{-0.6}$
43	31.62 – 11.22	4.54 – 4.50	4.66 – 4.50	8.53 – 6.22	(15.83, 2.39)	$6.9^{+0.7}_{-0.6}$
53	35.10 – 13.56	6.06 – 5.98	6.33 – 5.97	10.64 – 8.10	(15.77, 2.44)	6.6 ± 0.6
63	38.46 – 16.32	7.66 – 7.74	8.03 – 7.74	15.79 – 10.60	(15.73, 2.47)	$6.4^{+0.6}_{-0.5}$
14	33.70 – 12.39	5.43 – 5.29	5.66 – 5.28	9.80 – 7.17	(15.79, 2.42)	$6.7^{+0.6}_{-0.4}$
24	32.54 – 11.45	4.94 – 4.76	5.15 – 4.76	9.09 – 6.47	(15.81, 2.41)	$6.7^{+0.7}_{-0.6}$
34	30.14 – 9.82	4.02 – 3.83	4.14 – 3.83	7.71 – 5.11	(15.84, 2.38)	$6.9^{+0.7}_{-0.6}$
44	31.50 – 10.95	4.46 – 4.37	4.60 – 4.37	8.49 – 6.06	(15.84, 2.38)	$6.9^{+0.7}_{-0.6}$
54	34.93 – 13.23	5.96 – 5.80	6.24 – 5.79	10.56 – 7.86	(15.78, 2.44)	6.6 ± 0.6
64	38.18 – 15.89	7.5 – 7.48	7.87 – 7.47	15.49 – 10.27	(15.74, 2.47)	$6.4^{+0.6}_{-0.5}$
15	32.81 – 11.45	5.22 – 4.91	5.18 – 4.90	8.46 – 5.96	(15.91, 2.32)	$7.2^{+0.6}_{-0.5}$
25	31.79 – 10.66	4.79 – 4.48	4.76 – 4.47	7.86 – 5.35	(15.92, 2.31)	$7.3^{+0.7}_{-0.6}$
35	33.86 – 9.26	3.99 – 3.71	3.99 – 3.70	6.69 – 4.35	(15.95, 2.29)	$7.5^{+0.8}_{-0.7}$
45	30.64 – 10.19	4.21 – 4.07	4.20 – 4.06	7.30 – 5.01	(15.95, 2.29)	$7.5^{+0.7}_{-0.6}$
55	36.51 – 12.17	5.68 – 5.33	5.63 – 5.32	9.11 – 6.45	(15.89, 2.34)	$7.2^{+0.7}_{-0.6}$
65	29.76 – 14.42	6.91 – 6.67	6.83 – 6.66	12.91 – 8.34	(15.85, 2.37)	7.0 ± 0.6

TABLE 7.2: $\tilde{\chi}^2$ for all MOG *flavours* (MW, SG, C) parameters obtained as described in the text. The coding for the baryonic morphologies is as follows: First and second numbers correspond to the number of bulge and disc morphology, respectively, as presented in chapter 3. For instance, the baryonic morphology 11 corresponds to *bulge 1* plus *disc 1*. For all morphologies, the gas profile taken from Ferrière 1998; Ferrière et al. 2007. MW baryonic mass computed self-consistently.

$(\alpha, \mu\ [\mathrm{kpc}^{-1}])$	*Huang et al* (Huang et al. 2016)	`galkin` (Pato and Iocco 2017)
$(15.01, 3.13 \cdot 10^{-2})^{\mathrm{MW}}$	1.58	1.26
$(8.89, 4.2 \cdot 10^{-2})^{\mathrm{SG}}$	1.32	1.27
$(15.98, 2.26 \cdot 10^{-2})^{\mathrm{C}}$	3.82	1.84
$(16.60, 2.52 \times 19^{-2})^{\mathrm{BF}}$	2.78	2.22

TABLE 7.3: Reduced χ^2-values for the *best-fitting* morphology (Ferrière 1998; Bissantz and Gerhard 2002; Ferrière et al. 2007; Bovy and Rix 2013). For this morphology, the baryonic mass of the MW is $\mathrm{M}_{\mathrm{C}}^{\mathrm{MW}}$ =$(7.7^{+0.8}_{-0.7}) \times 10^{10}\,\mathrm{M}_{\odot}$. Notice that the statistical significance of the reduced $\tilde{\chi}^2$ changes given to different number of degrees of freedom in the two data compilation. We remind that for the *Huang et al* and `galkin` compilations the 5σ equivalent are $\tilde{\chi}^2_{5\sigma}$=2.41 and $\tilde{\chi}^2_{5\sigma}$=1.14, respectively.

one among the ones considered (a *maximal* disc[5]), and thus carries the overall normalisation of the obtained RC closer to the observed one in the innermost regions, thus reducing the value of the χ^2 with respect to other morphologies.

We select the morphology that systematically produces the best χ^2 (baryonic morphology *41*). This morphology is composed of *disc 1* (Bovy and Rix 2013), *bulge 4* (Bissantz and Gerhard 2002) and the gas from Ferrière 1998; Ferrière et al. 2007. We report the reduced χ^2 values for this morphology in table 7.3. When tested against the *Huang et al* compilation, the MW and SG points bear a significance at better than 2σ and 1σ, respectively. Although, rejected at more than 5σ when tested against the `galkin` data compilation. The baryonic mass for this morphology is $\mathrm{M}_{\mathrm{C}}^{\mathrm{MW}} = (7.7^{+0.8}_{-0.7}) \times 10^{10}\,\mathrm{M}_{\odot}$, and the parameter space scanned is $\alpha \in [14.7, 16.6]$ and $\mu \in [2.14, 2.52] \times 10^{-2}\,\mathrm{kpc}^{-1}$. Within this range, the best fitting point is $(\alpha, \mu)^{\mathrm{BF}} = (16.6, 2.52{\times}10^{-2}\,\mathrm{kpc}^{-1})$, bearing the reduced $\tilde{\chi}^2$=2.78, which for the degrees of freedom of the *Huang et al* compilation is incompatible at more than 5σ In figure 7.2, we show the data together with the rotation curve for this best-fitting morphology, for all the significant points (MW, SG, C) in the parameter space, including the best fit (BF) point identified as described above.

As it can be appreciated, while evidently performing much better than the representative morphology shown in the previous figure (and of any other morphology), none of these curves manage to capture the very behaviour in the central 15 kpc -the entirety of the visible MW- always producing RCs below the observed ones. We test the points above against the `galkin` data compilation, richer of data in the region in object, and report the corresponding χ^2 values in table 7.3. Whereas better than for any other case, they indicate an incompatibility at more than 5σ for all the cases in object, thus again bearing the conclusion that MOG theory can not explain the observed RC of the MW, not even for this best-fitting morphology, in the best-fitting parameter point, within the range indicated by the theory itself.

---

[5] The disc is assumed to dominate the dynamics within the Solar circle where it contributes the maximum amount possible without exceeding the RC anywhere

7.2.3 Conclusions

We have performed a test of MOG theories against the MW dynamics, improving with respect to previous analysis, on one hand, by using two recent-most compilations of data for the observed RC and, on the other hand, by adopting a large set of observationally inferred morphologies for the baryonic component of the Galaxy. Within the constant field approximation, we have reconstructed the RC expected in the MOG theory individually for each of the possible morphologies, and separately for each set of parameters suggested originally in the theory. We find that for each of this set of parameters, and for each of the individual morphologies, the RC thus obtained disagrees with the observed one, providing strong statistical evidence against the theory -in its original formulation- to be able to explain the observed RC of the MW. In addition to the above, we have also modified the key-parameters of the theory, in order to match them to the baryonic mass of the MW as self-consistently obtained within the morphologies we adopt. Applying the MOG theory with this *corrected*, self-consistent new parameters, still brings the obtained RCs to disagree with the observed one with a strong statistical evidence for the entire set of morphologies. In light of this analysis, we conclude that modifying the gravitational potential according to the current version of MOG theory, does not seem to offer a viable solution to the discrepancy between the observed RC of the MW and that generated by the baryons only.

7.3 Final Remarks

As shown in the previous section, the RC method can be used to test modifications of gravity in the weak gravitational field regime. Although, we have tested a specific theory of gravity by means of the RC of our Galaxy, the methodology of this analysis can be easily adapted for testing the validity of other theories of modified gravity at the scale of spiral galaxies.

cross-section

Chapter 8

Conclusions

In this thesis, I present a study of the distribution of dark matter (DM) in our Galaxy, the Milky Way (MW). In chapter 4, we constrained the DM distribution by means of kinematical tracers of the total gravitational potential between 2.5 and 100 kpc from the Galactic centre (GC). Particularly, we used the rotation curve (RC) method, also known in the literature as the mass modelling technique. Tangential velocities from the disc trace the total enclosed mass, which indeed probe the gravitational pull that balances the circular motion. By subtracting from the observed rotation velocities, the velocities predicted for the visible component, by the pure effect of Newtonian gravity, we set constraints on the distribution of DM. These constraints rely on the assumption that the halo of DM in the MW is spherically symmetric and its density profile is well described by a generalised Navarro-Frenk-White (gNFW) density profile. Rather than relying on a given parameterisation for the distribution of the visible matter (stars plus gas) in the Galaxy, we adopt a set of observationally inferred three-dimensional density profiles for the stellar bulge and stellar disc components. By individually combining each bulge and disc morphologies, we end up with a set of parameterisations that are alternative descriptions of the mass distribution of baryons in the Galaxy. The spread in morphologies is considered a satisfactory indicator of the systematic uncertainties due to baryonic modelling, with the conclusion that the actual physical reality must reasonably lie within them.

As concluded in chapter 4, our determination of the averaged DM density in the solar neighbourhood -by means of the RC method- is robust against systematic uncertainties due to baryonic modelling and the reconstruction procedure. For a Sun's galactocentric distance $R_0 = 8.34$ kpc and velocity $\Theta_0 = 239.89$ km/s, once weighted with respect to all baryonic morphologies, we obtained the value:

$$\rho_0 = 0.43 \pm 0.03, \tag{8.1}$$

where the quoted uncertainty is purely statistical. This 7% relative uncertainty brackets the precision of our reconstruction procedure. Systematic uncertainties due to the variation of the baryonic morphology and statistical bias are $\lesssim 6\%$.

By means of the RC technique, the inner slope of the DM density profile, γ, and the scale radius, R_s, can not be individually determined. These parameters are degenerate and with the present precision in the measurements, we can not break this correlation.

The above quoted value for the local DM density, and its corresponding uncertainty, does not include all astrophysical uncertainties that affect the determination of the distribution of DM in the MW. For example, it does not include uncertainties on the Galactic parameters R_0, Θ_0 and $(U_\odot, V_\odot, W_\odot)$. In chapter 6, we

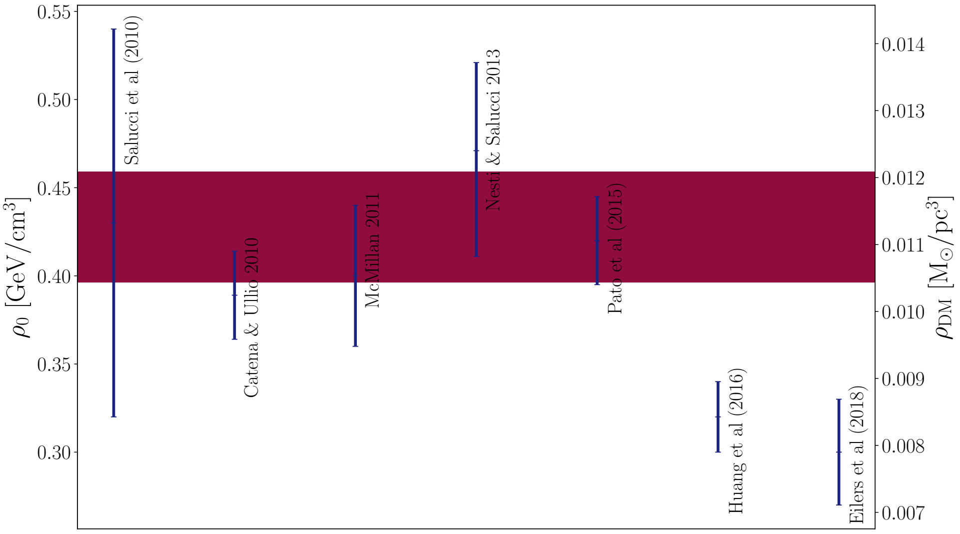

FIGURE 8.1: Value of ρ_0 found in this work (coloured band) compared with the values obtained in Catena and Ullio 2010; Salucci et al. 2010; McMillan 2011; Nesti and Salucci 2013; Pato et al. 2015; Huang et al. 2016; Eilers et al. 2018 (error bars).

described a full data-driven analysis that accounts for these uncertainties, together with systematic uncertainties due to the modelling of the baryonic component of the Galaxy. We thus obtained a value of ρ_0 in the range 0.3-0.8 GeV/cm^3. This analysis aims at providing a practical tool that can be further used by the community in order to propagate astrophysical uncertainties while interpreting results from indirect and direct DM searches. The likelihood profile of this analysis is available at https://github.com/mariabenitocst/UncertaintiesDMinTheMW. It is worth stressing here that this latter analysis only includes kinematical tracers of the total gravitational potential up to galactocentric distances ~ 22 kpc, while the analysis presented in chapter 4 includes tracers up to 100 kpc from the GC. Nonetheless, the analyses from both chapters 4 and 6 are perfectly compatibility between each other.

The major source of uncertainty on the determination of the local DM density by means of the RC is due to uncertainties on the Galactic parameters (R_0, Θ_0). In this regard, the European Space Agency (ESA) mission *Gaia*[1] would help in reducing uncertainties on the spherically average value of ρ_0 (e.g. Kawata et al. 2019).

8.1 Comparison with Other Results

8.1.1 Comparison with *Global* Estimations of the Local Dark Matter Density

Figure 8.1 compares the value of ρ_0 obtained in the analysis from chapter 4 -quoted in (8.1)- with other estimations of the local DM density using the RC technique. Our estimation is compatible with the values obtained in Catena and Ullio 2010, Salucci et al. 2010, McMillan 2011, Nesti and Salucci 2013 and Pato et al. 2015. However, Huang et al. 2016 and Eilers et al. 2018 obtained lower values, incompatible at 1σ with respect to our estimated ρ_0.

---

[1] https://www.cosmos.esa.int/web/gaia

Huang et al. 2016 used the same compilation for the observed RC in the outer Galaxy (i.e. 8-100 kpc from the GC) and the same Galactic parameters R_0, Θ_0 and $(U_\odot, V_\odot, W_\odot)$ as in our analysis from chapter 4. The reason for the discrepancy between the value obtained in Huang et al. 2016 and ours might be the fact that Huang et al. 2016 modelled two ring-like structures -together with the stellar bulge, stellar disc and gas components- in order to explain the dips in the observed RC at ~ 11 and ~ 20 kpc. These ring-like structures contribute to the total enclosed mass, thus leaving less space for the DM component and lowering the estimated local DM density.

Eilers et al. 2018 reconstructed the RC of the MW between 5 to 25 kpc from the GC by means of ~ 23000 red-giant stars. The authors transformed the six-dimensional phase-space of the sample of red-giants into circular velocities around the GC by means of a spherically Jeans analysis. Eilers et al. 2018 obtained $\Theta_0 = 229.0 \pm 0.2\,\mathrm{km/s}$ for the circular velocity of the Sun. This value is at odds with recent estimations that obtained higher values for the local circular velocity (c.f. Sysoliatina et al. 2018; Kawata et al. 2019). For instance, Kawata et al. 2019 report $\Theta_0 = 236 \pm 3\,\mathrm{km/s}$. The lower values for the rotational velocities obtained in Eilers et al. 2018 might be due to the ignorance of the coupling between vertical and radial motions in the Jeans equations (Büdenbender et al. 2015) and/or disequilibria in the data sample. This might explain the reported lower value $\rho_0 = 0.30 \pm 0.03\,\mathrm{GeV cm^3}$.

Nonetheless, it is important to stress here that different estimations of ρ_0 assumed different values for the Galactic parameters and, indeed, all estimations are compatible with the range 0.3-0.8 GeV/cm^3, obtained by varying the Sun's galactocentric distance between 7.5-8.5 kpc.

8.1.2 Comparison with *Local* Estimations of the Local Dark Matter Density

The local DM density in the solar neighbourhood inferred by means of the RC is actually a spherically average estimation of this quantity. Whether this estimation is an unbiased estimator of ρ_0 depends on the degree of sphericity of the DM halo. By comparing *global* and *local* estimations[2] of ρ_0 we can infer constraints on the triaxiality of the DM halo (e.g. Read 2014).

Recent *local* estimations of ρ_0 found values in the range 0.4-0.7 GeV/cm^3 (Xia et al. 2016; Buch et al. 2018; Hagen and Helmi 2018; Sivertsson et al. 2018). Discrepancies between different works might have different origins, such as, different assumptions in the Jeans analysis, different stellar populations used as tracers of the local kinematics and/or disequilibria of the stellar tracers. This latter effect, if not taken into account, might induce systematic errors larger than 25% (Banik et al. 2017).

The actual level of precision both in *global* and *local* estimations of ρ_0 does not allow to set constraints on the degree of sphericity of the DM halo in the MW, and both types of estimations are perfectly compatible.

---

[2] *Global* estimations of ρ_0 rely on the RC technique, whether *local* estimations rely on studies of the gravitational vertical force in the Solar neighbourhood by means of the Jeans equations (see chapter 2 for more details).

8.2 Inner Slope of the Dark Matter Density Profile

By means of the RC analysis, we are unable to determine the inner slope of the DM density profile or γ due to the degeneracy between this parameter and the scale radius in a gNFW profile and present level of uncertainties. The RC technique applies for galactocentric distances larger than 2.5 kpc in order to avoid the inner region of the Galaxy where objects might follow non-circular orbits and the gravitational potential departures from axisymmetry due to the triaxial morphology of the Galactic bulge. Therefore, any inference on the inner slope within the very inner region of the MW, by means of rotation velocities, is just an extrapolation.

In chapter 5, we studied the distribution of DM in the inner ~ 2.5 kpc of the Galaxy. In order to do so we adopted an estimation of the total dynamical mass within the Galactic bulge region. By subtracting from this value the stellar mass -within the very same region- we inferred the allowed DM mass. We adopted a large array of observationally inferred stellar bulge and stellar disc morphologies, while neglecting the gas contribution. The allowed DM mass is, therefore, a function of stellar morphology. Allowed DM mass values are compatible with zero at the 1σ-level for half of the adopted baryonic morphologies. This is not surprising since uncertainties on the mass estimations are large and the central region of the Galaxy is dynamically dominated by baryons. We further studied how the constraints on the allowed DM mass propagate into the parameter space of a gNFW density profile. We concluded that both cusp ($\gamma \sim 1$) and core ($\gamma \sim 0$) DM profiles are allowed. Furthermore, due to uncertainties on the normalisation of the stellar component and on the actual distribution of stars in the Galactic bulge region, we can not infer strong constraints on the distribution of DM in the very inner region of the Galaxy.

8.3 Mass of the Milky Way

An accurate and precise estimation of the MW's mass is important for several reasons. First, the mass of the MW is a key element for comparing our Galaxy with results from N-body simulations. For instance, the number density of satellites of a galaxy depends on its mass. Furthermore, the mass of the MW is important for placing our Galaxy in a cosmological context. For example, it is fundamental in order to understand how our Galaxy relates with galaxy-halo relations found for other galaxies such as, e.g., the stellar versus virial mass (Kravtsov et al. 2018) or the galaxy size versus virial radius relations (Somerville et al. 2018).

There are several techniques for measuring the mass of our Galaxy. These methods include the timing argument (e.g. Li and White 2008), the dynamics of the Local Group (LG) (Peñarrubia et al. 2014), kinematics of MW satellites such as the Large Magellanic Clouds (Sales et al. 2007; Busha et al. 2011; Boylan-Kolchin et al. 2013; González et al. 2013; Barber et al. 2014; Cautun et al. 2014), modelling of tidal streams (Gibbons et al. 2014; Küpper et al. 2015), escape velocity constraints (Smith et al. 2007; Piffl et al. 2014), the RC (McMillan 2011; Nesti and Salucci 2013) and the use of kinematical tracers of the disc and/or halo (e.g. Wilkinson and Evans 1999; Sakamoto et al. 2003; Battaglia et al. 2005; Xue et al. 2008; Gnedin et al. 2010; Watkins et al. 2010; Deason et al. 2012; Kafle et al. 2012, 2014; Eadie et al. 2015).

Figure 8.2 shows a compilation of MW's virial mass estimations taken from figure 1 of Wang et al. 2015. As seen from this figure, different measurements of the virial mass of the MW, even those that use the same methodology, do not converge into a single value. Estimations of the mass of the MW range from $\sim 0.5 \times 10^{12}$ $M_\odot$ (Gibbons et al. 2014) up to $2 - 3 \times 10^{12}$ $M_\odot$ (e.g. Sakamoto et al. 2003).

We have estimated M_{200} using the RC technique and the constraints on the distribution of DM in the MW from the analysis described in chapter 4 (see appendix C for details). Our estimations for M_{200}, which are summarised in appendix C, are shown in figure 8.2 by the coloured band. This band brackets systematic uncertainties due to the Galactic modelling, i.e. variations of baryonic morphology. Variations in the baryonic morphology imply a shift $< 16\%$ in the inferred virial mass of the MW. Whether this shift is dominated by the assumption of different stellar disc morphologies, adopting different bulge configurations has a minor effect. The dispersion on the virial mass values due to uncertainties on the actual distribution of baryons is smaller than statistical uncertainties (which are $< 30\%$).

Since *Gaia* would help constraining the stellar disc profile, this mission would further reduce the precision on MW's mass estimations by means of the RC technique. It is important to highlight that uncertainties on the Galactic parameters are not taken into account here. Nonetheless, it is reasonable to assume that uncertainties on Galactic parameters, which are related to the dynamics in the Solar neighbourhood, would have a smaller impact on the virial mass estimation than uncertainties on the actual three-dimensional distribution of the stellar disc.

8.4 Final Remarks and Future Steps

In this thesis, I adopted a gNFW profile for describing the DM mass distribution in our Galaxy. The constraints on the distribution of DM rely, therefore, on this particular parameterisation. I would like to study how these constraints on the distribution of DM vary by adopting different descriptions for the DM density profile. Particularly, I would like to repeat the analysis from chapter 5 by assuming, instead, an isothermal or a Burkert (Burkert 1995) DM density profile. These empirical descriptions of the DM mass distribution of galaxies assume that DM halos have a central core. By studying how the constraints on the allowed DM mass in the inner Galactic region propagate into the parameter space of these empirical DM profiles, I aim to constrain the maximum size of a (possible) core in the DM halo of the MW. It is important to stress here that the existence of a core in the DM profile of the MW is still debatable. In this thesis, we found that, due to present size of uncertainties in the actual distribution of baryons and their normalisation, we are unable to set strong constraints on the inner slope of the DM distribution in the inner 2.5 kpc of the Galaxy. Nonetheless, there are other works claiming the existence of a core in the Galaxy (e.g. Nesti and Salucci 2013; Portail et al. 2017).

I would like to further generalise the full data-driven analysis from chapter 6, that quantifies astrophysical uncertainties that affect the interpretation of results from particle DM searches, for other DM density profiles. The goal of this analysis is to provide a practical tool that can be used by the community in order to account for astrophysical uncertaintes while interpreting, among others, results from indirect experiments within the GC or Galactic halo in γ-rays at GeV or TeV energies, DM neutrinos searches and local DM searches with antimatter. It might be useful for the community to provide the likelihood profile that quantifies astrophysical uncertainties

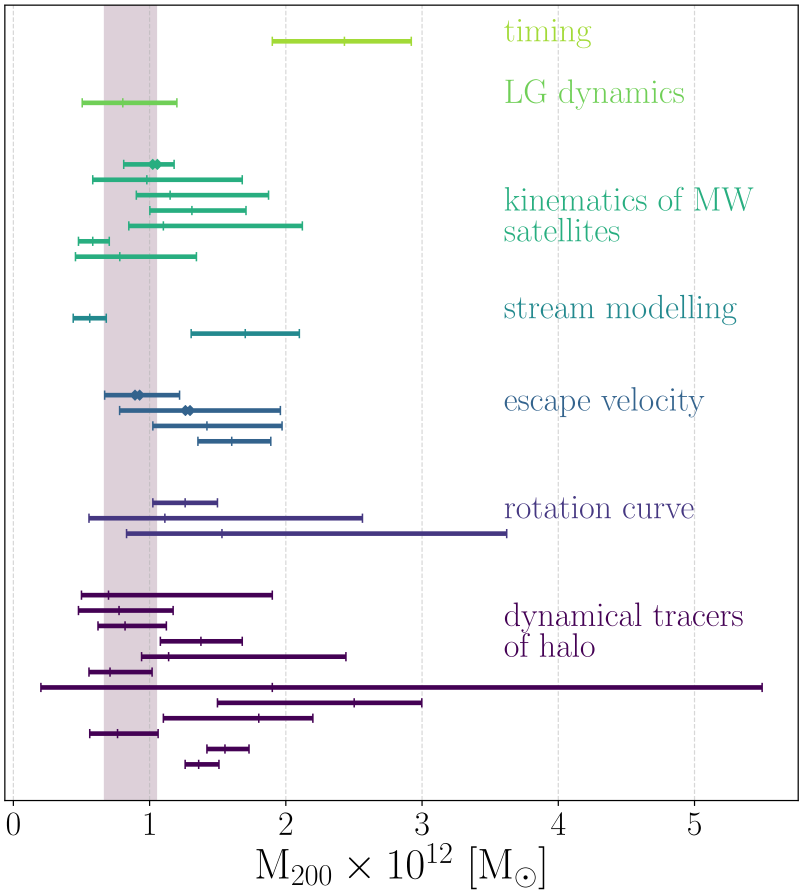

FIGURE 8.2: Compilation of measurements of M_{200}, with corresponding 1σ uncertainties, taken from figure 1 of Wang et al. 2015 (+ marks) and using Gaia data (× marks). Estimations using different methods are plotted with different colours. From top to bottom, measurements are taken from: Li and White 2008 which used the timing argument. Peñarrubia et al. 2014 that used the dynamics of the LG. Then, Posti and Helmi 2018, Busha et al. 2011, González et al. 2013, Boylan-Kolchin et al. 2013, Barber et al. 2014, Sales et al. 2007 and Cautun et al. 2014 used the kinematics of satellites of the MW. Gibbons et al. 2014 and Küpper et al. 2015 modelled the orbits of tidal streams. Monari et al. 2018, Deason et al. 2019, Smith et al. 2007 and Piffl et al. 2014 used constraints on the escape velocity. McMillan 2011 and Nesti and Salucci 2013 used the RC of the MW. We quoted two values from Nesti and Salucci 2013: The first under the assumption of a Burkert DM density profile and the second under the assumption of a NFW profile. Finally, Battaglia et al. 2005, Kafle et al. 2012, Xue et al. 2008, Gnedin et al. 2010, Watkins et al. 2010, Kafle et al. 2014, Wilkinson and Evans 1999, Sakamoto et al. 2003, Sakamoto et al. 2003 (without Leo I) Deason et al. 2012, Eadie et al. 2015 and Eadie et al. 2015 (without Pal 3) used dynamical tracers of the halo. The coloured band brackets our estimation of M_{200} obtained by means of the RC technique and summarised in appendix C (see this appendix for more details).

on the determination of the DM distribution in the MW while adopting other DM parameterisations still consider viable to date.

Finally, I would like to study how departures from sphericity of the DM halo affect the reconstructed local DM density by means of the Bayesian inference procedure described in chapter 4.

Appendix A

Data Sets in `galkin` Compilation

The `galkin` rotation curve (RC) is a compilation of different kinematic tracers of the total gravitational potential of our Galaxy (Pato and Iocco 2017) . It contains a large number of tracers within the visible region of the Galaxy, approximately up to 22 kpc from the Galactic centre (GC), and consists of 25 different data sets summarised in table A.1. The aim of this table is to highlight the 12 compatible data sets, `galkin`$_{12}$, obtained through the compatibility procedure described in chapter 4 (see this chapter for more details).

Tracer type	**Reference**	
gas kinematics	Burton and Gordon 1978	
	Clemens 1985	X
	Knapp et al. 1985	X
	Fich et al. 1989	
	Fich et al. 1989	
	Turbide and Moffat 1993	
	Brand and Blitz 1993	
	Malhotra 1995	X
	Honma and Sofue 1997	
	Luna et al. 2006	
	McClure-Griffiths and Dickey 2007	
	Hou et al. 2009	
	Hou et al. 2009	
star kinematics	Pont et al. 1994	X
	Pont et al. 1997	X
	Durand et al. 1998	
	Demers and Battinelli 2007	X
	Frinchaboy and Majewski 2008	
	Battinelli et al. 2013	X
masers	Stepanishchev and Bobylev 2011	X
	Honma et al. 2012	X
	Xu et al. 2013	X
	Bobylev and Bajkova 2013	X
	Reid et al. 2014	X

Table A.1: Data sets which are included in the `galkin` compilation (Pato and Iocco 2017). In the last column, we use a mark to highlight the 12 compatible data sets following the compatibility procedure presented in chapter 4.

Appendix B

Stellar and Dark Matter Masses in the Inner Region

In the following tables we summarise the stellar and dark matter (DM) masses found, in the analysis presented in chapter 5, for a squared box, centred at the Galactic centre, with coordinates,

$$[x,\, y,\, z] = [\pm 2.2,\, \pm 1.4,\, \pm 1.2]\,\mathrm{kpc}. \tag{B.1}$$

Each table corresponds to a given stellar disc morphology. The total dynamical mass within this very same region is $M_{\mathrm{tot}} = (1.85 \pm 0.05) \times 10^{10}\,\mathrm{M}_\odot$ (Portail et al. 2017). See the mentioned chapter for more details.

Bulge	Reference	M_*^{bulge} $(\times 10^{10}\,M_\odot)$	M_* $(\times 10^{10}\,M_\odot)$	BD	M_{DM} $(\times 10^{9}\,M_\odot)$	γ
1	Stanek et al. 1997 (G2)	0.4 ± 0.4	1.4 ± 0.4	0.4	4 ± 4	0.00 - 1.59
2	Stanek et al. 1997 (E2)	0.4 ± 0.4	1.4 ± 0.4	0.3	4 ± 4	0.00 - 1.57
3	Vanhollebeke et al. 2009	0.5 ± 0.5	1.5 ± 0.5	0.4	3 ± 5	0.00 - 1.58
4	Bissantz and Gerhard 2002	0.6 ± 0.4	1.7 ± 0.5	0.6	2 ± 5	0.00 - 1.43
5	Zhao 1996	0.3 ± 0.4	1.4 ± 0.4	0.3	4 ± 4	0.00 - 1.59
6	Robin et al. 2012	0.3 ± 0.3	1.3 ± 0.3	0.3	5 ± 3	0.69 - 1.58

TABLE B.1: Values of stellar mass and allowed DM mass for all bulge morphologies presented in chapter 3. BD stands for bulge-to-disc mass ratio (i.e. M_*^{bulge}/M_*^{disc}). The value of the inner slope of the DM density profile, γ, as allowed at 1σ within the local DM density ρ_0 band identified by the RC analysis in Benito et al. 2017. Stellar disc morphology given in Bovy and Rix 2013 (identified in this thesis as *disc 1*), $M_*^{disc} = (1.06 \pm 0.11) \times 10^{10}\,M_\odot$; $R_s = 20$ kpc, R_0=8.0 kpc.

Bulge	Reference	M_*^{bulge} ($\times 10^{10}\,M_\odot$)	M_* ($\times 10^{10}\,M_\odot$)	BD	M_{DM} ($\times 10^9\,M_\odot$)	γ
1	Stanek et al. 1997 (G2)	0.9 ± 0.4	1.5 ± 0.4	1.7	4 ± 4	0.00 - 1.46
2	Stanek et al. 1997 (E2)	0.9 ± 0.4	1.4 ± 0.4	1.5	4 ± 4	0.00 - 1.48
3	Vanhollebeke et al. 2009	1.1 ± 0.5	1.7 ± 0.5	2.0	2 ± 5	0.00 - 1.38
4	Bissantz and Gerhard 2002	1.1 ± 0.4	1.6 ± 0.4	2.0	2 ± 5	0.00 - 1.35
5	Zhao 1996	0.8 ± 0.4	1.4 ± 0.4	1.5	5 ± 4	0.00 - 1.49
6	Robin et al. 2012	0.6 ± 0.3	1.2 ± 0.3	1.2	6 ± 3	0.96 - 1.56

TABLE B.2: Values of stellar mass and allowed DM mass for all bulge morphologies presented in chapter 3. The value of the inner slope of the DM density profile, γ, as allowed at 1σ within the local DM density ρ_0 band identified by the RC analysis in Benito et al. 2017. Stellar disc from Han and Gould 2003 (*disc 2*), $M_*^{disc} = (0.55 \pm 0.06) \times 10^{10}\,M_\odot$; $R_s = 20$ kpc, R_0=8.0 kpc.

Bulge	Reference	M_*^{bulge} ($\times 10^{10}\,M_\odot$)	M_* ($\times 10^{10}\,M_\odot$)	BD	M_{DM} ($\times 10^9\,M_\odot$)	γ
1	Stanek et al. 1997 (G2)	0.2 ± 0.4	1.1 ± 0.4	0.2	7 ± 4	1.28 - 2.00
2	Stanek et al. 1997 (E2)	0.2 ± 0.4	1.1 ± 0.4	0.2	7 ± 4	1.34 - 2.00
3	Vanhollebeke et al. 2009	0.2 ± 0.5	1.2 ± 0.5	0.2	7 ± 5	0.96 - 2.00
4	Bissantz and Gerhard 2002	0.4 ± 0.4	1.3 ± 0.5	0.4	5 ± 5	0.46 - 2.00
5	Zhao 1996	0.2 ± 0.4	1.1 ± 0.4	0.2	7 ± 4	1.38 - 2.00
6	Robin et al. 2012	0.1 ± 0.3	1.1 ± 0.3	0.2	8 ± 3	1.55 - 2.00

TABLE B.3: Values of stellar mass and allowed DM mass for all bulge morphologies presented in chapter 3. The value of the inner slope of the DM density profile, γ, as allowed at 1σ within the local DM density ρ_0 band identified by the RC analysis in Benito et al. 2017. Stellar disc from Calchi Novati and Mancini 2011 (*disc 3*), $M_*^{disc} = (0.93 \pm 0.10) \times 10^{10}\,M_\odot$; $R_s = 20$ kpc, R_0=8.0 kpc.

Bulge	Reference	M_*^{bulge} ($\times 10^{10}\,M_\odot$)	M_* ($\times 10^{10}\,M_\odot$)	BD	M_{DM} ($\times 10^9\,M_\odot$)	γ
1	Stanek et al. 1997 (G2)	1.0 ± 0.4	1.5 ± 0.4	2.1	4 ± 4	0.00 - 1.49
2	Stanek et al. 1997 (E2)	0.9 ± 0.4	1.4 ± 0.4	1.9	4 ± 4	0.00 - 1.52
3	Vanhollebeke et al. 2009	1.2 ± 0.5	1.7 ± 0.5	2.5	2 ± 5	0.00 - 1.39
4	Bissantz and Gerhard 2002	1.2 ± 0.4	1.7 ± 0.4	2.4	2 ± 4	0.00 - 1.38
5	Zhao 1996	0.9 ± 0.4	1.4 ± 0.4	1.9	4 ± 4	0.00 - 1.52
6	Robin et al. 2012	0.7 ± 0.3	1.2 ± 0.3	1.4	7 ± 3	1.04 - 1.61

TABLE B.4: Values of stellar mass and allowed DM mass for all bulge morphologies presented in chapter 3. The value of the inner slope of the DM density profile, γ, as allowed at 1σ within the local DM density ρ_0 band identified by the RC analysis in Benito et al. 2017. Stellar disc given in de Jong et al. 2010 (*disc 4*), $M_*^{disc} = (0.48 \pm 0.05) \times 10^{10}\,M_\odot$; $R_s = 20$ kpc, R_0=8.0 kpc.

Bulge	Reference	M_*^{bulge} ($\times 10^{10}\, M_\odot$)	M_* ($\times 10^{10}\, M_\odot$)	BD	M_{DM} ($\times 10^{9}\, M_\odot$)	γ
1	Stanek et al. 1997 (G2)	0.9 ± 0.4	1.5 ± 0.4	1.5	3 ± 4	0.00 - 1.49
2	Stanek et al. 1997 (E2)	0.9 ± 0.4	1.5 ± 0.5	1.4	4 ± 4	0.00 - 1.52
3	Vanhollebeke et al. 2009	1.1 ± 0.5	1.7 ± 0.5	1.9	1 ± 5	0.00 - 1.39
4	Bissantz and Gerhard 2002	1.1 ± 0.4	1.7 ± 0.4	1.8	1 ± 5	0.00 - 1.35
5	Zhao 1996	0.8 ± 0.4	1.5 ± 0.4	1.4	4 ± 4	0.00 - 1.52
6	Robin et al. 2012	0.6 ± 0.3	1.3 ± 0.3	1.1	6 ± 3	0.99 - 1.61

TABLE B.5: Values of stellar mass and allowed DM mass for all bulge morphologies presented in chapter 3. The value of the inner slope of the DM density profile, γ, as allowed at 1σ within the local DM density ρ_0 band identified by the RC analysis in Benito et al. 2017. Stellar disc Jurić et al. 2008 (*disc 5*), $M_*^{disc} = (0.60 \pm 0.06) \times 10^{10}\, M_\odot$; $R_s = 20$ kpc, R_0=8.0 kpc.

Appendix C

Virial Mass of Dark Matter Halo

The virial mass of a DM halo is defined as,

$$\mathrm{M}_{\mathrm{vir}} = \frac{4}{3}\pi\, R_{\mathrm{vir}}^{3} \Delta \rho_{m}, \tag{C.1}$$

where the mean background density is $\rho_m = \Omega_m \rho_{\mathrm{crit}}$. Following Klypin et al. 2002 and Kafle et al. 2014, we adopt the value $\Delta = 340$. The virial radius R_{vir} is the radius of the sphere which contains an average density $\Delta\rho_m$.

The DM mass within a sphere of radius r for a generalised Navarro-Frenk-White (gNFW) profile takes the form,

$$\mathrm{M}(< r) = -4\pi \frac{\rho_0 \left(\frac{R_0}{R_s}\right)^{\gamma} \left(1 + \frac{R_0}{R_s}\right)^{3-\gamma}}{\gamma - 3} r^3 \left(\frac{r}{R_s}\right)^{-\gamma} {}_2\mathrm{F}_1(3-\gamma, 3-\gamma; 4-\gamma; -\frac{r}{R_s}), \tag{C.2}$$

where R_0 is the Sun's galactocentric distance and ${}_2\mathrm{F}_1(a, b; c; d)$ is the Gauss hypergeometric function.

By combining equations (C.1) and (C.2), we obtain:

$$\frac{3\rho_0 \left(\frac{R_0}{R_s}\right)^{\gamma} \left(1 + \frac{R_0}{R_s}\right)^{3-\gamma}}{\Delta\rho_m\,(\gamma - 3)} = -\frac{\left(\frac{R_{\mathrm{vir}}}{R_s}\right)^{\gamma}}{{}_2\mathrm{F}_1(3-\gamma, 3-\gamma; 4-\gamma; -\frac{R_{\mathrm{vir}}}{R_s})}. \tag{C.3}$$

By solving this equation, we can infer the virial radius, R_{vir}, and the corresponding virial mass, $\mathrm{M}_{\mathrm{vir}}$, of the DM halo.

It is straightforward to rewrite equation (C.3) in case the mass of the DM halo is defined as,

$$\mathrm{M}_{200} = \frac{4}{3}\pi\, R_{200}^{3} 200 \rho_{\mathrm{crit}}. \tag{C.4}$$

From the posterior distribution functions obtained in chapter 4, we derive the corresponding probability densities for R_{vir} and $\mathrm{M}_{\mathrm{vir}}$ (or equivalently R_{200} and M_{200}). For doing this, we adopt a gNFW density profile formulated in terms of (γ, R_s, ρ_0). We apply the Bayesian inference methodology described in chapter 4. We, then, make a change of variables from (γ, R_s, ρ_0) into $(R_{\mathrm{vir}}, \mathrm{M}_{\mathrm{vir}})$. This is, for each point $\Theta^i = (\gamma^i, R_s^i, \rho_0^i)$ of the obtained Markov chain, we compute the corresponding R_{vir}^i and $\mathrm{M}_{\mathrm{vir}}^{\mathrm{i}}$ by solving equations (C.3) and (C.1), respectively. The final sample of points R_{vir}^i and $\mathrm{M}_{\mathrm{vir}}^{\mathrm{i}}$ is assumed to be drawn from the probability distribution functions for the virial radius, $\mathrm{P}(R_{\mathrm{vir}}|data)$, and virial mass, $\mathrm{P}(\mathrm{M}_{\mathrm{vir}}|data)$, respectively. Table C.1 summarises the values obtained for R_{vir}, $\mathrm{M}_{\mathrm{vir}}$, R_{200} and M_{200}. We report the median and 1σ credible interval (i.e. 15.9 and 84.1 percentile estimations). For completeness, table C.1 includes the total baryonic mass for each of the adopted baryonic morphologies. Figure C.1 show the density functions obtained for R_{200} and M_{200}, for the heaviest (top), central (medium) and lightest (bottom) disc morphologies.

Baryonic Morph.	$R_{\rm vir}$ [kpc]	$\mathrm{M}_{\rm vir}$ [$10^{12}\,\mathrm{M}_\odot$]	R_{200} [kpc]	M_{200} [$10^{12}\,\mathrm{M}_\odot$]	$\mathrm{M}_{\rm bar}$ [$10^{10}\,\mathrm{M}_\odot$]
11	268^{+10}_{-9}	1.1 ± 0.1	208 ± 7	1.0 ± 0.1	$7.4^{+0.7}_{-0.6}$
21	268^{+10}_{-9}	1.1 ± 0.1	209 ± 7	1.0 ± 0.1	$7.4^{+0.8}_{-0.7}$
31	268^{+10}_{-9}	1.1 ± 0.1	209 ± 7	1.0 ± 0.1	$7.5^{+0.8}_{-0.7}$
41	268^{+10}_{-9}	1.1 ± 0.1	209 ± 7	1.0 ± 0.1	$7.7^{+0.8}_{-0.7}$
51	268^{+10}_{-9}	1.1 ± 0.1	209 ± 7	1.0 ± 0.1	7.4 ± 0.7
61	268^{+10}_{-9}	1.1 ± 0.1	208 ± 7	1.0 ± 0.1	$7.3^{+0.7}_{-0.6}$
12	262^{+13}_{-11}	$1.0^{+0.2}_{-0.1}$	203^{+10}_{-8}	0.9 ± 0.1	$6.6^{+0.6}_{-0.4}$
22	261^{+13}_{-11}	$1.0^{+0.2}_{-0.1}$	203^{+9}_{-8}	0.9 ± 0.1	$6.7^{+0.7}_{-0.6}$
32	261^{+13}_{-11}	$1.0^{+0.2}_{-0.1}$	203^{+10}_{-8}	0.9 ± 0.1	$6.8^{+0.7}_{-0.6}$
42	261^{+13}_{-12}	$1.0^{+0.2}_{-0.1}$	203^{+10}_{-9}	0.9 ± 0.1	$6.8^{+0.7}_{-0.6}$
52	261^{+13}_{-11}	$1.0^{+0.2}_{-0.1}$	203^{+10}_{-8}	0.9 ± 0.1	6.6 ± 0.6
62	260^{+13}_{-11}	$1.0^{+0.2}_{-0.1}$	202^{+9}_{-8}	0.9 ± 0.1	$6.4^{+0.6}_{-0.5}$
13	256^{+13}_{-11}	$0.9^{+0.2}_{-0.1}$	199^{+10}_{-8}	0.8 ± 0.1	$6.6^{+0.6}_{-0.4}$
23	256^{+14}_{-11}	$0.9^{+0.2}_{-0.1}$	199^{+10}_{-8}	0.8 ± 0.1	$6.7^{+0.7}_{-0.6}$
33	259^{+14}_{-11}	$1.0^{+0.2}_{-0.1}$	201^{+10}_{-8}	0.9 ± 0.1	$6.9^{+0.7}_{-0.6}$
43	255^{+12}_{-11}	1.0 ± 0.1	199^{+9}_{-8}	0.8 ± 0.1	$6.9^{+0.7}_{-0.6}$
53	257^{+15}_{-12}	$1.0^{+0.2}_{-0.1}$	200^{+11}_{-9}	0.9 ± 0.1	6.6 ± 0.6
63	255^{+13}_{-11}	0.9 ± 0.1	199^{+9}_{-8}	0.8 ± 0.1	$6.4^{+0.6}_{-0.5}$
14	259^{+15}_{-12}	$1.0^{+0.2}_{-0.1}$	202^{+11}_{-9}	0.9 ± 0.1	$6.7^{+0.6}_{-0.4}$
24	257^{+13}_{-12}	0.9 ± 0.1	200 ± 9	0.9 ± 0.1	$6.7^{+0.7}_{-0.6}$
34	258^{+14}_{-11}	$1.0^{+0.2}_{-0.1}$	201^{+10}_{-9}	0.9 ± 0.1	$6.9^{+0.7}_{-0.6}$
44	255^{+14}_{-11}	$1.0^{+0.2}_{-0.1}$	201^{+10}_{-9}	0.9 ± 0.1	$6.9^{+0.7}_{-0.6}$
54	258^{+13}_{-11}	$1.0^{+0.2}_{-0.1}$	201^{+10}_{-8}	0.9 ± 0.1	6.6 ± 0.6
64	256^{+14}_{-12}	$0.9^{+0.2}_{-0.1}$	200^{+10}_{-9}	0.8 ± 0.1	$6.4^{+0.6}_{-0.5}$
15	262^{+14}_{-12}	$1.0^{+0.2}_{-0.1}$	203^{+10}_{-9}	0.9 ± 0.1	$7.2^{+0.6}_{-0.5}$
25	259^{+15}_{-11}	$1.0^{+0.2}_{-0.1}$	202^{+11}_{-8}	0.9 ± 0.1	$7.3^{+0.7}_{-0.6}$
35	262^{+14}_{-12}	$1.0^{+0.2}_{-0.1}$	204^{+10}_{-9}	0.9 ± 0.1	$7.5^{+0.8}_{-0.7}$
45	261^{+14}_{-12}	$1.0^{+0.2}_{-0.1}$	203^{+10}_{-9}	0.9 ± 0.1	$7.5^{+0.7}_{-0.6}$
55	259^{+14}_{-11}	$1.0^{+0.2}_{-0.1}$	202^{+10}_{-8}	0.9 ± 0.1	$7.2^{+0.7}_{-0.6}$
65	259^{+13}_{-11}	$1.0^{+0.2}_{-0.1}$	202^{+10}_{-8}	0.9 ± 0.1	7.0 ± 0.6

TABLE C.1: Median and 1σ uncertainty (15.9 and 84.1 percentile estimations) of $R_{\rm vir}$, $\mathrm{M}_{\rm vir}$, R_{200} and M_{200}. Last column corresponds to the total baryonic mass.

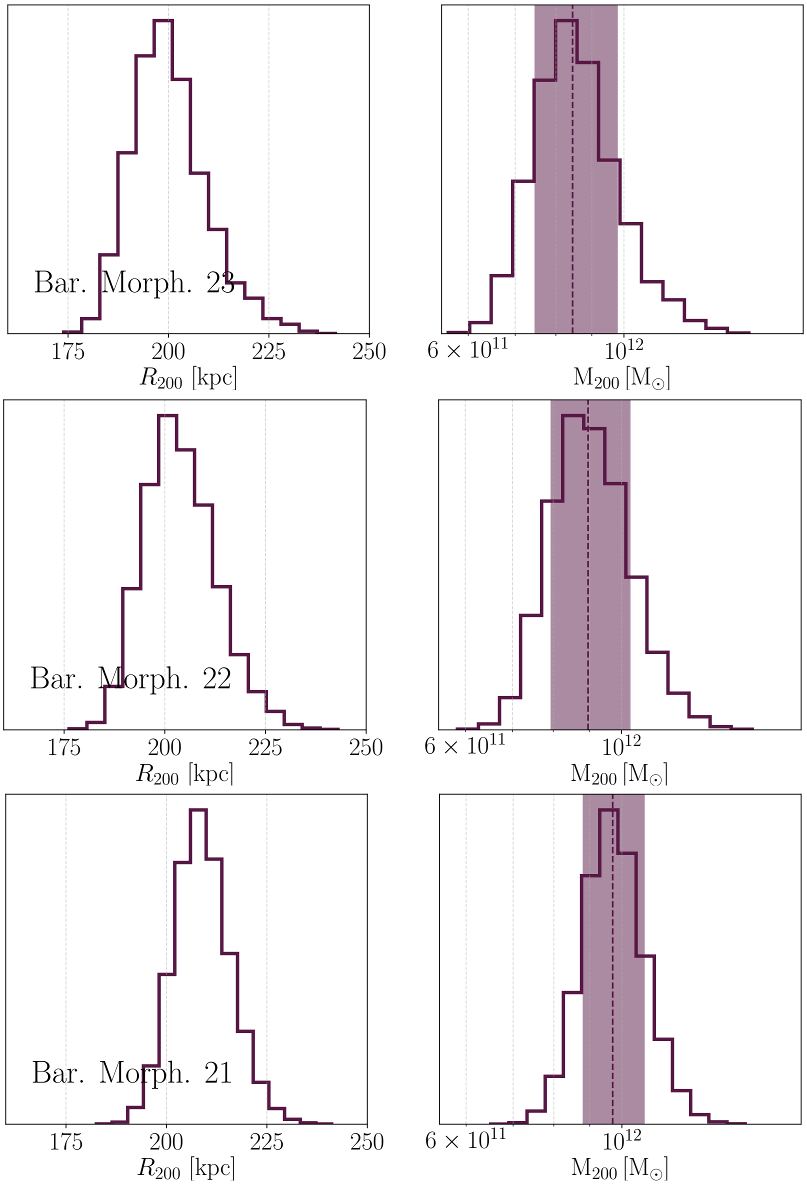

FIGURE C.1: R_{200} and M_{200} density distribution functions for the heaviest (*disc 1* given in Bovy and Rix 2013) (top panel), the central (*disc 2* given in Han and Gould 2003) (central panel) and the lightest (*disc 3* given in Calchi Novati and Mancini 2011) (bottom panel) disc morphologies. We assume *bulge 2* taken from Stanek et al. 1997. The dashed line corresponds to the median value and the coloured band bracket the 1σ credible interval (i.e. 15.9 and 84.1 percentile estimations).

Bibliography

Refsdal, S. (1964). “On the possibility of determining Hubble’s parameter and the masses of galaxies from the gravitational lens effect”. In: *MNRAS* 128, p. 307. DOI: 10.1093/mnras/128.4.307.

Einasto, J. (1965). “On the Construction of a Composite Model for the Galaxy and on the Determination of the System of Galactic Parameters”. In: *Trudy Astrofizicheskogo Instituta Alma-Ata* 5, pp. 87–100.

Lynden-Bell, D. (1967). “Statistical mechanics of violent relaxation in stellar systems”. In: *MNRAS* 136, p. 101. DOI: 10.1093/mnras/136.1.101.

Gunn, J. E. and J. R. Gott III (1972). “On the Infall of Matter Into Clusters of Galaxies and Some Effects on Their Evolution”. In: *The Astrophysical Journal* 176, p. 1. DOI: 10.1086/151605.

de Vaucouleurs, G. (1974). “Structures of Central Bulges and Nuclei of Galaxies”. In: *The Formation and Dynamics of Galaxies*. Ed. by J. R. Shakeshaft. Vol. 58. IAU Symposium, p. 335.

Gott III, J. R. (1975). “On the Formation of Elliptical Galaxies”. In: *The Astrophysical Journal* 201, pp. 296–310. DOI: 10.1086/153887.

Gunn, J. E. (1977). “Massive galactic halos. I - Formation and evolution”. In: *The Astrophysical Journal* 218, pp. 592–598. DOI: 10.1086/155715.

Tully, R. B. and J. R. Fisher (1977). “A new method of determining distances to galaxies”. In: *Astron. Astrophys.* 54, pp. 661–673.

Burton, W. B. and M. A. Gordon (1978). “Carbon monoxide in the Galaxy. III - The overall nature of its distribution in the equatorial plane”. In: *Astron. Astrophys.* 63, pp. 7–27.

Rubin, V. C. et al. (1978). “Extended rotation curves of high-luminosity spiral galaxies. II - The anemic SA galaxy NGC 4378”. In: *The Astrophysical Journal* 224, pp. 782–795. DOI: 10.1086/156426.

Bosma, A. and P. C. van der Kruit (1979). “The local mass-to-light ratio in spiral galaxies”. In: *Astron. Astrophys.* 79, pp. 281–286.

Schwarzschild, M. (1979). “A numerical model for a triaxial stellar system in dynamical equilibrium”. In: *The Astrophysical Journal* 232, pp. 236–247. DOI: 10.1086/157282.

Rubin, V. C., W. K. Ford Jr., and N. Thonnard (1980). “Rotational properties of 21 SC galaxies with a large range of luminosities and radii, from NGC 4605 /R = 4kpc/ to UGC 2885 /R = 122 kpc/”. In: *The Astrophysical Journal* 238, pp. 471–487. DOI: 10.1086/158003.

Milgrom, M. (1983). “A modification of the Newtonian dynamics as a possible alternative to the hidden mass hypothesis”. In: *The Astrophysical Journal* 270, pp. 365–370. DOI: 10.1086/161130.

Blumenthal, G. R. et al. (1984). “Formation of galaxies and large-scale structure with cold dark matter”. In: *Nature* 311, pp. 517–525. DOI: 10.1038/311517a0.

Fillmore, J. A. and P. Goldreich (1984). “Self-similar gravitational collapse in an expanding universe”. In: *The Astrophysical Journal* 281, pp. 1–8. DOI: 10.1086/162070.

White, S. D. M. (1984). “Angular momentum growth in protogalaxies”. In: *The Astrophysical Journal* 286, pp. 38–41. DOI: 10.1086/162573.

Bertschinger, E. (1985). “Self-similar secondary infall and accretion in an Einstein-de Sitter universe”. In: *The Astrophysical Journal Supp. Series* 58, pp. 39–65. DOI: 10.1086/191028.

Clemens, D. P. (1985). “Massachusetts-Stony Brook Galactic plane CO survey - The Galactic disk rotation curve”. In: *The Astrophysical Journal* 295, pp. 422–428. DOI: 10.1086/163386.

Davis, M. et al. (1985). “The evolution of large-scale structure in a universe dominated by cold dark matter”. In: *The Astrophysical Journal* 292, pp. 371–394. DOI: 10.1086/163168.

Knapp, G. R., A. A. Stark, and R. W. Wilson (1985). “The global properties of the Galaxy. III - Maps of the (C-12)(O) emission in the first quadrant of the Galaxy”. In: *Astronomic. J.* 90, pp. 254–300. DOI: 10.1086/113729.

van Albada, T. S. et al. (1985). “Distribution of dark matter in the spiral galaxy NGC 3198”. In: *The Astrophysical Journal* 295, pp. 305–313. DOI: 10.1086/163375.

Blumenthal, G. R. et al. (1986). “Contraction of dark matter galactic halos due to baryonic infall”. In: *The Astrophysical Journal* 301, pp. 27–34. DOI: 10.1086/163867.

Paczynski, B. (1986). “Gravitational microlensing by the galactic halo”. In: *The Astrophysical Journal* 304, pp. 1–5. DOI: 10.1086/164140.

White, S. D. M. et al. (1987). “Clusters, filaments, and voids in a universe dominated by cold dark matter”. In: *The Astrophysical Journal* 313, pp. 505–516. DOI: 10.1086/164990.

Carignan, C. and K. C. Freeman (1988). “DDO 154 - A ’dark’ galaxy?” In: *The Astrophysical Journal Letters* 332, pp. L33–L36. DOI: 10.1086/185260.

Frenk, C. S. et al. (1988). “The formation of dark halos in a universe dominated by cold dark matter”. In: *The Astrophysical Journal* 327, pp. 507–525. DOI: 10.1086/166213.

Fich, M., L. Blitz, and A. A. Stark (1989). “The rotation curve of the Milky Way to 2 R(0)”. In: *The Astrophysical Journal* 342, pp. 272–284. DOI: 10.1086/167591.

Kuijken, K. and G. Gilmore (1989). “The mass distribution in the galactic disc. I - A technique to determine the integral surface mass density of the disc near the sun.” In: *MNRAS* 239, pp. 571–603. DOI: 10.1093/mnras/239.2.571.

Jobin, M. and C. Carignan (1990). “The dark side of NGC 3109”. In: *Astronomic. J.* 100, pp. 648–662. DOI: 10.1086/115548.

Blitz, Leo and David N Spergel (1991). “Direct evidence for a bar at the Galactic center”. In: *The Astrophysical Journal* 379, pp. 631–638.

Combes, F. (1991). “Distribution of CO in the Milky Way”. In: *Annu. Rev. Astron. Astrophys.* 29, pp. 195–237. DOI: 10.1146/annurev.aa.29.090191.001211.

Cordes, J. M. et al. (1991). “The Galactic distribution of free electrons”. In: *Nature* 354, pp. 121–124. DOI: 10.1038/354121a0.

Dubinski, J. and R. G. Carlberg (1991). “The structure of cold dark matter halos”. In: *The Astrophysical Journal* 378, pp. 496–503. DOI: 10.1086/170451.

Navarro, J. F. and W. Benz (1991). “Dynamics of cooling gas in galactic dark halos”. In: *The Astrophysical Journal* 380, pp. 320–329. DOI: 10.1086/170590.

Brand, J. and L. Blitz (1993). “The Velocity Field of the Outer Galaxy”. In: *Astron. Astrophys.* 275, p. 67.

Kaiser, N. and G. Squires (1993). “Mapping the dark matter with weak gravitational lensing”. In: *The Astrophysical Journal* 404, pp. 441–450. DOI: 10.1086/172297.

Moore, B., C. S. Frenk, and S. D. M. White (1993). "Galaxy Groups - Abundance by Luminosity and by Velocity Dispersion". In: *MNRAS* 261, p. 827. DOI: `10.1093/mnras/261.4.827`.

Padmanabhan, T. (1993). *Structure Formation in the Universe*, p. 499.

Turbide, L. and A. F. J. Moffat (1993). "Precision photometry of young stellar groups towards the outer Galactic disk and the Galactic rotation curve". In: *Astronomic. J.* 105, pp. 1831–1854. DOI: `10.1086/116558`.

Fort, B. and Y. Mellier (1994). "Arc(let)s in clusters of galaxies". In: *A&AS* 5, pp. 239–292. DOI: `10.1007/BF00877691`.

Kormann, R., P. Schneider, and M. Bartelmann (1994). "Isothermal elliptical gravitational lens models". In: *Astron. Astrophys.* 284, pp. 285–299.

Moore, B. (1994). "Evidence against dissipation-less dark matter from observations of galaxy haloes". In: *Nature* 370, pp. 629–631. DOI: `10.1038/370629a0`.

Mushotzky, R. F. et al. (1994). "ASCA observation of NGC 4636: Dark matter and metallicity gradient". In: *The Astrophysical Journal Letters* 436, pp. L79–L82. DOI: `10.1086/187637`.

Pont, F., M. Mayor, and G. Burki (1994). "New radial velocities for classical cepheids. Local galactic rotation revisited". In: *Astron. Astrophys.* 285, pp. 415–439.

Weiland, JL et al. (1994). "COBE diffuse infrared background experiment observations of the galactic bulge". In: *The Astrophysical Journal* 425, pp. L81–L84.

Burkert, A. (1995). "The Structure of Dark Matter Halos in Dwarf Galaxies". In: *The Astrophysical Journal Letters* 447, pp. L25–L28. DOI: `10.1086/309560`. eprint: `astro-ph/9504041`.

Dwek, E. et al. (1995). "Morphology, near infrared luminosity, and mass of the galactic bulge from Cobe dirbe observations". In: *Astrophys. J.* 445, p. 716. DOI: `10.1086/175734`.

Malhotra, Sangeeta (1995). "The Vertical Distribution and Kinematics of H i and Mass Models of the Galactic Disk". In: *The Astrophysical Journal* 448, p. 138. DOI: `10.1086/175946`. arXiv: `astro-ph/9411088 [astro-ph]`.

Navarro, J. F., C. S. Frenk, and S. D. M. White (1995). "Simulations of X-ray clusters". In: *MNRAS* 275, pp. 720–740. DOI: `10.1093/mnras/275.3.720`. eprint: `astro-ph/9408069`.

Liszt, H. S. and W. B. Burton (1996). "Motions and Deformations of the Inner-Galaxy Neutral Gas Layer". In: *Unsolved Problems of the Milky Way*. Ed. by L. Blitz and P. J. Teuben. Vol. 169. IAU Symposium, p. 297.

Narayan, Ramesh and Matthias Bartelmann (1996). "Lectures on Gravitational Lensing". In: *arXiv e-prints*, astro-ph/9606001, astro–ph/9606001. arXiv: `astro-ph/9606001 [astro-ph]`.

Navarro, J. F., C. S. Frenk, and S. D. M. White (1996). "The Structure of Cold Dark Matter Halos". In: *The Astrophysical Journal* 462, p. 563. DOI: `10.1086/177173`. eprint: `astro-ph/9508025`.

Syer, D. and S. Tremaine (1996). "Made-to-measure N-body systems". In: *MNRAS* 282, pp. 223–233. DOI: `10.1093/mnras/282.1.223`. eprint: `astro-ph/9605061`.

Syer, D. and Simon D. M. White (1996). "Dark halo mergers and the formation of a universal profile". In: *arXiv e-prints*, astro-ph/9611065, astro–ph/9611065. arXiv: `astro-ph/9611065 [astro-ph]`.

Zhao, HongSheng (1996). "A self-consistent dynamical model for the COBE detected galactic bar". In: *Mon. Not. Roy. Astron. Soc.* 283, pp. 149–166. DOI: `10.1093/mnras/283.1.149`. arXiv: `astro-ph/9512064 [astro-ph]`.

Fukushige, T. and J. Makino (1997). “On the Origin of Cusps in Dark Matter Halos”. In: *The Astrophysical Journal Letters* 477, pp. L9–L12. DOI: 10.1086/310516. eprint: astro-ph/9610005.

Honma, M. and Y. Sofue (1997). “Rotation Curve of the Galaxy”. In: *Publ. Astron. Soc. Japan* 49, pp. 453–460. DOI: 10.1093/pasj/49.4.453.

Pont, F. et al. (1997). “Rotation of the outer disc from classical cepheids.” In: *Astron. Astrophys.* 318, pp. 416–428.

Stanek, K. Z. et al. (1997). “Modeling the Galactic Bar Using Red Clump Giants”. In: *The Astrophysical Journal* 477, pp. 163–175. DOI: 10.1086/303702. arXiv: astro-ph/9605162.

Bryan, G. L. and M. L. Norman (1998). “Statistical Properties of X-Ray Clusters: Analytic and Numerical Comparisons”. In: *The Astrophysical Journal* 495, pp. 80–99. DOI: 10.1086/305262. eprint: astro-ph/9710107.

Durand, S., A. Acker, and A. Zijlstra (1998). “The kinematics of 867 galactic planetary nebulae”. In: *Astron. Astrophys. Supp. Series* 132, pp. 13–20. DOI: 10.1051/aas:1998356.

Ferrière, K. (1998). “Global Model of the Interstellar Medium in Our Galaxy with New Constraints on the Hot Gas Component”. In: *Astrophys. J.* 497, p. 759. DOI: 10.1086/305469.

Schmidt, B. P. et al. (1998). “The High-Z Supernova Search: Measuring Cosmic Deceleration and Global Curvature of the Universe Using Type IA Supernovae”. In: *The Astrophysical Journal* 507, pp. 46–63. DOI: 10.1086/306308. eprint: astro-ph/9805200.

Moore, B. et al. (1999). “Cold collapse and the core catastrophe”. In: *MNRAS* 310, pp. 1147–1152. DOI: 10.1046/j.1365-8711.1999.03039.x. eprint: astro-ph/9903164.

Wilkinson, M. I. and N. W. Evans (1999). “The present and future mass of the Milky Way halo”. In: *MNRAS* 310, pp. 645–662. DOI: 10.1046/j.1365-8711.1999.02964.x. arXiv: astro-ph/9906197 [astro-ph].

Bergström, Lars (2000). “Non-baryonic dark matter: observational evidence and detection methods”. In: *Reports on Progress in Physics* 63, pp. 793–841. DOI: 10.1088/0034-4885/63/5/2r3. arXiv: hep-ph/0002126 [hep-ph].

McGaugh, S. S. et al. (2000). “The Baryonic Tully-Fisher Relation”. In: *The Astrophysical Journal Letters* 533, pp. L99–L102. DOI: 10.1086/312628. eprint: astro-ph/0003001.

Navarro, Julio F. and Matthias Steinmetz (2000). “Dark Halo and Disk Galaxy Scaling Laws in Hierarchical Universes”. In: *The Astrophysical Journal* 538, pp. 477–488. DOI: 10.1086/309175. arXiv: astro-ph/0001003 [astro-ph].

Subramanian, Kandaswamy, Renyue Cen, and Jeremiah P. Ostriker (2000). “The Structure of Dark Matter Halos in Hierarchical Clustering Theories”. In: *The Astrophysical Journal* 538, pp. 528–542. DOI: 10.1086/309152. arXiv: astro-ph/9909279 [astro-ph].

van der Marel, R. P. et al. (2000). “The Velocity and Mass Distribution of Clusters of Galaxies from the CNOC1 Cluster Redshift Survey”. In: *Astronomic. J.* 119, pp. 2038–2052. DOI: 10.1086/301351. eprint: astro-ph/9910494.

Bell, E. F. and R. S. de Jong (2001). “Stellar Mass-to-Light Ratios and the Tully-Fisher Relation”. In: *The Astrophysical Journal* 550, pp. 212–229. DOI: 10.1086/319728. eprint: astro-ph/0011493.

Burles, S., K. M. Nollett, and M. S. Turner (2001). “Big Bang Nucleosynthesis Predictions for Precision Cosmology”. In: *The Astrophysical Journal Letters* 552, pp. L1–L5. DOI: 10.1086/320251. eprint: astro-ph/0010171.

de Blok, W. J. G. et al. (2001). "Mass Density Profiles of Low Surface Brightness Galaxies". In: *The Astrophysical Journal Letters* 552, pp. L23–L26. DOI: `10.1086/320262`. eprint: `astro-ph/0103102`.

Ferrière, K. M. (2001). "The interstellar environment of our galaxy". In: *Reviews of Modern Physics* 73, pp. 1031–1066. DOI: `10.1103/RevModPhys.73.1031`. eprint: `astro-ph/0106359`.

Fukushige, Toshiyuki and Junichiro Makino (2001). "Structure of Dark Matter Halos from Hierarchical Clustering". In: *The Astrophysical Journal* 557, pp. 533–545. DOI: `10.1086/321666`. arXiv: `astro-ph/0008104 [astro-ph]`.

Klypin, A. et al. (2001). "Resolving the Structure of Cold Dark Matter Halos". In: *The Astrophysical Journal* 554, pp. 903–915. DOI: `10.1086/321400`. eprint: `astro-ph/0006343`.

Rusin, D. and C.-P. Ma (2001). "Constraints on the Inner Mass Profiles of Lensing Galaxies from Missing Odd Images". In: *The Astrophysical Journal Letters* 549, pp. L33–L37. DOI: `10.1086/319129`. eprint: `astro-ph/0009079`.

Sofue, Y. and V. Rubin (2001). "Rotation Curves of Spiral Galaxies". In: *Annu. Rev. Astron. Astrophys.* 39, pp. 137–174. DOI: `10.1146/annurev.astro.39.1.137`. eprint: `astro-ph/0010594`.

Zheng, Z. et al. (2001). "M Dwarfs from Hubble Space Telescope Star Counts. IV." In: *The Astrophysical Journal* 555, pp. 393–404. DOI: `10.1086/321485`. eprint: `astro-ph/0102442`.

Bissantz, N. and O. Gerhard (2002). "Spiral arms, bar shape and bulge microlensing in the Milky Way". In: *MNRAS* 330, pp. 591–608. DOI: `10.1046/j.1365-8711.2002.05116.x`. eprint: `astro-ph/0110368`.

Kelson, D. D. et al. (2002). "Determination of the Dark Matter Profile of A2199 from Integrated Starlight". In: *The Astrophysical Journal* 576, pp. 720–737. DOI: `10.1086/341891`. eprint: `astro-ph/0205316`.

Klypin, Anatoly, HongSheng Zhao, and Rachel S. Somerville (2002). "ΛCDM-based Models for the Milky Way and M31. I. Dynamical Models". In: *The Astrophysical Journal* 573, pp. 597–613. DOI: `10.1086/340656`. arXiv: `astro-ph/0110390 [astro-ph]`.

Salaris, M. and L. Girardi (2002). "Population effects on the red giant clump absolute magnitude: the K band". In: *MNRAS* 337, pp. 332–340. DOI: `10.1046/j.1365-8711.2002.05917.x`. eprint: `astro-ph/0208057`.

Barnes III, T. G. et al. (2003). "A Bayesian Analysis of the Cepheid Distance Scale". In: *The Astrophysical Journal* 592, pp. 539–554. DOI: `10.1086/375583`. eprint: `astro-ph/0303656`.

Han, C. and A. Gould (2003). "Stellar Contribution to the Galactic Bulge Microlensing Optical Depth". In: *The Astrophysical Journal* 592, pp. 172–175. DOI: `10.1086/375706`. eprint: `astro-ph/0303309`.

Sakamoto, T., M. Chiba, and T. C. Beers (2003). "The mass of the Milky Way: Limits from a newly assembled set of halo objects". In: *Astron. Astrophys.* 397, pp. 899–911. DOI: `10.1051/0004-6361:20021499`. arXiv: `astro-ph/0210508 [astro-ph]`.

Bekenstein, J. D. (2004). "Relativistic gravitation theory for the modified Newtonian dynamics paradigm". In: *Phys. Rev. D* 70.8, 083509, p. 083509. DOI: `10.1103/PhysRevD.70.083509`. eprint: `astro-ph/0403694`.

Buote, D. A. and A. D. Lewis (2004). "The Dark Matter Radial Profile in the Core of the Relaxed Cluster A2589". In: *The Astrophysical Journal* 604, pp. 116–124. DOI: `10.1086/381793`. eprint: `astro-ph/0312109`.

Kazantzidis, S. et al. (2004). “The Effect of Gas Cooling on the Shapes of Dark Matter Halos”. In: *The Astrophysical Journal Letters* 611, pp. L73–L76. DOI: `10.1086/423992`. eprint: `astro-ph/0405189`.

Navarro, J. F. et al. (2004). “The inner structure of ΛCDM haloes - III. Universality and asymptotic slopes”. In: *MNRAS* 349, pp. 1039–1051. DOI: `10.1111/j.1365-2966.2004.07586.x`. eprint: `astro-ph/0311231`.

Bailin, J. et al. (2005). “Internal Alignment of the Halos of Disk Galaxies in Cosmological Hydrodynamic Simulations”. In: *The Astrophysical Journal Letters* 627, pp. L17–L20. DOI: `10.1086/432157`. eprint: `astro-ph/0505523`.

Battaglia, Giuseppina et al. (2005). “The radial velocity dispersion profile of the Galactic halo: constraining the density profile of the dark halo of the Milky Way”. In: *MNRAS* 364, pp. 433–442. DOI: `10.1111/j.1365-2966.2005.09367.x`. arXiv: `astro-ph/0506102 [astro-ph]`.

Dekel, A. et al. (2005). “Lost and found dark matter in elliptical galaxies”. In: *Nature* 437, pp. 707–710. DOI: `10.1038/nature03970`. eprint: `astro-ph/0501622`.

Famaey, B. and J. Binney (2005). “Modified Newtonian dynamics in the Milky Way”. In: *MNRAS* 363, pp. 603–608. DOI: `10.1111/j.1365-2966.2005.09474.x`. eprint: `astro-ph/0506723`.

Popowski, P. et al. (2005). “Microlensing Optical Depth toward the Galactic Bulge Using Clump Giants from the MACHO Survey”. In: *The Astrophysical Journal* 631, pp. 879–905. DOI: `10.1086/432246`. arXiv: `astro-ph/0410319 [astro-ph]`.

Rolke, Wolfgang A., Angel M. López, and Jan Conrad (2005). “Limits and confidence intervals in the presence of nuisance parameters”. In: *Nuclear Instruments and Methods in Physics Research A* 551, pp. 493–503. DOI: `10.1016/j.nima.2005.05.068`. arXiv: `physics/0403059 [physics.data-an]`.

Springel, V. et al. (2005). “Simulations of the formation, evolution and clustering of galaxies and quasars”. In: *Nature* 435, pp. 629–636. DOI: `10.1038/nature03597`. eprint: `astro-ph/0504097`.

Brownstein, J. R. and J. W. Moffat (2006). “Galaxy Rotation Curves without Non-baryonic Dark Matter”. In: *The Astrophysical Journal* 636, pp. 721–741. DOI: `10.1086/498208`. eprint: `astro-ph/0506370`.

Cappellari, M. et al. (2006). “The SAURON project - IV. The mass-to-light ratio, the virial mass estimator and the Fundamental Plane of elliptical and lenticular galaxies”. In: *MNRAS* 366, pp. 1126–1150. DOI: `10.1111/j.1365-2966.2005.09981.x`. eprint: `astro-ph/0505042`.

Clowe, D. et al. (2006). “A Direct Empirical Proof of the Existence of Dark Matter”. In: *The Astrophysical Journal Letters* 648, pp. L109–L113. DOI: `10.1086/508162`. eprint: `astro-ph/0608407`.

Dehnen, W., D. E. McLaughlin, and J. Sachania (2006). “The velocity dispersion and mass profile of the Milky Way”. In: *MNRAS* 369, pp. 1688–1692. DOI: `10.1111/j.1365-2966.2006.10404.x`. eprint: `astro-ph/0603825`.

Gustafsson, M., M. Fairbairn, and J. Sommer-Larsen (2006). “Baryonic pinching of galactic dark matter halos”. In: *Phys. Rev. D* 74.12, 123522, p. 123522. DOI: `10.1103/PhysRevD.74.123522`. eprint: `astro-ph/0608634`.

Hahn, T. (2006). “The CUBA library”. In: *Nucl. Instrum. Meth.* A559, pp. 273–277. DOI: `10.1016/j.nima.2005.11.150`. arXiv: `hep-ph/0509016 [hep-ph]`.

Hamadache, C. et al. (2006). “Galactic Bulge microlensing optical depth from EROS-2”. In: *Astron. Astrophys.* 454, pp. 185–199. DOI: `10.1051/0004-6361:20064893`. arXiv: `astro-ph/0601510 [astro-ph]`.

Luna, A. et al. (2006). “Molecular Gas, Kinematics, and OB Star Formation in the Spiral Arms of the Southern Milky Way”. In: *The Astrophysical Journal* 641, pp. 938–948. DOI: `10.1086/500163`. arXiv: `astro-ph/0512046 [astro-ph]`.

Merritt, D. et al. (2006). “Empirical Models for Dark Matter Halos. I. Nonparametric Construction of Density Profiles and Comparison with Parametric Models”. In: *Astronomic. J.* 132, pp. 2685–2700. DOI: `10.1086/508988`. eprint: `astro-ph/0509417`.

Moffat, J. W. (2006). “Scalar tensor vector gravity theory”. In: *JCAP* 3, 004, p. 004. DOI: `10.1088/1475-7516/2006/03/004`. eprint: `gr-qc/0506021`.

Sumi, T. et al. (2006). “Microlensing Optical Depth toward the Galactic Bulge Using Bright Sources from OGLE-II”. In: *The Astrophysical Journal* 636, pp. 240–260. DOI: `10.1086/497951`. arXiv: `astro-ph/0502363 [astro-ph]`.

Brownstein, J. R. and J. W. Moffat (2007). “The Bullet Cluster 1E0657-558 evidence shows modified gravity in the absence of dark matter”. In: *MNRAS* 382, pp. 29–47. DOI: `10.1111/j.1365-2966.2007.12275.x`. eprint: `astro-ph/0702146`.

de Lorenzi, F. et al. (2007). “NMAGIC: a fast parallel implementation of a χ^2-made-to-measure algorithm for modelling observational data”. In: *MNRAS* 376, pp. 71–88. DOI: `10.1111/j.1365-2966.2007.11434.x`. eprint: `astro-ph/0701582`.

Demers, S. and P. Battinelli (2007). “C stars as kinematic probes of the Milky Way disk from 9 to 15 kpc”. In: *Astron. Astrophys.* 473, pp. 143–148. DOI: `10.1051/0004-6361:20077691`.

Ferrière, K., W. Gillard, and P. Jean (2007). “Spatial distribution of interstellar gas in the innermost 3 kpc of our galaxy”. In: *Astron. Astrophys.* 467, pp. 611–627. DOI: `10.1051/0004-6361:20066992`. eprint: `astro-ph/0702532`.

Gavazzi, R. et al. (2007). “The Sloan Lens ACS Survey. IV. The Mass Density Profile of Early-Type Galaxies out to 100 Effective Radii”. In: *The Astrophysical Journal* 667, pp. 176–190. DOI: `10.1086/519237`. eprint: `astro-ph/0701589`.

McClure-Griffiths, N. M. and John M. Dickey (2007). “Milky Way Kinematics. I. Measurements at the Subcentral Point of the Fourth Quadrant”. In: *The Astrophysical Journal* 671, pp. 427–438. DOI: `10.1086/522297`. arXiv: `0708.0870 [astro-ph]`.

Rattenbury, N. J. et al. (2007). “Proper motion dispersions of red clump giants in the galactic bulge: observations and model comparisons”. In: *MNRAS* 378, pp. 1165–1176. DOI: `10.1111/j.1365-2966.2007.11851.x`. arXiv: `0704.1619`.

Rich, R. Michael et al. (2007). “The Bulge Radial Velocity Assay: Techniques and a Rotation Curve”. In: *The Astrophysical Journal* 658, pp. L29–L32. DOI: `10.1086/513509`. arXiv: `astro-ph/0611403 [astro-ph]`.

Sales, Laura V. et al. (2007). “Satellites of simulated galaxies: survival, merging and their relationto the dark and stellar haloes”. In: *MNRAS* 379, pp. 1464–1474. DOI: `10.1111/j.1365-2966.2007.12024.x`. arXiv: `0704.1770 [astro-ph]`.

Sanders, R. H. and E. Noordermeer (2007). “Confrontation of MOdified Newtonian Dynamics with the rotation curves of early-type disc galaxies”. In: *MNRAS* 379, pp. 702–710. DOI: `10.1111/j.1365-2966.2007.11981.x`. eprint: `astro-ph/0703352`.

Schmidt, R. W. and S. W. Allen (2007). “The dark matter haloes of massive, relaxed galaxy clusters observed with Chandra”. In: *MNRAS* 379, pp. 209–221. DOI: `10.1111/j.1365-2966.2007.11928.x`. eprint: `astro-ph/0610038`.

Smith, Martin C. et al. (2007). “The RAVE survey: constraining the local Galactic escape speed”. In: *MNRAS* 379, pp. 755–772. DOI: `10.1111/j.1365-2966.2007.11964.x`. arXiv: `astro-ph/0611671 [astro-ph]`.

Bolton, Adam S. et al. (2008a). “The Sloan Lens ACS Survey. V. The Full ACS Strong-Lens Sample”. In: *The Astrophysical Journal* 682, pp. 964–984. DOI: `10.1086/589327`. arXiv: `0805.1931 [astro-ph]`.

Bolton, Adam S. et al. (2008b). “The Sloan Lens ACS Survey. VII. Elliptical Galaxy Scaling Laws from Direct Observational Mass Measurements”. In: *The Astrophysical Journal* 684, pp. 248–259. DOI: 10.1086/589989. arXiv: 0805.1932 [astro-ph].

de Blok, W. J. G. et al. (2008). “High-Resolution Rotation Curves and Galaxy Mass Models from THINGS”. In: *Astronomic. J.* 136, pp. 2648–2719. DOI: 10.1088/0004-6256/136/6/2648. arXiv: 0810.2100 [astro-ph].

Feroz, Farhan et al. (2008). “Bayesian selection of sign μ within mSUGRA in global fits including WMAP5 results”. In: *Journal of High Energy Physics* 2008, 064, p. 064. DOI: 10.1088/1126-6708/2008/10/064. arXiv: 0807.4512 [hep-ph].

Frinchaboy, Peter M. and Steven R. Majewski (2008). “Open Clusters as Galactic Disk Tracers. I. Project Motivation, Cluster Membership, and Bulk Three-Dimensional Kinematics”. In: *Astronomic. J.* 136, pp. 118–145. DOI: 10.1088/0004-6256/136/1/118. arXiv: 0804.4630 [astro-ph].

Hayashi, E. and S. D. M. White (2008). “Understanding the halo-mass and galaxy-mass cross-correlation functions”. In: *MNRAS* 388, pp. 2–14. DOI: 10.1111/j.1365-2966.2008.13371.x. arXiv: 0709.3933.

Howard, Christian D. et al. (2008). “The Bulge Radial Velocity Assay (BRAVA). I. Sample Selection and a Rotation Curve”. In: *The Astrophysical Journal* 688, pp. 1060–1077. DOI: 10.1086/592106. arXiv: 0807.3967 [astro-ph].

Jurić, M. et al. (2008). “The Milky Way Tomography with SDSS. I. Stellar Number Density Distribution”. In: *The Astrophysical Journal* 673, pp. 864–914. DOI: 10.1086/523619. eprint: astro-ph/0510520.

Li, Y.-S. and S. D. M. White (2008). “Masses for the Local Group and the Milky Way”. In: *MNRAS* 384, pp. 1459–1468. DOI: 10.1111/j.1365-2966.2007.12748.x. arXiv: 0710.3740.

McGaugh, S. S. (2008). “Milky Way Mass Models and MOND”. In: *The Astrophysical Journal* 683, pp. 137–148. DOI: 10.1086/589148. arXiv: 0804.1314.

Moffat, J. W. and V. T. Toth (2008). “Testing Modified Gravity with Globular Cluster Velocity Dispersions”. In: *The Astrophysical Journal* 680, 1158-1161, pp. 1158–1161. DOI: 10.1086/587926. arXiv: 0708.1935.

Peirani, S., S. Kay, and J. Silk (2008). “Active galactic nuclei and massive galaxy cores”. In: *Astron. Astrophys.* 479, pp. 123–129. DOI: 10.1051/0004-6361:20077956. eprint: astro-ph/0612468.

Randall, Scott W. et al. (2008). “Constraints on the Self-Interaction Cross Section of Dark Matter from Numerical Simulations of the Merging Galaxy Cluster 1E 0657-56”. In: *The Astrophysical Journal* 679, pp. 1173–1180. DOI: 10.1086/587859. arXiv: 0704.0261 [astro-ph].

Xue, X. X. et al. (2008). “The Milky Way’s Circular Velocity Curve to 60 kpc and an Estimate of the Dark Matter Halo Mass from the Kinematics of ˜2400 SDSS Blue Horizontal-Branch Stars”. In: *The Astrophysical Journal* 684, pp. 1143–1158. DOI: 10.1086/589500. arXiv: 0801.1232.

Barnabè, M. et al. (2009). “Two-dimensional kinematics of SLACS lenses - II. Combined lensing and dynamics analysis of early-type galaxies at z = 0.08-0.33”. In: *MNRAS* 399, pp. 21–36. DOI: 10.1111/j.1365-2966.2009.14941.x. arXiv: 0904.3861 [astro-ph.CO].

Brownstein, J. R. (2009). “Modified gravity and the phantom of dark matter”. PhD thesis. University of Waterloo, Canada.

Feroz, F. et al. (2009). “Are BR($\bar{B} \to X_s \gamma$) and $(g-2)_\mu$ consistent within the Constrained MSSM?” In: *arXiv e-prints*. arXiv: 0903.2487 [hep-ph].

Goodenough, Lisa and Dan Hooper (2009). "Possible Evidence For Dark Matter Annihilation In The Inner Milky Way From The Fermi Gamma Ray Space Telescope". In: *arXiv e-prints*, arXiv:0910.2998, arXiv:0910.2998. arXiv: `0910.2998 [hep-ph]`.

Hou, L. G., J. L. Han, and W. B. Shi (2009). "The spiral structure of our Milky Way Galaxy". In: *Astron. Astrophys.* 499, pp. 473–482. DOI: `10.1051/0004-6361/200809692`. arXiv: `0903.0721 [astro-ph.GA]`.

Iocco, F. et al. (2009). "Primordial nucleosynthesis: From precision cosmology to fundamental physics". In: *Phys. Rep.* 472, pp. 1–76. DOI: `10.1016/j.physrep.2009.02.002`. arXiv: `0809.0631`.

Scannapieco, Cecilia et al. (2009). "The formation and survival of discs in a ΛCDM universe". In: *MNRAS* 396, pp. 696–708. DOI: `10.1111/j.1365-2966.2009.14764.x`. arXiv: `0812.0976 [astro-ph]`.

Stadel, J. et al. (2009). "Quantifying the heart of darkness with GHALO - a multibillion particle simulation of a galactic halo". In: *MNRAS* 398, pp. L21–L25. DOI: `10.1111/j.1745-3933.2009.00699.x`. arXiv: `0808.2981`.

Vanhollebeke, E., M. A. T. Groenewegen, and L. Girardi (2009). "Stellar populations in the Galactic bulge". In: *ArXiv e-prints*. arXiv: `0903.0946 [astro-ph.GA]`.

Auger, M. W. et al. (2010). "The Sloan Lens ACS Survey. X. Stellar, Dynamical, and Total Mass Correlations of Massive Early-type Galaxies". In: *The Astrophysical Journal* 724, pp. 511–525. DOI: `10.1088/0004-637X/724/1/511`. arXiv: `1007.2880 [astro-ph.CO]`.

Catena, R. and P. Ullio (2010). "A novel determination of the local dark matter density". In: *JCAP* 8, 004, p. 004. DOI: `10.1088/1475-7516/2010/08/004`. arXiv: `0907.0018`.

de Blok, W. J. G. (2010). "The Core-Cusp Problem". In: *Advances in Astronomy* 2010, 789293, p. 789293. DOI: `10.1155/2010/789293`. arXiv: `0910.3538`.

de Jong, J. T. A. et al. (2010). "Mapping the Stellar Structure of the Milky Way Thick Disk and Halo Using SEGUE Photometry". In: *The Astrophysical Journal* 714, pp. 663–674. DOI: `10.1088/0004-637X/714/1/663`. arXiv: `0911.3900 [astro-ph.GA]`.

Gnedin, Oleg Y. et al. (2010). "The Mass Profile of the Galaxy to 80 kpc". In: *The Astrophysical Journal* 720, pp. L108–L112. DOI: `10.1088/2041-8205/720/1/L108`. arXiv: `1005.2619 [astro-ph.GA]`.

Governato, F. et al. (2010). "Bulgeless dwarf galaxies and dark matter cores from supernova-driven outflows". In: *Nature* 463, pp. 203–206. DOI: `10.1038/nature08640`. arXiv: `0911.2237`.

Kazantzidis, S., M. G. Abadi, and J. F. Navarro (2010). "The Sphericalization of Dark Matter Halos by Galaxy Disks". In: *The Astrophysical Journal Letters* 720, pp. L62–L66. DOI: `10.1088/2041-8205/720/1/L62`. arXiv: `1006.0537`.

McMillan, Paul J. and James J. Binney (2010). "The uncertainty in Galactic parameters". In: *Mon. Not. Roy. Astron. Soc.* 402, p. 934. DOI: `10.1111/j.1365-2966.2009.15932.x`. arXiv: `0907.4685 [astro-ph.GA]`.

McWilliam, A. and M. Zoccali (2010). "Two Red Clumps and the X-shaped Milky Way Bulge". In: *The Astrophysical Journal* 724, pp. 1491–1502. DOI: `10.1088/0004-637X/724/2/1491`. arXiv: `1008.0519`.

Mo, H., F. C. van den Bosch, and S. White (2010). *Galaxy Formation and Evolution.*

Nataf, D. M. et al. (2010). "The Split Red Clump of the Galactic Bulge from OGLE-III". In: *The Astrophysical Journal Letters* 721, pp. L28–L32. DOI: `10.1088/2041-8205/721/1/L28`. arXiv: `1007.5065`.

Navarro, J. F. et al. (2010). "The diversity and similarity of simulated cold dark matter haloes". In: *MNRAS* 402, pp. 21–34. DOI: `10.1111/j.1365-2966.2009.15878.x`. arXiv: `0810.1522`.

Pato, M. et al. (2010). "Systematic uncertainties in the determination of the local dark matter density". In: *Phys. Rev. D* 82.2, 023531, p. 023531. DOI: `10.1103/PhysRevD.82.023531`. arXiv: `1006.1322 [astro-ph.HE]`.

Reid, B. A. et al. (2010). "Cosmological constraints from the clustering of the Sloan Digital Sky Survey DR7 luminous red galaxies". In: *MNRAS* 404, pp. 60–85. DOI: `10.1111/j.1365-2966.2010.16276.x`. arXiv: `0907.1659 [astro-ph.CO]`.

Salucci, P. et al. (2010). "The dark matter density at the Sun's location". In: *Astron. Astrophys.* 523, A83, A83. DOI: `10.1051/0004-6361/201014385`. arXiv: `1003.3101 [astro-ph.GA]`.

Schönrich, Ralph, James Binney, and Walter Dehnen (2010). "Local kinematics and the local standard of rest". In: *MNRAS* 403, pp. 1829–1833. DOI: `10.1111/j.1365-2966.2010.16253.x`. arXiv: `0912.3693 [astro-ph.GA]`.

Sotiriou, T. P. and V. Faraoni (2010). "f(R) theories of gravity". In: *Reviews of Modern Physics* 82, pp. 451–497. DOI: `10.1103/RevModPhys.82.451`. arXiv: `0805.1726 [gr-qc]`.

Suyu, S. H. et al. (2010). "Dissecting the Gravitational lens B1608+656. II. Precision Measurements of the Hubble Constant, Spatial Curvature, and the Dark Energy Equation of State". In: *The Astrophysical Journal* 711, pp. 201–221. DOI: `10.1088/0004-637X/711/1/201`. arXiv: `0910.2773 [astro-ph.CO]`.

Treu, Tommaso (2010). "Strong Lensing by Galaxies". In: *Annual Review of Astronomy and Astrophysics* 48, pp. 87–125. DOI: `10.1146/annurev-astro-081309-130924`. arXiv: `1003.5567 [astro-ph.CO]`.

Watkins, L. L., N. W. Evans, and J. H. An (2010). "The masses of the Milky Way and Andromeda galaxies". In: *MNRAS* 406, pp. 264–278. DOI: `10.1111/j.1365-2966.2010.16708.x`. arXiv: `1002.4565`.

Weber, M. and W. de Boer (2010). "Determination of the local dark matter density in our Galaxy". In: *Astron. Astrophys.* 509, A25, A25. DOI: `10.1051/0004-6361/200913381`. arXiv: `0910.4272 [astro-ph.CO]`.

Binney, James and Scott Tremaine (2011). *Galactic dynamics*. Princeton university press.

Brook, C. B. et al. (2011). "Hierarchical formation of bulgeless galaxies: why outflows have low angular momentum". In: *MNRAS* 415, pp. 1051–1060. DOI: `10.1111/j.1365-2966.2011.18545.x`. arXiv: `1010.1004 [astro-ph.CO]`.

Busha, Michael T. et al. (2011). "Statistics of Satellite Galaxies around Milky-Way-like Hosts". In: *The Astrophysical Journal* 743, 117, p. 117. DOI: `10.1088/0004-637X/743/2/117`. arXiv: `1011.6373 [astro-ph.CO]`.

Calchi Novati, S. and L. Mancini (2011). "Microlensing towards the Large Magellanic Cloud: self-lensing for OGLE-II and OGLE-III". In: *MNRAS* 416, pp. 1292–1301. DOI: `10.1111/j.1365-2966.2011.19123.x`. arXiv: `1105.4615 [astro-ph.GA]`.

Deffayet, C., G. Esposito-Farèse, and R. P. Woodard (2011). "Nonlocal metric formulations of modified Newtonian dynamics with sufficient lensing". In: *Phys. Rev. D* 84.12, 124054, p. 124054. DOI: `10.1103/PhysRevD.84.124054`. arXiv: `1106.4984 [gr-qc]`.

Dodelson, S. (2011). "The Real Problem with MOND". In: *International Journal of Modern Physics D* 20, pp. 2749–2753. DOI: `10.1142/S0218271811020561`. arXiv: `1112.1320 [astro-ph.CO]`.

Hooper, Dan and Lisa Goodenough (2011). "Dark matter annihilation in the Galactic Center as seen by the Fermi Gamma Ray Space Telescope". In: *Physics Letters B*

697, pp. 412–428. DOI: `10.1016/j.physletb.2011.02.029`. arXiv: `1010.2752 [hep-ph]`.

Iocco, Fabio et al. (2011). “Dark Matter distribution in the Milky Way: microlensing and dynamical constraints”. In: *Journal of Cosmology and Astro-Particle Physics* 2011, 029, p. 029. DOI: `10.1088/1475-7516/2011/11/029`. arXiv: `1107.5810 [astro-ph.GA]`.

Klypin, A. A., S. Trujillo-Gomez, and J. Primack (2011). “Dark Matter Halos in the Standard Cosmological Model: Results from the Bolshoi Simulation”. In: *The Astrophysical Journal* 740, 102, p. 102. DOI: `10.1088/0004-637X/740/2/102`. arXiv: `1002.3660`.

McMillan, P. J. (2011). “Mass models of the Milky Way”. In: *MNRAS* 414, pp. 2446–2457. DOI: `10.1111/j.1365-2966.2011.18564.x`. arXiv: `1102.4340`.

Muñoz-Cuartas, J. C. et al. (2011). “The redshift evolution of Λ cold dark matter halo parameters: concentration, spin and shape”. In: *MNRAS* 411, pp. 584–594. DOI: `10.1111/j.1365-2966.2010.17704.x`. arXiv: `1007.0438`.

Stepanishchev, A. S. and V. V. Bobylev (2011). “Galactic rotation curve from the space velocities of selected masers”. In: *Astronomy Letters* 37, pp. 254–266. DOI: `10.1134/S1063773711030054`.

Trotta, R. et al. (2011). “Constraints on Cosmic-ray Propagation Models from A Global Bayesian Analysis”. In: *The Astrophysical Journal* 729, 106, p. 106. DOI: `10.1088/0004-637X/729/2/106`. arXiv: `1011.0037 [astro-ph.HE]`.

Vera-Ciro, C. A. et al. (2011). “The shape of dark matter haloes in the Aquarius simulations: evolution and memory”. In: *MNRAS* 416, pp. 1377–1391. DOI: `10.1111/j.1365-2966.2011.19134.x`. arXiv: `1104.1566`.

Ackermann, M. et al. (2012). “Fermi-LAT Observations of the Diffuse γ-Ray Emission: Implications for Cosmic Rays and the Interstellar Medium”. In: *The Astrophysical Journal* 750, 3, p. 3. DOI: `10.1088/0004-637X/750/1/3`. arXiv: `1202.4039 [astro-ph.HE]`.

Bovy, J. et al. (2012). “The Milky Way’s Circular-velocity Curve between 4 and 14 kpc from APOGEE data”. In: *The Astrophysical Journal* 759, 131, p. 131. DOI: `10.1088/0004-637X/759/2/131`. arXiv: `1209.0759 [astro-ph.GA]`.

Deason, A. J. et al. (2012). “Broken degeneracies: the rotation curve and velocity anisotropy of the Milky Way halo”. In: *MNRAS* 424, pp. L44–L48. DOI: `10.1111/j.1745-3933.2012.01283.x`. arXiv: `1204.5189 [astro-ph.GA]`.

Gao, L. et al. (2012). “The Phoenix Project: the dark side of rich Galaxy clusters”. In: *MNRAS* 425, pp. 2169–2186. DOI: `10.1111/j.1365-2966.2012.21564.x`. arXiv: `1201.1940 [astro-ph.CO]`.

Honma, Mareki et al. (2012). “Fundamental Parameters of the Milky Way Galaxy Based on VLBI astrometry”. In: *Publications of the Astronomical Society of Japan* 64, 136, p. 136. DOI: `10.1093/pasj/64.6.136`. arXiv: `1211.3843 [astro-ph.GA]`.

Kafle, P. R. et al. (2012). “Kinematics of the Stellar Halo and the Mass Distribution of the Milky Way Using Blue Horizontal Branch Stars”. In: *The Astrophysical Journal* 761, 98, p. 98. DOI: `10.1088/0004-637X/761/2/98`. arXiv: `1210.7527 [astro-ph.GA]`.

Kunder, Andrea et al. (2012). “The Bulge Radial Velocity Assay (BRAVA). II. Complete Sample and Data Release”. In: *Astronomic. J.* 143, 57, p. 57. DOI: `10.1088/0004-6256/143/3/57`. arXiv: `1112.1955 [astro-ph.SR]`.

Martizzi, D., R. Teyssier, and B. Moore (2012). “The formation of the brightest cluster galaxies in cosmological simulations: the case for active galactic nucleus feedback”. In: *MNRAS* 420, pp. 2859–2873. DOI: `10.1111/j.1365-2966.2011.19950.x`. arXiv: `1106.5371 [astro-ph.CO]`.

Mazziotta, M. N. et al. (2012). "A model-independent analysis of the Fermi Large Area Telescope gamma-ray data from the Milky Way dwarf galaxies and halo to constrain dark matter scenarios". In: *Astroparticle Physics* 37, pp. 26–39. DOI: 10.1016/j.astropartphys.2012.07.005. arXiv: 1203.6731 [astro-ph.IM].

Pontzen, A. and F. Governato (2012). "How supernova feedback turns dark matter cusps into cores". In: *MNRAS* 421, pp. 3464–3471. DOI: 10.1111/j.1365-2966.2012.20571.x. arXiv: 1106.0499.

Robin, A. C. et al. (2012). "Stellar populations in the Milky Way bulge region: towards solving the Galactic bulge and bar shapes using 2MASS data". In: *Astron. Astrophys.* 538, A106, A106. DOI: 10.1051/0004-6361/201116512. arXiv: 1111.5744.

Schneider, M. D., C. S. Frenk, and S. Cole (2012). "The shapes and alignments of dark matter halos". In: *JCAP* 5, 030, p. 030. DOI: 10.1088/1475-7516/2012/05/030. arXiv: 1111.5616.

Astropy Collaboration et al. (2013). "Astropy: A community Python package for astronomy". In: *Astron. Astrophys.* 558, A33, A33. DOI: 10.1051/0004-6361/201322068. arXiv: 1307.6212 [astro-ph.IM].

Battinelli, P. et al. (2013). "Extension of the C Star Rotation Curve of the Milky Way to 24 kpc". In: *Astrophysics* 56, pp. 68–75. DOI: 10.1007/s10511-013-9268-7. arXiv: 1212.1116 [astro-ph.SR].

Bobylev, V. V. and A. T. Bajkova (2013). "Galactic rotation curve and spiral density wave parameters from 73 masers". In: *Astronomy Letters* 39, pp. 809–818. DOI: 10.1134/S1063773713120037. arXiv: 1310.7189 [astro-ph.GA].

Bovy, J. and H.-W. Rix (2013). "A Direct Dynamical Measurement of the Milky Way's Disk Surface Density Profile, Disk Scale Length, and Dark Matter Profile at 4 kpc $\leq$ R $\leq$ 9 kpc". In: *The Astrophysical Journal* 779, 115, p. 115. DOI: 10.1088/0004-637X/779/2/115. arXiv: 1309.0809 [astro-ph.GA].

Boylan-Kolchin, Michael et al. (2013). "The Space Motion of Leo I: The Mass of the Milky Way's Dark Matter Halo". In: *The Astrophysical Journal* 768, 140, p. 140. DOI: 10.1088/0004-637X/768/2/140. arXiv: 1210.6046 [astro-ph.CO].

Bozorgnia, Nassim, Riccardo Catena, and Thomas Schwetz (2013). "Anisotropic dark matter distribution functions and impact on WIMP direct detection". In: *Journal of Cosmology and Astro-Particle Physics* 2013, 050, p. 050. DOI: 10.1088/1475-7516/2013/12/050. arXiv: 1310.0468 [astro-ph.CO].

Bryan, S. E. et al. (2013). "The impact of baryons on the spins and shapes of dark matter haloes". In: *MNRAS* 429, pp. 3316–3329. DOI: 10.1093/mnras/sts587. arXiv: 1207.4555.

Deason, A. J. et al. (2013). "The Velocity Anisotropy of Distant Milky Way Halo Stars from Hubble Space Telescope Proper Motions". In: *The Astrophysical Journal* 766, 24, p. 24. DOI: 10.1088/0004-637X/766/1/24. arXiv: 1302.5111 [astro-ph.GA].

Dékány, I. et al. (2013). "VVV Survey Near-infrared Photometry of Known Bulge RR Lyrae Stars: The Distance to the Galactic Center and Absence of a Barred Distribution of the Metal-poor Population". In: *The Astrophysical Journal Letters* 776, L19, p. L19. DOI: 10.1088/2041-8205/776/2/L19. arXiv: 1309.5933.

Foreman-Mackey, D. et al. (2013). "emcee: The MCMC Hammer". In: *PASP* 125, p. 306. DOI: 10.1086/670067. arXiv: 1202.3665 [astro-ph.IM].

González, R. E., A. V. Kravtsov, and N. Y. Gnedin (2013). "Satellites in Milky-Way-like Hosts: Environment Dependence and Close Pairs". In: *The Astrophysical Journal* 770, 96, p. 96. DOI: 10.1088/0004-637X/770/2/96. arXiv: 1301.2605.

Malkin, Z. M. (2013). "Analysis of determinations of the distance between the sun and the galactic center". In: *Astronomy Reports* 57, pp. 128–133. DOI: 10.1134/S1063772913020078. arXiv: 1301.7011 [astro-ph.GA].

Moffat, J. and V. Toth (2013). “Cosmological Observations in a Modified Theory of Gravity (MOG)”. In: *Galaxies* 1, pp. 65–82. DOI: `10.3390/galaxies1010065`.

Moffat, J. W. and S. Rahvar (2013). “The MOG weak field approximation and observational test of galaxy rotation curves”. In: *MNRAS* 436, pp. 1439–1451. DOI: `10.1093/mnras/stt1670`. arXiv: `1306.6383`.

Ness, M. et al. (2013). “ARGOS - III. Stellar populations in the Galactic bulge of the Milky Way”. In: *MNRAS* 430, pp. 836–857. DOI: `10.1093/mnras/sts629`. arXiv: `1212.1540`.

Nesti, Fabrizio and Paolo Salucci (2013). “The Dark Matter halo of the Milky Way, AD 2013”. In: *Journal of Cosmology and Astro-Particle Physics* 2013, 016, p. 016. DOI: `10.1088/1475-7516/2013/07/016`. arXiv: `1304.5127 [astro-ph.GA]`.

Newman, A. B. et al. (2013a). “The Density Profiles of Massive, Relaxed Galaxy Clusters. I. The Total Density Over Three Decades in Radius”. In: *The Astrophysical Journal* 765, 24, p. 24. DOI: `10.1088/0004-637X/765/1/24`. arXiv: `1209.1391`.

Newman, A. B. et al. (2013b). “The Density Profiles of Massive, Relaxed Galaxy Clusters. II. Separating Luminous and Dark Matter in Cluster Cores”. In: *The Astrophysical Journal* 765, 25, p. 25. DOI: `10.1088/0004-637X/765/1/25`. arXiv: `1209.1392`.

Rich, R. M. (2013). “The Galactic Bulge”. In: *Planets, Stars and Stellar Systems. Volume 5: Galactic Structure and Stellar Populations*. Ed. by T. D. Oswalt and G. Gilmore, p. 271. DOI: `10.1007/978-94-007-5612-0_6`.

Silk, J., A. Di Cintio, and I. Dvorkin (2013). “Galaxy formation”. In: *ArXiv e-prints*. arXiv: `1312.0107 [astro-ph.CO]`.

Ting, Y.-S. et al. (2013). “Constraining the Galactic potential via action-based distribution functions for mono-abundance stellar populations”. In: *MNRAS* 434, pp. 652–660. DOI: `10.1093/mnras/stt1053`. arXiv: `1212.0006`.

Wegg, Christopher and Ortwin Gerhard (2013). “Mapping the three-dimensional density of the Galactic bulge with VVV red clump stars”. In: *MNRAS* 435, pp. 1874–1887. DOI: `10.1093/mnras/stt1376`. arXiv: `1308.0593 [astro-ph.GA]`.

Xu, Y. et al. (2013). “On the Nature of the Local Spiral Arm of the Milky Way”. In: *The Astrophysical Journal* 769, 15, p. 15. DOI: `10.1088/0004-637X/769/1/15`. arXiv: `1304.0526 [astro-ph.GA]`.

Di Cintio, A. et al. (2014b). “The dependence of dark matter profiles on the stellar-to-halo mass ratio: a prediction for cusps versus cores”. In: *MNRAS* 437, pp. 415–423. DOI: `10.1093/mnras/stt1891`. arXiv: `1306.0898`.

Barber, C. et al. (2014). “The orbital ellipticity of satellite galaxies and the mass of the Milky Way”. In: *MNRAS* 437, pp. 959–967. DOI: `10.1093/mnras/stt1959`. arXiv: `1310.0466`.

Bernal, N. et al. (2014). “Systematic uncertainties from halo asphericity in dark matter searches”. In: *JCAP* 9, 004, p. 004. DOI: `10.1088/1475-7516/2014/09/004`. arXiv: `1405.6240`.

Bhattacharjee, P., S. Chaudhury, and S. Kundu (2014). “Rotation Curve of the Milky Way out to ˜200 kpc”. In: *The Astrophysical Journal* 785, 63, p. 63. DOI: `10.1088/0004-637X/785/1/63`. arXiv: `1310.2659`.

Cautun, Marius et al. (2014). “Milky Way mass constraints from the Galactic satellite gap”. In: *MNRAS* 445, pp. 2049–2060. DOI: `10.1093/mnras/stu1849`. arXiv: `1405.7697 [astro-ph.CO]`.

Di Cintio, Arianna et al. (2014a). “A mass-dependent density profile for dark matter haloes including the influence of galaxy formation”. In: *MNRAS* 441, pp. 2986–2995. DOI: `10.1093/mnras/stu729`. arXiv: `1404.5959 [astro-ph.CO]`.

Gibbons, S. L. J., V. Belokurov, and N. W. Evans (2014). "'Skinny Milky Way please', says Sagittarius". In: *MNRAS* 445, pp. 3788–3802. DOI: `10.1093/mnras/stu1986`. arXiv: `1406.2243 [astro-ph.GA]`.

Kafle, P. R. et al. (2014). "On the Shoulders of Giants: Properties of the Stellar Halo and the Milky Way Mass Distribution". In: *The Astrophysical Journal* 794, 59, p. 59. DOI: `10.1088/0004-637X/794/1/59`. arXiv: `1408.1787`.

Milgrom, M. (2014). "Gravitational waves in bimetric MOND". In: *Phys. Rev. D* 89.2, 024027, p. 024027. DOI: `10.1103/PhysRevD.89.024027`. arXiv: `1308.5388 [gr-qc]`.

Moffat, J. W. and S. Rahvar (2014). "The MOG weak field approximation - II. Observational test of Chandra X-ray clusters". In: *MNRAS* 441, pp. 3724–3732. DOI: `10.1093/mnras/stu855`. arXiv: `1309.5077`.

Peñarrubia, Jorge et al. (2014). "A dynamical model of the local cosmic expansion". In: *MNRAS* 443, pp. 2204–2222. DOI: `10.1093/mnras/stu879`. arXiv: `1405.0306 [astro-ph.GA]`.

Petrović, Jovana, Pasquale Dario Serpico, and Gabrijela Zaharijaš (2014). "Galactic Center gamma-ray "excess" from an active past of the Galactic Centre?" In: *Journal of Cosmology and Astro-Particle Physics* 2014, 052, p. 052. DOI: `10.1088/1475-7516/2014/10/052`. arXiv: `1405.7928 [astro-ph.HE]`.

Piffl, T. et al. (2014). "The RAVE survey: the Galactic escape speed and the mass of the Milky Way". In: *Astron. Astrophys.* 562, A91, A91. DOI: `10.1051/0004-6361/201322531`. arXiv: `1309.4293 [astro-ph.GA]`.

Read, J. I. (2014). "The local dark matter density". In: *Journal of Physics G Nuclear Physics* 41, 063101, p. 063101. DOI: `10.1088/0954-3899/41/6/063101`. arXiv: `1404.1938 [astro-ph.GA]`.

Reid, M. J. et al. (2014). "Trigonometric Parallaxes of High Mass Star Forming Regions: The Structure and Kinematics of the Milky Way". In: *The Astrophysical Journal* 783, 130, p. 130. DOI: `10.1088/0004-637X/783/2/130`. arXiv: `1401.5377 [astro-ph.GA]`.

Vera-Ciro, C. A. et al. (2014). "The shape of dark matter subhaloes in the Aquarius simulations". In: *MNRAS* 439, pp. 2863–2872. DOI: `10.1093/mnras/stu153`. arXiv: `1402.0903`.

Vogelsberger, M. et al. (2014). "Dwarf galaxies in CDM and SIDM with baryons: observational probes of the nature of dark matter". In: *MNRAS* 444, pp. 3684–3698. DOI: `10.1093/mnras/stu1713`. arXiv: `1405.5216`.

Ackermann, M. et al. (2015). "Searching for Dark Matter Annihilation from Milky Way Dwarf Spheroidal Galaxies with Six Years of Fermi Large Area Telescope Data". In: *Phys. Rev. Lett.* 115, 231301, p. 231301. DOI: `10.1103/PhysRevLett.115.231301`. arXiv: `1503.02641 [astro-ph.HE]`.

Bonnivard, V. et al. (2015a). "Dark matter annihilation and decay in dwarf spheroidal galaxies: the classical and ultrafaint dSphs". In: *MNRAS* 453, pp. 849–867. DOI: `10.1093/mnras/stv1601`. arXiv: `1504.02048 [astro-ph.HE]`.

Bonnivard, V. et al. (2015b). "Dark Matter Annihilation and Decay Profiles for the Reticulum II Dwarf Spheroidal Galaxy". In: *The Astrophysical Journal Letters* 808, L36, p. L36. DOI: `10.1088/2041-8205/808/2/L36`. arXiv: `1504.03309 [astro-ph.HE]`.

Büdenbender, Alex, Glenn van de Ven, and Laura L. Watkins (2015). "The tilt of the velocity ellipsoid in the Milky Way disc". In: *MNRAS* 452, pp. 956–968. DOI: `10.1093/mnras/stv1314`. arXiv: `1407.4808 [astro-ph.GA]`.

Calamida, A. et al. (2015). "New Insights on the Galactic Bulge Initial Mass Function". In: *The Astrophysical Journal* 810, 8, p. 8. DOI: `10.1088/0004-637X/810/1/8`. arXiv: `1505.07128 [astro-ph.SR]`.

Calore, Francesca, Ilias Cholis, and Christoph Weniger (2015). "Background model systematics for the Fermi GeV excess". In: *Journal of Cosmology and Astro-Particle Physics* 2015, 038, p. 038. DOI: `10.1088/1475-7516/2015/03/038`. arXiv: `1409.0042 [astro-ph.CO]`.

Eadie, Gwendolyn M., William E. Harris, and Lawrence M. Widrow (2015). "Estimating the Galactic Mass Profile in the Presence of Incomplete Data". In: *The Astrophysical Journal* 806, 54, p. 54. DOI: `10.1088/0004-637X/806/1/54`. arXiv: `1503.07176 [astro-ph.GA]`.

Iocco, F., M. Pato, and G. Bertone (2015a). "Evidence for dark matter in the inner Milky Way". In: *Nature Physics* 11, pp. 245–248. DOI: `10.1038/nphys3237`. arXiv: `1502.03821`.

– (2015b). "Testing modified Newtonian dynamics in the Milky Way". In: *Phys. Rev. D* 92.8, 084046, p. 084046. DOI: `10.1103/PhysRevD.92.084046`. arXiv: `1505.05181`.

Küpper, Andreas H. W. et al. (2015). "Globular Cluster Streams as Galactic High-Precision Scales—the Poster Child Palomar 5". In: *The Astrophysical Journal* 803, 80, p. 80. DOI: `10.1088/0004-637X/803/2/80`. arXiv: `1502.02658 [astro-ph.GA]`.

Lee, Y.-W., S.-J. Joo, and C. Chung (2015). "The Milky Way without X: an alternative interpretation of the double red clump in the Galactic bulge". In: *MNRAS* 453, pp. 3906–3911. DOI: `10.1093/mnras/stv1980`. arXiv: `1508.05942`.

Moffat, J. W. and V. T. Toth (2015). "Rotational velocity curves in the Milky Way as a test of modified gravity". In: *Phys. Rev. D* 91.4, 043004, p. 043004. DOI: `10.1103/PhysRevD.91.043004`. arXiv: `1411.6701`.

Oh, S.-H. et al. (2015). "High-resolution Mass Models of Dwarf Galaxies from LITTLE THINGS". In: *Astronomic. J.* 149, 180, p. 180. DOI: `10.1088/0004-6256/149/6/180`. arXiv: `1502.01281`.

Pato, Miguel, Fabio Iocco, and Gianfranco Bertone (2015). "Dynamical constraints on the dark matter distribution in the Milky Way". In: *Journal of Cosmology and Astro-Particle Physics* 2015, 001, p. 001. DOI: `10.1088/1475-7516/2015/12/001`. arXiv: `1504.06324 [astro-ph.GA]`.

Petrović, Jovana, Pasquale D. Serpico, and Gabrijela Zaharijas (2015). "Millisecond pulsars and the Galactic Center gamma-ray excess: the importance of luminosity function and secondary emission". In: *Journal of Cosmology and Astro-Particle Physics* 2015, 023, p. 023. DOI: `10.1088/1475-7516/2015/02/023`. arXiv: `1411.2980 [astro-ph.HE]`.

Pietrukowicz, P. et al. (2015). "Deciphering the 3D Structure of the Old Galactic Bulge from the OGLE RR Lyrae Stars". In: *The Astrophysical Journal* 811, 113, p. 113. DOI: `10.1088/0004-637X/811/2/113`. arXiv: `1412.4121`.

Portail, M. et al. (2015). "Made-to-measure models of the Galactic box/peanut bulge: stellar and total mass in the bulge region". In: *MNRAS* 448, pp. 713–731. DOI: `10.1093/mnras/stv058`. arXiv: `1502.00633 [astro-ph.GA]`.

Schaye, J. et al. (2015). "The EAGLE project: simulating the evolution and assembly of galaxies and their environments". In: *MNRAS* 446, pp. 521–554. DOI: `10.1093/mnras/stu2058`. arXiv: `1407.7040`.

Wang, W. et al. (2015). "Estimating the dark matter halo mass of our Milky Way using dynamical tracers". In: *MNRAS* 453, pp. 377–400. DOI: `10.1093/mnras/stv1647`. arXiv: `1502.03477`.

Wegg, C., O. Gerhard, and M. Portail (2015). "The structure of the Milky Way's bar outside the bulge". In: *MNRAS* 450, pp. 4050–4069. DOI: `10.1093/mnras/stv745`. arXiv: `1504.01401`.

Abazajian, Kevork N. and Ryan E. Keeley (2016). "Bright gamma-ray Galactic Center excess and dark dwarfs: Strong tension for dark matter annihilation despite Milky

Way halo profile and diffuse emission uncertainties". In: *Phys. Rev. D* 93, 083514, p. 083514. DOI: `10.1103/PhysRevD.93.083514`. arXiv: `1510.06424 [hep-ph]`.

Ajello, M. et al. (2016). "Fermi-LAT Observations of High-Energy Gamma-Ray Emission toward the Galactic Center". In: *The Astrophysical Journal* 819, 44, p. 44. DOI: `10.3847/0004-637X/819/1/44`. arXiv: `1511.02938 [astro-ph.HE]`.

Bland-Hawthorn, J. and O. Gerhard (2016). "The Galaxy in Context: Structural, Kinematic, and Integrated Properties". In: *Annu. Rev. Astron. Astrophys.* 54, pp. 529–596. DOI: `10.1146/annurev-astro-081915-023441`. arXiv: `1602.07702`.

Cuoco, Alessandro et al. (2016). "A global fit of the γ-ray galactic center excess within the scalar singlet Higgs portal model". In: *Journal of Cosmology and Astro-Particle Physics* 2016, 050, p. 050. DOI: `10.1088/1475-7516/2016/06/050`. arXiv: `1603.08228 [hep-ph]`.

Daylan, Tansu et al. (2016). "The characterization of the gamma-ray signal from the central Milky Way: A case for annihilating dark matter". In: *Physics of the Dark Universe* 12, pp. 1–23. DOI: `10.1016/j.dark.2015.12.005`. arXiv: `1402.6703 [astro-ph.HE]`.

Gonzalez, O. A. and D. Gadotti (2016). "The Milky Way Bulge: Observed Properties and a Comparison to External Galaxies". In: *Galactic Bulges*. Ed. by E. Laurikainen, R. Peletier, and D. Gadotti. Vol. 418. Astrophysics and Space Science Library, p. 199. DOI: `10.1007/978-3-319-19378-6_9`. arXiv: `1503.07252`.

Huang, Y. et al. (2016). "The Milky Way's rotation curve out to 100 kpc and its constraint on the Galactic mass distribution". In: *MNRS* 463, pp. 2623–2639. DOI: `10.1093/mnras/stw2096`. arXiv: `1604.01216`.

Israel, N. S and J. W Moffat (2016). "The Train Wreck Cluster Abell 520 and the Bullet Cluster 1E0657-558 in a Generalized Theory of Gravitation". In: *ArXiv e-prints*. arXiv: `1606.09128`.

López-Corredoira, M. (2016). "A case against an X-shaped structure in the Milky Way young bulge". In: *Astron. Astrophys.* 593, A66, A66. DOI: `10.1051/0004-6361/201527074`. arXiv: `1606.09627`.

McGaugh, S. S., F. Lelli, and J. M. Schombert (2016). "Radial Acceleration Relation in Rotationally Supported Galaxies". In: *Physical Review Letters* 117.20, 201101, p. 201101. DOI: `10.1103/PhysRevLett.117.201101`. arXiv: `1609.05917`.

Ness, M. and D. Lang (2016). "The X-shaped Bulge of the Milky Way Revealed by WISE". In: *Astronomic. J.* 152, 14, p. 14. DOI: `10.3847/0004-6256/152/1/14`. arXiv: `1603.00026`.

Planck Collaboration et al. (2016a). "Planck 2015 results. I. Overview of products and scientific results". In: *Astron. Astrophys.* 594, A1, A1. DOI: `10.1051/0004-6361/201527101`. arXiv: `1502.01582 [astro-ph.CO]`.

Planck Collaboration et al. (2016b). "Planck 2015 results. XIII. Cosmological parameters". In: *Astron. Astrophys.* 594, A13, A13. DOI: `10.1051/0004-6361/201525830`. arXiv: `1502.01589 [astro-ph.CO]`.

Shen, J. and Z.-Y. Li (2016). "Theoretical Models of the Galactic Bulge". In: *Galactic Bulges*. Ed. by E. Laurikainen, R. Peletier, and D. Gadotti. Vol. 418. Astrophysics and Space Science Library, p. 233. DOI: `10.1007/978-3-319-19378-6_10`. arXiv: `1504.05136`.

Silverwood, H. et al. (2016). "A non-parametric method for measuring the local dark matter density". In: *MNRAS* 459, pp. 4191–4208. DOI: `10.1093/mnras/stw917`. arXiv: `1507.08581 [astro-ph.GA]`.

Tollet, E. et al. (2016). "NIHAO - IV: core creation and destruction in dark matter density profiles across cosmic time". In: *MNRAS* 456, pp. 3542–3552. DOI: `10.1093/mnras/stv2856`. arXiv: `1507.03590`.

Xia, Qiran et al. (2016). “Determining the local dark matter density with LAMOST data”. In: *MNRAS* 458, pp. 3839–3850. DOI: `10.1093/mnras/stw565`. arXiv: `1510.06810 [astro-ph.GA]`.

Albert, A. et al. (2017). “Searching for Dark Matter Annihilation in Recently Discovered Milky Way Satellites with Fermi-Lat”. In: *The Astrophysical Journal* 834, 110, p. 110. DOI: `10.3847/1538-4357/834/2/110`. arXiv: `1611.03184 [astro-ph.HE]`.

Aprile, E. et al. (2017). “The XENON1T dark matter experiment”. In: *European Physical Journal C* 77, 881, p. 881. DOI: `10.1140/epjc/s10052-017-5326-3`. arXiv: `1708.07051 [astro-ph.IM]`.

Banik, Nilanjan, Lawrence M. Widrow, and Scott Dodelson (2017). “Galactoseismology and the local density of dark matter”. In: *MNRAS* 464, pp. 3775–3783. DOI: `10.1093/mnras/stw2603`. arXiv: `1608.03338 [astro-ph.GA]`.

Benito, Maria et al. (2017). “Particle Dark Matter constraints: the effect of Galactic uncertainties”. In: *Journal of Cosmology and Astro-Particle Physics* 2017, 007, p. 007. DOI: `10.1088/1475-7516/2017/02/007`. arXiv: `1612.02010 [hep-ph]`.

Bensby, T. et al. (2017). “Chemical evolution of the Galactic bulge as traced by microlensed dwarf and subgiant stars. VI. Age and abundance structure of the stellar populations in the central sub-kpc of the Milky Way”. In: *Astron. Astrophys.* 605, A89, A89. DOI: `10.1051/0004-6361/201730560`. arXiv: `1702.02971 [astro-ph.GA]`.

Bullock, J. S. and M. Boylan-Kolchin (2017). “Small-Scale Challenges to the ΛCDM Paradigm”. In: *Annu. Rev. Astron. Astrophys.* 55, pp. 343–387. DOI: `10.1146/annurev-astro-091916-055313`. arXiv: `1707.04256`.

Chan, Man Ho and Chung Hei Leung (2017). “Ruling out dark matter interpretation of the galactic GeV excess by gamma-ray data of galaxy clusters”. In: *Scientific Reports* 7, 14895, p. 14895. DOI: `10.1038/s41598-017-14950-4`. arXiv: `1710.08123 [astro-ph.HE]`.

Choi, E. et al. (2017). “Physics of Galactic Metals: Evolutionary Effects due to Production, Distribution, Feedback, and Interaction with Black Holes”. In: *The Astrophysical Journal* 844, 31, p. 31. DOI: `10.3847/1538-4357/aa7849`. arXiv: `1610.09389`.

Hooper, Dan (2017). “The density of dark matter in the Galactic bulge and implications for indirect detection”. In: *Physics of the Dark Universe* 15, pp. 53–56. DOI: `10.1016/j.dark.2016.11.005`. arXiv: `1608.00003 [astro-ph.HE]`.

Iocco, Fabio and Maria Benito (2017). “An estimate of the DM profile in the Galactic bulge region”. In: *Physics of the Dark Universe* 15, pp. 90–95. DOI: `10.1016/j.dark.2016.12.004`. arXiv: `1611.09861 [astro-ph.GA]`.

Joo, S.-J., Y.-W. Lee, and C. Chung (2017). “New Insight on the Origin of the Double Red Clump in the Milky Way Bulge”. In: *The Astrophysical Journal* 840, 98, p. 98. DOI: `10.3847/1538-4357/aa6d4f`. arXiv: `1609.01294`.

Lelli, F. et al. (2017a). “One Law to Rule Them All: The Radial Acceleration Relation of Galaxies”. In: *The Astrophysical Journal* 836, 152, p. 152. DOI: `10.3847/1538-4357/836/2/152`. arXiv: `1610.08981`.

– (2017b). “One Law to Rule Them All: The Radial Acceleration Relation of Galaxies”. In: *The Astrophysical Journal* 836, 152, p. 152. DOI: `10.3847/1538-4357/836/2/152`. arXiv: `1610.08981`.

López-Corredoira, M. (2017). “Absence of an X-shaped Structure in the Milky Way Bulge Using Mira Variable Stars”. In: *The Astrophysical Journal* 836, 218, p. 218. DOI: `10.3847/1538-4357/836/2/218`. arXiv: `1702.02539`.

Ludlow, A. D. et al. (2017). “Mass-Discrepancy Acceleration Relation: A Natural Outcome of Galaxy Formation in Cold Dark Matter Halos”. In: *Physical Review*

Letters 118.16, 161103, p. 161103. DOI: 10.1103/PhysRevLett.118.161103. arXiv: 1610.07663.

Macciò, A. V. et al. (2017). "The edge of galaxy formation - I. Formation and evolution of MW-satellite analogues before accretion". In: *MNRAS* 472, pp. 2356–2366. DOI: 10.1093/mnras/stx2048. arXiv: 1707.01106.

McMillan, P. J. (2017). "The mass distribution and gravitational potential of the Milky Way". In: *MNRAS* 465, pp. 76–94. DOI: 10.1093/mnras/stw2759. arXiv: 1608.00971.

Moffat, J. W. and M. H. Zhoolideh Haghighi (2017). "Modified gravity (MOG) and the Abell 1689 cluster acceleration data". In: *European Physical Journal Plus* 132, p. 417. DOI: 10.1140/epjp/i2017-11684-4.

Pato, M. and F. Iocco (2017). "galkin: A new compilation of Milky Way rotation curve data". In: *SoftwareX* 6, pp. 54–62. DOI: 10.1016/j.softx.2016.12.006. arXiv: 1703.00020.

Portail, M. et al. (2017). "Dynamical modelling of the galactic bulge and bar: the Milky Way's pattern speed, stellar and dark matter mass distribution". In: *MNRAS* 465, pp. 1621–1644. DOI: 10.1093/mnras/stw2819. arXiv: 1608.07954.

Zhoolideh Haghighi, M. H. and S. Rahvar (2017). "Testing MOG, non-local gravity and MOND with rotation curves of dwarf galaxies". In: *MNRAS* 468, pp. 4048–4055. DOI: 10.1093/mnras/stx692. arXiv: 1609.07851.

Akerib, D. S. et al. (2018). "Projected WIMP sensitivity of the LUX-ZEPLIN (LZ) dark matter experiment". In: *arXiv e-prints*, arXiv:1802.06039, arXiv:1802.06039. arXiv: 1802.06039 [astro-ph.IM].

Astropy Collaboration et al. (2018). "The Astropy Project: Building an Open-science Project and Status of the v2.0 Core Package". In: *Astronomic. J.* 156, 123, p. 123. DOI: 10.3847/1538-3881/aabc4f. arXiv: 1801.02634 [astro-ph.IM].

Benitez-Llambay, A. et al. (2018). "Baryon-induced dark matter cores in the EAGLE simulations". In: *ArXiv e-prints*. arXiv: 1810.04186.

Boran, S. et al. (2018). "GW170817 falsifies dark matter emulators". In: *Phys. Rev. D* 97.4, 041501, p. 041501. DOI: 10.1103/PhysRevD.97.041501. arXiv: 1710.06168 [astro-ph.HE].

Bose, S. et al. (2018). "No cores in dark matter-dominated dwarf galaxies with bursty star formation histories". In: *ArXiv e-prints*. arXiv: 1810.03635.

Buch, J., J. S. Chau Leung, and J. Fan (2018). "Using Gaia DR2 to Constrain Local Dark Matter Density and Thin Dark Disk". In: *ArXiv e-prints*. arXiv: 1808.05603.

Calore, Francesca, Pasquale Dario Serpico, and Bryan Zaldivar (2018). "Dark matter constraints from dwarf galaxies: a data-driven analysis". In: *Journal of Cosmology and Astro-Particle Physics* 2018, 029, p. 029. DOI: 10.1088/1475-7516/2018/10/029. arXiv: 1803.05508 [astro-ph.HE].

Du, N. et al. (2018). "Search for Invisible Axion Dark Matter with the Axion Dark Matter Experiment". In: *Phys. Rev. Lett.* 120, 151301, p. 151301. DOI: 10.1103/PhysRevLett.120.151301. arXiv: 1804.05750 [hep-ex].

Eilers, Anna-Christina et al. (2018). "The Circular Velocity Curve of the Milky Way from \$5\$ to \$25\$ kpc". In: *arXiv e-prints*, arXiv:1810.09466, arXiv:1810.09466. arXiv: 1810.09466 [astro-ph.GA].

Finch, A. and J. L. Said (2018). "Galactic rotation dynamics in f(T) gravity". In: *European Physical Journal C* 78, 560, p. 560. DOI: 10.1140/epjc/s10052-018-6028-1. arXiv: 1806.09677.

Genina, A. et al. (2018). "The core-cusp problem: a matter of perspective". In: *MNRAS* 474, pp. 1398–1411. DOI: 10.1093/mnras/stx2855. arXiv: 1707.06303.

Hagen, Jorrit H. J. and Amina Helmi (2018). "The vertical force in the solar neighbourhood using red clump stars in TGAS and RAVE. Constraints on the local dark matter density". In: *Astron. Astrophys.* 615, A99, A99. DOI: `10.1051/0004-6361/201832903`. arXiv: `1802.09291 [astro-ph.GA]`.

Han, D. and Y.-W. Lee (2018). "On the claimed X-shaped structure in the Milky Way bulge". In: *Rediscovering Our Galaxy.* Ed. by C. Chiappini et al. Vol. 334. IAU Symposium, pp. 263–264. DOI: `10.1017/S1743921317006470`. arXiv: `1801.03940`.

Kravtsov, A. V., A. A. Vikhlinin, and A. V. Meshcheryakov (2018). "Stellar Mass-Halo Mass Relation and Star Formation Efficiency in High-Mass Halos". In: *Astronomy Letters* 44, pp. 8–34. DOI: `10.1134/S1063773717120015`. arXiv: `1401.7329 [astro-ph.CO]`.

Li, P. et al. (2018). "Fitting the radial acceleration relation to individual SPARC galaxies". In: *Astron. Astrophys.* 615, A3, A3. DOI: `10.1051/0004-6361/201732547`. arXiv: `1803.00022`.

Monari, G. et al. (2018). "The escape speed curve of the Galaxy obtained from Gaia DR2 implies a heavy Milky Way". In: *Astron. Astrophys.* 616, L9, p. L9. DOI: `10.1051/0004-6361/201833748`. arXiv: `1807.04565 [astro-ph.GA]`.

Negrelli, C. et al. (2018). "Testing modified gravity theory in the Milky Way". In: *Phys. Rev. D* 98.10, 104061, p. 104061. DOI: `10.1103/PhysRevD.98.104061`. arXiv: `1810.07200`.

Nieuwenhuizen, T. M., A. Morandi, and M. Limousin (2018). "Modified Gravity (MOG) and its test on galaxy clusters". In: *Mon. Not. Roy. Astron.Soc.* DOI: `10.1093/mnras/sty380`. arXiv: `1802.04891`.

Planck Collaboration et al. (2018a). "Planck 2018 results. VI. Cosmological parameters". In: *ArXiv e-prints.* arXiv: `1807.06209`.

– (2018b). "Planck 2018 results. VI. Cosmological parameters". In: *ArXiv e-prints.* arXiv: `1807.06209`.

Posti, L. and A. Helmi (2018). "Mass and shape of the Milky Way's dark matter halo with globular clusters from Gaia and Hubble". In: *ArXiv e-prints.* arXiv: `1805.01408`.

Rodrigues, D. C. et al. (2018). "Absence of a fundamental acceleration scale in galaxies". In: *Nature Astronomy* 2, pp. 668–672. DOI: `10.1038/s41550-018-0498-9`. arXiv: `1806.06803`.

Sivertsson, S. et al. (2018). "The local dark matter density from SDSS-SEGUE G-dwarfs". In: *MNRAS* 478, pp. 1677–1693. DOI: `10.1093/mnras/sty977`. arXiv: `1708.07836`.

Somerville, R. S. et al. (2018). "The relationship between galaxy and dark matter halo size from z∼3 to the present". In: *MNRAS* 473, pp. 2714–2736. DOI: `10.1093/mnras/stx2040`. arXiv: `1701.03526`.

Sysoliatina, K. et al. (2018). "The local rotation curve of the Milky Way based on SEGUE and RAVE data". In: *Astron. Astrophys.* 614, A63, A63. DOI: `10.1051/0004-6361/201731143`. arXiv: `1802.07658 [astro-ph.GA]`.

Deason, Alis J. et al. (2019). "The local high velocity tail and the Galactic escape speed". In: *MNRAS*, p. 611. DOI: `10.1093/mnras/stz623`. arXiv: `1901.02016 [astro-ph.GA]`.

Kawata, D. et al. (2019). "Galactic rotation from Cepheids with Gaia DR2 and effects of non-axisymmetry". In: *MNRAS* 482, pp. 40–51. DOI: `10.1093/mnras/sty2623`. arXiv: `1803.05927`.